



The author of the doctoral dissertation: Aleksander Grabowski  
Scientific discipline: Civil Engineering, Geodesy and Transport

## **DOCTORAL DISSERTATION**

Title of doctoral dissertation: Numerical investigation of mesostructural phenomena in shear zone during confined granular flow in a laboratory-scale silo using Discrete Element Method

Title of doctoral dissertation (in Polish): Numeryczne badanie zjawisk mezostrukturalnych w strefie ścinania podczas ograniczonego przepływu materiału sypkiego w silosie w skali laboratoryjnej za pomocą Metody Elementów Dyskretnych

|                    |
|--------------------|
| Supervisor         |
| <i>signature</i>   |
| D.Sc. Michał Nitka |



**GDAŃSK UNIVERSITY  
OF TECHNOLOGY**

**EMPTY PAGE**



## **STATEMENT**

The author of the doctoral dissertation: Aleksander Grabowski

I, the undersigned, declare that I am aware that in accordance with the provisions of Art. 27 (1) and (2) of the Act of 4<sup>th</sup> February 1994 on Copyright and Related Rights (Journal of Laws of 2021, item 1062), the university may use my doctoral dissertation entitled:

Numerical investigation of mesostructural phenomena in shear zone during confined granular flow in a laboratory-scale silo using Discrete Element Method

for scientific or didactic purposes.<sup>1</sup>

Gdańsk,.....

.....  
*signature of the PhD student*

Aware of criminal liability for violations of the Act of 4<sup>th</sup> February 1994 on Copyright and Related Rights and disciplinary actions set out in the Law on Higher Education and Science (Journal of Laws 2021, item 478), as well as civil liability, I declare, that the submitted doctoral dissertation is my own work.

I declare, that the submitted doctoral dissertation is my own work performed under and in cooperation with the supervision of D.Sc. Michał Nitka.

This submitted doctoral dissertation has never before been the basis of an official procedure associated with the awarding of a PhD degree.

All the information contained in the above thesis which is derived from written and electronic sources is documented in a list of relevant literature in accordance with Art. 34 of the Copyright and Related Rights Act.

I confirm that this doctoral dissertation is identical to the attached electronic version.

Gdańsk,.....

.....  
*signature of the PhD student*

I, the undersigned, agree to include an electronic version of the above doctoral dissertation in the open, institutional, digital repository of Gdańsk University of Technology.

Gdańsk,.....

.....  
*signature of the PhD student*

---

<sup>1</sup> Art 27. 1. Educational institutions and entities referred to in art. 7 sec. 1 points 1, 2 and 4–8 of the Act of 20 July 2018 – Law on Higher Education and Science, may use the disseminated works in the original and in translation for the purposes of illustrating the content provided for didactic purposes or in order to conduct research activities, and to reproduce for this purpose disseminated minor works or fragments of larger works.

2. If the works are made available to the public in such a way that everyone can have access to them at the place and time selected by them, as referred to in para. 1, is allowed only for a limited group of people learning, teaching or conducting research, identified by the entities listed in paragraph 1.





GDAŃSK UNIVERSITY  
OF TECHNOLOGY

EMPTY PAGE



## DESCRIPTION OF DOCTORAL DISSERTATION

**The Author of the doctoral dissertation:** Aleksander Grabowski

**Title of doctoral dissertation:** Numerical investigation of mesostructural phenomena in shear zone during confined granular flow in a laboratory-scale silo using Discrete Element Method

**Title of doctoral dissertation in Polish:** Numeryczne badanie zjawisk mezostrukturalnych w strefie ścinania podczas ograniczonego przepływu materiału sypkiego w silosie w skali laboratoryjnej za pomocą Metody Elementów Dyskretnych

**Language of doctoral dissertation:** English

**Supervisor:** Michał Nitka

**Date of doctoral defense:**

**Keywords of doctoral dissertation in Polish:** strefa ścinania, materiał sypki, silos, mezostruktura, metoda elementów dyskretnych

**Keywords of doctoral dissertation in English:** shear zone, granular material, silo, mesostructure, discrete element method



GDAŃSK UNIVERSITY  
OF TECHNOLOGY

EMPTY PAGE

## *Abstract*

Shear zones are a fundamental phenomenon associated with the deformation of granular materials. Under significant load, these materials develop zones of plasticity concentrated in a narrow layer, characterized by a substantial increase in deformation and frictional resistance between the grains. The main objective of this doctoral thesis was to investigate the formation of shear zones in a cohesionless granular material (sand) at the grain-level using the Discrete Element Method (DEM) during silo flow in a laboratory-scale setup. The numerical model of the sand consisted of discrete particles with diameters enabling the analysis of shear zones at the mesoscale level. This approach allowed for detailed studies of the shear localizations and its impact on silo structures.

In the first part of the work, the numerical model was calibrated based on experimental studies available in the literature, such as tests in a triaxial compression apparatus and a direct shear apparatus. The calculations considered various initial densities, different load applied to the samples, and different surface geometries (e.g., their roughness) in the case of interface studies. The calibration tests focused on examining the shear zone at the boundary between the granular material and structures with varying geometries. Another part of the thesis involved experimental studies of shear zones at the contact area between sand and a sinusoidal corrugated surface using the direct shear apparatus. The Digital Image Correlation (DIC) method was used in the experiments.

In the second part of the work, the numerical results of quasi-static and gravitational flows in laboratory-scale silos were presented. The analysis examined the sand structure at the grain-level, determining distributions of such characteristics as grain displacements, grain rotations, voids between grains, contact force chains, and internal stresses within the material. The DEM results were directly compared with experimental results available in the literature. The flow studies considered various initial densities of the granular material, different silo wall roughness, and different locations and sizes of the silo discharge outlet. A good agreement was obtained between the discrete model and the experiments, both in terms of the forces acting on the silo structure and the propagation of shear zones in the granular material.

The results presented in the thesis can contribute to a better understanding of the phenomena occurring within the localization during granular material flows and the interaction of the material with silo walls. Finally, this can improve silo design safety.



## Streszczenie

Strefy ścinania są fundamentalnym zjawiskiem związanym z deformacją materiałów sypkich. W przypadku znacznego obciążenia w materiałach tych powstają strefy uplastycznienia skoncentrowane w wąskiej warstwie, charakteryzujące się znacznym przyrostem deformacji oraz oporem związanym z tarciem między ziarnami. Głównym celem pracy doktorskiej było zbadanie zjawiska powstawania stref ścinania w materiale sypkim (piasku) bez kohezji na poziomie ziarna przy zastosowaniu Metody Elementów Dyskretnych (ang.: DEM) w trakcie przepływów silosowych w skali laboratoryjnej. Model numeryczny piasku składał się z dyskretnych cząsteczek o średnicy umożliwiającej analizę stref ścinania na poziomie mezostruktury. Zastosowane podejście pozwoliło to na szczegółowe badania strefy lokalizacji oraz na określeniu sposobu jej oddziaływania na konstrukcje silosu.

W pierwszej części pracy model numeryczny został skalibrowany na podstawie badań doświadczalnych zawartych w literaturze, takich jak testy w aparacie trójosiowego ściskania i aparacie bezpośredniego ścinania. W obliczeniach uwzględniono różne początkowe zagęszczenie, różną wielkość obciążenia przyłożonego do próbek oraz różną geometrię powierzchni (np. jej szorstkość) w przypadku badań tzw. interfejsów. W testach kalibracyjnych nacisk położono na zbadanie strefy ścinania na granicy materiału sypkiego i struktury o zróżnicowanej geometrii. Elementem dodatkowym pracy są własne badania doświadczalne stref ścinania w strefie kontaktu między piaskiem a powierzchnią falistą sinusoidalną w aparacie bezpośredniego ścinania. W doświadczeniach użyto metody korelacji obrazów cyfrowych (ang.: DIC).

W drugiej części pracy przedstawiono rezultaty numeryczne quasi-statycznych oraz grawitacyjnych przepływów w silosach w skali modelowej. W trakcie analizy zbadano strukturę piasku na poziomie ziarna, czyli wyznaczono rozkłady m.in. przemieszczeń ziaren, obrotów ziaren, pustek między ziarnami, łańcuchów sił kontaktowych oraz naprężeń wewnątrz materiału. Wyniki DEM zostały bezpośrednio porównane z wynikami badań doświadczalnych zawartymi w literaturze. W przypadku badań przepływów uwzględniono różne początkowe zagęszczenie materiału sypkiego, różną szorstkość ścian silosu oraz różną lokalizację i wielkość otworu wysypowego silosu. Uzyskano dobrą zgodność rezultatów między dyskretnym modelem a doświadczeniami, zarówno pod względem sił działających na konstrukcję silosu, jak i propagacji stref ścinania w materiale sypkim.

Wyniki zawarte w doktoracie mogą posłużyć do lepszego zrozumienia zjawisk zachodzących wewnątrz lokalizacji w czasie przepływów materiałów sypkich oraz oddziaływania materiału na ściany silosów. Ostatecznie może to poprawić bezpieczeństwo projektowania konstrukcji silosowych.





## Acknowledgements

I would like to express my sincere gratitude to my supervisor, Professor M. Nitka, for his invaluable help, guidance, and support throughout my research. I also thank him for the insightful discussions in the field of discrete element method.

I extend my thanks to Professor J. Tejchman for his guidance, assistance, and engaging discussions.

I am also deeply grateful to Professor M. Wójcik for sharing his extensive knowledge of silo constructions and experimental methodologies.

Many thanks to my friends from the Gdańsk University of Technology (and beyond) for the valuable insights and engaging discussions.

Finally, my special thanks go to my family. I am deeply grateful to my parents for their unwavering support and motivation. I would like to express my sincerest gratitude to my wife, Ania, and our children, Miłek and Ida, for their patience, understanding, and constant smiles over the past few years.

The research work has been carried out within the project "*Autogenous coupled dynamic-acoustic effects in granular materials-experiments and combined DEM/CFD approach*" financed by the National Science Centre, Poland (NCN) (UMO-2017/27/B/ST8/02306).

Additionally, part of the research work has also been carried out within the project "*Experimental and numerical (DEM) analysis of the contact zone between granular material and corrugated surface during silo flow*" financed by the National Science Centre, Poland (NCN) (UMO-2022/45/N/ST8/03567).

# Contents

|  |             |
|--|-------------|
| <b>Statement</b>   | <b>iii</b>  |
| <b>Abstract</b>  | <b>vii</b>  |
| <b>Streszczenie</b>  | <b>viii</b> |
| <b>Acknowledgements</b>  | <b>x</b>    |
| <b>1 Introduction</b>  | <b>1</b>    |
| 1.1 Phenomenon and problem . . . . .                           | 1           |
| 1.2 Aims . . . . .   | 3           |
| 1.3 Thesis scope and structure . . . . .                       | 4           |
| 1.4 Innovative elements . . . . .                              | 5           |
| <b>2 State of the art</b>                                      | <b>7</b>    |
| 2.1 Introduction . . . . .                                     | 7           |
| 2.2 Experimental methods . . . . .                             | 7           |
| 2.3 Numerical methods . . . . .                                | 14          |
| 2.3.1 Continuum methods . . . . .                              | 14          |
| 2.3.2 Discrete methods . . . . .                               | 18          |
| 2.4 Research opportunities . . . . .                           | 21          |
| <b>3 Discrete Element Method</b>                               | <b>22</b>   |
| 3.1 Overview . . . . .   | 22          |
| 3.2 Calculation procedure . . . . .                            | 24          |
| 3.2.1 Motion integration . . . . .                             | 25          |
| 3.2.2 Contact model . . . . .                                  | 26          |
| 3.3 Particle shapes . . . . .                                  | 29          |
| <b>4 Preliminary discrete analysis of soil mechanics tests</b> | <b>32</b>   |
| 4.1 Triaxial compression test . . . . .                        | 34          |
| 4.1.1 Introduction . . . . .                                   | 34          |
| 4.1.2 Numerical model and methodology . . . . .                | 34          |
| 4.1.3 Numerical results . . . . .                              | 36          |
| 4.1.4 Summary . . . . .  | 41          |
| 4.2 Direct shear test . . . . .                                | 43          |
| 4.2.1 Introduction . . . . .                                   | 43          |
| 4.2.2 Numerical model and methodology . . . . .                | 43          |
| 4.2.3 Numerical results . . . . .                              | 45          |
| 4.2.4 Summary . . . . .  | 60          |



|          |   |            |
|----------|---|------------|
| 4.3      | Interface shear test between sand and surface of different roughness . . . . .          | 62         |
| 4.3.1    | Introduction . . . . .  | 62         |
| 4.3.2    | Numerical model and methodology . . . . .   | 62         |
| 4.3.3    | Numerical results . . . . .   | 65         |
| 4.3.4    | Summary . . . . .   | 90         |
| 4.4      | Interface shear test between sand and corrugated sinusoidal surfaces . . . . .          | 92         |
| 4.4.1    | Introduction . . . . .  | 92         |
| 4.4.2    | Numerical model and methodology . . . . .   | 94         |
| 4.4.3    | Numerical results . . . . .   | 96         |
| 4.4.4    | Summary . . . . .   | 112        |
| <b>5</b> | <b>Modeling of granular flow in laboratory-scale silo with DEM</b>                      | <b>113</b> |
| 5.1      | Introduction . . . . .  | 113        |
| 5.2      | Numerical model and methodology . . . . .   | 114        |
| 5.3      | Numerical results . . . . .   | 118        |
| 5.3.1    | Quasi-static flow in silo . . . . .   | 118        |
| 5.3.2    | Gravitational flow in silo . . . . .  | 136        |
| 5.4      | Summary . . . . .   | 160        |
| <b>6</b> | <b>Conclusions and future research directions</b>                                       | <b>162</b> |
| 6.1      | Conclusions . . . . .   | 162        |
| 6.2      | Future research directions . . . . .  | 164        |
| <b>A</b> | <b>Experimental analysis of interface behavior between sand and corrugated surfaces</b> | <b>165</b> |
| A.1      | Introduction . . . . .  | 165        |
| A.2      | Experimental methods and materials . . . . .  | 165        |
| A.2.1    | Shear apparatus and granular material . . . . .   | 165        |
| A.2.2    | Interface shear test procedure . . . . .  | 170        |
| A.2.3    | Digital Image Correlation (DIC) . . . . .   | 170        |
| A.3      | Experimental results . . . . .  | 171        |
| A.3.1    | Evolution of mobilized shear stress and volumetric strain . . . . .                     | 172        |
| A.3.2    | Friction of sand on corrugated sinusoidal surface . . . . .                             | 173        |
| A.3.3    | DIC analysis . . . . .  | 174        |
| A.4      | Summary . . . . .   | 183        |
|          | <b>Bibliography</b>   | <b>185</b> |
|          | <b>Publications</b>   | <b>200</b> |
|          | <b>Conferences</b>  | <b>201</b> |
|          | <b>List of Symbols</b>  | <b>202</b> |
|          | <b>List of Figures</b>  | <b>223</b> |
|          | <b>List of Tables</b>   | <b>224</b> |



## Chapter 1

# Introduction

### 1.1 Phenomenon and problem

Silos are engineering structures commonly used in the construction, chemical, and agricultural industries for storing various types of granular materials (Jenike, 1964; Rotter, 2001). They are mostly constructed of materials such as steel, concrete, and aluminum. In general, the construction of a silo is expected to withstand the loads exerted on the structure by the bulk and powders stored inside. Unfortunately, the structural analysis of these constructions is not always straightforward due to the complex behavior of the granular material during silo filling, storage, and discharge. Although some aspects of silo design are relatively well characterized, many issues related to the granular flow are still not fully covered and need to be adequately analyzed. The characteristic phenomena that complicate the analysis of the granular flow in the silo are, for example, a sudden and strong increase of loads exerted on the walls, different flow patterns, pressure fluctuations, and formation and propagation of shear zones (Gutfraind and Pouliquen, 1996; Wójcik and Tejchman, 2009; Tejchman and Wójcik, 2011; Tejchman, 2013).

Generally, silo flow characteristics depend on the current state of granular material, including factors such as its type and density. At the same time, these flow characteristics are significantly influenced by various parameters of the silo's structural elements, including the geometry and profile of the walls, the size and location of the outlet, and the geometry of the hopper. The structural analysis of these systems requires a comprehensive understanding of several complex phenomena that occur during granular flow. The fundamental one, inherent to the flow of bulk materials in a silo, is the localization of deformation in the form of narrow zones of shearing granular material, known as shear zones (Cutress and Pulfer, 1967; Drescher et al., 1978; Nedderman and Laohakul, 1980; Michalowski, 1987; Tejchman, 1989). Inside these zones, granular media is divided into two quasi-rigid blocks of material separated by the region of pronounced volume changes and intense shearing due to differential motion of the bulk material (Vardoulakis, 1980; Uesugi and Kishida, 1986b; Tejchman and Wu, 1995; Desrues et al., 1996).

During the flow in silo, the deformation of granular material is strictly associated with the formation of shear zones. In the case of silo discharge, shear zones are either located in the interior domain or at interfaces where the granular material interacts with silo structure (Moore et al., 1984; Uesugi and Kishida, 1986b; Tejchman and Wu, 1995). In general, when the flow is initialized, these zones occur primarily in the region adjacent to the outlet. As the flow continues, the granular material tends



to subsequently form patterns of shear zones that propagate through the flowing bulk. As the strain localizations develop towards the upper boundary of the granular mass, the bulk solid moves towards the outlet. At the same time, the shear zones may occur in the region adjacent to the silo walls where the granular material interacts with structural elements (Wójcik and Tejchman, 2009). The trajectories of the shear zones may vary, depending on various characteristics of the system such as wall roughness or silo geometry (Cutress and Pulfer, 1967; Michalowski, 1987). Numerous research studies have indicated that the formation of shear zones is closely related to the flow type (Moore et al., 1984; Wójcik and Tejchman, 2009; Tejchman, 2013). As a result, strain localization patterns are difficult to capture and characterize. Furthermore, the behavior of these zones is crucial, since the failure of granular media is usually closely related to this phenomenon, and therefore it should be considered in the analysis (Vardoulakis and Graf, 1985).

In the case of silo flow, the appearance of these zones can lead to the unstable behavior of granular material. During discharge, the occurrence of shear zones creates significant discontinuities and uneven distribution of the density within the flowing granular material (Cutress and Pulfer, 1967; Drescher et al., 1978). As a result the pressures acting on the silo structure are also of nonuniform nature usually showing significant fluctuations in the region from where the shear zone propagates (Gutfraind and Pouliquen, 1996; Wójcik and Tejchman, 2009; Grudzien et al., 2012). Therefore, one of the key factors affected by the occurrence of shear zones are the loads acting on the silo structure. The locations of these shear zones play a major role in estimating the magnitude of loads transferred from the granular material to the construction (Moore et al., 1984). This aspect is crucial because the loads exerted on the silo structure are one of the fundamental parameters in calculating the silo wall thickness. Moreover, the underestimation of nonuniform and dynamic loading can have structural implications potentially leading to the damage or failure of the silo structure.

To fully understand the mechanism of shear zone formation and propagation, it is necessary to have knowledge not only of the overall state of the granular material stored inside the silo structure, but also of the granular properties at the grain-level. These properties were comprehensively studied under various conditions in numerous studies. Inside the shear zone, significant changes in the void ratio have been observed, e.g. during the shearing under moderate confining pressure initially dense samples show dilatancy, and initially loose samples show contraction. Despite the differences in initial void ratio, the granular material inside the shear zone tends to reach the same constant value of porosity during shearing (Desrues et al., 1996). Within the localization, the grain rotations and the forces between them increase significantly. As a result, quasi-rigid columns are established with distinct grains. During shearing, the differential motion of the bulk causes these columns to form and collapse sequentially (Oda et al., 2004; Rechenmacher, 2006; Chupin et al., 2011). The current knowledge is, that the shear zone characteristics, such as its thickness depends on the individual grain characteristics (Tejchman and Wu, 1995; Fenistein and Hecke, 2003; Hall et al., 2010; Saleh et al., 2018). Therefore the determination of the grain-level properties, e.g. particles rotations, displacements, and forces between them is of major importance for the description of the mechanics of

the granular media-silo structure system.

Over the decades, numerous methods have been used to study the characteristics and phenomena associated with silo flow. The most popular approach has been laboratory investigations (Jenike, 1961; Cutress and Pulfer, 1967; Nedderman and Laohakul, 1980; Michalowski, 1987; Tejchman, 1989; Rotter et al., 1998) and numerical methods in the field of continuum mechanics (Tejchman, 1989; Böhrnsen et al., 2004; Więckowski, 2004; Zhu et al., 2008; Wójcik, 2008; Wójcik and Tejchman, 2009; Tejchman, 2013). Unfortunately, these methods do not provide insight into the behavior that occurs at the scale of individual grains. New possibilities came with the Discrete Element Method (DEM) (Cundall and Strack, 1979), which brought a completely new point of view to the problem of deformation of granular material during flow in a silo. Today, thanks to advances in computational efficiency, this method allows to study the microstructure and mesostructure of the flowing bulk material, taking into account the grain-level behavior of the granular material within the localized zones and their impact on the flow and the silo structure. The discrete approach allows to describe in detail the mechanism of strain localization within the heterogeneous material. Therefore, this method is perfectly suited to study the shear zone formation and propagation during confined flow in silo.

## 1.2 Aims

The main objective of the research presented in the thesis is to use the Discrete Element Method to study the granular flow in a silo, by taking into account the formation and propagation of shear zones. While this method has been used in the past for the simulations of granular flow with the focus on flow patterns, discharge rate, wall pressure distributions, and segregation phenomena, its application to the study of shear zone initiation and propagation has been limited. In this thesis, special attention has been paid to the mesoscopic characteristics of deforming granular material which are fundamental to capture the mechanical behavior of granular flow. As a result, the relationship between the grain-level characteristics of the bulk solid and the macroscopic behavior of the granular flow and its effect on the silo structure was captured.

In order to achieve the objectives, a series of discrete simulations has been carried out, taking into account different initial states and boundary conditions. This allowed a comprehensive analysis of the granular material deformation and its effect on the silo structure. The study presented in the thesis was divided into two parts and includes:

1. Discrete simulations of tests in the field of soil mechanics to calibrate and validate the local parameters of the discrete model. A comprehensive study of various tests, such as triaxial compression, direct shear and interface shear test was carried out on cohesionless sand. The influence of the grain-level characteristics on the global bulk material response was evaluated for different initial conditions, such as the initial void ratio of granular specimen or the magnitude of loads applied to it. The soil mechanics tests focused on analyzing the shear

zone at the boundary between the granular material and structures with varying geometries.

2. Discrete simulations of confined granular flow of cohesionless sand in a laboratory-scale silo to analyze the effect of shear zone formation on the behavior of the bulk solid-silo structure system. The investigation was performed for rectangular silo made of perspex for two types of flow: a quasi-static flow in silo with slowly movable bottom and gravitational flow. During the simulations, different boundaries and initial conditions were studied, such as various roughness of the wall, initial porosity, and outlet location and size.

The discrete model used during the investigation has been experimentally verified and found to be in good agreement with laboratory data.

### 1.3 Thesis scope and structure

The thesis includes 6 chapters and one appendix. A brief overview of the chapters is described as follows.

Chapter 1 introduces the phenomenon, outline the research problems, presents the objectives of the study and describes the innovative elements of the work.

Chapter 2 presents a literature review on the shear zone phenomena occurring during silo flow. Selected experimental studies were referenced and discussed to evaluate the impact of shear zone formation and propagation on the mechanics of the bulk material-silo structure system. Following this, emphasis was placed on the results obtained from numerical models, including both continuum and discrete approaches.

Chapter 3 outlines the basic formulations of the Discrete Element Method for granular materials in the YADE environment. In addition to a brief historical overview of discrete methods, the chapter covers several key aspects necessary for the calculation of valid results. This includes an introduction to contact laws and motion integration scheme within discrete software, as well as a methodology for representing particle shapes.

Chapter 4 presents the selected preliminary discrete simulations of selected soil mechanics tests. First, the chapter describes a comprehensive parametric study of the local input material parameters for DEM and their effect on the global bulk material response. Then, the procedure for discrete model calibration based on the comparison between laboratory and numerical results is presented. On the basis of the parametric study, the local parameters are determined using a triaxial test. Finally, direct shear and interface shear tests were studied, taking into account different initial conditions to analyze the ability of the model to reproduce the shear zone formation within the granular material. Finally, based on these latter tests, the mesostructure of the shear zone was studied.

Chapter 5 presents the results of the discrete simulations of the confined granular flow in the laboratory-scale silo. The investigation was performed for rectangular silo made of perspex for a quasi-static and gravitational confined flow. During the simulations, the forces on the silo bottom and side walls were measured in order to compare them with experimental results available in the literature. In addition,



during the silo discharge, the particle-level characteristics within the granular material were evaluated, with particular attention to the shear zones. The formation and propagation of these zones were established for different types of granular material flow. The simulations were performed for different initial conditions, such as different wall roughness, initial porosity, and outlet location and size.

Chapter 6 summarizes the general conclusions and states recommendations for future work.

Appendix A presents an investigation of a typical interface mechanism occurring during the flow in a silo made of corrugated steel sheets supported by thin-walled columns. This mechanism was captured during interface shear tests between granular material (cohesionless sand) and a sinusoidal corrugated surface in a direct shear apparatus. The characteristics of the shear zone were determined, allowing for the description of the relationship between the surface geometry and the forces exerted on the structure. The experimental study provided a basis for the calibration of a discrete element model. In addition, the study presented in the appendix presents a path for the natural continuation of the issues discussed in earlier chapters of the thesis regarding shear zone formation in silo structures.

## 1.4 Innovative elements

Although the phenomena related to silo flow have been studied experimentally and numerically in numerous research works, there are few key aspects of the investigation presented in the thesis that make the results of the study unique. The innovative elements of the thesis are:

1. Application of the Discrete Element Method to the simulations of flows in silo with the particle size allowing for a detailed macro- and mesoscopic analysis of the deforming granular material. In simulations the shear zones were established both within the granular material and in the regions adjacent to the silo walls. Discrete approach allowed for the investigation of the grain-level characteristics of the granular material, such as particle displacements, rotations, void ratio distribution and forces between the grains. The relation between these characteristics and the bulk solid deformation was examined. During the analysis, the influence of shear zone propagation on the flow pattern and the pressures exerted on the walls were investigated.
2. Comprehensive discrete analysis of granular material deformation during shearing in numerous soil mechanics tests. The analysis allowed for a detailed study of the shear zone formation in a controlled manner, where the shear zone location is known from the beginning due to the geometric constraints. The simulations were performed for triaxial compression, direct shear and interface shear tests, under various boundary conditions. The real-size particles allowed for a detailed mesoscopic analysis. The discrete calculations provided insight into the behavior of the granular material in the shear zone in terms of breakable force chains, sphere rotations, and empty voids distribution.
3. Comparative macro- and mesoscale analysis of granular material behavior composed of perfectly spherical particles with rotational resistance versus

clumped particles composed of spheres. The real-size particles were used in both simulations allowing for an investigation of shape significance in the discrete simulations of the granular material. The emphasis was placed on studying the shear zone at the interface between the granular material and the structure with different roughness. In addition, the grain-level characteristics were used to propose micropolar boundary conditions at the interface for the 2D continuum models.

4. Experimental and numerical study of the interface between granular material (cohesionless sand) and sinusoidal corrugated surfaces of different wave depths in a direct shear apparatus. Emphasis was placed on the determination of the extent of shear localization within the granular material and on the corrugated surface based on the overall strength of the interfaces and on the deformation of the sand. In the experimental part, the displacements and strains of the granular material were calculated using the Digital Image Correlation (DIC) method. As a result, the study allowed to qualitatively and quantitatively determine the wall contact factor as a function of the surface profile.

The results presented in this thesis have been partially covered in six published papers, among four of them were published in three JCR journals from Web of Science database:

1. *Acta Geotechnica* (Grabowski et al., 2020),
2. *Acta Geotechnica* (Grabowski et al., 2021a),
3. *Powder Technology* (Nitka and Grabowski, 2021) and
4. *Computer and Geotechnics* (Grabowski et al., 2021b),

and two in Web of Science database:

1. *Studia Geotechnica et Mechanica* (Grabowski and Nitka, 2020) and
2. *Multiscale Processes of Instability, Deformation and Fracturing in Geomaterials* (Grabowski et al., 2022).



## Chapter 2

# State of the art

### 2.1 Introduction

The flow of granular materials in silo constructions has been studied extensively by many scientists and engineers over the past several decades. The investigation has included the study of the various phenomena associated with granular flow, such as shear zone formation, stress fluctuations, wave propagation, velocity discontinuities, and many others (Janssen, 1895; Jenike, 1961; Walker, 1966; Cutress and Pulfer, 1967; Pariseau, 1969; Walters, 1973; Michalowski, 1987; Tejchman, 1989; Lee, 1994; Rotter et al., 1998; Chen et al., 2005; Wójcik and Tejchman, 2009; Wiącek et al., 2021). Despite this extensive research, there are still many challenges and issues in silo design that need to be adequately analyzed. This literature review does not attempt to provide a comprehensive overview of the entire field of research on the behavior of granular materials. Instead, this chapter focuses on specific topics that are directly relevant to the research discussed in this thesis, i.e., the formation of shear zones and their effect on the behavior of granular flow in the silo.

The following chapter presents the literature on this subject, including studies of this problem through laboratory experiments and theoretical analysis, using both continuum and discrete approaches. In each section, the publications related to shear zone formation in the field of soil mechanics as well as in the field of confined granular flow are presented.

### 2.2 Experimental methods

#### Shear zone formation in granular materials

The deformation of granular materials, with special attention to the analysis of the shear zone, has been studied in numerous experimental studies using different measurement techniques, such as radiography (Cutress and Pulfer, 1967; Michalowski, 1987), computed tomography (Desrues et al., 1996; Hall et al., 2010) and stereophotogrammetry (Desrues and Viggiani, 2004). Some contributions on strain localization have been made based on the investigation of various problems under confined boundaries and quasi-static conditions, e.g. biaxial tests (Roscoe, 1970; Vardoulakis and Graf, 1985; Han and Drescher, 1993; Oda and Kazama, 1998; Desrues and Viggiani, 2004), interface shear tests (Moore et al., 1984; Uesugi et al., 1988; Hu and Pu, 2004), triaxial compression tests (Roscoe, 1970; Oda, 1972; Desrues et al., 1985; Desrues et al., 1996), geotechnical structures, such as retaining walls and others

(Niedostatkiewicz et al., 2011; Leśniewska et al., 2020). In general, in these experiments, a given state is imposed on the granular sample with the use of boundaries (e.g. plates, walls and membranes), resulting in deformation of the bulk media. These studies allowed to measure the strength and deformation of the materials, as well as the basic characteristics of the shear zones, such as its thickness and orientation, localization criteria, void ratio distribution and contact force network. The simplicity of these laboratory tests allowed to better understand the mechanism of strain localization.

During the experiments, the origin and evolution of the shear zone was described, showing that the different localization trajectory significantly depend on the boundary conditions (Desrues et al., 1996; Desrues and Viggiani, 2004). The studies showed that the shear zone is not always a clear straight line, but it can be slightly curved (Oda and Kazama, 1998). In addition, it was shown that the shear zone does not start simultaneously at each point, but propagates from an initiating point in a constant direction. The initiation of the localization was observed from the beginning of the deformation process. Therefore, the shear zone can be established in the hardening part of the test, far before the peak stress (Desrues et al., 1985; Hall et al., 2010).

Within the shear zone, significant changes in the behavior of grains have been noticed. Noticeable rotations of individual grains have been observed in numerous studies Tejchman, 1989; Oda and Kazama, 1998. Hall et al., 2010 tracked the deformation of sand during triaxial compression test, with special emphasis on the kinematics of individual grains. This was possible through the use of X-ray microtomography ( $\mu$ CT) imaging combined with Volumetric Digital Image Correlation (V-DIC) technique. Grains within the shear zone showed a sudden increase in rotation at the beginning of the granular material deformation, while grains outside the shear zone showed a relatively constant increase in rotation as the test progressed (Figures 2.1 and 2.2).

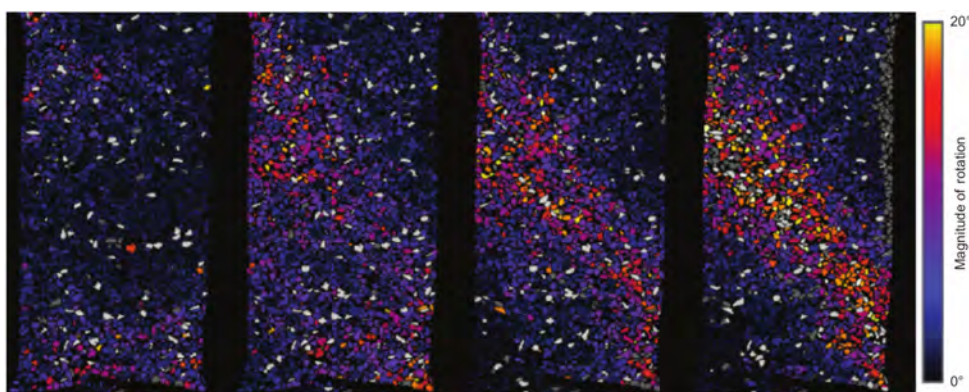


Figure 2.1: Magnitude of the grain rotations plotted for vertical slices through the middle of the specimen during triaxial compression test obtained with V-DIC (Hall et al., 2010).

In addition, inside the localized region a local changes in the porosity were observed (Oda and Kazama, 1998; Desrues et al., 1996). The limit void ratio was measured during the shearing, which means that the porosity within the shear zone shows a strong tendency to stabilize in the residual phase of shearing (Figure 2.3). Initially loose samples within the localization exhibit local contraction and initially

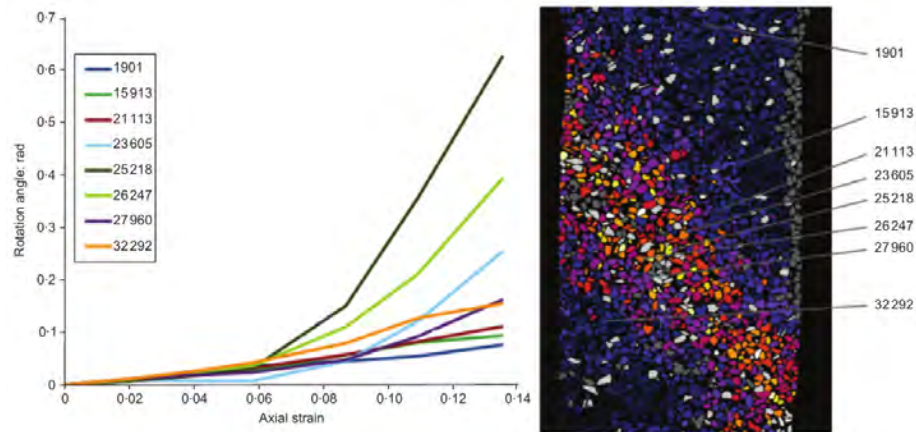


Figure 2.2: History of rotations for a selected grains positioned inside and outside the shear zone during the triaxial compression test (left: plot of total rotations for each selected grain as a function of nominal axial strain of the specimen, and right: the selected grains indicated on the located through a slice of a sample) (Hall et al., 2010).

dense sample shows dilatancy. Numerous research works have shown that the large voids in the localized region of granular material are caused by the dilatancy taking place within the zone (Oda et al., 2004; Rechenmacher, 2006; Chupin et al., 2011). During shearing, the particles inside the shear zone rearrange to form columnar structures responsible for stress transfer (Figure 2.4). Due to the differential motion of the bulk material, these columns are repeatedly broken and re-established in a sequential manner. In addition, the approximate shape and location of the shear zone can be determined based on the laboratory analysis of the contact force network (Figure 2.5) (Leśniewska et al., 2020).

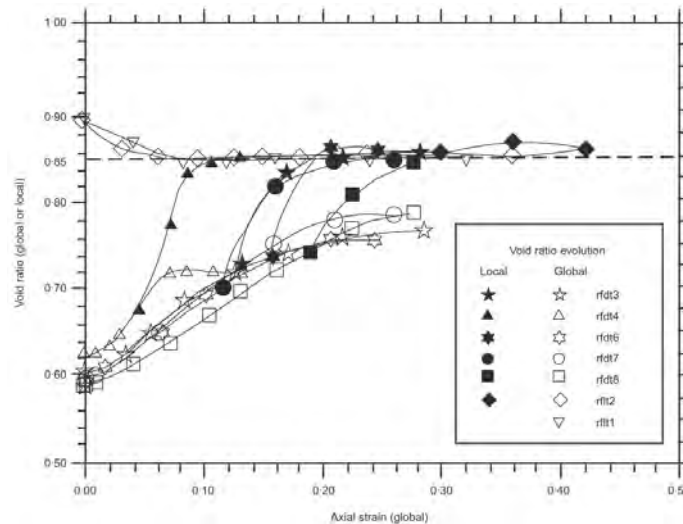


Figure 2.3: Global and local evolution of the void ratio in loose and dense sand specimens submitted to axisymmetric triaxial test (Desrues et al., 1996)

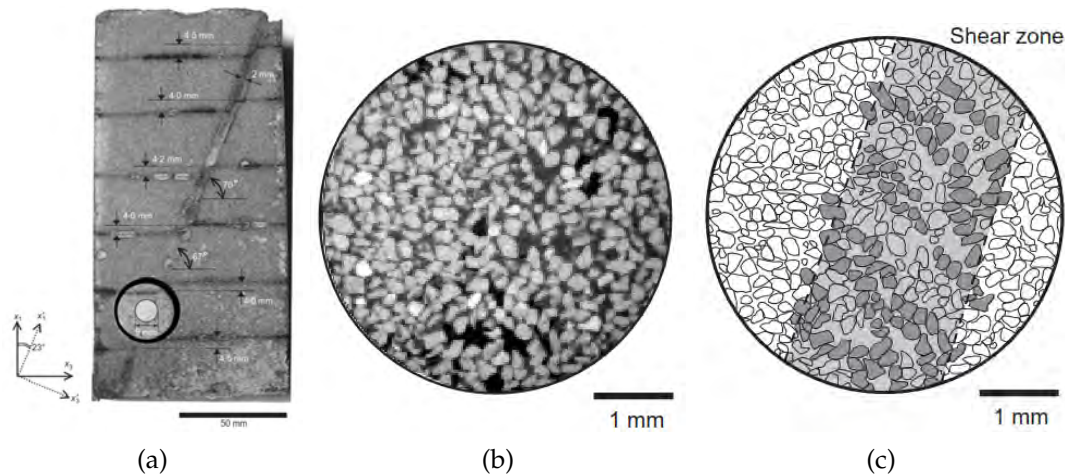


Figure 2.4: A photograph of a shear zone obtained during plain strain compression test in: a) a cylindrical sample of 24 mm diameter and 38 mm height, b) a magnified image of the mesostructure within the localized zone and c) a sketch of the shear zone to emphasize the column-like structures noted (Oda et al., 2004).

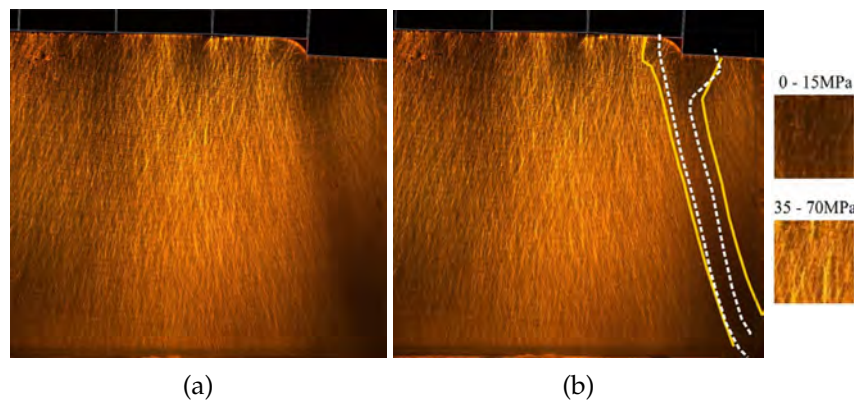


Figure 2.5: Raw photo-elastic image of the force network in granular media composed of: a) glass beads with b) approximate localization of the shear strain in the active earth pressure state (the brightest areas represent the strongest grain contacts, while the darkest areas represent the weaker ones) (Leśniewska et al., 2020).

### Shear zone formation in granular materials during confined flow in silo

The confined flow in silos with special attention to the initiation and development of the shear zones has been extensively studied in numerous laboratory investigations (Cutress and Pulfer, 1967; Nedderman and Laohakul, 1980; Michalowski, 1987; Tejchman, 1989; Niedostatkiewicz et al., 2011; Grudzien et al., 2012). Research on this subject has been carried out primarily through experiments in laboratory-scale silos, but also includes investigations in full-scale silos. A number of different methods have been used to study the mechanism of strain localization. These methods were mainly based on the description of the deformation of the granular material during the flow. For example, the observation of shear zones was performed using layers of colored sand (Takahashi and Yanai, 1973; Stazhevskii, 1982; Tejchman, 1989), x-rays (Cutress and Pulfer, 1967; Michalowski, 1984; Michalowski, 1987; Michalowski, 1990; Drescher, 1992; Drescher, 1998), electrical capacitance tomography (ECT) (Grudzien et al., 2012) and Particle Image Velocimetry (PIV) technique

(Slominski et al., 2007). These studies have provided valuable data on shear zone characteristics such as orientation, width, and thickness, as well as on various patterns of shear zone propagation.

The primary method employed for the purpose of investigation of strain localization involved measurements of the density distribution within the granular material using X-rays. Studies of shear zone propagation mechanism with the use of x-radiographs on laboratory-scale silos and hoppers were conducted by Cutress and Pulfer (1967) and Michalowski (1984) and Michalowski (1987). Each of these works captured shear zones in form of discontinuous lines of low granular material density formed during silo flow. In the papers, different patterns of shear zones were distinguished for two different types of flow. Both mechanisms have been described by Michalowski (1987) in the case of granular flow in converging plane hopper silo. In the first case, at the beginning of the mass flow, two shear zones appear in the region adjacent to the outlet (Figure 2.6). As the flow progresses, these discontinuities propagate upward, cross each other and reach the opposite walls. Upon reaching the walls, another pair of shear zones is initiated. As the discharge continues, subsequent shear zones propagate toward the upper boundary of the granular mass. On the other hand, it was shown that the propagation of shear zones in funnel flow differs from the mass mechanism (Figure 2.7). First, a funnel zone is established at the beginning of the flow, characterized by significant velocity of the grains. The flowing material is separated from the stagnant one with two vertical and almost parallel shear zones. During the discharge, the funnel zone propagates towards the upper parts of the mass, gradually extending its range. As the flow continues, subsequent shear zones are formed within the granular material, similar to the formation of discontinuities during mass flow. Observations from x-radiographs taken during the discharge of the model silo showed that localization zones appear gradually rather than simultaneously. Furthermore, they form sequentially as the granular flow progresses (Figure 2.8). Similar behavior was observed in tests of laboratory scale silo by Slominski et al. (2007).

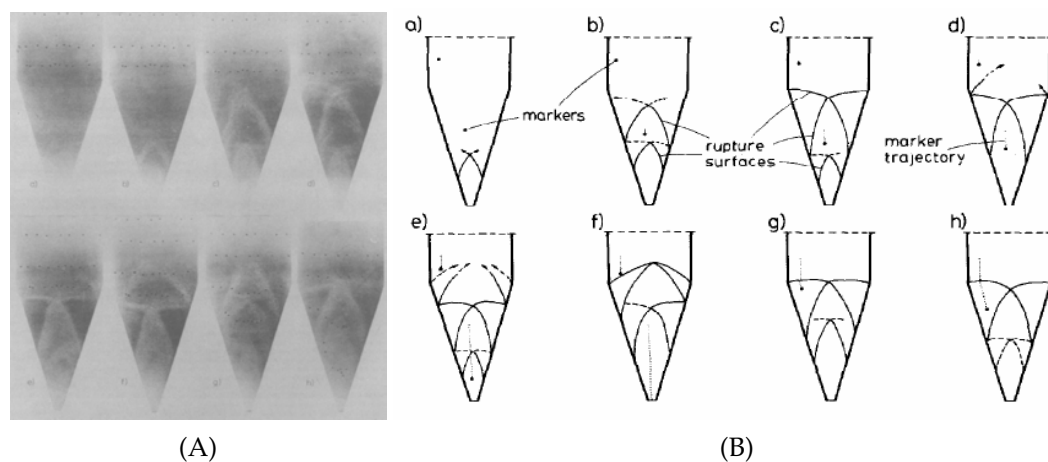


Figure 2.6: Illustrations of: A) x-radiographs and B) schemes of shear localizations during mass flow of sand in a plane parallel/converging silo (Michalowski, 1987)

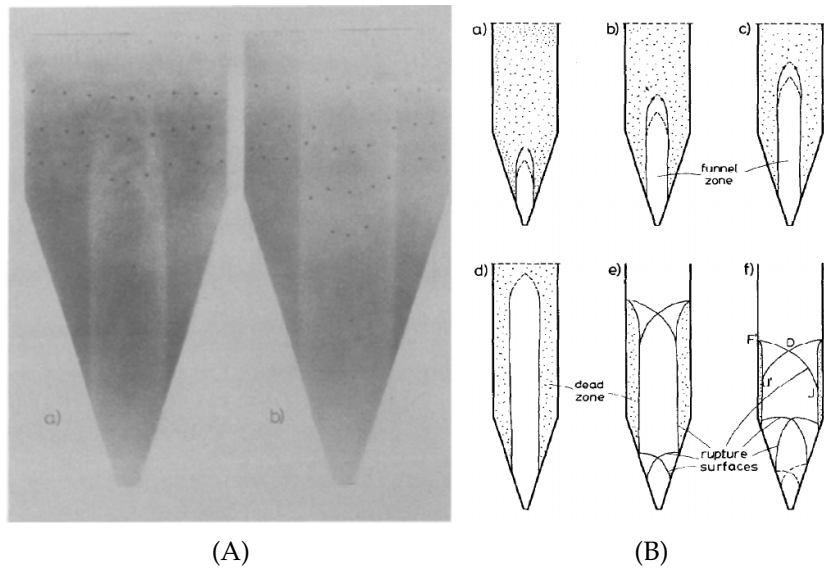


Figure 2.7: Illustrations of: A) x-radiographs and B) schemes of shear localizations during funnel flow of sand in a plane parallel/converging silo (Michalowski, 1987)

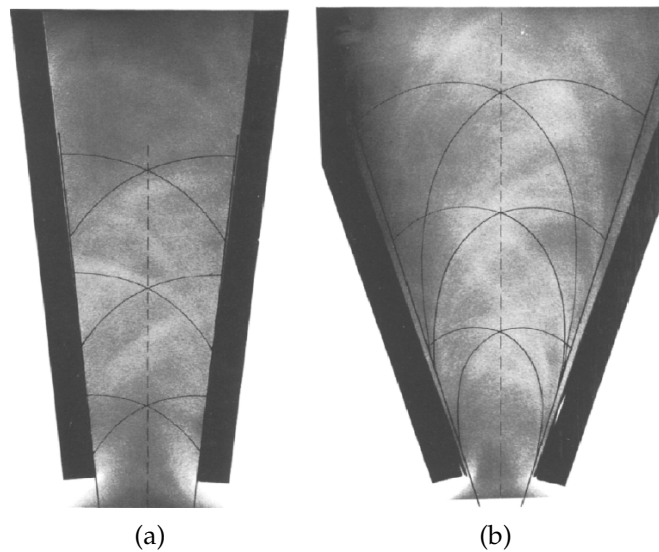


Figure 2.8: X-radiographs of shear localizations during: a) mass and b) funnel flow of dry powder in a hoppers with different wall inclination (Cutress and Pulfer, 1967)

Another technique used to estimate shear zone characteristics in laboratory-scale silos are colored horizontal layers of bulk material. It is the simplest method to study the deformation of granular material during flow. It was used by Tejchman (1989), Slominski et al. (2007), and Tejchman (2013) to analyze the confined granular flow for silos with different width, wall inclination and wall roughness. The study was mainly focused on the determination of the resultant forces acting on the walls, but it also included the investigation of deformation measurements in dry cohesionless sand during quasi-static flow. The displacement profiles showed the presence of

shear zones. The granular flow of the initially loose sample was considered symmetrical with a narrow shear zone near the walls (Figure 2.9a,b). On the contrary, for the initially dense sand, the flow became gradually asymmetric with increasing wall roughness. The asymmetry was caused by the propagation of the shear zones towards the upper surface of the sand (Figure 2.9c,d). The flowing and stagnant regions of granular material are separated by the successive formation of shear zones. During the discharge of the hopper with very rough walls filled with initially dense sand, a characteristic stair-like displacement profile was observed (Figure 2.9d). Similar shear zone characteristics were obtained by means of velocity profiles measured during the flow by Nedderman and Laohakul (1980).

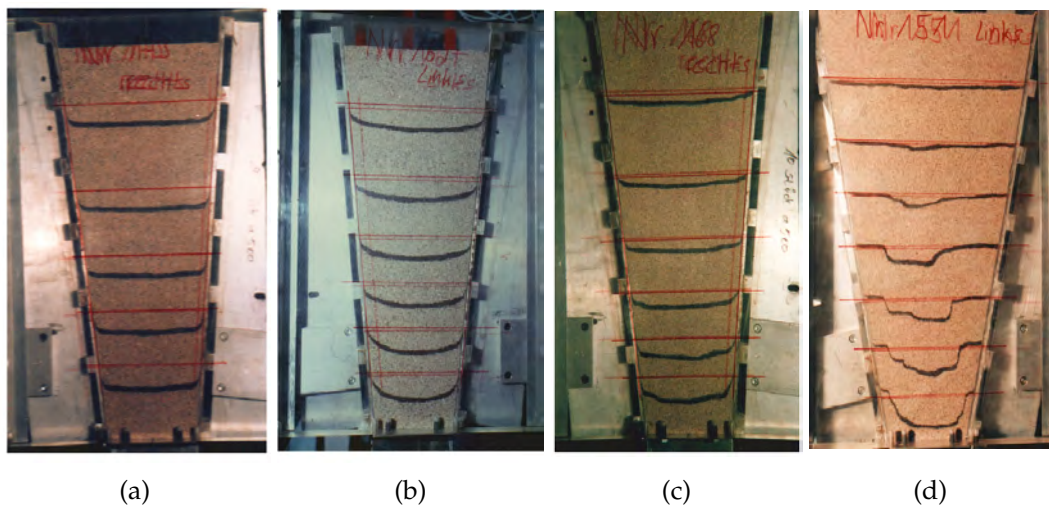


Figure 2.9: Measured displacements in model silo with convergent walls using colored layers during quasi-static flow for different initial conditions: a) smooth walls and initially loose sand, b) rough walls and initially loose sand, c) rough walls and initially dense sand and d) very rough walls and initially dense sand (wall inclination  $\alpha=5.6^\circ$ ) (Tejchman, 1989)

The formation of shear zones under various conditions was studied using the PIV technique by Slominski et al. (2007). During the laboratory experiments in a model silo, the shear zone localization and thickness were captured for initially loose and initially dense sand (Figure 2.10). In the study, the shear zones were located mainly in the area adjacent to the silo walls. The shape of the shear zones during the flow of initially loose and initially medium-dense sand was quite chaotic. Only in the case of initially dense sand the shape of the shear zones was more regular, similar to a parabolic shape. Based on the PIV results, the shear zone thickness was measured. It ranged from 7 mm ( $=7 \times d_{50}$ ) for initially dense sand and smooth walls to 18 mm ( $=18 \times d_{50}$ ) for initially loose sand and very rough walls.

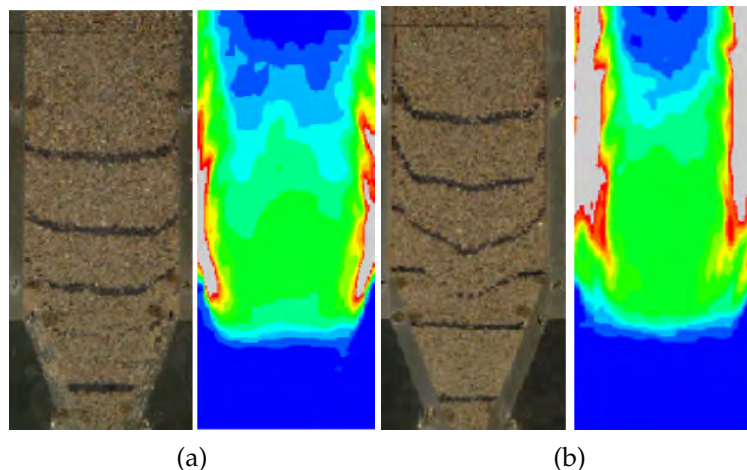


Figure 2.10: Shear zones during mass flow visualized by displacements profiles in sand (left) and distribution of deviatoric strain obtained with PIV technique (right) for: a) initially dense sand and smooth walls and b) initially dense sand and very rough walls (Slominski et al., 2007).

## 2.3 Numerical methods

### 2.3.1 Continuum methods

#### Shear zone formation in granular materials

Despite their heterogeneous, discontinuous and nonlinear nature, granular media can be reasonably described by continuum methods, which are mainly based the Finite Element Method (FEM). The great advantage of the FEM is the possibility to model large systems and to calculate deformations and stresses in each point of granular material (Tejchman, 2013). This is the most common and powerful method for simulating the behavior of granular materials consisting of billions of particles. The mechanism of strain localization was extensively studied using different FE approaches. To study the shear zones formation an enhanced continuum models including a characteristic length of a microstructure were used. The most common approach involves elasto-plastic constitutive law (Lade, 1977; Desrues and Chambon, 1989; Vardoulakis et al., 1992) and hypoplastic constitutive law (Mühlhaus, 1990; Tejchman and Wu, 1995; Bauer, 1996) with the aid of polar, non-local, second-gradient, and viscous theory.

The FE calculation of the strain localization characteristics involved different tests commonly employed in soil mechanics, such as simple and direct shear test (Tejchman and Wu, 1995; Tejchman and Bauer, 2005), plane strain compression test (Tejchman, 2004; Tejchman and Górski, 2009), biaxial test (Vardoulakis and Graf, 1985; Mühlhaus and Vardoulakis, 1987), interface shear test (Tejchman and Wu, 2010), and others. The thickness of the shear zone was found to be of few grain diameters (Mühlhaus and Vardoulakis, 1987) and depends mainly on the pressure level, initial void ratio, mean grain diameter and shearing velocity (Tejchman and Wu, 2010; Kozicki et al., 2013) (Figure 2.11). Its worth to notice that in order to obtain a shear zone inside the specimen in e.g. plane strain compression test, local

discontinuity in form of a weaker element with a high initial void-ratio was inserted (Tejchman, 2004).

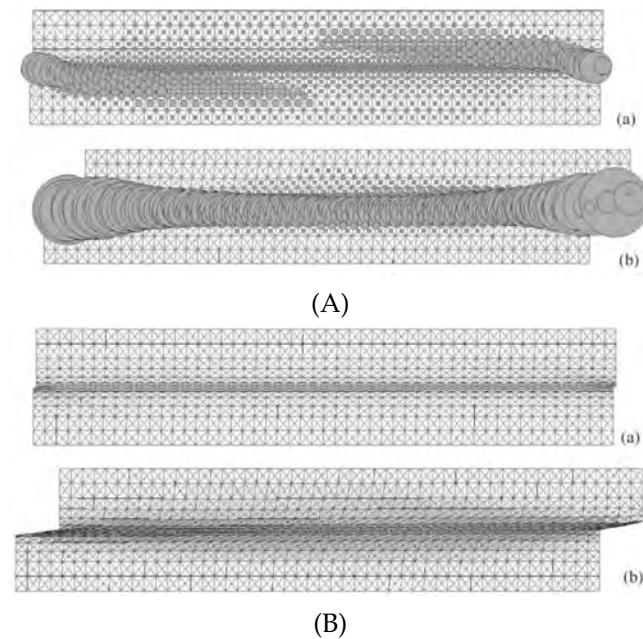


Figure 2.11: Deformation of initially medium dense sand during direct shear test with the distribution of: A) Cosserat rotation and B) void ratio at the different stages of the test (Kozicki et al., 2013).

### Shear zone formation in granular materials during confined flow in silo

In the FE calculations, granular media is treated as a continuum, and the behavior of it is described by the constitutive models able to predict the behavior of granular material during silo flow. The most widely used approaches for solving the problems are elasto-plastic and hypoplastic models. Both models have the ability to analyze various aspects of granular flow mechanics, such as flow patterns, shear zone formation, and pressures exerted on silo walls. They take into account properties characteristic for granular media, such as incremental nonlinearity, dependence on pressure level, density and direction of strain rate (Tejchman, 2013). In the case of silo flows, where granular material undergoes large deformations, the models have been extended by a characteristic length of the microstructure to properly capture the properties of the shear localization (Tejchman, 2004; Krzyżanowski et al., 2021).

The confined flow of granular materials in a silo has been analyzed using various approaches, including Eulerian, Lagrangian, and Arbitrary Lagrangian-Eulerian (ALE) descriptions of motion. However, the use of pure Lagrangian or pure Eulerian approaches for modeling silo flow is relatively limited. Using the Lagrangian approach to solve problems with large displacements and large strains can lead to distortion of the original finite element mesh, particularly near the outlet region (Więckowski et al., 1999; Wójcik, 2008). As a result, only the initial phase of the flow can be accurately resolved. Although large mesh distortions can be avoided by using the Eulerian description of motion, this approach is primarily suited for the simulation of granular flow with continuous refilling of the silo (Więckowski

et al., 1999; Wójcik, 2008). To overcome these limitations, an Arbitrary Lagrangian-Eulerian description of motion can be used, which combines the advantages of both Lagrangian and Eulerian methods, allowing for a more accurate analysis of silo flow dynamics (Wójcik, 2008). However, it should be noted that this approach may be problematic in specific cases, such as when modeling silo flow with inserts (Wójcik and Tejchman, 2009).

The propagation of both internal and wall shear zones has been studied by Wójcik (2008, 2009) in the case of quasi-static plane strain granular flow with controlled outlet velocity. In this study, an Arbitrary Lagrangian-Eulerian motion description was used, which allowed to simulate almost the entire discharge process, in combination with a nonlocal hypoplastic model. Two types of bins with varying surface roughness were examined: a bin with vertical walls and a hopper. A pattern of periodic internal shear zones was observed in both configurations. In the case of the bin with vertical walls, shear zones were detected only when the walls were very rough and the bin was filled with initially dense sand (Figure 2.12a). For the hopper, internal shear zones occurred regardless of wall roughness (Figure 2.12b). A mechanism of propagation similar to that described by Michalowski (1987) and Cutress and Pulfer (1967) was observed. The shape of the internal shear localizations depended on the wall roughness, initial void ratio of the granular material and silo geometry. The interior shear zones contributed to the oscillation and non-uniform distribution of pressure and density (Wójcik and Tejchman, 2009).

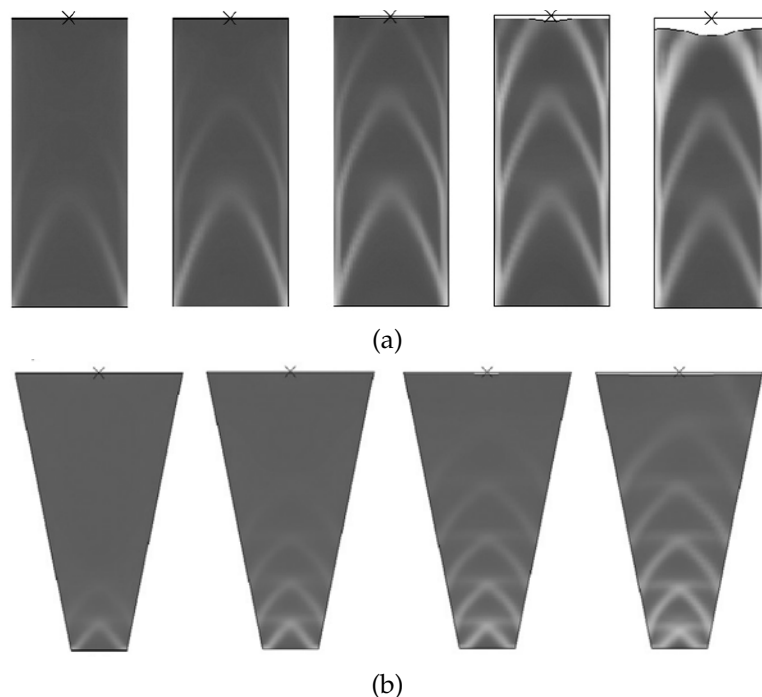


Figure 2.12: Evolution of void ratio during quasi-static plane strain granular flow in silo for: a) initially dense sand in a bin with very rough vertical walls and b) a hopper with smooth walls (Wójcik and Tejchman, 2009).

Another group of particle-oriented methods has been developed within continuum mechanics to address large strain problems. Methods such as particle-in-cell (PIC), smoothed particle hydrodynamics (SPH), and material point method (MPM)



allow to overcome the previously mentioned problems related to mesh distortions. This group of meshless methods traces the history of state variables at points or particles that are independent of the computational mesh (Więckowski et al., 1999; Więckowski, 2004; Krzyżanowski et al., 2021). Particle-based methods have been successfully applied to large strain engineering problems, including the tracking of shear zones during silo flow (Więckowski, 2004; Krzyżanowski et al., 2021; Krzyżanowski et al., 2021). Numerical simulations of quasi-static confined flow in model silo with movable bottom were carried out by Krzyżanowski et al. (2021) using Material Point Method. The study allowed to capture realistically both the shear zones located near the walls and curvilinear ones located within the granular material (Figure 2.13). Significant influence on the shear zone thickness had the initial void ratio of the bulk solid and the roughness of the silo walls. The strain localization trajectories were also affected by the location of the outlet (Figure 2.13). These parameters influenced also the patterns of the internal shear zones. The wall pressures were strictly affected by the appearance of the shear zones and their thickness. These zones caused the oscillation and non-uniform distribution of forces exerted on walls, in particular for silo with very rough wall filled with initially dense sand. The void ratio within the shear zone gradually change depending on the initial conditions. Initially loose samples within the localization exhibit local contraction and initially dense sample shows dilatancy. Similar conclusions were drawn by Desrues et al. (1996) in experimental analysis of the triaxial compression test.

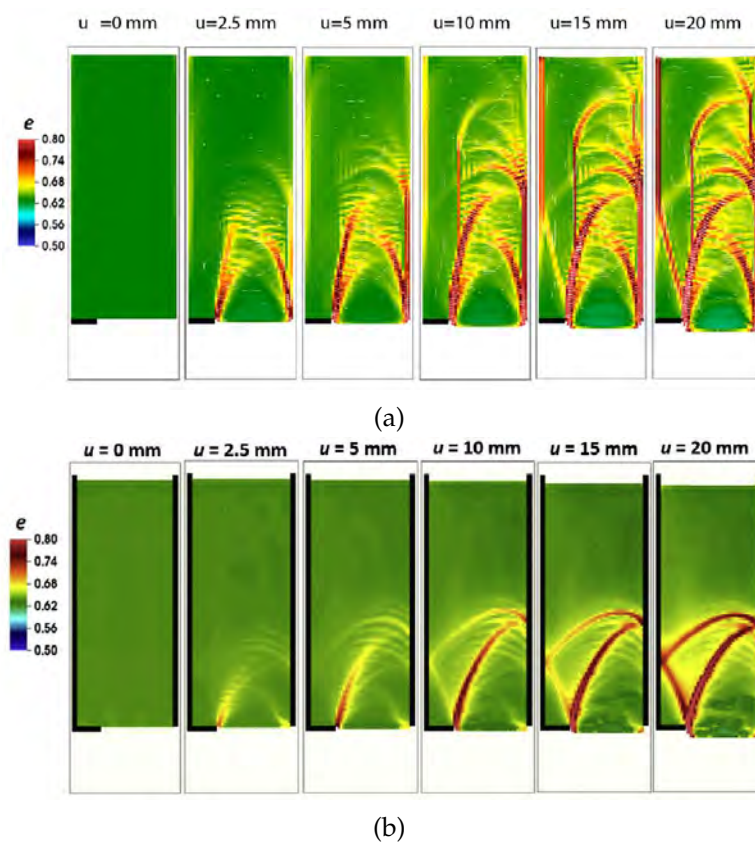


Figure 2.13: Evolution of void ratio in initially dense sand in quasi-static plane strain granular flow after bottom displacement  $u$  for silo with: a) asymmetric outlet and very rough walls, and b) with smooth walls (Krzyżanowski et al., 2021).

### 2.3.2 Discrete methods

#### Shear zone formation in granular materials

Previous studies of strain localization in granular materials have mainly focused on laboratory experiments and continuum models. However, these approaches are usually unable to provide insight into the micro- and mesoscopic properties of granular materials. The basic understanding and application of the results is limited by the lack of the grain-level information. This limitation can be overcome by numerical simulations performed with Discrete Element Method (DEM). In the discrete approach, it is possible to simulate the macroscopic behavior of bulk solids by assuming the characteristics of individual grains, such as their geometry and size, and material parameters.

A number of DEM models have been developed to predict the behavior of granular materials. These models, discussed in Chapter 3, take into account the formation of shear zones during the study of various soil mechanics problems, such as geotechnical testing (Iwashita and Oda, 1998; Oda and Iwashita, 2000; Zhang and Thornton, 2007; Kozicki et al., 2013), foundations (Liu et al., 2019), passive/active state soil problems (Nitka et al., 2015; Leśniewska et al., 2020), and more. These studies allowed a comprehensive description of the deformation of granular material in the localized region. Due to the heterogeneous and discontinuous structure of the discrete models, they were able to capture the mesoscopic changes in the behavior of individual grains within the shear zone.

Shear zone formation was studied by Iwashita and Oda (1998) in biaxial compression tests using granular material composed of spherical discs. During the analysis, the strains, force chains, and voids were measured within the numerical specimen (Figure 2.14). The large voids are aligned along the localization so that the dilation is concentrated within the shear zone. Therefore, the strain softening behavior is a natural result of weakening along this zone. Significant particle rotations were observed along the shear band boundaries. Column like structures parallel to the major principal stress direction within the shear zone were captured. The consecutive formation and breakage of these columns may be responsible for the generation of large voids and particle rotations. Kozicki et al. (2013) studied the grain level properties of granular materials during shearing in a direct shear apparatus, such as displacement profiles, grain rotations, force chains, and local void ratio fluctuations (Figure 2.15). During the study, the two-dimensional medium-dense granular sample composed of 22 000 real-size spherical particles was used. The localized region began to appear after the granular material reached the maximum shear resistance. The shape and thickness of the shear zone, as determined from e.g. rotations, was non-uniform and varied along the shear box. The localization was thickest in the center and thinnest near the edges of the specimen. Similar conclusions regarding the thickness of the shear zone were drawn by Zhang and Thornton (2007). Within the shear zone, local void ratio fluctuations were observed, which appeared to be periodic in nature (Figure 2.15d). They were related to the unstable force chains that occur during shearing of the granular material. These chains are well correlated with the approximate orientation of the principal principal stresses (Zhang and Thornton, 2007).

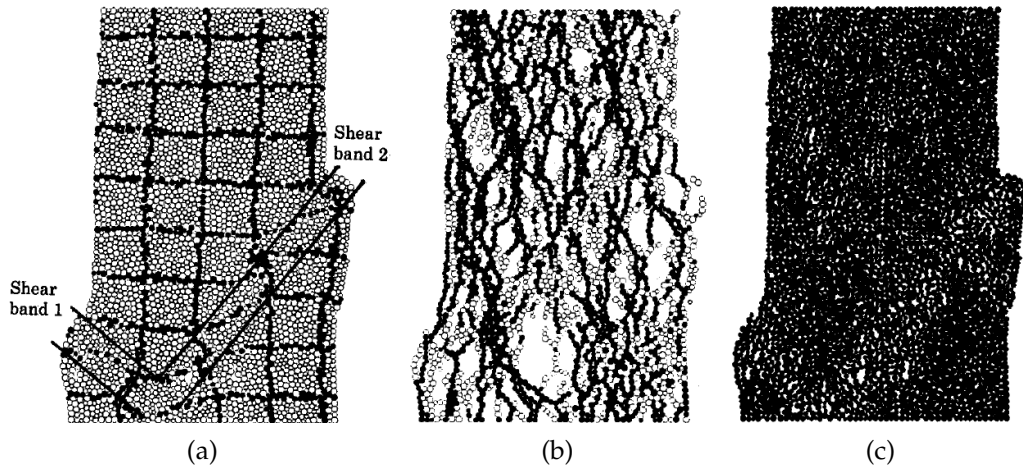


Figure 2.14: Illustrations of: a) specimen deformation, b) development of column-like structures, and c) porosity changes in biaxial compression test using granular material composed of spherical discs (Iwashita and Oda, 1998).

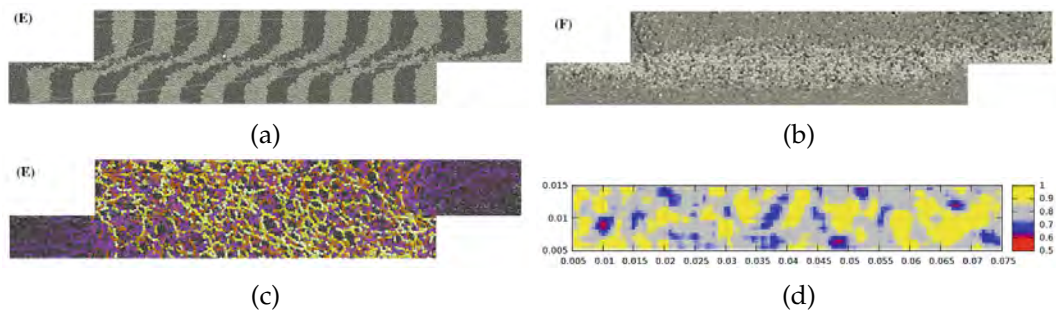


Figure 2.15: Evolution of: a) specimen deformation, b) grain rotations, c) internal forces in the entire specimen, and d) void ratio distribution within the shear zone during direct shear test of initially medium dense sand for horizontal displacement of  $u=20$  mm obtained with DEM (Kozicki et al., 2013).

### Shear zone formation in granular materials during confined flow in silo

Due to systematic advances in computational efficiency, both in terms of software and hardware improvements, simulations of granular flow in silos using the Discrete Element Method have gained more attention from researchers. Over the past three decades, numerous discrete simulations have been performed to study the characteristic phenomena related to silo flow (Langston et al., 1995; Zuriguel et al., 2005; Ketterhagen et al., 2009; Balevičius et al., 2011; González-Montellano et al., 2011; Kobyłka and Molenda, 2013; Zeng et al., 2017; Wan et al., 2018; Gallego et al., 2019; Han et al., 2019). The calculations were mainly focused on flow patterns, discharge rate, wall pressure distributions, avalanches, jamming and arching mechanisms, and segregation phenomena. To the author best knowledge, despite its common occurrence, the phenomena related to the formation of shear zones during granular flow in silo has not been sufficiently studied by means of discrete element method. There are only few publications regarding mechanism of the shear zones formation during confined granular flow in silo.

The formation of these zones during quasi-static flow in two-dimensional environment was studied by Gutfraind and Pouliquen (1996). In the paper the shear

zone formation near the structure walls was presented during mass flow. The granular material composed of approximately 3 500 disks was filled into the structure of a silo with rough walls constituted by equal-size particles. The simulations were carried out for two types of structure width: one was 15 diameter wide and second was 20 diameter wide. During the quasi-static flow, the velocity profiles were measured (Figure 2.16). Based on those results shear zone were observed in the region near the walls. Based on the velocity profiles, the thickness of the shear zone was measured and was equal approximately 6 medium particle diameters wide. In the paper the structure and distribution of force chains was studied (Figure 2.17). During the flow significant stress fluctuations were measured. They were related to the consecutive establishing and collapsing of large stress zones in form of arched chains of particles. The occurrence of the shear zones near the wall of the bin was reliant on these stress zones. The collapse of the arch led to the generation of the shear zone next to the wall (Figure 2.17).

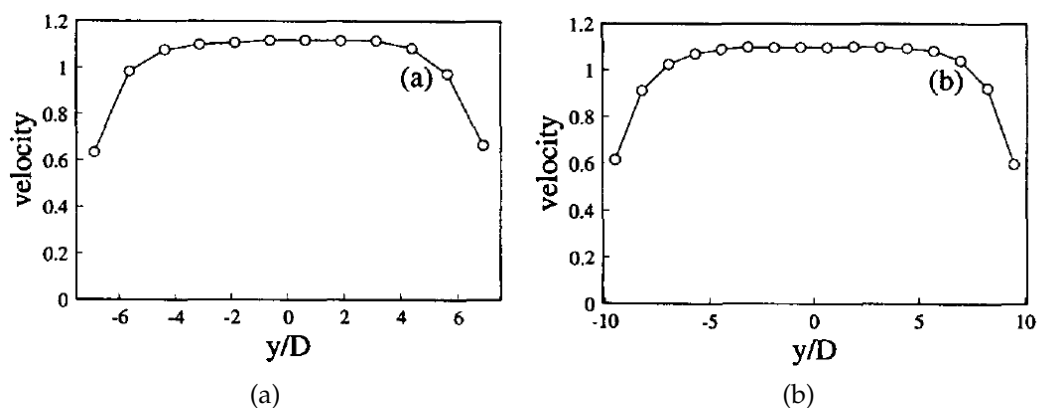


Figure 2.16: Shear zone location near the walls captured with velocity profiles for: a) the bin 15 particle diameters wide and b) for the bin 20 particle diameters wide (Gutfraind and Pouliquen, 1996).

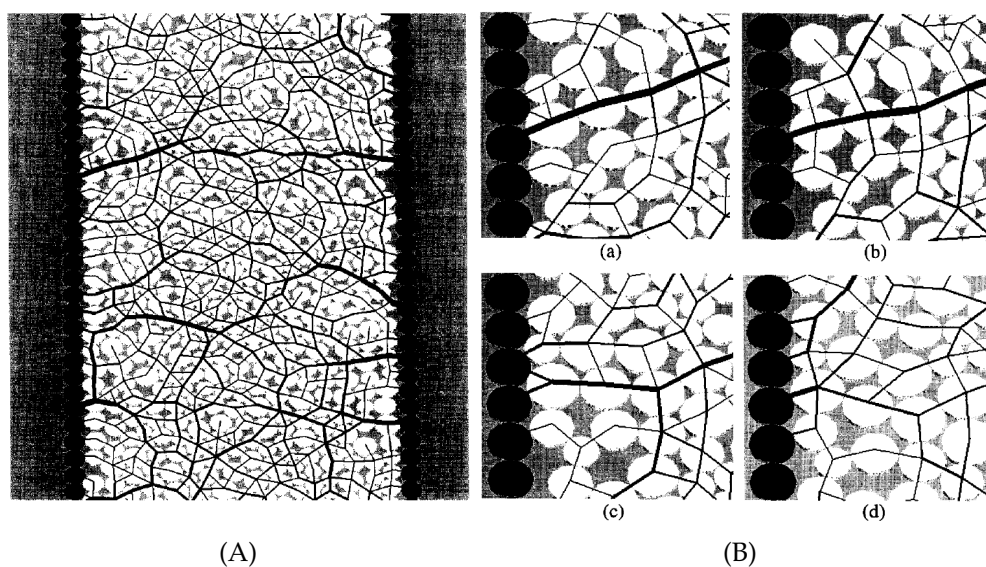


Figure 2.17: Normal force chain network in granular material during: A) quasi-static flow in a bin and B) a close-up on the normal force chains at four different time steps of (A) (Gutfraind and Pouliquen, 1996).

## 2.4 Research opportunities

In this chapter, a general review of shear zone formation was presented, with special attention to that occurring during confined granular flow in a silo. Despite extensive study over the past decades this phenomenon cause significant challenges during flow analysis. As presented, this issue has been analyzed mainly based on the experimental approach or by means of continuum methods. Unfortunately, these methods have their limitations. The experimental techniques are usually unable to provide insights into the mesoscopic characteristics of granular materials. Obtaining some of the grain-level data through experimental analysis can be difficult, time-consuming, expensive, or even impossible. Typically, experimental studies that investigate the deformation of granular material at the mesoscale tend to provide primarily qualitative information. On the other hand, when it comes to the finite element approach, especially in the context of shear localization, the analysis is not always straightforward. These methods face significant challenges when computing systems that undergo large deformations. Moreover, the majority of the results obtained within the continuum mechanics discussed in the chapter, are strictly limited to the calculations of granular flow in the quasi-static regime. It is important to note that the granular material flow within a silo is frequently dynamic, which can create additional challenges for the numerical analysis.

Many of these limitations can potentially be overcome by employing the Discrete Element Method for the simulation of confined granular flow in silos. DEM can provide insights directly related to the dynamic behavior of particles and the internal properties of granular materials in various applications. As far as the author is aware, the phenomena associated with shear zones formation during granular flow in the silo have not been sufficiently studied using this method. While numerous discrete analyses regarding other aspects of silo flow exist, a comprehensive study focusing on shear zone formation using a discrete approach is lacking. Therefore, the research presented in this thesis focuses on this understudied phenomenon with the aim of making a modest contribution to the understanding of the mesoscopic mechanisms behind shear zone formation in granular flow within silo structures.

## Chapter 3

# Discrete Element Method

### 3.1 Overview

The Discrete Element Method (DEM), also known as the Distinct Element Method or Discrete Particle Method (DPM), was originally proposed by Cundall and Strack (1979) for solving problems in geotechnical engineering. This method is closely related to Molecular Dynamics (MD), which was developed in the early 1950s for the numerical simulation of molecular gases and simple liquids (Pöschel and Schwager, 2005). However, unlike MD, which is mainly used to model the physical motion of atoms and molecules, DEM is generally used to simulate the motion of macro- and mesoscopic particles and grains. Since the early 1980s, the Discrete Element Method has gained popularity and has been widely adopted for analysis in numerous industries, including chemical, mining, pharmaceutical, agricultural, and others. Today, DEM is commonly accepted as an efficient method for solving scientific and engineering problems in both solid mass materials, such as concrete and rocks, and discontinuous materials, such as powders and granulates. In addition, DEM can be used for the analysis of engineering problems, such as particle-fluid flows by coupling with Computational Fluid Dynamics (CFD) (Tsuji et al., 1993; Zeghal and Shamy, 2004; Caulk et al., 2020a; Krzaczek et al., 2020) and multiscale modeling of e.g. geotechnical problems by using coupled Finite-Discrete Element Method (Munjiza et al., 1995; Munjiza, 2004; Oñate and Rojek, 2004; Nitka et al., 2011; Nguyen et al., 2022). In recent days, the popularity of this method is a result of significant advances in computing power and efficiency, as well as improvements in numerical algorithms. As a consequence, it has become possible to simulate materials consisting of millions of particles (Caulk et al., 2020b). Application of this method to model granular material is wide (Zhu et al., 2008), ranging from fluidized beds phenomenon (Xu and Yu, 1997; Kawaguchi et al., 1998), sintering process in powder metallurgy (Parhami and McMeeking, 1998; Rojek et al., 2017; Nosewicz et al., 2013; Nisar et al., 2024), granular flow in silo (Rotter et al., 1998; González-Montellano et al., 2011; Balevičius et al., 2011; Parafiniuk et al., 2013; Wiącek et al., 2024), soil mechanics problems (Thornton and Zhang, 2003; Hall et al., 2010; Kozicki et al., 2014), and many others.

DEM is a very effective tool for studying granular materials at the macro-, meso- and microscale levels. One of the main advantages of DEM is the possibility to directly simulate the heterogeneous structure of materials by considering different material properties (e.g., size and shape of particles) and random structure of the



granular assembly composed of finite number of distinct elements. Another major advantage of this method is its ability to provide a high level of detail in the output data describing the behavior of the granular material. It takes into account various factors such as particle trajectories, forces acting between the bodies, and other dynamic data at each time step of the numerical simulation. Obtaining such information through experimental analysis can be difficult or even impossible (Zhu et al., 2008). On the other hand, the Discrete Element Method has several significant drawbacks. Although it is possible to simulate granular media consisting of millions of particles, the method is mostly used to solve small-scale problems rather than macroscopic engineering problems. This is due to the significant computational cost associated with the large number of discrete elements required to accurately reproduce the structure of granular materials. Despite recent significant advances in computational algorithms, certain computational procedures, such as collision detection, remain time-consuming processes. Another drawback of this method is the lack of grain-level variables, resulting in a calibration procedure that relies primarily on the measurement of global material properties in laboratory tests.

In discrete calculations of particulates and granular assemblies, two main types of contact between the bodies can be distinguished: the soft particle model and the hard particle model. The hard particle model is based on the instantaneous collisions between perfectly rigid bodies. In this approach, the time step during the simulation is variable and event dependent (Luding et al., 2017). The collision between particles is binary, meaning that only one contact between a particle and neighboring bodies is possible at a given time step. If multiple contacts are established, they are solved sequentially. On the other hand, when there is no interaction between a particle and neighboring bodies, the particles are in free, undisturbed motion (Hogue and Newland, 1994). The hard particle approach finds application in loose and diluted systems, e.g. in the field of molecular dynamics (Hoomans et al., 1996). For more dense systems, like granular media assemblies, a soft particle approach is commonly employed. On the contrary to the hard particle approach, the soft particle approach allows for a multiple long-lasting particle contacts which are common in typical granular assemblies (Buist et al., 2016). In this approach, the material is considered to be composed of distinct particles that interact with each other by applying Newton's second law and a contact law within an explicit numerical scheme. The Newton's second law determines the motion of a particle based on the forces acting on it, while the contact law is used to calculate forces between the bodies based on their displacements. In the soft particle method the interaction forces between the bodies are related to the deformation or mostly to the overlap of contacting particles, which is interpreted as a local contact deformation. In soft particle models, an adequately small time steps must be used to obtain reliable results, which can increase computation time. Throughout the simulation, the time step is usually fixed and is related to the local modulus of elasticity of the contact, the particle radius, the material density, and the normal/shear stiffness ratio. The duration of the interaction increases with the softening of the interaction (Hoomans et al., 1996).

In this thesis, the numerical analysis was performed with the three-dimensional discrete software called YADE (Yet Another Dynamic Engine) which was developed at the University of Grenoble (Kozicki and Donzé, 2008; Smilauer et al., 2023). The

YADE software, which takes advantage of the soft-particle approach, has already been successfully used to describe the behavior of granular materials (Modenese et al., 2012; Bourrier et al., 2013; Aboul Hosn et al., 2016; Dosta et al., 2023), including shear localization (Widuliński et al., 2011; Kozicki et al., 2013; Nitka et al., 2015; Kozicki and Tejchman, 2017; Leśniewska et al., 2020).

### 3.2 Calculation procedure

The granular material is described in the Discrete Element Method by the positions and orientations of its constituent particles and by the corresponding time derivatives. The simulation loop performed in the discrete software YADE is shown in Figure 3.1. The calculation procedure is based on the application of Newton's second law to the distinct elements and an interaction law at the contacts between them.

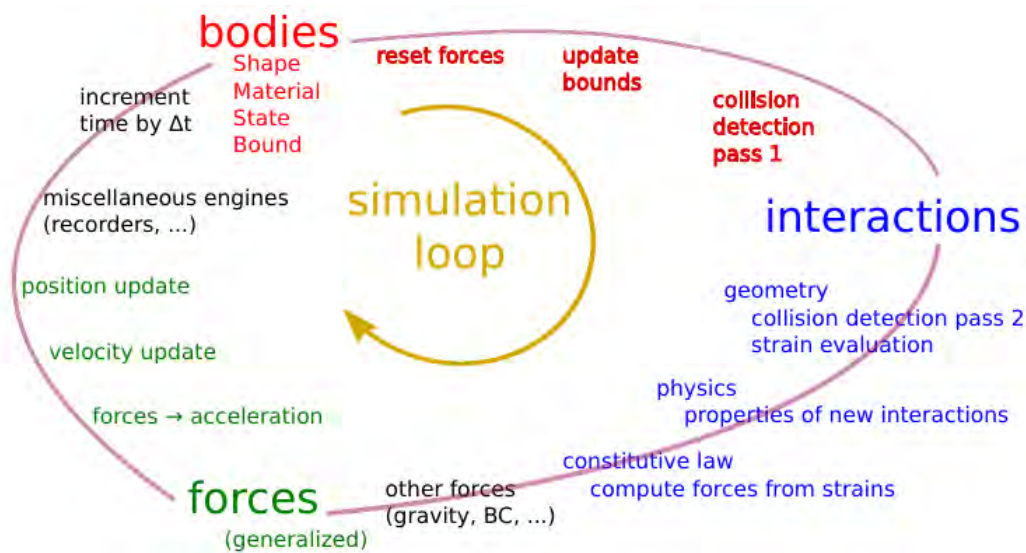


Figure 3.1: Simulation loop in discrete software YADE that includes: body-centered calculations (red color) followed by interaction calculations (blue color), force estimation (green color), and other engines, such as user-defined components (black color) (Smilauer et al., 2023).

In a typical discrete simulation, a granular assembly is composed of distinct particles, each of them defined by its properties (e.g., material and shape). The simulation proceeds in discrete time steps, in each of this steps the procedures presented in Figure 3.1 are run repeatedly. In the first phase of a cycle, the forces acting on each particle from the previous step are reset. Then collisions between the bodies are detected. In YADE, the detection process is performed in two phases: a fast and approximate phase followed by an exact collision detection procedure. This is due to the fact that the exact computation of a collision between two particles can be relatively computationally expensive. Next, based on the collision detection, the interactions between the particles are solved using contact laws, with calculation of the general forces acting on the bodies, including external conditions such as gravity. The contact forces are derived from properties of interacting particles. Finally, the equations of motion are integrated for all particles, resulting in updated positions and orientations.

### 3.2.1 Motion integration

The motion of particles in DEM was well described in detail in work by Cundall and Strack (1979) and discrete software manuals, such as PFC-Particle Flow Code manual (2019) and YADE manual (2023.) During the simulation, each distinct rigid particle accumulates resultant forces acting on it from the contacts in which it participates (with other particles and boundaries) or from external forces. These resultant forces are then used to integrate the particle motion separately for each particle, following Newton's second law. The particle behavior can be described in terms of two vector equations: one related to the translational motion of the particle and the second related to the rotational motion of the particle. The motion of the center of mass in the translational degree is described in terms of its position  $\mathbf{x}$ , velocity  $\dot{\mathbf{x}}$ , and acceleration  $\ddot{\mathbf{x}}$ . The equation of motion for each particle for translation can be expressed as:

$$\mathbf{F} = m(\ddot{\mathbf{x}} - \mathbf{g}) \quad (3.1)$$

where,  $\mathbf{F}$  is the resultant force, i.e. the sum of all forces acting on the particle,  $m$  is the mass of the particle, and  $\mathbf{g}$  is the acceleration caused by body forces (e.g., gravitational load). To integrate the motion equations YADE uses Verlet scheme, in which known derivatives of position and orientation are calculated at on-step points and the odd derivatives, such as velocities are calculated at mid-step points. Let us consider that the sum of all forces acting on a particle and its mass  $m$  is known at the time  $t$  and the time step used for the calculation cycle is  $\Delta t$ . Therefore, the mid-step velocity  $\dot{\mathbf{x}}^{(t+\Delta t/2)}$  is calculated with the following expression:

$$\dot{\mathbf{x}}^{(t+\Delta t/2)} = \dot{\mathbf{x}}^{(t-\Delta t/2)} + \left( \frac{\mathbf{F}^{(t)}}{m} + \mathbf{g} \right) \Delta t \quad (3.2)$$

These calculated values of mid-step velocities may be used to update the positions of the particles at the time  $t + \Delta t$  by a further numerical integration:

$$\mathbf{x}^{(t+\Delta t)} = \mathbf{x}^{(t)} + \dot{\mathbf{x}}^{(t+\Delta t/2)} \Delta t \quad (3.3)$$

The rotational motion of the particle is described in terms of its angular velocity vector  $\boldsymbol{\omega}$  and angular acceleration vector  $\dot{\boldsymbol{\omega}}$ . The equation of motion for a distinct particle is described by an equation:

$$\mathbf{M} = \mathbf{I}\dot{\boldsymbol{\omega}} \quad (3.4)$$

where  $\mathbf{M}$  is the resultant angular moment (torque) acting on the rigid body and  $\mathbf{I}$  represents moment of inertia of the rigid body. Assuming that angular acceleration  $\dot{\boldsymbol{\omega}}$  is constant over the time step  $\Delta t$  the mid step angular velocity is expressed by:

$$\dot{\boldsymbol{\omega}}^{(t+\Delta t/2)} = \dot{\boldsymbol{\omega}}^{(t-\Delta t/2)} + \left( \frac{\mathbf{M}^{(t)}}{\mathbf{I}} \right) \Delta t \quad (3.5)$$

The calculated angular velocity vector is used then to update the particle rotation with equation:

$$\boldsymbol{\omega}^{(t+\Delta t)} = \boldsymbol{\omega}^{(t)} + \dot{\boldsymbol{\omega}}^{(t+\Delta t/2)} \Delta t \quad (3.6)$$

Both translational and rotational equations of motion are applied to each particle in a each cycle. The finite difference equations 3.1-3.6 represent a time-centered system.

### 3.2.2 Contact model

A number of DEM models have been developed to predict the behavior of granular materials. In DEM, this behavior is described by a set of contact laws that model the interactions between individual particles. In each calculation cycle, these contact laws are applied at each contact point, resulting in new interparticle forces. Unfortunately, modeling the actual deformation of the particles is too complicated, so the interaction is typically replaced by a system of springs, dashpots, no-tension joints, and sliders (Iwashita and Oda, 1998). As a result, particle deformation is simulated as an overlap between two particles, where the magnitude of the overlap determines the magnitude of the contact force between the bodies. Several types of contact laws can be used to model the behavior of granular materials, which have been extensively described in the literature (Mishra, 2003; Horabik and Molenda, 2016; Luding et al., 2017). Usually the normal contact force between the particles is modeled with the linear (Cundall and Strack, 1979; Iwashita and Oda, 1998; Oda and Iwashita, 2000; Kozicki and Donzé, 2008; Nitka et al., 2015; Rojek et al., 2018; Zhao and Zhao, 2019) or nonlinear contact models (Zhao et al., 2006; Zhang and Thornton, 2007; Modenese et al., 2012; Podlozhnyuk et al., 2016; Wiacek et al., 2023). In the most commonly used linear contact model, the mechanical behavior results in a typical linear force-displacement relationship. The nonlinear models, such as the Hertzian type model, allow to obtain more realistic results (Luding et al., 2017), but they can decrease the computational efficiency (Mishra, 2003). Modeling the particle interaction also includes solving the sliding, rolling, and torsional components of the contact. These forces are mainly calculated using either linear elasto-plastic or nonlinear Hertz-Mindlin models (Mindlin and Deresiewicz, 1953).

In the thesis the cohesive elastic-frictional contact model with moment transfer law (MTL) (or else called rotational resistance) implemented in YADE was used (Figure 3.2). Although the model is able to consider the cohesion force between the bodies, this component was not used in the presented numerical simulations (non-cohesive sand was simulated only) (Figure 3.2). The normal force component between the bodies is calculated using linear spring with constant normal stiffness  $K_n$  (Figure 3.2a). The linear spring provide linear elastic no-tension behavior of the interaction. The tangential component of the contact force is computed with respect to constant elastic shear stiffness  $K_s$  and is limited by the Mohr-Coulomb friction criterion, using interparticle friction coefficient  $\mu_c$  (Figure 3.2b,c). Moreover, in the model linear elastic-plastic rotational resistance is implemented. Contact moments are computed with respect to the rotational stiffness  $K_r$  (Figure 3.2d,e). The maximum value of interparticle moments above which the behavior is perfectly plastic is defined by the dimensionless limit rolling coefficient  $\eta$  (but also depends on normal stiffness and element radii).

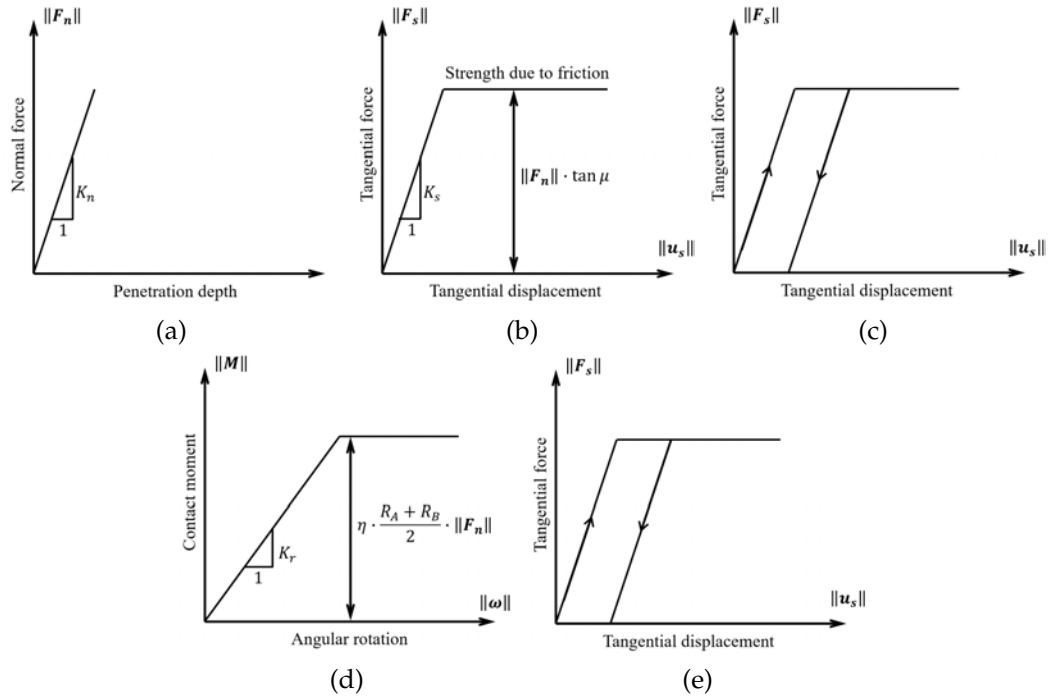


Figure 3.2: Mechanical response of linear contact model with rotational resistance: a) normal contact model, b) tangential contact model, c) loading and unloading path for tangential force and d) rolling contact model, e) loading and unloading path for rolling contact model (Kozicki et al., 2013).

To illustrate how interaction forces and displacements of the discrete bodies during a discrete simulation are calculated, let us consider basic assembly of two distinct elements in three-dimensional space. Figure 3.3 presents an example of interaction between two purely spherical particles with rotational resistance, indexed as *A* and *B* (Iwashita and Oda, 1998; Belheine et al., 2009). At the beginning of the simulation loop, the bodies are defined by their position (e.g., center coordinates  $x$ ,  $y$ , and  $z$  for spheres), shape (e.g., radius  $r$  for spheres), and material parameters (e.g., mass density  $\rho$ , local modulus of elasticity  $E_c$  and shear/normal stiffness ratio  $\nu = K_s/K_n$ ). When two bodies are in contact, a force vector  $\mathbf{F}$  between them is established which may be decomposed into a normal and a shear vector ( $\mathbf{F}_n$  and  $\mathbf{F}_s$ , respectively). These forces may be computed with respect to the contact normal and shear stiffness ( $K_n$  and  $K_s$ , respectively):

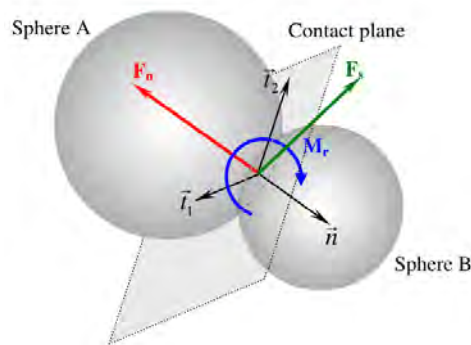


Figure 3.3: Interaction between two spheres in DEM at time  $t$  (Belheine et al., 2009).

$$\mathbf{F}_n = K_n \cdot u_n \cdot \mathbf{n} \quad (3.7)$$

$$\Delta \mathbf{F}_s = K_s \cdot \Delta \mathbf{u}_s \quad (3.8)$$

where  $u_n$  is the relative normal displacement between two elements (positive if overlap exists),  $\mathbf{n}$  is the unit normal vector at each contact point and  $\Delta \mathbf{u}_s$  is the incremental tangential displacement. The shear force  $\mathbf{F}_s$  acting between the bodies is obtained by summing the  $\Delta \mathbf{F}_s$  increments:

$$\mathbf{F}_s = \mathbf{F}_{s,prev} + \Delta \mathbf{F}_s \quad (3.9)$$

where  $\mathbf{F}_{s,prev}$  represents the shear force at the beginning of the time step. Normal and shear stiffnesses are related to the sphere modulus of elasticity  $E_c$  and particles radii  $R_A$  and  $R_B$ . In this study, a linear elastic normal contact model was used. Therefore,  $K_N$  and  $K_s$  are calculated with harmonic mean:

$$K_n = E_c \cdot \frac{2 \cdot R_A \cdot R_B}{R_A + R_B} \quad (3.10)$$

$$K_s = v_c \cdot E_c \cdot \frac{2 \cdot R_A \cdot R_B}{R_A + R_B} \quad (3.11)$$

with  $v_c$  as the shear/normal stiffness ratio. The force components are connected by a frictional Mohr-Coulomb contact law. The sliding between the elements occurs when the inequality is satisfied:

$$\|\mathbf{F}_s\| \geq \|\mathbf{F}_n\| \cdot \tan \mu_c \quad (3.12)$$

where  $\|\mathbf{F}_s\|$  is the norm (length) of the shear force,  $\|\mathbf{F}_n\|$  is the norm of the normal force and  $\mu_c$  represents interparticle friction angle.

In addition, to model the grain roughness moment transfer law (MTL) was introduced to increase the rolling resistance of purely spherical particles, as proposed by Iwashita and Oda (1998). The contact moment  $\mathbf{M}$  acting between the bodies is obtained by summing the  $\Delta \mathbf{M}$  increments:

$$\mathbf{M} = \mathbf{M}_{prev} + \Delta \mathbf{M} \quad (3.13)$$

where  $\mathbf{M}_{prev}$  represents the moment at the beginning of the time step. The increment of the contact moment  $\Delta \mathbf{M}$  acting in the contact plane is calculated using the rolling stiffness  $K_r$ :

$$\Delta \mathbf{M} = K_r \cdot \Delta \boldsymbol{\omega} \quad (3.14)$$

where the  $\Delta \boldsymbol{\omega}$  represents the incremental resultant angular rotation between two elements. The rolling stiffness  $K_r$  is calculated with following equation:

$$K_r = \beta \cdot K_s \cdot R_A \cdot R_B \quad (3.15)$$

where  $\beta$  is the dimensionless coefficient used for the rolling stiffness. The rolling occurs when the moment exceeds the value:

$$\|\mathbf{M}\| \geq \eta \cdot \frac{R_A + R_B}{2} \|\mathbf{F}_n\| \quad (3.16)$$

where  $\eta$  is the dimensionless limit rolling coefficient which controls the elastic limit of the rolling behavior.

In simulations of quasi-static phenomena, it is desirable to dissipate kinetic energy of particles. The damping used in YADE is similar to that one described in Cundall and Strack (1979). YADE employs artificial numerical damping  $\lambda_d$ , which is a non-physical damping force component added to the equations of motion. The basic idea is to decrease forces which increase the particle velocities:

$$\mathbf{F}_{damped} = \mathbf{F} - \lambda_d \cdot \text{sgn}(\dot{\mathbf{x}}) \cdot \mathbf{F} \quad (3.17)$$

and

$$\mathbf{M}_{damped} = \mathbf{M} - \lambda_d \cdot \text{sgn}(\dot{\omega}) \cdot \mathbf{M} \quad (3.18)$$

where  $\mathbf{F}_{damped}$  and  $\mathbf{M}_{damped}$  are the damped force and moment vectors acting on particle,  $\mathbf{F}$  and  $\mathbf{M}$  are the resultant contact force and moment vectors, respectively. Finally,  $\dot{\mathbf{x}}$  and  $\dot{\omega}$  denote the particle's translational and angular velocity. The function  $\text{sgn}(\ast)$  returns the sign of the components of the translational and rotational velocities of the spheres. As a result, it ensures that the damping forces oppose the direction of motion, effectively dissipating kinetic energy.

### 3.3 Particle shapes

In DEM calculations of granular material, grains can have shapes of varying complexity, some of which are shown in Figure 3.4. Most DEM software uses spherical grains within a specified diameter range (Figure 3.4A). To capture the irregularity of real grains, the rotational resistance is typically introduced which simulates the frictional contact between purely spherical particles (Belheine et al., 2009). In addition to pure spheres, many DEM software packages use the *multisphere method*, in which distinct spheres are combined to form a clumped body. These combined spheres can form a rigid or a deformable particle with finite adhesion forces between the spheres (Figure 3.4Ab-1). Recent studies have introduced other methods to faithfully reproduce particle shapes. First group of particles with complex shapes are the ones described by closed-form mathematical expressions, such as poly-superellipsoid particles (Figure 3.4B) and superquadric particles (Figure 3.4C). In other studies, the particles are simulated as polyhedral ones described by a set of planes (Figure 3.4D). Different methods of particle simulation have their own advantages and disadvantages. The use of sphere-based particles significantly simplifies and accelerates the calculation process, allowing a larger number of particles to be simulated. On the other hand, poly-superellipsoid or superquadric particles provide a better representation of actual granular material behavior due to their similarity to real grain shapes. However, this comes at the cost of longer computation time due to the more

complex collision detection process required for these particles. Polyhedral particles offer a simple way to define actual particle geometry using faces, vertices, and points. However, these shapes also often come at a significant computational cost, especially for highly complex geometries. In the thesis, two of the described approaches were used to simulate frictional grains of bulk materials: one involving purely spherical particles with rotational resistance (also referred to as spheres in the thesis), and the other involving clumps composed of spheres (also referred to as clumped particles in the thesis).

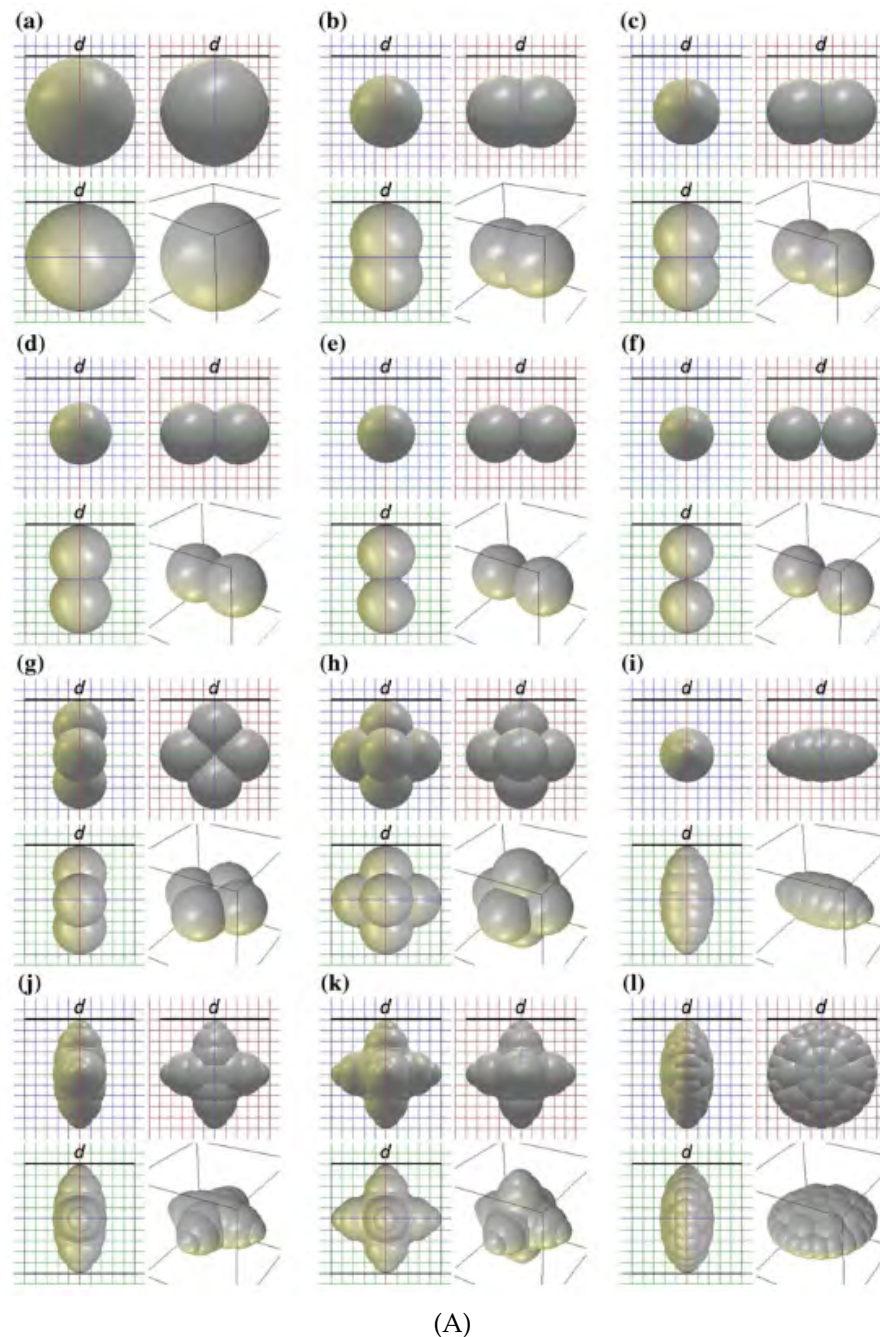


Figure 3.4: Overview of typical particle shapes used in DEM simulations: A) spheres and clumps composed of spheres (Kozicki et al., 2012), B) poly-superellipsoid particles (Zhao and Zhao, 2019), C) superquadric particles (Podlozhnyuk et al., 2016) and D) polyhedral particles (Zhao et al., 2006).

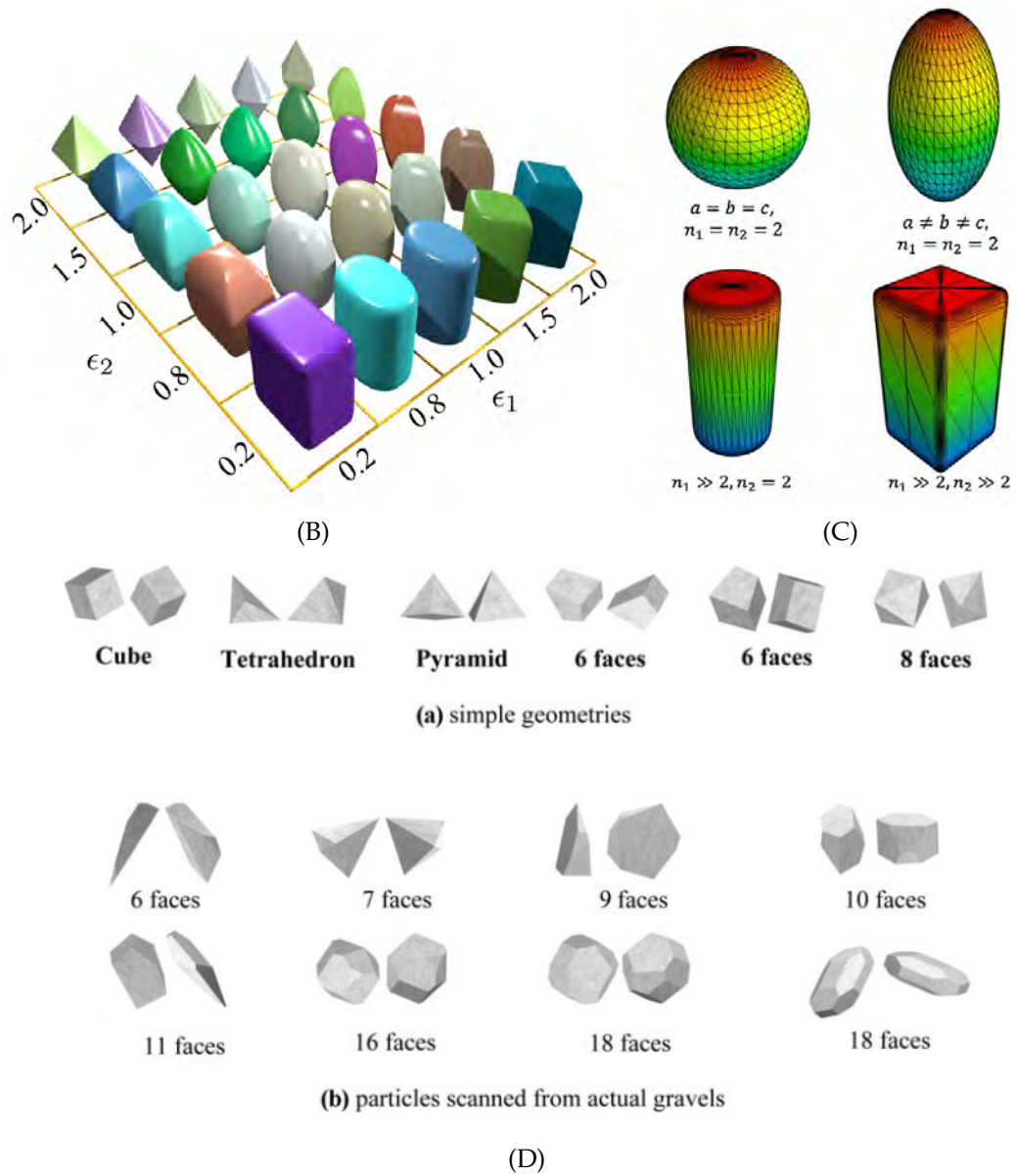


Figure 3.4: (continued).

## Chapter 4

# Preliminary discrete analysis of soil mechanics tests

The confined granular flow in a silo is a complicated and nonlinear process due to the multiple variables and dynamic interactions between individual particles and their interactions with the surrounding silo structure. The formation and propagation of shear zones during discharge can vary depending on numerous aspects of the bulk material-silo system. Therefore, in order to determine the ability of the discrete model to capture the complicated phenomena associated with the flow of granular materials, preliminary calculations of selected soil mechanics tests were performed with DEM. These tests allowed to calibrate the numerical model and to capture the typical behavior of the deforming granular material under precisely controlled conditions. Based on the comparison with laboratory data available in the literature, the numerical model was validated. The preliminary simulations provided a solid basis for the subsequent analysis of the mechanism of shear zone formation during silo flow. The chapter includes the numerical analysis of:

- triaxial compression test of cohesionless sand,
- direct shear test of cohesionless sand (Grabowski and Nitka, 2020; Nitka and Grabowski, 2021),
- interface shear test between cohesionless sand and rigid surface of different roughness (Grabowski et al., 2020; Grabowski et al., 2021a),
- interface shear test between cohesionless sand and rigid sinusoidal corrugated surface of different geometry.

First, a comprehensive parametric study of the influence of local discrete parameters on the granular material behavior was performed. The study was based on the triaxial compression test, as it is a typical tool for calibrating the input parameters in the DEM. Therefore, a series of these tests were performed to determine the local variable of the discrete model of cohesionless sand.

Then, simulations of the direct shear test were carried out. This test is typically used in soil mechanics to study the macroscopic response of the soil subjected to shearing. As a result, it is possible to obtain, for example, the total shear resistance of the sample. In addition, by means of discrete simulations, this test allowed also to study the mesoscopic characteristics of the deforming granular material, with particular attention to the formation of the shear zone. The great advantage of the direct



shear test is that the location of the shear zone can be easily predicted, as it typically occurs between the shear frames.

Later, the interface shear test between cohesionless sand and rigid surface of different roughness was studied. This test was selected because it allows the study of the shear zone occurring in the granular material in the region adjacent to the structure. The mechanisms that occur in the contact zone between these two regimes is one of the critical aspects affecting the granular flow in silos. Therefore, conducting this test was a necessary step before performing silo calculations.

Finally, the interface shear test between cohesionless sand and rigid sinusoidal corrugated surface of different geometry was investigated. This type of interfaces is often encountered in silo constructions, particularly in corrugated metal silos supported by surrounding thin-walled columns. The properties of this interface, such as the effective coefficient of friction against the corrugated wall, are critical for the accurate determination of pressures exerted on silo walls. The study of this test allowed to analyze the formation of the shear zone in the area adjacent to the surface similar to the structure of the silo, under precisely controlled quasi-static conditions.

## 4.1 Triaxial compression test

### 4.1.1 Introduction

The triaxial compression test has been extensively investigated by means of experimental techniques (Desrues et al., 1985; Kolymbas and Wu, 1990; Desrues et al., 1996; Matsushima et al., 2006; Cui et al., 2016) and numerical methods (Salot et al., 2009; Belheine et al., 2009; Kozicki et al., 2012; Kozicki et al., 2014). In laboratory studies, this test is usually used to measure the strength of the granular materials, but with the use of computed tomography it allows the deformation of the bulk solid to be measured in detail (Hall et al., 2010). In a typical triaxial test, the granular sample is placed between a top and bottom cap surrounded by a flexible membrane. During the test, axial stress is applied to the caps while hydrostatic pressure is applied to the membrane. As a result, the strength and strain of the soil are measured. In addition, advanced experimental techniques (e.g. micro-computed tomography) (Desrues et al., 1996) or discrete methods (Kozicki et al., 2014; Kozicki and Tejchman, 2017) can be used to study the strain localization within the bulk solid during the triaxial compression test.

This section presents the calibration and validation of the discrete model as a result of a comprehensive parametric study of the local material variables. The standard procedure for determining the parameters of the discrete model is by comparing macroscopic results from numerical analyses with experimental results (Belheine et al., 2009; Kozicki et al., 2012). This approach allows to reproduce the macroscopic behavior of the granular material based on the estimation of the local material characteristics of the discrete particles. In the presented study, the calibration of the properties of the numerical material was performed on the basis of the typical and commonly used triaxial compression test.

### 4.1.2 Numerical model and methodology

At the beginning, a parametric study was performed to investigate the effect of the key parameters of the DEM on the macroscopic behavior of the granular material. The analysis included the study of factors such as global specimen Young's modulus  $E$ , peak stress  $\sigma_1^{max}$  and residual normal stress  $\sigma_1^{res}$ . During the investigation spherical particles with rotational resistance were used. Therefore, the influence of five main local variables on the stress-strain curves was investigated: interparticle friction angle  $\mu_c$ , local modulus of elasticity  $E_c$ , shear/normal local stiffness ratio  $\nu_c$ , limit rolling coefficient  $\eta$  and rolling stiffness coefficient  $\beta$ . In each case, only one parameter was varied, while all other factors were kept constant. Table 4.1 contains the range of values of the material parameters considered during the parametric study.

A series of discrete triaxial compression tests were performed on the 'Karlsruhe' sand used in the experiments by Kolymbas and Wu (1990). The properties of this sand are listed in Table 4.2. The tests were conducted on a cubic specimen composed of spherical particles with rotational stiffness. The size of the sample was 100 mm × 100 mm × 100 mm, as shown in Figure 4.1. In the discrete simulations, the particles were scaled by a factor of 10 compared to the real size of the 'Karlsruhe' sand grains. If real-size particles were used, it would result in a sample composed

Table 4.1: Discrete material local variables used in parametric study.

| Parameter                                  | Value       |
|--|-------------|
| interparticle friction angle $\mu_c$       | 5-25°       |
| local modulus of elasticity $E_c$          | 20-2000 MPa |
| shear/normal local stiffness ratio $\nu_c$ | 0.05-0.6    |
| limit rolling coefficient $\eta$           | 0.1-2.0     |
| rolling stiffness coefficient $\beta$      | 0.1-2.0     |

of approximately 8 000 000 particles. Although the DEM software used is capable of handling such a number of particles, it would result in significantly longer computation and data processing times. Therefore, before the actual parametric study it was necessary to investigate the effect of the mean particle diameter  $d_{50}$  on the macroscopic response of granular sample. This investigation ensured that particle scaling did not affect the macroscopic outcomes of the triaxial compression test. Figure 4.2 shows the effect of the grain size used in the calculations on the resultant vertical normal stress  $\sigma_1$  and volumetric strain  $\varepsilon_v$ . Three samples composed of particles with different mean grain diameter  $d_{50}$  were examined:  $d_{50}=5.0$  mm (total number of 7 000 particles),  $d_{50}=2.5$  mm (total number of 56 000 particles), and  $d_{50}=1.25$  mm (total number of 450 000 particles). In each case, a uniform distribution of particle diameters was used, ranging from  $0.5 \times d_{50}$  to  $1.5 \times d_{50}$ . In all cases, the evolution of the shear resistance and the deformation of the sample was similar throughout the test. The tests were performed using smooth rigid wall elements, without inducing shear localization (Kozicki et al., 2013; Kozicki et al., 2014). Therefore, the particle scaling effect was assumed to be negligible and the mean particle diameter was set to  $d_{50}=5.0$  mm (with particle diameters varying between 2.5 mm and 7.5 mm).

Table 4.2: Properties of the 'Karlsruhe' sand (Kolymbas and Wu, 1990).

| Material property                        | Value                  |
|--|------------------------|
| mean grain diameter $d_{50}$             | 0.5 mm                 |
| grain size distribution                  | 0.08-1.8 mm            |
| uniformity coefficient $U_c$             | 2                      |
| minimum specific weight $\gamma_d^{min}$ | 14.6 kN/m <sup>3</sup> |
| maximum specific weight $\gamma_d^{max}$ | 17.4 kN/m <sup>3</sup> |
| minimum void ratio $e_{min}$             | 0.53                   |
| maximum void ratio $e_{max}$             | 0.84                   |

During the parametric study each test was performed on initially dense sand sample ( $e_0=0.55$ ) composed of the same assembly of distinct particles under confining stress  $\sigma_c=200$  kPa. The mass density of grains was 2600 kg/m<sup>3</sup>. The numerical procedure for the triaxial compression test was divided into two stages: specimen preparation and the actual test execution. In the first stage, particles were randomly packed inside the box composed of six smooth, rigid wall elements. The particles were then subjected to isotropic compression until the desired confining pressure and void ratio were achieved. During the preparation phase, the interparticle friction angle was varied to achieve the assumed specimen characteristics. The initial stage was completed when the kinetic energy of the specimen became negligible.

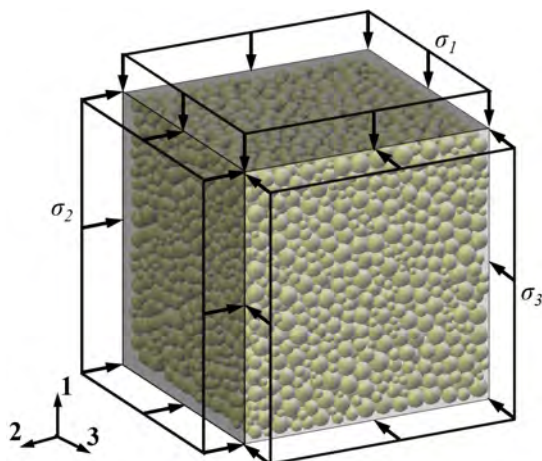
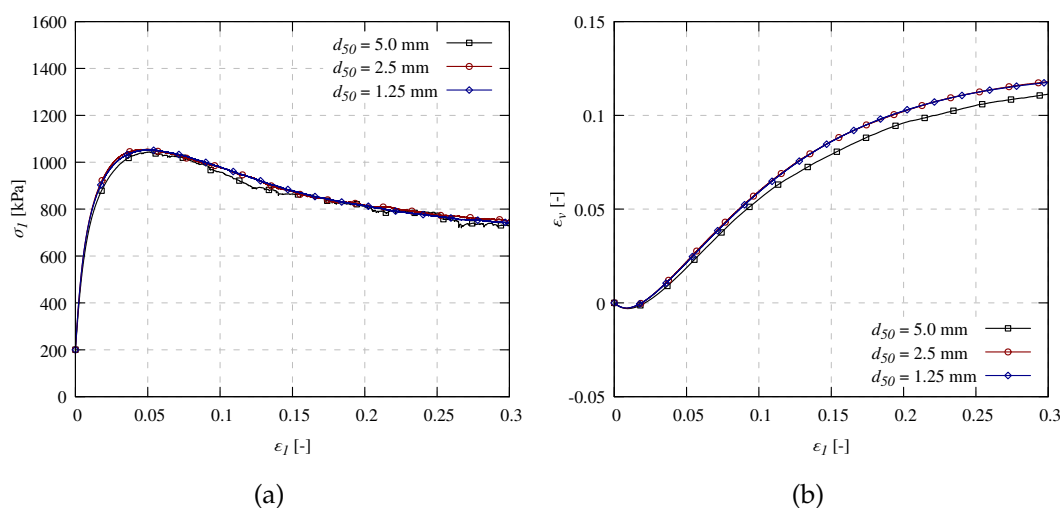


Figure 4.1: Numerical setup for triaxial compression test.

Figure 4.2: Triaxial compression test on initially dense sand ( $e_0=0.55$  and  $\sigma_c=200$  kPa): a) vertical normal stress  $\sigma_1$  and b) volumetric strain  $\epsilon_v$  versus vertical normal strain  $\epsilon_1$  from DEM for different mean grain diameter  $d_{50}$  ( $\mu_c=18^\circ$ ,  $E_c=300$  kPa,  $\nu_c=0.3$ ,  $\eta=0.4$  and  $\beta=0.7$ ).

After that, during the second stage the bottom and top walls moved vertically towards the center of the specimen, inducing triaxial compression. As a result, the  $\sigma_1$  stress increased, while the  $\sigma_2$  and  $\sigma_3$  stresses remained constant due to the side walls being able to move horizontally in response to the confining stress. The tests were performed under quasi-static conditions (the inertial number was kept below  $1e-04$  (Roux and Chevoir, 2005)) and under gravity-free conditions, with a damping coefficient set to  $\lambda_d=0.08$  (Kozicki et al., 2012).

### 4.1.3 Numerical results

In this section, the results of a series of triaxial compression tests on cohesionless sand are presented. First, the effect of the discrete material local variables on the granular material behavior is presented during the parametric study. Next, the calibration of the discrete model local variables and the comparison between the numerical results and the laboratory results are shown.

### Parametric study of discrete material local variables

At the beginning of the parametric study, the effect of a local interparticle friction angle  $\mu_c$  on the global response of the granular material was investigated. During the study three different values of  $\mu_c$  were studied:  $5^\circ$ ,  $15^\circ$  and  $25^\circ$ . As shown in Figure 4.3, the local friction has a significant impact on both the vertical normal stress  $\sigma_1$  and volumetric strain  $\varepsilon_v$ . Figure 4.3a shows that the peak normal stress value increased proportionally from  $\sigma_1^{\max} = 400$  kPa to  $\sigma_1^{\max} = 1400$  kPa as the local interparticle friction angle increased. Similarly, the residual normal stress value  $\sigma_1^{\text{res}}$  was dependent on  $\mu_c$  and varied between  $\sigma_1^{\text{res}} = 400$  kPa and  $\sigma_1^{\text{res}} = 950$  kPa (Figure 4.3a). In addition, the interparticle friction strongly influenced the evolution of the volumetric strain curves (Figure 4.3b). As  $\mu_c$  increased, the specimens exhibited greater contraction at the beginning of the test and greater dilation throughout the rest of the test.

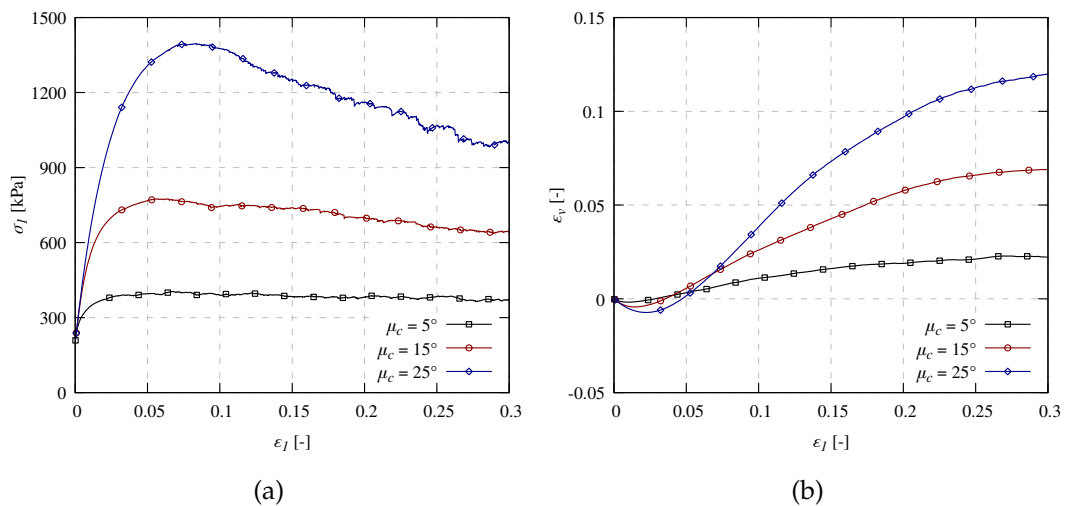


Figure 4.3: Triaxial compression test on initially dense sand ( $e_0=0.55$  and  $\sigma_c=200$  kPa): a) vertical normal stress  $\sigma_1$  and b) volumetric strain  $\varepsilon_v$  versus vertical normal strain  $\varepsilon_1$  from DEM for different interparticle friction angle  $\mu_c$  ( $E_c=200$  MPa,  $\nu_c=0.3$ ,  $\eta=1.0$  and  $\beta=1.0$ ).

Second, the influence of the local modulus of elasticity  $E_c$  on the granular material behavior was investigated. Figure 4.4 demonstrates the  $\sigma_1/\varepsilon_1$  and  $\varepsilon_v/\varepsilon_1$  curves obtained for three different  $E_c$  values: 20 MPa, 200 MPa, and 2000 MPa. The maximum value of local modulus of elasticity resulted in the highest peak normal stress and global stiffness of the specimen (Figure 4.4a). These values decreased proportionally with decreasing local modulus of elasticity. On the other hand, the modulus of elasticity had a smaller effect on the magnitude of the stresses in the residual phase. There is a clear difference in the evolution of the curves between the sample with  $E_c = 20$  MPa and the other two samples. During the test, the first exhibited only continuous hardening, unlike the latter two, where the initial hardening turned into softening after the peak. In addition, similar differences were observed in the deformation of the latter two samples. For the specimen with  $E_c = 200$  MPa and  $E_c = 2000$  MPa (Figure 4.4b), dilatancy occurred approximately from the beginning of the test. On the other hand, the sample with  $E_c = 20$  MPa showed a significant

contraction for almost the entire first half of the test, with a slight dilation in the residual phase (Figure 4.4b).

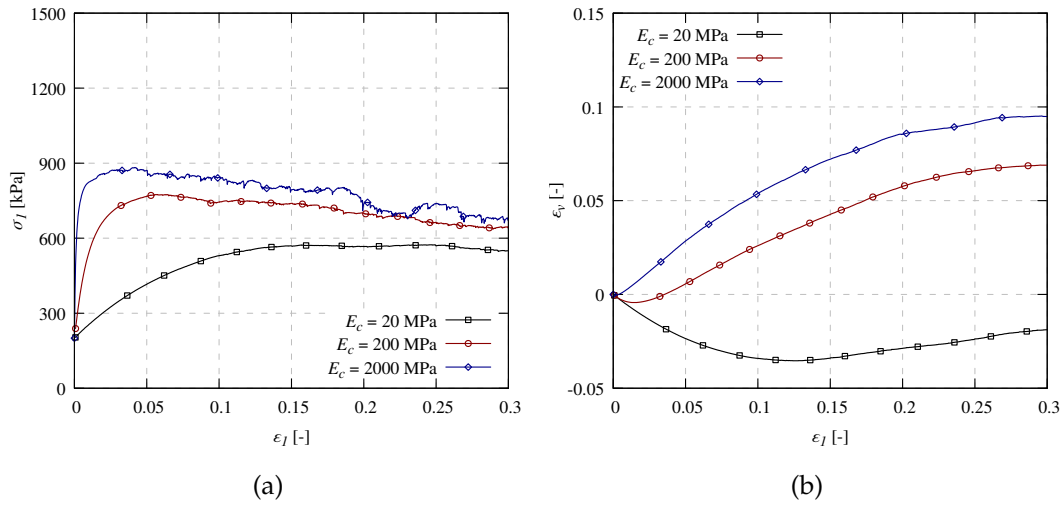


Figure 4.4: Triaxial compression test on initially dense sand ( $e_0=0.55$  and  $\sigma_c=200$  kPa): a) vertical normal stress  $\sigma_1$  and b) volumetric strain  $\epsilon_v$  versus vertical normal strain  $\epsilon_1$  from DEM for different local modulus of the elasticity  $E_c$  ( $\mu_c=15^\circ$ ,  $\nu_c=0.3$ ,  $\eta=1.0$  and  $\beta=1.0$ ).

Next, the effect of the shear/normal local stiffness ratio  $\nu_c$  on the macroscopic results of the triaxial test was investigated. During the study three different values of  $\nu_c$  were examined: 0.05, 0.3 and 0.6. Figure 4.5 shows that this ratio has a significant effect on the material behavior up to a certain point. Increasing  $\nu_c$  from 0.3 to 0.6 did not result in any serious changes in the evolution of the stress-strain and volume strain-strain curves (Figure 4.5). Depending on the value of  $\nu_c$ , the calculated peak and residual normal stresses were in the range of 680-770 kPa and 600-650 kPa, respectively (Figure 4.5a). The maximum volumetric strain at the end of the tests ranged from 0.057 to 0.075 (Figure 4.5b). All samples behaved similarly, exhibiting a small contraction at the beginning of the test followed by subsequent dilation.

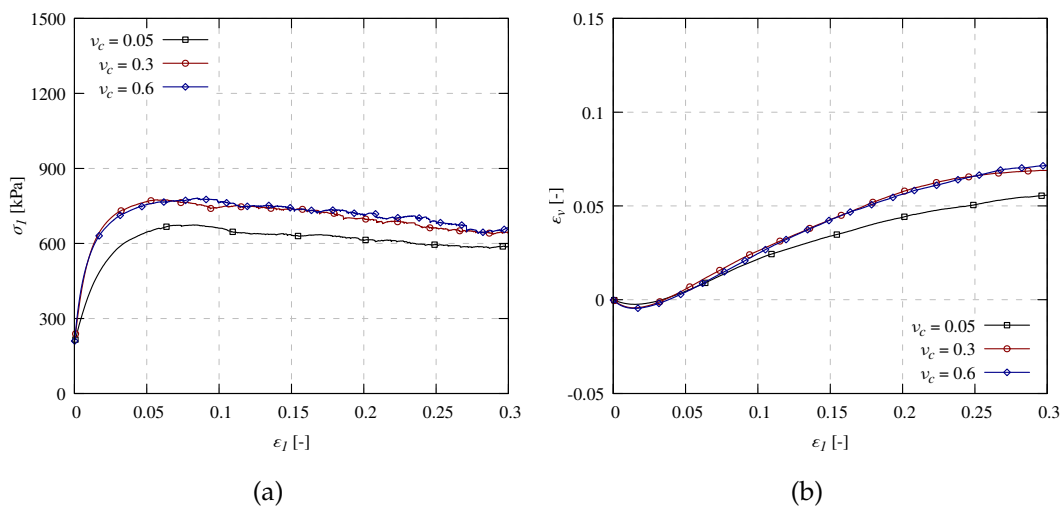


Figure 4.5: Triaxial compression test on initially dense sand ( $e_0=0.55$  and  $\sigma_c=200$  kPa): a) vertical normal stress  $\sigma_1$  and b) volumetric strain  $\epsilon_v$  versus vertical normal strain  $\epsilon_1$  from DEM for different shear/normal local stiffness ratio  $\nu_c$  ( $\mu_c=15^\circ$ ,  $E_c=200$  MPa,  $\eta=1.0$  and  $\beta=1.0$ ).

The last two figures presents the effect on the numerical results of two key parameters responsible for simulating the roughness of perfectly spherical grains: the limit rolling coefficient  $\eta$  (Figure 4.6) and the rolling stiffness coefficient  $\beta$  (Figure 4.7). These parameters are crucial because the development of the shear zones within the deforming granular materials composed of spherical particles can be obtained only by incorporating the rolling resistance in the discrete model (Iwashita and Oda, 1998). By taking these contact law components into account in the interaction between particles, it is possible, for example, to reproduce large voids and particle rotations that occur in real soils.

During the study the three values of  $\eta$  and  $\beta$  were studied: 0.1, 1.0 and 2.0. As shown in Figure 4.6, the influence of  $\eta$  on the triaxial test outcomes is negligible, particularly in regards to the volumetric changes of the samples. Normal stresses and deformations during the simulations increased only slightly with the growth of the limit rolling coefficient. On the other hand, the effect of the rolling stiffness coefficient  $\beta$  on the granular material behavior is more substantial. Figure 4.7 illustrates that the normal stresses at the peak and residual states increased from  $\sigma_1^{\max} = 680$  to  $\sigma_1^{\max} = 800$  kPa and from  $\sigma_1^{\text{res}} = 600$  to  $\sigma_1^{\text{res}} = 740$  kPa, respectively. As the rolling stiffness coefficient increased, the final deformation of the specimen changed from  $\varepsilon_v = 0.062$  (for  $\beta = 0.1$ ) to  $\varepsilon_v = 0.075$  (for  $\beta = 2.0$ ). Although no significant influence on macroscopic results was found (due to the lack of localizations in this test), the value of rolling resistance can still affect the mesoscopic behavior.

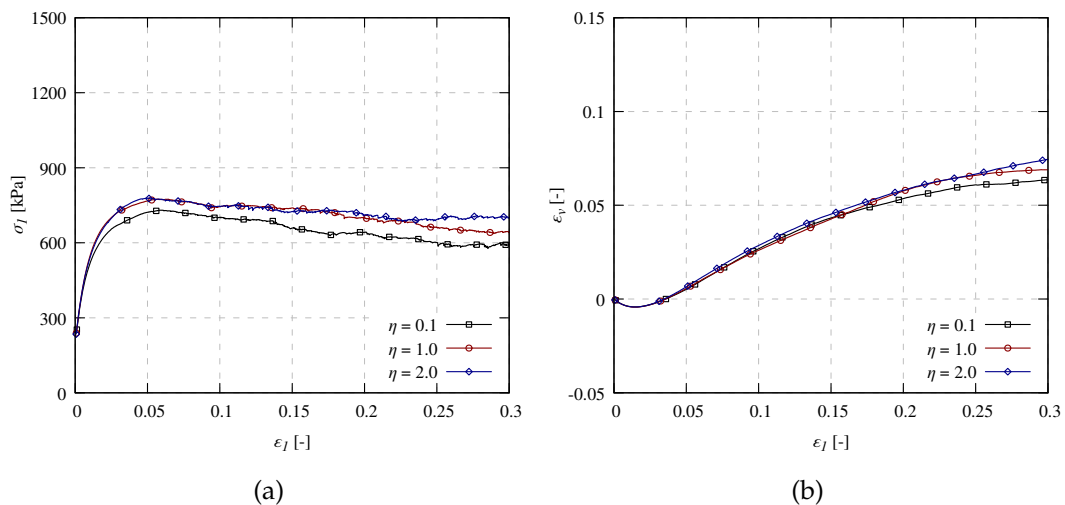


Figure 4.6: Triaxial compression test on initially dense sand ( $e_0=0.55$  and  $\sigma_c=200$  kPa): a) vertical normal stress  $\sigma_1$  and b) volumetric strain  $\varepsilon_v$  versus vertical normal strain  $\varepsilon_1$  from DEM for different limit rolling coefficient  $\eta$  ( $\mu_c=15^\circ$ ,  $E_c=200$  MPa,  $\nu_c=0.3$  and  $\beta=1.0$ ).

In summary, several attempts were made to evaluate the influence of the input local variables on the deformation and the strength of the sand specimen. The investigated local parameters had a pronounced effect on the granular material behavior. The most significant differences in the evolution of the curves were obtained by changing the interparticle friction angle  $\mu_c$  and the local modulus of elasticity  $E_c$ . Both parameters strongly influenced the peak and post-peak stress values on the stress-strain curve. In addition, the study showed that by changing the local

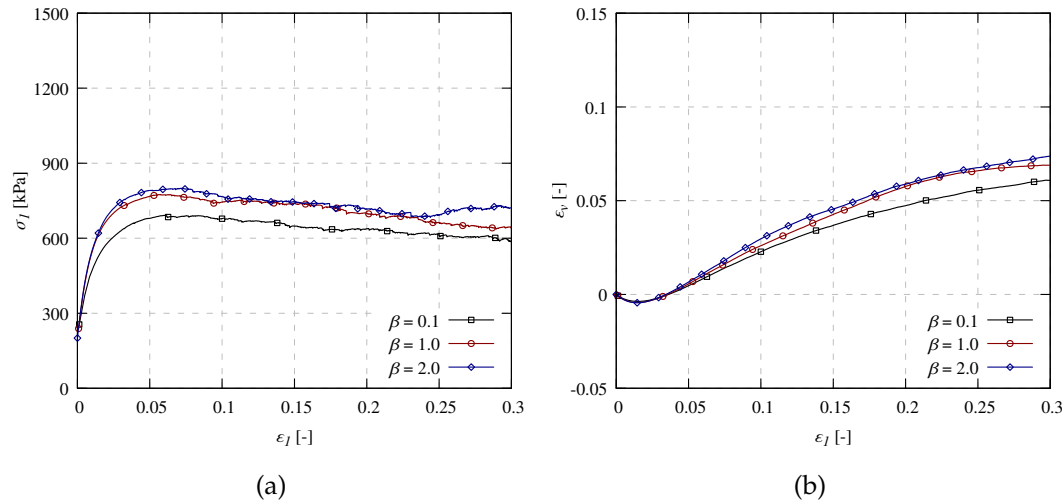


Figure 4.7: Triaxial compression test on initially dense sand ( $e_0=0.55$  and  $\sigma_c=200$  kPa): a) vertical normal stress  $\sigma_1$  and b) volumetric strain  $\epsilon_v$  versus vertical normal strain  $\epsilon_1$  from DEM for different rolling stiffness coefficient  $\beta$  ( $\mu_c=15^\circ$ ,  $E_c=200$  MPa,  $\nu_c=0.3$  and  $\eta=1.0$ ).

modulus of elasticity, the deformation of the sample, in particular its global stiffness, can be affected. In addition to the effects of  $\mu_c$  and  $E_c$ , it is worth highlighting the prominent effects of  $\nu_c$ ,  $\beta$ , and  $\eta$  on the peak strength of the sample. The volumetric strain curve in the initial phase of the test was substantially affected by  $\mu_c$  and  $E_c$ . The rest of the local parameters mostly affected the final deformation of the samples. The dilatancy angle was found to be strongly related to the interparticle friction angle, while its relationship with the rolling stiffness coefficient was noticeable but relatively small. The numerical results of the parametric study are in acceptable agreement with the existing literature regarding the triaxial test (Belheine et al., 2009; Widulinski et al., 2009) or the plain strain tests (Iwashita and Oda, 1998; Mohamed and Gutierrez, 2010). The results show that, with the accurate calibration, the numerical model is able to capture the nonlinear stress-strain behavior of sand.

### Numerical model calibration

As a result of the parametric study, a set of local material parameters for the granular material model was determined (Table 4.3). The calibration process involved setting the value of the discrete variables, which were adjusted using the corresponding homogeneous axisymmetric triaxial laboratory test results on the 'Karlsruhe' sand (Kolymbas and Wu, 1990). Such procedure of calibration of granular material model is commonly employed in the literature (Belheine et al., 2009; Kozicki et al., 2012; Kozicki et al., 2014; Leśniewska et al., 2020). The calibration procedure was conducted by comparing the macroscopic stress-strain and volume-strain curves for different confining pressures. The material properties of the sand used in the referenced experiments were listed at the beginning of the section (Table 4.2). The numerical procedure for the triaxial test used for calibration was identical to that used in the parametric study. Similar to the experiments, the DEM calculations were performed on an initially dense sample (initial void ratio  $e_0 = 0.53$ ) for three different confining pressures ( $\sigma_c = 50$  kPa,  $\sigma_c = 200$  kPa, and  $\sigma_c = 500$  kPa).

Table 4.3: Determined discrete material local variables.

| Parameter                                  | Value   |
|--|---------|
| interparticle friction angle $\mu_c$       | 18°     |
| local modulus of elasticity $E_c$          | 300 MPa |
| shear/normal local stiffness ratio $\nu_c$ | 0.3     |
| limit rolling coefficient $\eta$           | 0.4     |
| rolling stiffness coefficient $\beta$      | 0.7     |

Figure 4.8 presents the comparison between the numerical results and the experimental ones. The numerical model successfully captured the nonlinear behavior of the sand. The stress-strain curves (Figure 4.8a) were in a good agreement, while the volumetric strain curves (Figure 4.8b) were in acceptable agreement with the experimental outcomes. The numerical model demonstrated an accurate correlation between the confining pressure and the global stiffness and peak strength of the sand sample. Minor differences were observed for the confining pressure  $\sigma_c = 500$  kPa, where the peak stress and the global stiffness of the sample were slightly higher compared to the experiments. The discrepancies between the laboratory results and numerical simulations of sand regarding the volumetric strain curves were attributed to the shape of the numerical grains. The use of idealized spherical particles with rolling resistance in the simulations resulted in artificial dilatancy (Zhao et al., 2018).

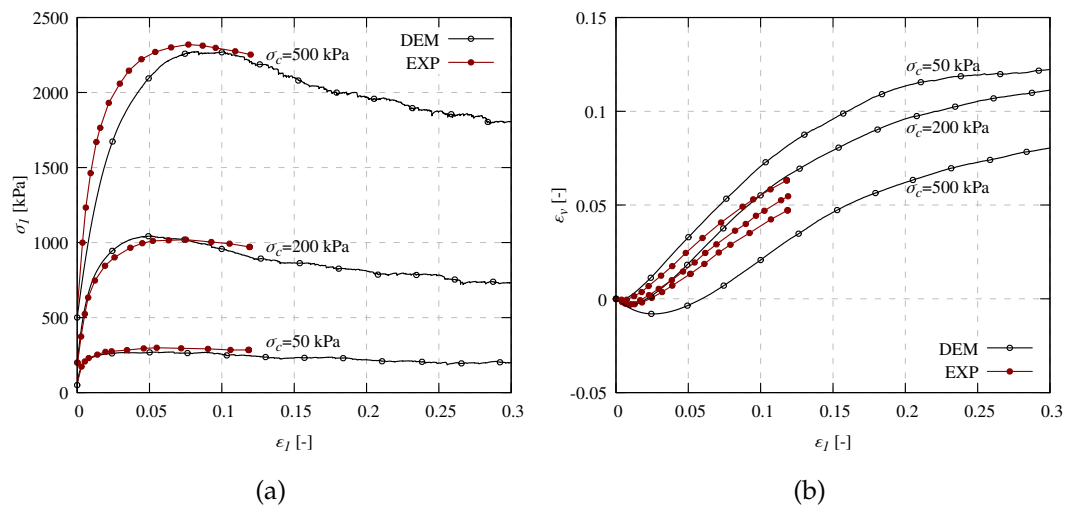


Figure 4.8: Triaxial compression test on initially dense sand ( $e_0 = 0.53$ ): a) calculated vertical normal stress  $\sigma_1$  and b) volumetric strain  $\epsilon_v$  versus vertical normal strain  $\epsilon_1$  from: DEM calculations (black empty dots) compared to laboratory experiments (red full dots) (Kolymbas and Wu, 1990) for different initial confining pressure  $\sigma_c$  ( $\mu_c = 18^\circ$ ,  $E_c = 300$  MPa,  $\nu_c = 0.3$ ,  $\eta = 0.4$  and  $\beta = 0.7$ ).

#### 4.1.4 Summary

In this section a detailed discrete analysis of the triaxial compression test was carried out. The effect of some local discrete parameter on the response of the 'Karlsruhe'

sand specimen was investigated during the parametric study. In addition, the discrete model of the sand was calibrated by comparison with experimental data. The following main conclusions were drawn from the discrete simulations:

- During the parametric study the influence of the interparticle friction angle  $\mu_c$  and the local modulus of elasticity  $E_c$  on the global response of the specimen (e.g. specimen peak strength, residual strength) was found to be the most significant. A less considerable effect on the specimen response was found when changing the  $\nu_c$ ,  $\eta$  and  $\beta$ . In the latter cases, only small changes in the curves evolution were found, mainly in the final phase of the test.
- The discrete model of granular material, consisting of spherical particles with rotational resistance, can accurately reproduce the nonlinear behavior of sand during triaxial compression test. Furthermore, this test can be used to calibrate the local parameters of the numerical model. In the presented studies, these parameters were determined as follows:  $\mu_c=18^\circ$ ,  $E_c=300$  MPa,  $\nu_c=0.3$ ,  $\eta=0.4$  and  $\beta=0.7$ . The numerical results obtained for different loads applied to the specimen were in good agreement with the experimental data, both in terms of shear resistance and volumetric changes of the sand specimen.

Based on the calculations presented in this section, the discrete model characteristics for further simulations were determined. Using this model, the analysis of the shear zone was performed in the subsequent chapters.

## 4.2 Direct shear test

### 4.2.1 Introduction

In this section, discrete simulations of direct shear test of cohesionless sand under constant normal pressure are presented. Direct shear test is a very common and simple procedure for the determination of the shear resistance of soils. It has been studied extensively in numerous experimental (Shibuya et al., 1997; Chandler and Hamilton, 1999; Härtl and Ooi, 2008; Salazar et al., 2015; Alhakim et al., 2023) and numerical investigations, both using continuum (Tejchman and Bauer, 2005; Gutierrez et al., 2009; Kozicki et al., 2013) and discrete approaches (Thornton and Zhang, 2003; Härtl and Ooi, 2008; Zhou et al., 2009; Kozicki et al., 2013; Salazar et al., 2015). In a typical direct shear test, the granular sample is placed inside the shear box, which is constructed of lower and upper steel or brass frames. During the test, one of the frames is locked and the other one is moving at a constant horizontal speed to induce shearing within the granular material.

The main aim of this section is to study the shear zone formation under precisely controlled constraints. As presented in the previous section, the discrete model accurately predicted the macroscopic behavior of the sand. However, it did not consider the strain localization due to the rigid boundary conditions. In this section, the direct shear test was employed to verify the ability of the numerical model to capture the mesoscale phenomena occurring in the granular material, with particular attention to the shear zone. The main advantage of the selected test is that the shear localization can be predicted in most cases, as it typically occurs between the lower and upper frames of the shear box.

The results presented in this section are partially covered in two publications: Grabowski and Nitka (2020) and Nitka and Grabowski (2021).

### 4.2.2 Numerical model and methodology

The simulations of the direct shear test were performed using spherical particles with rotational resistance. The material parameters of the direct shear test numerical model were the same as those determined using the calibration procedure based on the triaxial compression test presented in the previous section (see Table 4.3 in Chapter 4.1). However, this time, compared to the previous simulations, the 'Karlsruhe' sand composed of real-size grains was used. Therefore, the mean grain diameter was equal  $d_{50} = 0.5$  mm and varied between  $d = 0.25$  mm and  $d = 0.75$  mm. The numerical simulations (model setup shown in Figure 4.9) were carried out under full 3D conditions, with the specimen depth reduced from 60 mm ( $120 \times d_{50}$ ) to 5 mm ( $10 \times d_{50}$ ) to shorten the computation time (Figure 4.9). The reduction of the sample depth had a negligible effect on the numerical results (Figure 4.10, Kozicki et al. (2014)). The height and width of the specimen were 25 mm ( $50 \times d_{50}$ ) and 60 mm ( $120 \times d_{50}$ ), respectively. The upper and the lower parts of the shear box were created with rigid box elements.

The standard direct shear test procedure was followed for all tests. The first step involved creating the granular assembly composed of approximately 55 000 spherical particles inside the shear box, followed by the application of constant initial

normal pressure  $\sigma_n$  to the top frame. To obtain a desired initial density of the granular sample due to grain overlap, the interparticle friction angle  $\mu_c$  was varied during sample preparation. To obtain a sample with a lower initial void ratio, the interparticle friction angle was set between  $0^\circ$  and  $18^\circ$ . On the other hand, to obtain a sample with a higher initial void ratio, the interparticle friction angle was gradually changed from  $45^\circ$  to  $18^\circ$ . In the latter case, the global damping  $\lambda_d$  was also varied during the preparation, i.e. it was set higher than during the actual test. As a result, the porosity of the sample was increased due to the lack of vibration and movement of the particles. Once the desired void ratio of the sand mass was achieved and the kinetic energy of the assembly was negligible, the upper frame moved horizontally (inducing horizontal displacement  $u$ ) at a constant velocity (Figure 4.9c). The loading rate was slow enough to ensure the test was conducted under quasi-static conditions. During the shearing the upper frame was free to move vertically while the bottom frame was fixed. The space equal to the maximum grain diameter was left between the lower and upper frame walls (see the zoom in Figure 4.9a), as in the experiment, to prevent particles from getting stuck at the lower corners during shearing. The loss of sand during the shearing had a small effect on the void ratio and the volumetric strain (less than 1% of the particles leaked out through the gap during the test).

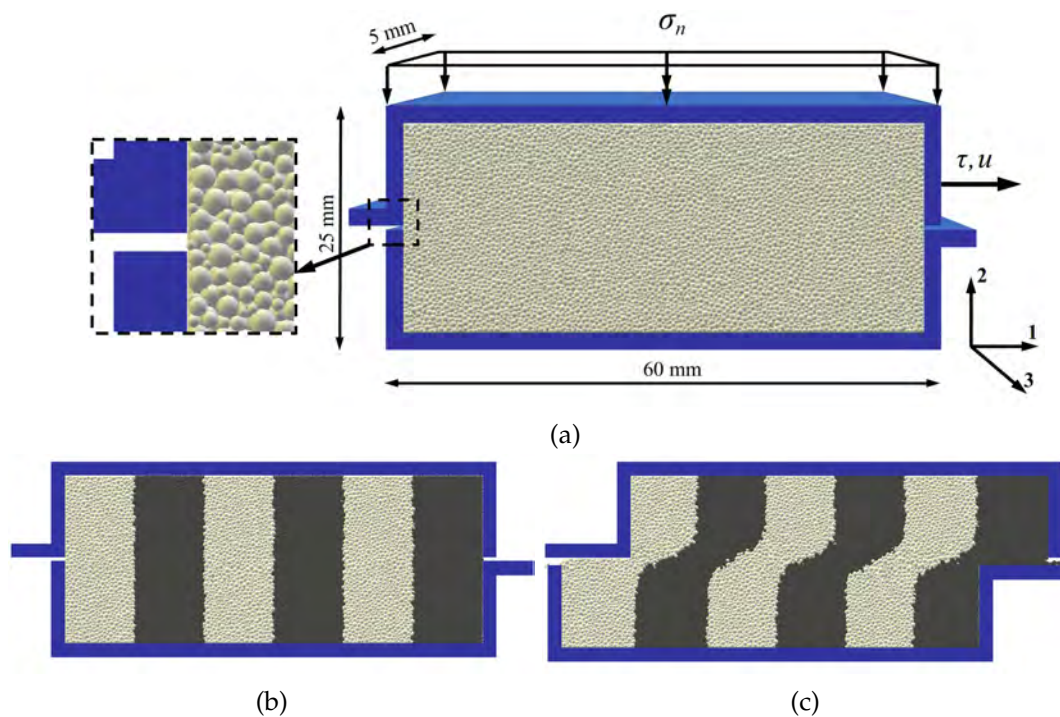


Figure 4.9: Direct shear test in DEM: a) numerical setup, b) sample at the initial state and c) deformed sample at the final state (Grabowski and Nitka, 2020; Nitka and Grabowski, 2021).

The procedure of sample preparation based on the compaction of randomly distributed particles confined in the shear box can result in anisotropy and inhomogeneity of the granular material. Before each test, the distribution of: initial void ratio, normal force chains, and contact orientation was analyzed. The exemplary results for the medium-dense specimen with initial void ratio  $e_0=0.63$  subjected to the

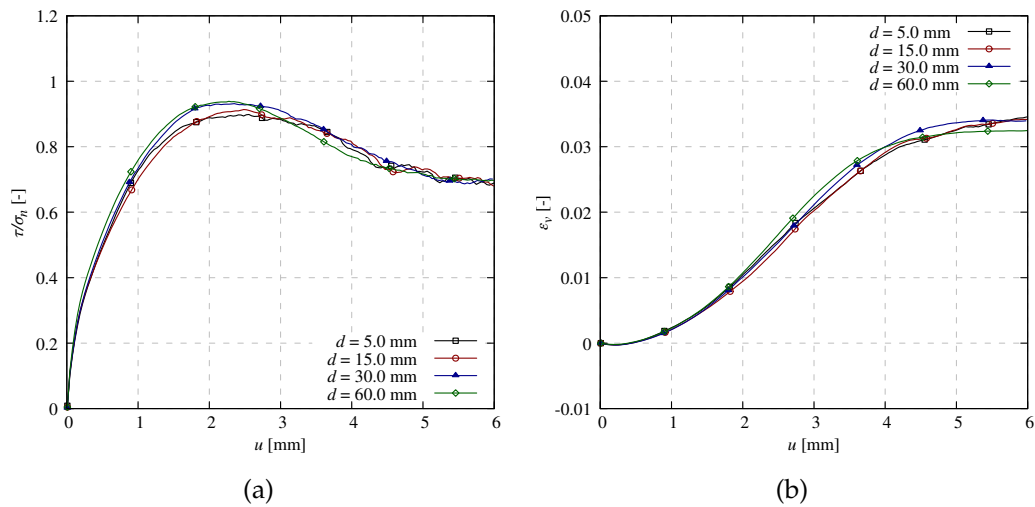


Figure 4.10: Direct shear test on initially medium-dense sand ( $e_0 = 0.63$  and  $\sigma_n = 50$  kPa): a) calculated shear stress ratio  $\tau/\sigma_n$  and b) volumetric strain  $\varepsilon_v$  versus total horizontal displacement  $u$  for different depth of the sand specimen  $d$ .

vertical load of  $\sigma_n = 200$  kPa are presented in Figure 4.11. The distribution of pores and voids between the particles did not vary with the location within the shear box (e.g., the porosity near the boundaries is similar to that in the center of the specimen). The assumed initial void ratio of  $e_0 = 0.63$  (represented by the blue color) was obtained for the whole sample with minor local deviations ( $< 5\%$  of the average value) (Figure 4.11a). The uniform color and size of the normal force chains between the particles indicates that the forces are evenly distributed throughout the sample and are approximately the same size (Figure 4.11b). This is complemented by the polar histogram of the contact orientation (Figure 4.11c), which shows the average value of the normal forces between the particles for angles between  $0^\circ$  and  $360^\circ$ . The vertical load applied on the upper frame caused the negligible anisotropy in contact orientation. As a result, the forces oriented from angles between  $60^\circ$  and  $120^\circ$  are slightly larger than the horizontal forces. In summary, according to the analysis of the parameters presented in Figure 4.11, the prepared sand sample was considered as isotropic and homogeneous.

A series of direct shear tests were performed throughout the investigation, considering different variations of normal pressure  $\sigma_n$  applied to the shear box (50 kPa, 200 kPa, and 500 kPa were studied), as well as different initial void ratios  $e_0$  of the sand sample (0.53, 0.60, and 0.75 were studied).

### 4.2.3 Numerical results

In this section, the results of a series of direct shear tests of cohesionless sand under various conditions are presented. First, a comparison between the shear resistance and granular material deformation obtained with numerical simulations and with laboratory experiments by Salazar et al. (2015) is presented. Next, the influence of

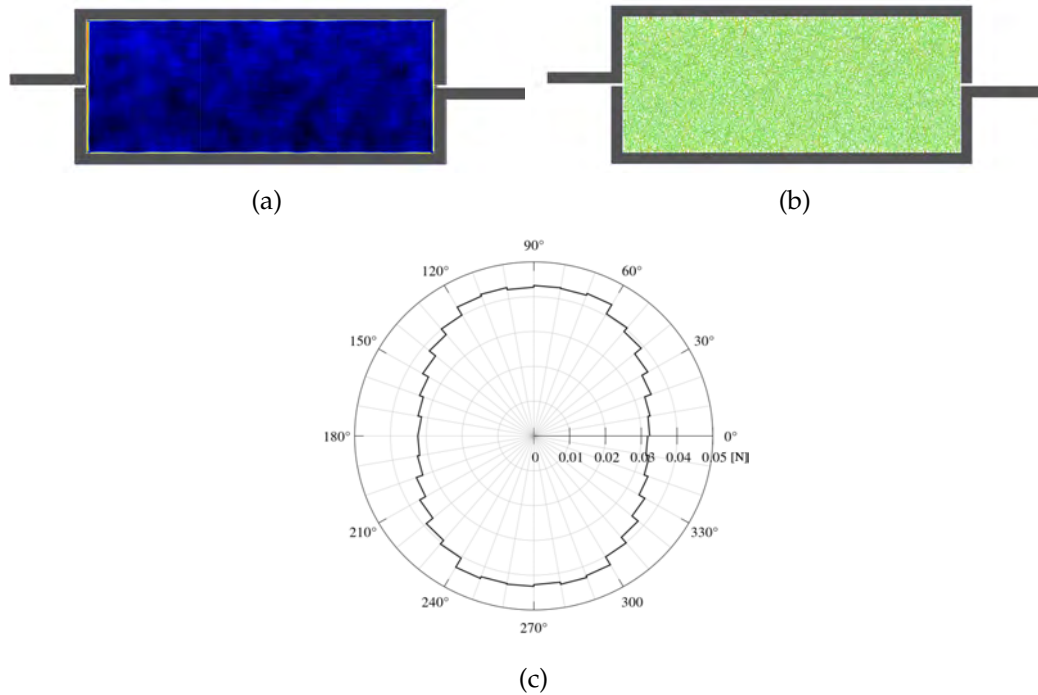


Figure 4.11: Example of: a) void ratio distribution, b) normal contact forces distribution, and c) contact orientation at the initial state of the test, prior to applying pressure ( $e_0 = 0.63$  and  $\sigma_n = 200$  kPa).

the normal pressure applied to the shear box and the initial void ratio of the specimen on the shear resistance and volumetric strains is shown. Finally, a comprehensive analysis of the granular material behavior, including its deformation, the distribution of sphere rotations, void ratios, and force chains at the final stage of shearing, has been performed. This analysis includes also the study of the shear zone evolution during shearing for selected case, with particular attention to the pre-peak phase.

#### Evolution of mobilized shear stress and volumetric strain

In the first step the validation of the numerical model was performed. The numerical results of the specimen with initial void ratio  $e_0 = 0.63$  and initial vertical pressure  $\sigma_n = 80$  kPa were compared with the experimental study of Salazar et al. (2015). The comparison in Figure 4.12 shows that the evolution of both stress and volumetric strain curves were in good agreement with the experimental results. The peak stress and the residual stress obtained in the calculations were slightly lower than in the experiments (about 5% and 15% respectively). The negligible fluctuations observed particularly in the residual state of the test were mainly caused by the continuous reorganization of the force chains within the shear zone during shearing. This behavior was related to the successive formation and collapse of particle columns inside the shear zone during granular material deformation (Rechenmacher, 2006; Chupin et al., 2011). Small discrepancy was also observed on the volumetric strain curve, with a larger residual value obtained in the numerical analysis. The artificial dilatancy of the material was caused by the use of spheres with rotational resistance instead of realistically shaped grains (Zhao et al., 2018). It is also important to note

that perfect agreement with the direct shear test results of Salazar et al. (2015) cannot be expected, since the material parameters used in the model were calibrated in triaxial experiments on 'Karlsruhe' sand.

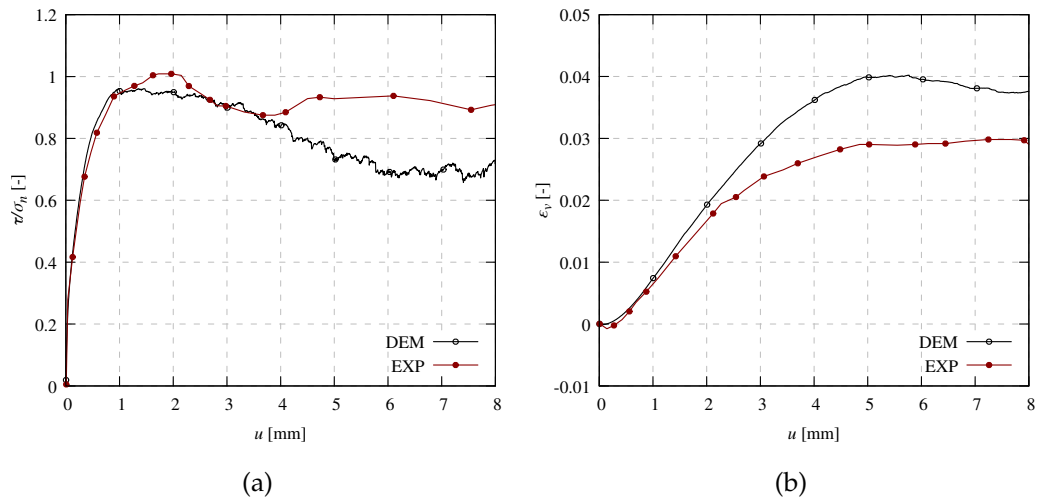


Figure 4.12: Direct shear test on initially medium-dense sand: a) calculated shear stress ratio  $\tau/\sigma_n$  and b) volumetric strain  $\varepsilon_v$  versus total horizontal displacement  $u$  from discrete simulation (Nitka and Grabowski, 2021) and laboratory test (Salazar et al., 2015) ( $e_0 = 0.63$  and  $\sigma_n = 80$  kPa).

After model validation, the effect of the normal pressure was checked (only for the initially medium-dense sample with void ratio of  $e_0 = 0.60$ ). Figure 4.13 shows the evolution of the shear stress ratio  $\tau/\sigma_n$  and the volumetric strain  $\varepsilon_v$  versus the total horizontal displacement  $u$  of the upper frame for three different vertical pressures  $\sigma_n = 50$  kPa, 200 kPa, and 500 kPa. The evolution of both curves is typical for the sand behavior during a direct shear test. The shear stress initially increased and reached a peak value at a displacement of approximately  $u = 1$  mm for  $\sigma_n = 50$  kPa,  $u = 2$  mm for  $\sigma_n = 200$  kPa, and  $u = 3$  mm for  $\sigma_n = 500$  kPa (Figure 4.13A). After reaching the peak value, the sand exhibited softening. The residual volumetric strain decreased with increasing pressure (Figure 4.13B) as in the experiment by Salazar et al., 2015. It is evident that the highest pressure resulted in the lowest volumetric strain with a small initial contraction, while the lowest pressure resulted in the highest peak shear stress ratio and global stiffness of the sample.

The effect of the initial void ratio  $e_0$  on the global response of the specimen was also investigated. Sand samples with void ratios of  $e_0 = 0.53$ , 0.60, and 0.75 were prepared under a constant vertical pressure  $\sigma_n = 200$  kPa (Figure 4.14). The initial porosities were intended to represent different density conditions (dense, medium-dense, and loose) of the granular media used in the study. The upper limit of the void ratio was set to  $e_0 = 0.75 - 0.80$  because it is difficult to achieve artificially void ratio greater than this threshold using perfectly spherical particles. Initially dense and medium-dense samples exhibited hardening, reaching the shear stress peak at  $u = 1.25$  mm ( $e_0 = 0.53$ ) and  $u = 2$  mm ( $e_0 = 0.60$ ), respectively, and then exhibited softening. In contrast, the initially loose sample showed continuous hardening throughout the test (Figure 4.14c). Overall, the initially dense and medium-dense sand dilated, while the initially loose sand contracted (Figure 4.14B). The results

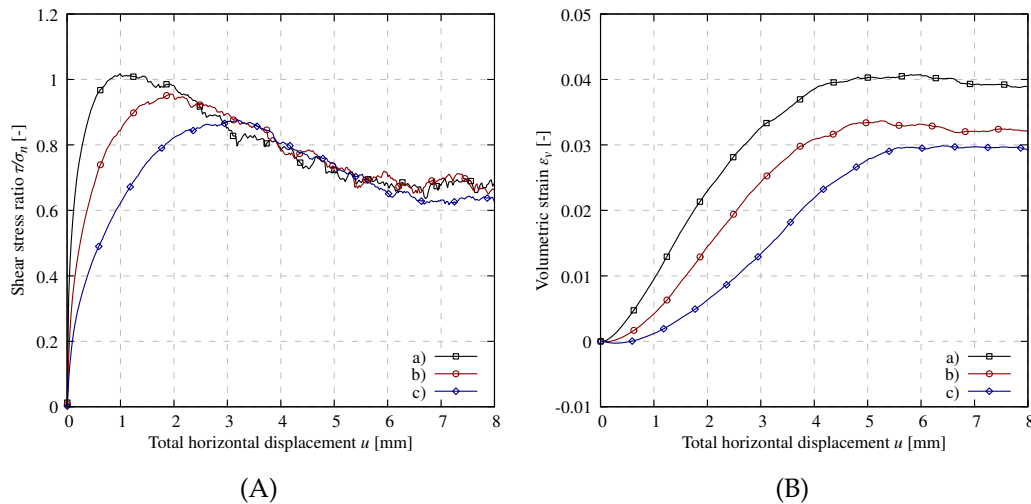


Figure 4.13: Calculated: A) shear stress ratio  $\tau/\sigma_n$  and B) volumetric strain  $\varepsilon_v$  versus total horizontal displacement  $u$  from discrete simulations of direct shear test for different normal stresses: a)  $\sigma_n = 50$  kPa, b)  $\sigma_n = 200$  kPa, and c)  $\sigma_n = 500$  kPa ( $e_0 = 0.60$ ) (Grabowski and Nitka, 2020; Nitka and Grabowski, 2021).

were consistent with general knowledge of the behavior of granular media (Salazar et al., 2015).

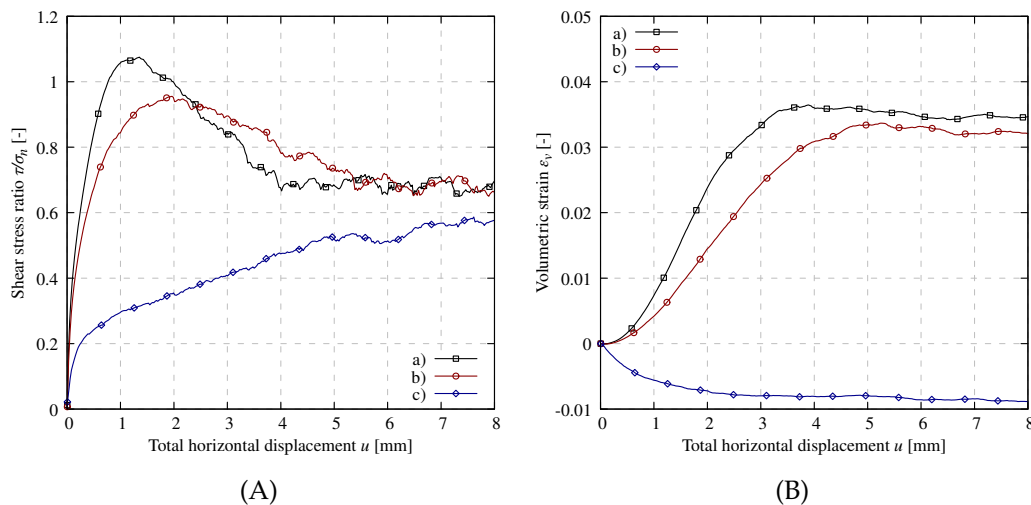


Figure 4.14: Calculated: A) shear stress ratio  $\tau/\sigma_n$  and B) volumetric strain  $\varepsilon_v$  versus total horizontal displacement  $u$  from discrete simulations of direct shear test for different initial void ratios: a)  $e_0 = 0.53$ , b)  $e_0 = 0.60$ , and c)  $e_0 = 0.75$  ( $\sigma_n = 200$  kPa) (Grabowski and Nitka, 2020; Nitka and Grabowski, 2021).

### Effect of the normal pressure on mesoscopic behavior of cohesionless sand

The research, described in previous section, has so far focused on the macroscopic behavior of the cohesionless sand sample under shearing in a direct shear apparatus. In this section, the numerical results for the grain-level characteristics, such as the deformation of the sample, the distribution of the normal force chains, sphere rotations, and the void ratio distribution are presented. The effect of the normal stress

applied to the shear box on the mesoscopic behavior of the granular material has been investigated. The presented results were obtained at the final state of shearing ( $u_x=6.0$  mm).

First, the influence of the vertical loads applied to the top shear box on the mesoscopic behavior of sand was investigated. Similarly, as in the previous section, three values of these loads were examined:  $\sigma_n = 50$  kPa, 200 kPa, and 500 kPa in case of a medium-dense sample ( $e_0=0.60$ ). Figure 4.15 presents the influence of the vertical load applied to the top frame on the behavior of the sand. Based on the displacements of the spheres, it can be seen that the deformation of the sample was similar in all cases. In each of these cases, the sand was divided into two quasi-rigid bodies separated by the uniform and horizontal shear zone located at the boundaries between the upper and lower frames. Particles in the lower frame were locked and particles above the shear zone followed the movement of the upper frame.

Figure 4.16 presents the distributions of particle rotations in the entire specimen. Red color represents clockwise rotation and blue color represents counterclockwise rotation. A clear horizontal shear zone appeared between the shear box frames in all cases. Small differences were observed only in the thickness of the shear zone, which increased from  $10 \times d_{50}$  to  $18 \times d_{50}$  in direct proportion to the decrease in load applied to the top frame (Figure 4.16). The thickness of the shear zones was calculated based on an inflection point in the vertical distribution of sphere rotations  $\omega$ . The point where the rotation  $\omega$  was  $\leq 5\%$  of the maximum sphere rotation  $\omega_{max}$  in the localization defined the lower boundary and the upper boundary of the shear zone. The direction of the sphere rotations in the localization was mainly clockwise, according to the shear direction, with only a few loose spheres rotating in the opposite direction (Figure 4.16). The largest sphere rotations occurred directly at the mid-height of the specimen and decreased in magnitude as they approached the top and bottom frames. Particles in the upper and lower frames mostly showed no rotation.

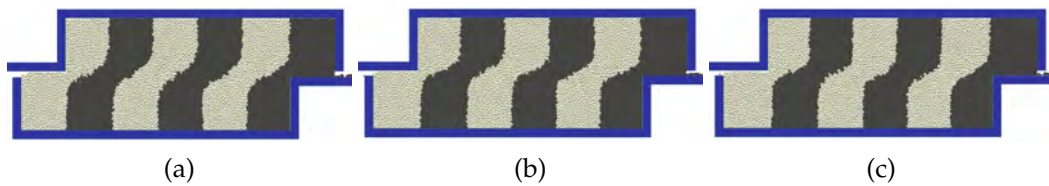


Figure 4.15: Front view of the specimen at the final state of the test for different vertical load: a)  $\sigma_n=50$  kPa, b)  $\sigma_n=200$  kPa and c)  $\sigma_n=500$  kPa ( $e_0=0.60$ ) (Grabowski and Nitka, 2020).

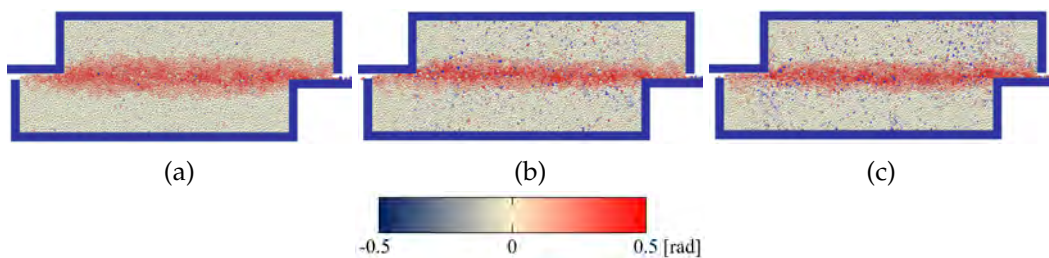


Figure 4.16: Distribution of sphere rotations  $\omega$  in granular specimen at the final state of the test for different vertical load: a)  $\sigma_n=50$  kPa, b)  $\sigma_n=200$  kPa and c)  $\sigma_n=500$  kPa ( $e_0=0.60$ ) (red color-clockwise rotations, blue color-counterclockwise rotations) (Grabowski and Nitka, 2020).

Next, the calculated void ratio distribution presented in Figure 4.17 was examined. The values of the void ratio  $e$  were calculated from the averaging cell (REV-represent element volume). The REV cell was  $5 \times d_{50}$  wide,  $5 \times d_{50}$  high, and  $10 \times d_{50}$  deep, and it was moved by  $1 \times d_{50}$  to obtain a better resolution of the plots. As a result the REV volume was equal  $15.625 \text{ mm}^3$  and contained approximately 250 grains. The selection of the size of REV was arbitrary, however this size was already successfully used in other studies, e.g. by Nitka et al. (2015). The REV size allowed to avoid large local fluctuations, without losing mesoscopic phenomena. The distribution of porosity within the sample corresponded well with the distribution of particle rotations with respect to the formation of the shear zone. The greatest increase in porosity was observed at the mid-height of the specimen and reached  $e=e_{res}=0.80$  at the final state of the test. It was observed that the significant dilation of the sand occurs mainly in the localized area. Outside the shear zone, negligible changes in porosity were observed.

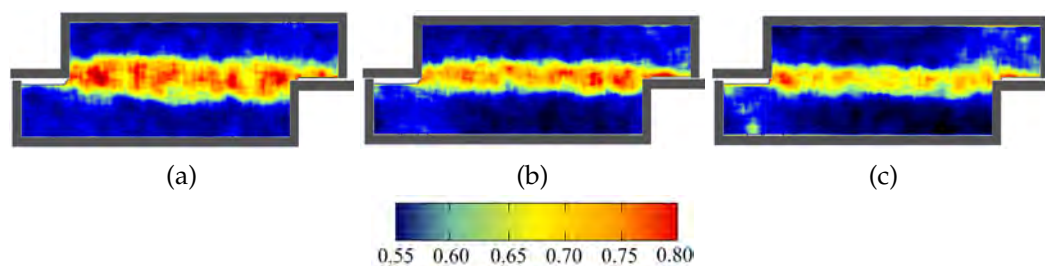


Figure 4.17: Distribution of void ratio  $e$  in granular specimen at the final state of the test for different vertical load: a)  $\sigma_n=50$  kPa, b)  $\sigma_n=200$  kPa and c)  $\sigma_n=500$  kPa ( $e_0=0.60$ ).

Figure 4.18 presents the normal force chains distribution in the sand specimen. The red lines indicate forces above the mean value, and the line thickness corresponds to the normal force value. The distribution of contact forces at the end of the test was highly non-uniform. The normal pressure applied to the upper frame had a significant effect on the contact force network. The magnitude of the forces transferred in each interaction increased in direct proportion to the applied pressure. The distribution of the force chains did not seem to be affected by the magnitude of the applied load. In all cases, the main horizontal forces occurred in the upper left and lower right regions of the specimen. These areas were connected by the diagonal forces established between them. The localization path and thickness cannot be determined based on the contact force network. The orientation of the force chains in the localized region was diagonal to the shear zone plane.

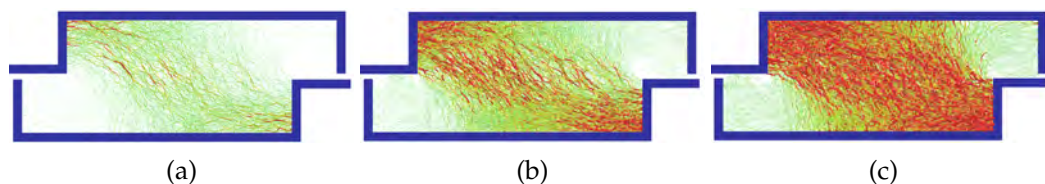


Figure 4.18: Distribution of normal force chains in granular specimen at the final state of the test for different vertical load: a)  $\sigma_n=50$  kPa, b)  $\sigma_n=200$  kPa and c)  $\sigma_n=500$  kPa ( $e_0=0.60$ ) (Grabowski and Nitka, 2020).

Figure 4.19 shows a polar distribution of contact forces in the 1-2 plane (mean amplitude and orientation to the horizontal). It can be seen that in all cases the direction of the mean contact forces changed from initially vertical to diagonal as the shearing process progressed. Similar to the previous results, the load applied to the sand specimen mostly affected the magnitude of the normal forces (note that the graph scale differs for each case). In all cases, the orientation of the mean contact forces to the horizontal in the residual state varied from  $130^\circ$  to  $170^\circ$ , which was a result of the significant horizontal and diagonal forces shown in Figure 4.18.

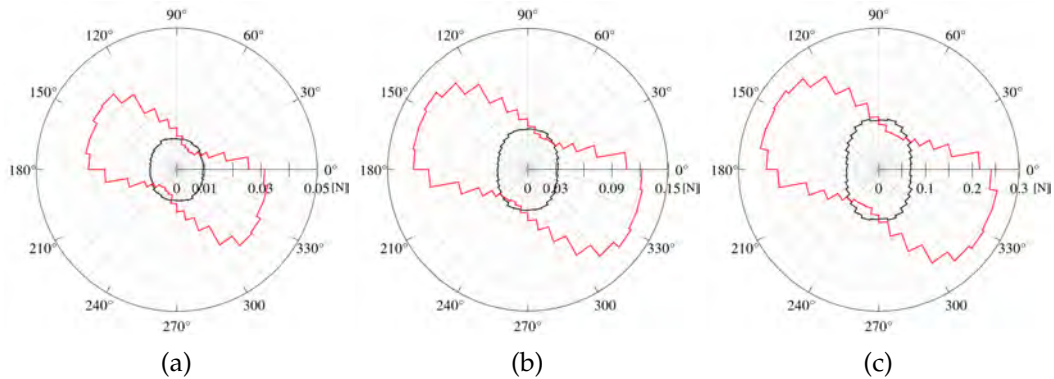


Figure 4.19: Polar mean contact force distribution in granular specimen at the initial state (black line) and final state of the test (red line) for different vertical load: a)  $\sigma_n=50$  kPa, b)  $\sigma_n=200$  kPa and c)  $\sigma_n=500$  kPa ( $e_0=0.60$ ) (the graphs scale has been adjusted to ensure good readability, considering the varying magnitudes of the vertical load).

### Effect of the initial void ratio on mesoscopic behavior of cohesionless sand

The effect of the initial void ratio of the sand sample on the mesoscopic behavior of the granular material has been investigated. Similarly as in the previous section, the final deformation of the specimen, the distribution of normal force chains, sphere rotations and void ratio distribution were investigated. The presented results were obtained at the final state of the shearing ( $u_x=6.0$  mm). The analysis was conducted for three different initial void ratios:  $e_0=0.53$  (dense sand),  $e_0=0.60$  (medium-dense sand) and  $e_0=0.75$  (loose sand) under constant normal pressure applied to the upper frame  $\sigma_n=200$  kPa.

Figure 4.20 presents the influence of the initial void ratio on the final deformation of the sand. For initially dense and medium-dense sand samples, the final shape of the localization was similar (Figure 4.20a,b). In these cases, the granular material was divided into two quasi-rigid bodies separated by the uniform and horizontal shear zone located at the boundaries between the upper and lower frames. In contrast to the first two cases, the initially loose sample (Figure 4.20c) did not exhibit a pronounced horizontal shear zone. During the test, the loose particles in the upper box started to compact near the upper left corner instead of moving as a homogeneous material in the horizontal direction. The similar mechanism as in the passive and active earth pressure problem was observed on both sides of the specimen. The central part of the sample remained unchanged during the test.

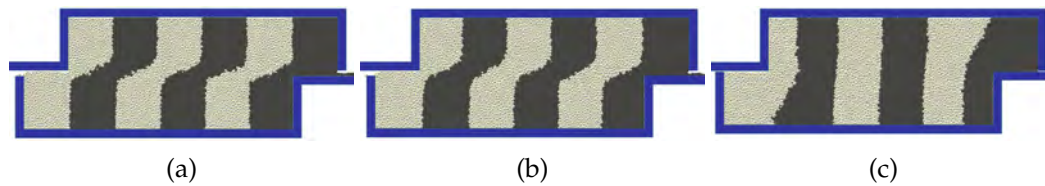


Figure 4.20: Front view of the specimen at the final state of the test for different initial void ratio  $e_0$ : a)  $e_0=0.53$ , b)  $e_0=0.60$  and c)  $e_0=0.75$  ( $\sigma_n=200$  kPa) (Grabowski and Nitka, 2020).

Next, the distribution of particle rotations was examined. In the case of the specimens with  $e_0=0.53$  and  $e_0=0.60$  the grain rotation clearly shown the location of the shear zone (Figure 4.21a,b). The final shape of the localization was similar in these cases and formed at the mid-height of the granular specimen, splitting it into two quasi-rigid solids. The shear zone thickness was uniform along both specimens and approximately equal to  $t_s=16-18 \times d_{50}$ . Particle rotations within the shear zone were mainly clockwise, corresponding to the direction of shear. In contrast to the dense and medium-dense samples, the largest particle rotations in the loose sample were not concentrated at the mid-height of the sand. Both clockwise and counterclockwise rotations were localized near the advancing and receding boundaries of the sample. Particles in the rest of the sample mostly showed no rotation.

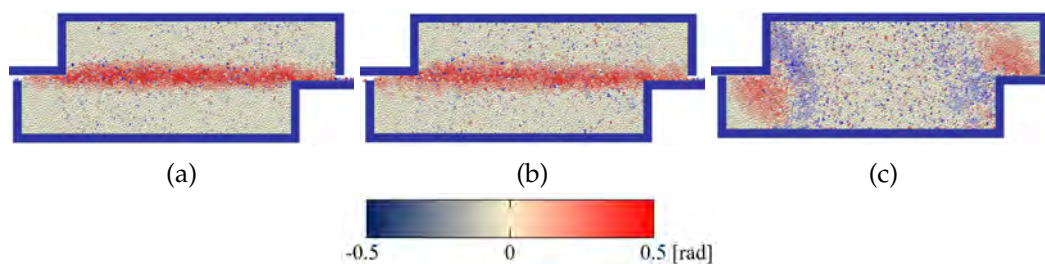


Figure 4.21: Distribution of sphere rotations  $\omega$  in granular specimen at the final state of the test for different initial void ratio  $e_0$ : a)  $e_0=0.53$ , b)  $e_0=0.60$  and c)  $e_0=0.75$  ( $\sigma_n=200$  kPa) (red color-clockwise rotations, blue color-counterclockwise rotations) (Grabowski and Nitka, 2020).

Next, the calculated void ratio distribution presented in Figure 4.22 was examined. The distribution of porosity within the sample corresponded well with the distribution of particle rotations with respect to the formation of the shear zone in case of dense and medium-dense samples (Figure 4.22a,b). In these cases, the increase in the porosity of the granular material was concentrated in the center of the sample height and reached the value of  $e_{res}=0.80$ . Outside the shear zone, negligible changes in porosity were observed. In contrast, in the initially loose sample (Figure 4.22c), the void distribution within the sand sample was non-uniform as compared to the previous cases. The clear horizontal shear plane did not occur.

Figure 4.23 presents the normal force chain distribution in the sand sample. In all cases, the contact network showed the existence of diagonal normal forces within the shear zone. Horizontal contact forces were observed in the upper left and lower right corners of the specimen. Similar as in the previous section, the normal force distribution does not provide sufficient information to determine the thickness or shape of the shear zone. The magnitude of the contact forces was similar, although the mean force slightly increased as the initial void ratio increased.

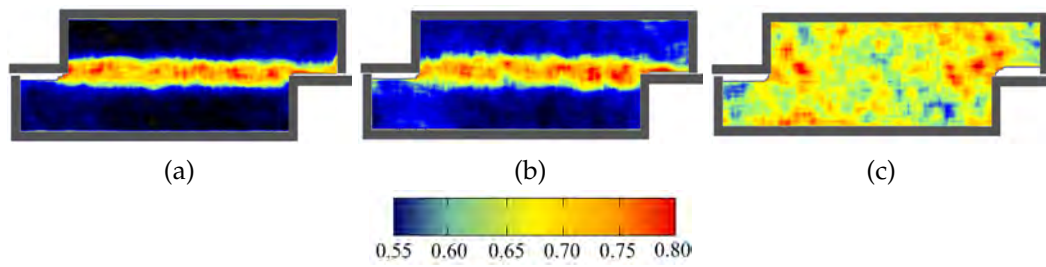


Figure 4.22: Distribution of void ratio in granular specimen at the final state of the test for different initial void ratio  $e_0$ : a)  $e_0=0.53$ , b)  $e_0=0.60$  and c)  $e_0=0.75$  ( $\sigma_n=200$  kPa).

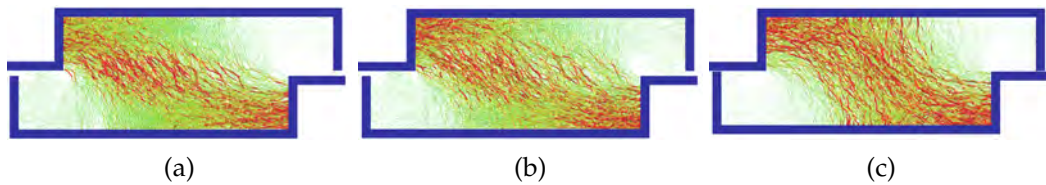


Figure 4.23: Distribution of normal force chains in granular specimen at the final state of the test for different initial void ratio  $e_0$ : a)  $e_0=0.53$ , b)  $e_0=0.60$  and c)  $e_0=0.75$  ( $\sigma_n=200$  kPa) (Grabowski and Nitka, 2020; Nitka and Grabowski, 2021).

Figure 4.24 shows a polar distribution of normal force network. It can be seen that initially the vertical mean contact forces (with an orientation to the horizontal of  $90^\circ$ ) dominated due to the constant normal load applied to the specimen. During the shearing, the direction of the mean contact forces changed from vertical to diagonal. In all cases, the dominant magnitudes of normal forces were observed within the range of  $130^\circ$  to  $180^\circ$  angles. Compared to the initially dense and medium-dense samples (Figure 4.24a,b), the mean contact forces in the initially loose sand (Figure 4.24c) were greater, particularly at the beginning of the test, due to the lower number of interactions between particles.

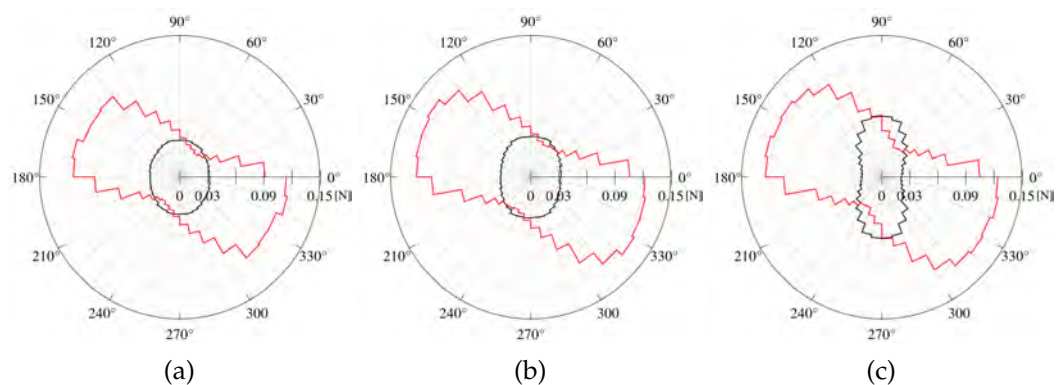


Figure 4.24: Polar mean contact force distribution in granular specimen at the initial state (black line) and final state of the test (red line) for different initial void ratio  $e_0$ : a)  $e_0=0.53$ , b)  $e_0=0.60$  and c)  $e_0=0.75$  ( $\sigma_n=200$  kPa).

### Evolution of the shear zone

The previous sections have focused on studying the effect of normal pressure and initial void ratio of the sand specimen response during shearing in a direct shear apparatus. The cumulative results in the final state of shearing for different boundary conditions were presented. In this section, the focus was placed on the development of the shear zone, with particular attention to its evolution in the initial phase of the direct shear test. The emphasis was on the localization shape rather than numerical values. In order to do so, the specimen with pronounced horizontal shear zone was selected for the analysis ( $e_0=0.60$ ,  $\sigma_n=200$  kPa) The analysis was performed at different stages, starting from the initial phase ( $u_x = 0.1$  mm) up to the final state of the test ( $u_x = 6.0$  mm).

First, the fluctuations of the displacement were calculated (Figure 4.25). The plots were obtained by calculating the fluctuations as  $\vec{u}_i - \vec{u}_{avg}$ , where  $\vec{u}_i$  represents the displacement of  $i$  sphere and  $\vec{u}_{avg}$  represents the mean displacement of all spheres in the entire specimen in the analyzed time step. The difference between the motion of individual grains and the motion of the entire granular mass can ensure valuable information about the granular material deformation (Abedi et al., 2012; Richefeu et al., 2012). To improve readability, black arrows representing the vectors are presented for every 50 elements and were multiplied by  $1.0e03$ . In the analyzed case, the various orientation and different magnitude of the arrows shows the shear zone location and shape. Interesting phenomena was observed at the beginning of the test, in the pre-peak regime of the shearing. In this stage, the shear zone formed an s-shape rather than a straight line between the shear boxes of the apparatus (Figure 4.25a-e). As the shearing proceeded, the shape of the shear zone flattened shaping the pure horizontal line in the residual phase of the test (Figure 4.25i). It occurred that the test was not homogeneous from the beginning. Not only did the material begin to shear in the middle part, but the entire specimen was mobilized. Similar evolution of the shear zone was captured and described in the numerical analysis performed by Wang et al. (2007a).

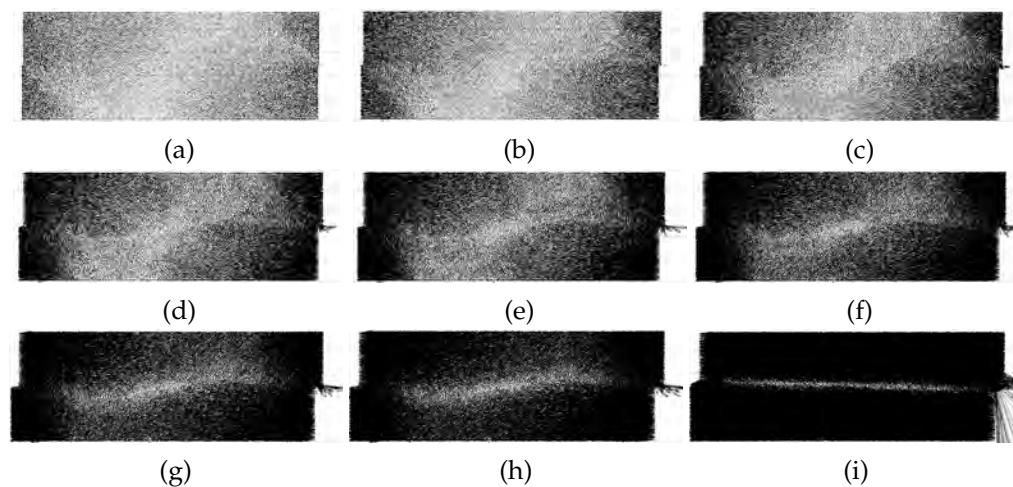


Figure 4.25: Evolution of displacements fluctuations  $\vec{u}_i - \vec{u}_{avg}$  in the entire specimen for: a)  $u_x=0.10$  mm, b)  $u_x=0.50$  mm, c)  $u_x=0.75$  mm, d)  $u_x=1.00$  mm, e)  $u_x=1.25$  mm, f)  $u_x=1.50$  mm, g)  $u_x=1.75$  mm, h)  $u_x=2.00$  mm and i)  $u_x=6.00$  mm ( $e_0=0.60$  and  $\sigma_n=200$  kPa) (black vectors, multiplied by  $1e03$ , shows only every 50 elements for readability) (Grabowski and Nitka, 2020).

Next, some other characteristic parameters of the deforming granular specimen were calculated. The values presented on the following graphs (Figures 4.26-4.32) were averaged from the REV cell of the same size as used in the previous section to calculate the distribution of the void ratio.

First, the changes in the position of the particles was analyzed. Figures 4.26 and 4.27 present the normalized horizontal and vertical displacements during the shearing. In the case of the horizontal displacement, the blue color represents the lack of the particles movement and the red color represents the largest displacements of the particles. Similar to the calculated fluctuations, the curvilinear s-shape of the shear zone was captured in the initial phase of the test (Figure 4.26a-d). The shear zone was depicted by a white line representing the mean value of the horizontal displacements. With the increase of the shear box displacement, the white line gradually flattened (Figure 4.26e,f), forming a horizontal line at the end of the test.

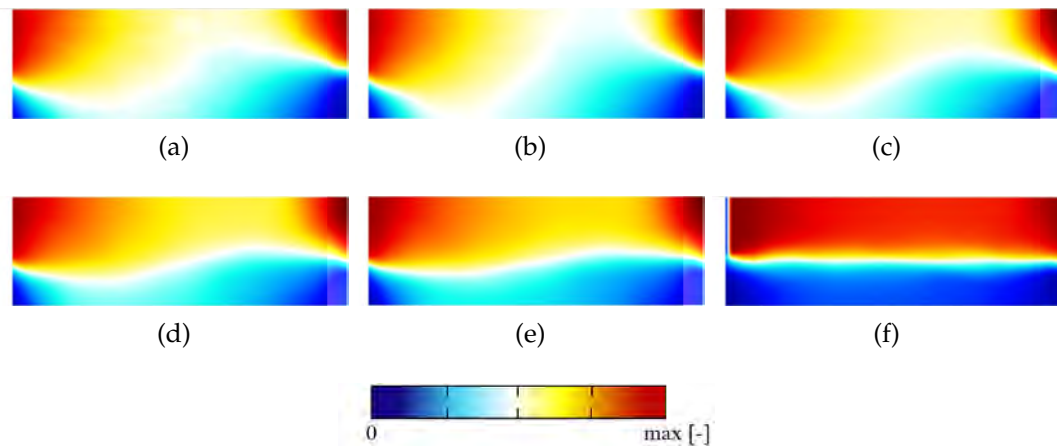


Figure 4.26: Evolution of horizontal displacements  $u_x$  in the entire specimen for: a)  $u_x=0.10$  mm, b)  $u_x=0.50$  mm, c)  $u_x=1.00$  mm, d)  $u_x=1.50$  mm, e)  $u_x=2.00$  mm and f)  $u_x=6.00$  mm ( $e_0=0.60$  and  $\sigma_n=200$  kPa) (Nitka and Grabowski, 2021).

Contrary to the horizontal displacement, the distribution of the normalized vertical displacement was not in agreement with the fluctuations. In this case, the blue color represents the greatest movement of particles towards the lower shear box, the red color represents the greatest movement toward the upper box, and the white color represents no vertical displacements. During the initial phase, the vertical movement of the particles was localized mainly close to both side boundaries. On the left side of the specimen, the particles were moved towards the bottom wall of the shear box. This movement was related to the contraction caused by the shear stress. On the other hand, on the right side of the specimen, the grains moved toward the upper wall of the shear box. Based on the calculated vertical displacements, no s-shape was detected. The no-displacement line ranged from the upper left corner to the bottom-right one. During the test, it flattened, but even in the residual state, it did not straighten. It was quite surprising that the vertical displacements of the particles showed a completely different behavior than the horizontal ones.

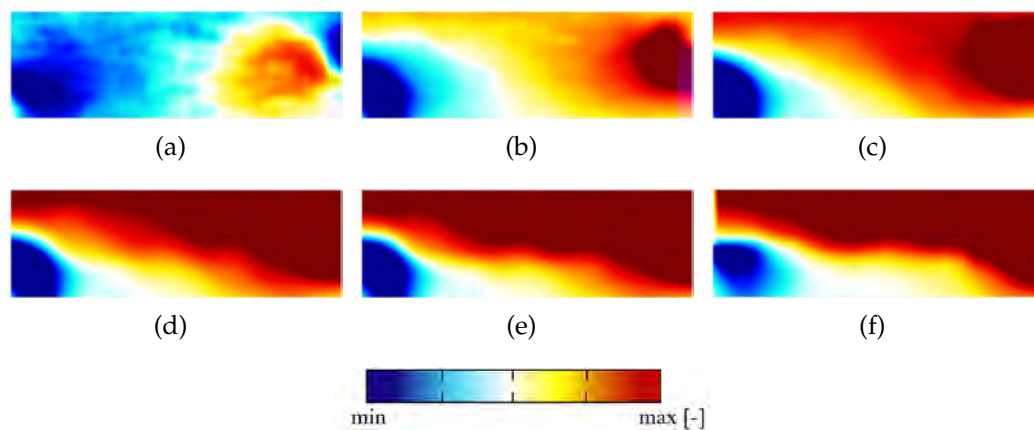


Figure 4.27: Evolution of vertical displacements  $u_y$  in the entire specimen for: a)  $u_x=0.10$  mm, b)  $u_x=0.50$  mm, c)  $u_x=1.00$  mm, d)  $u_x=1.50$  mm, e)  $u_x=2.00$  mm and f)  $u_x=6.00$  mm ( $e_0=0.60$  and  $\sigma_n=200$  kPa) (Nitka and Grabowski, 2021).

Next, the gradient of horizontal and vertical displacements were calculated (Figures 4.28 and 4.29). To calculate the gradients the specimen was divided into vertical strips of width equal to REV. In each vertical strip the gradient was calculated starting from the bottom up to the top of the shear box. Then, the gradient values were normalized by the maximum value in each vertical strip.

At the beginning, the gradient of the horizontal displacement  $u_x^*$  was studied (Figure 4.28). In the initial phase of the shearing, significant concentration was observed close to the gap between the lower and upper shear boxes. Near the left boundary, the inclination of the concentration was oriented downwards, on the contrary to the concentration near the right boundary where it was oriented upwards (Figure 4.28a). It can be clearly seen that the shear zone was not created as a uniform one, with sometimes two or three extremum found in one vertical strip. As the shearing proceeded, the gradient extremum propagated from the boundaries towards the center of the specimen creating one curve (Figure 4.28b-e). Finally, in the residual phase the curve flattened to almost completely straight line. However, still some minor fluctuations appeared (Figure 4.28f). A conclusion was drawn, that a lot of smaller localizations occur at different heights during the shearing. However, it appears that the granular material seeks an optimal shear pattern in accordance with its internal friction angle. Nonetheless, the design of the shear box constrains the material, compelling it to form a straight horizontal shear zone at the mid-height of the specimen.

Interesting behavior was also captured based on the calculated gradient of the vertical displacement  $u_y^*$  (Figure 4.29). At the beginning of the shearing, the chaotic distribution of the gradient was observed in the entire specimen (Figure 4.29a). Then the concentration occurred near the boundaries discontinuity, similarly as in the distribution of the horizontal displacement gradient (Figure 4.29b). In addition, a strong negative gradient was observed slightly below the discontinuity on the left side and slightly above the discontinuity on the right side of the shear box. A significant diagonal line occurred between the boundaries (Figure 4.29c), which shape was in contrast to the s-shape curve observed previously. The inclination of this line was approximately  $33^\circ$  which was related to the natural slope angle for sand. As the



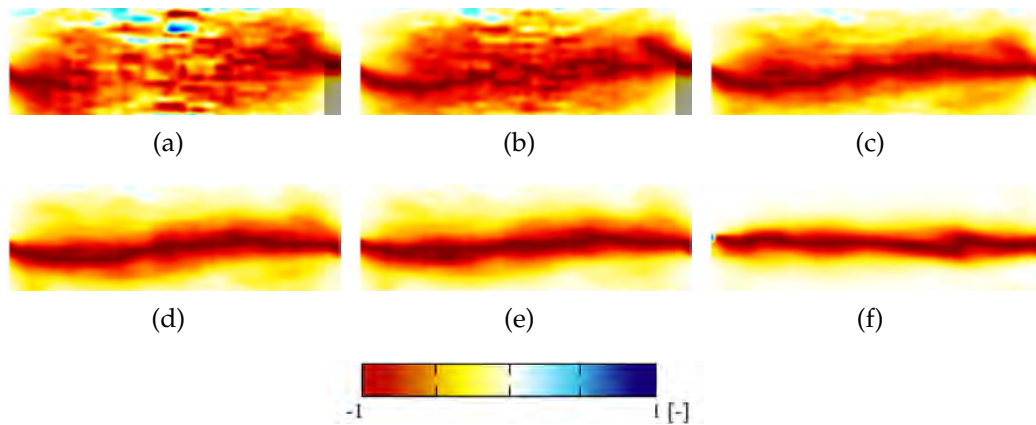


Figure 4.28: Evolution of the gradient of horizontal displacements  $u_x^*$  in the entire specimen for: a)  $u_x=0.10$  mm, b)  $u_x=0.50$  mm, c)  $u_x=1.00$  mm, d)  $u_x=1.50$  mm, e)  $u_x=2.00$  mm and f)  $u_x=6.00$  mm ( $e_0=0.60$  and  $\sigma_n=200$  kPa) (Nitka and Grabowski, 2021).

shearing proceeded, this maximum gradient lines started to propagate towards the boundaries, creating finally curved localization (Figure 4.29d-e). In the residual state, the maximum gradients line was still not a straight line. It is worth noting, that the region where gradient was equal zero formed similar s-shaped curve observed previously. Inside this area, the particles experienced highest vertical displacements connected to the granular material dilatancy. On the left side these displacements were oriented downwards and on the right side they were oriented upwards.

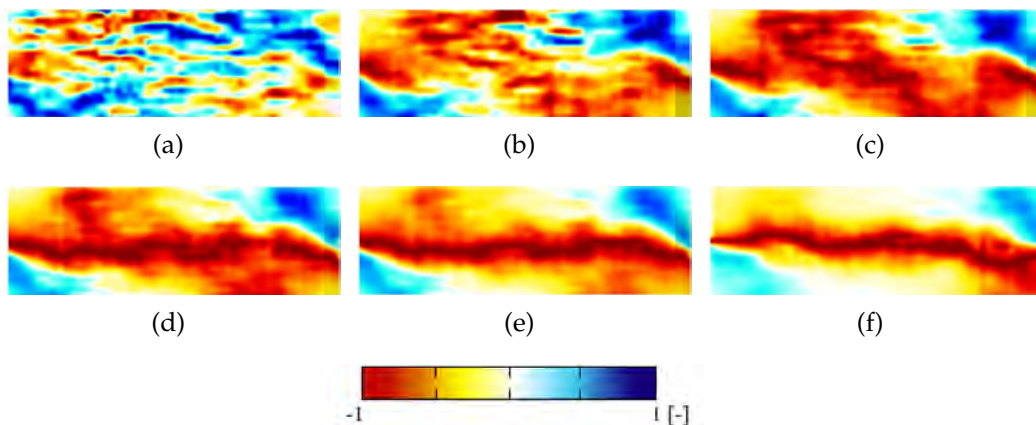


Figure 4.29: Evolution of the gradient of vertical displacements  $u_y^*$  in the entire specimen for: a)  $u_x=0.10$  mm, b)  $u_x=0.50$  mm, c)  $u_x=1.00$  mm, d)  $u_x=1.50$  mm, e)  $u_x=2.00$  mm and f)  $u_x=6.00$  mm ( $e_0=0.60$  and  $\sigma_n=200$  kPa) (Nitka and Grabowski, 2021).

The gradient of cumulative rotation within the samples was also examined (Figure 4.30). This particle-level parameter is one of the most commonly used techniques to determine shear localization in discrete simulations of granular materials. However, the distribution of rotations was quite chaotic, especially in the pre-peak regime. In the residual phase, a clear horizontal shear zone was captured using the cumulative rotations of the particles. The rotations appeared to be a result of the shear, not the cause.

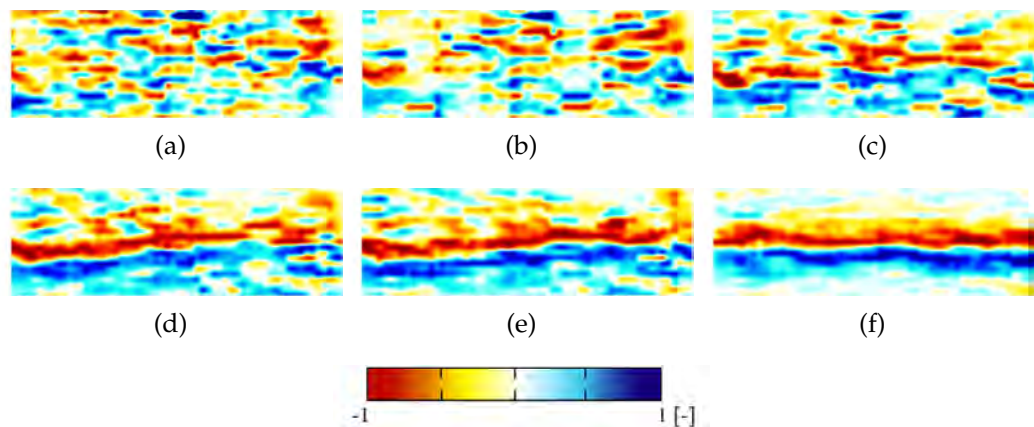


Figure 4.30: Evolution of the gradient of particle rotations  $\omega^*$  in the entire specimen for: a)  $u_x=0.10$  mm, b)  $u_x=0.50$  mm, c)  $u_x=1.00$  mm, d)  $u_x=1.50$  mm, e)  $u_x=2.00$  mm and f)  $u_x=6.00$  mm ( $e_0=0.60$  and  $\sigma_n=200$  kPa) (Nitka and Grabowski, 2021).

Finally, the distribution of stresses within the specimen was studied. The stresses were calculated according to the Love-Webber formula (Luding, 2004) formulated as:

$$\sigma_{ij} = \frac{1}{V_p} \sum_{c=1}^N x_i^c f_j^c \quad (4.1)$$

where  $N$  is the number of the contact points,  $x_i^c$  is the  $i^{\text{th}}$  component of branch vector jointing from the center of mass of the particle to the contact point ' $c$ ',  $f_j^c$  the  $j^{\text{th}}$  component of the total force at the contact point ' $c$ ' and  $V_p$  is the cell volume. The values of  $\sigma_{ij}$  were calculated from the same averaging cell (REV) used for the calculation of void ratio.

Figures 4.31-4.33 presents the gradients of horizontal normal stress  $\sigma_{11}$ , vertical normal stress  $\sigma_{22}$  and shear stresses  $\sigma_{12}$ . As in the previously calculated variables, in the pre-peak regime the highest changes in gradients of the normal horizontal stresses were observed near the left (blue color) and right discontinuity (red color) between the shear frames (Figure 4.31a). As the shearing proceeded, the maximum gradient lines were observed slightly above the mid-height of the specimen (blue color) and slightly below the mid-height of the specimen (red color) (Figure 4.31b-e). In the residual phase, these lines were connected by diagonal ones connecting upper left and lower right corners of the shear box. The distribution of horizontal stresses gradient in the final phase of the shearing (Figure 4.31f) was in agreement with the force chain network presented previously (see Figure 4.23b). The conclusion may be drawn in the analyzed case, that the displacement and stresses are not constant in the shear zone. Moreover, the final shear zone was neither perpendicular or parallel to the stress paths. This is in agreement with the other studies, which shows that the maximum normal force chains are diagonal to the shear zone (Kozicki et al., 2013; Salazar et al., 2015; Feng et al., 2018).

The changes in gradients of vertical stresses differed from the horizontal ones. After initially chaotic distribution (Figure 4.32a), the vertical stresses exhibited many diagonal lines with gradients extrema (Figure 4.32b-f). These lines were observed



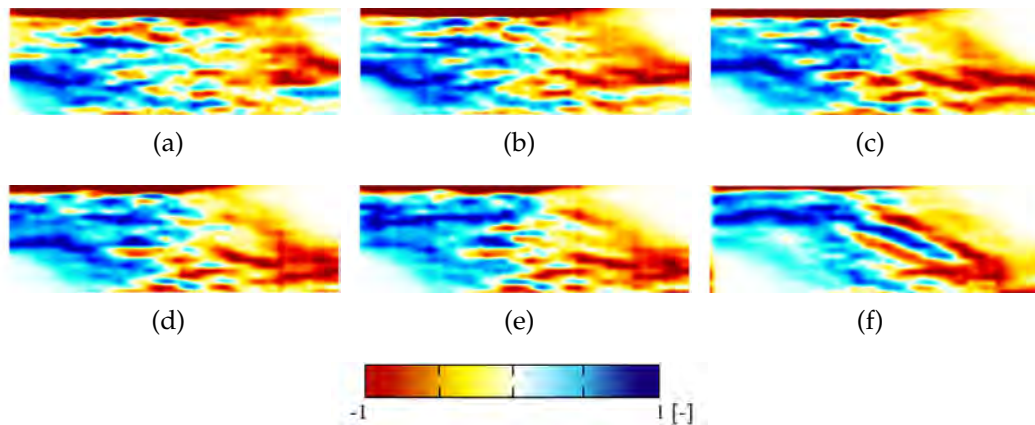


Figure 4.31: Evolution of gradient of horizontal stresses  $\sigma_{11}$  in the entire specimen for: a)  $u_x=0.10$  mm, b)  $u_x=0.50$  mm, c)  $u_x=1.00$  mm, d)  $u_x=1.50$  mm, e)  $u_x=2.00$  mm and f)  $u_x=6.00$  mm ( $e_0=0.60$  and  $\sigma_n=200$  kPa) (Nitka and Grabowski, 2021).

both in the pre-peak regime and also in the residual state of the test. The inclination of the gradients extrema was about  $60^\circ$  and was independent to the development of the shear zone. Such behavior was not observed in the literature, yet.

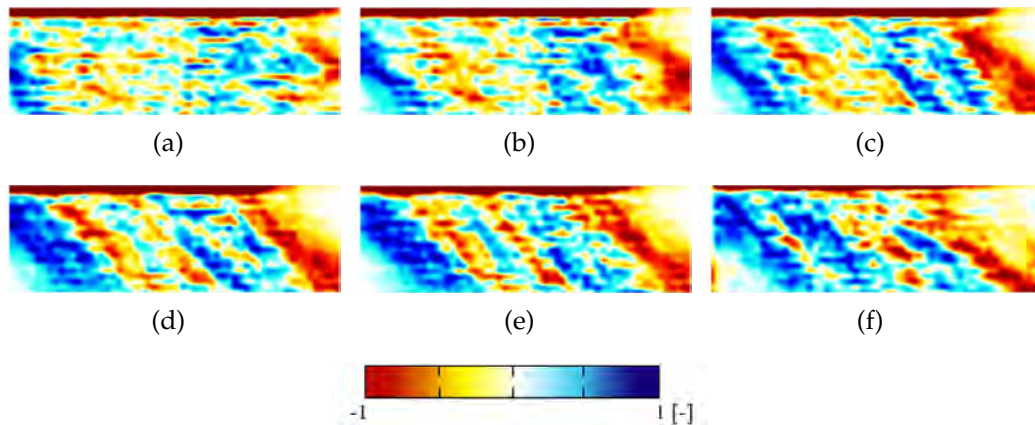


Figure 4.32: Evolution of gradient of vertical stresses  $\sigma_{22}$  in the entire specimen for: a)  $u_x=0.10$  mm, b)  $u_x=0.50$  mm, c)  $u_x=1.00$  mm, d)  $u_x=1.50$  mm, e)  $u_x=2.00$  mm and f)  $u_x=6.00$  mm ( $e_0=0.60$  and  $\sigma_n=200$  kPa) (Nitka and Grabowski, 2021).

Finally, the gradient of the shear stresses  $\sigma_{12}$  were calculated (Figure 4.33). From the initial phase of the test, the maximum shear stresses occurred in the middle part of the shear box. They changes propagated from the gap between the frames. The stresses increased with the specimen mid-height and then decreased (Figure 4.33a-d). This behavior was enforced by the construction of the shear box, which enforced shear zone to form in the mid-height of the specimen. However, as the shearing proceeded, the horizontal line started to deviate and become parallel to the gradient of the horizontal stresses (Figure 4.33f).

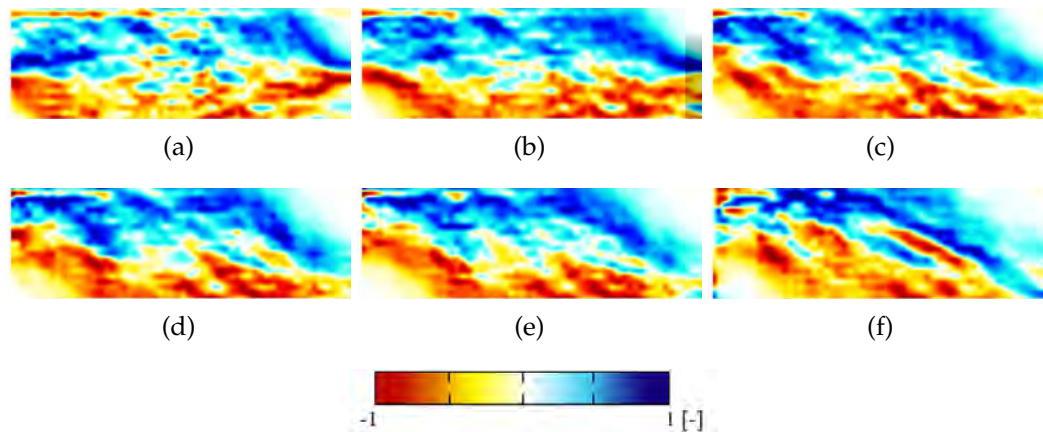


Figure 4.33: Evolution of gradient of shear stresses  $\sigma_{12}$  in the entire specimen for: a)  $u_x=0.10$  mm, b)  $u_x=0.50$  mm, c)  $u_x=1.00$  mm, d)  $u_x=1.50$  mm, e)  $u_x=2.00$  mm and f)  $u_x=6.00$  mm ( $e_0=0.60$  and  $\sigma_n=200$  kPa) (Nitka and Grabowski, 2021).

#### 4.2.4 Summary

In this section a detailed discrete analysis of the direct shear test of cohesionless sand with real sized particles was performed. The effect of the initial void ratio and the load applied to the shear box on the global response of the specimen was investigated. In addition, the analysis of the mesoscopic behavior of the shear zone in the pre-peak regime was performed. The analysis showed that the numerical model of granular material calibrated on the triaxial compression test can be used to simulate other types of soil mechanics problems. The following main conclusions were drawn from the discrete simulations:

- The discrete model of granular material, consisting of spherical particles with rotational resistance, can accurately reproduce the nonlinear behavior of sand during direct shear test. The numerical results were in good agreement with the experimental data and with general knowledge of the granular material behavior.
- The peak and the residual shear resistance of the sample increased with the decrease of both the initial void ratio of the sample and the normal load applied to the top platen. The volumetric strain of the sample at the end of the test increased with the decrease of both the initial void ratio of the sample and with the normal load applied to the sample.
- Discrete model allows for the detailed description of the sand deformation within the shear zone. The characteristics of the localization can be described mostly by means of geometric criteria, such as the horizontal displacements, gradients of horizontal and vertical displacements, fluctuations of displacements, particles rotations and void ratio distribution. The thickness of the shear zone  $t_s$  is in the range between  $10 \times d_{50}$  and  $18 \times d_{50}$ . It depends on the initial void ratio of the sample and on the load applied to the specimen.
- The distribution of forces and stresses within the sample cannot always be used for the determination of the localization characteristics. The highest normal forces between the particles occurs between the top left and bottom right

corners of the shear boxes. The orientation of these forces within the shear zone is not perpendicular and neither parallel to the shear zone. The dominant magnitudes of these forces is observed within the range of of  $130^\circ$  to  $180^\circ$  angles.

- The horizontal displacement and shear stress gradient were found to be the best indicators of the shear zone, showing localization from the beginning of the direct shear test. In contrast, particle rotations, one of the most common grain-level characteristics used to determine localization and its thickness in the DEM, indicate the shear zone rather late. Some grain-level characteristics, such as vertical displacements and horizontal and vertical stresses, cannot be used to determine the characteristics of the shear zone, even in the residual phase.
- The shear zone can be considered as a straight line almost only during the residual phase of the direct shear test. Initially, the shear zone seeks the most efficient path between the horizontal line imposed by the top and bottom frames of the shear box and the inclined line imposed by the natural shear angle of the granular material. The final shape of the localization is a sum of local shear zones rather than a coherent layer.
- In the direct shear test, the peak and residual shear resistances are slightly higher than those obtained in the triaxial compression tests. This difference is due to the fact that the shape of the shear zone in the direct shear test is constrained by the construction of the boxes, while in the triaxial compression test it is influenced only by the characteristics of the granular media.

## 4.3 Interface shear test between sand and surface of different roughness

### 4.3.1 Introduction

In this section, the results of the discrete simulation of the interface between cohesionless sand and a rigid surface of different roughness in the direct shear test under constant normal load are presented. This type of structural system is commonly associated with engineering structures such as foundations, piles, tunnels, and silos. Frictional resistance of the interface, which is influenced by both the properties of the granular material and the structure, is of major importance in the analysis of such systems in terms of mechanical behavior and durability of the structure. The behavior of the interface depends on the formation of an interface shear zone, which is characterized by its thickness and location in the region adjacent to the surface. The evaluation of the shear zone characteristics plays a key role in the determination of the forces transferred from the granular material to the structure. These characteristics depend on several variables such as the mean grain diameter of the bulk solid, the initial density of the soil, and the roughness and stiffness of the surface (Tejchman, 1989). Granular material-structure interfaces were extensively studied in numerous experimental (Potyondy, 1961; Moore et al., 1984; Uesugi and Kishida, 1986a; Uesugi and Kishida, 1986b; Uesugi et al., 1988; Tejchman and Wu, 1995; Porcino et al., 2003; Hu and Pu, 2004; Su et al., 2018) and numerical investigations (Tejchman and Wu, 1995; Wang et al., 2007b; Tejchman and Wu, 2010; Zhang and Evans, 2018; Zhou et al., 2019).

The study presented in this section focused on quantifying the effect of surface roughness on the overall behavior of the sand sample, with particular attention to the formation of interface shear zones. Different surface topographies were created by regularly placed triangular grooves in the form of a saw-tooth structure. The extensive analysis was made possible by the use of real-size particles, small enough to capture the shear zone formation under three-dimensional conditions. Calculations were performed using perfectly spherical particles with rotational resistance (referred to as spheres in this section) and asymmetric clumped particles composed of spheres using the multisphere method (referred to as clumps in this section).

The results presented in this section are partially covered in two publications: Grabowski et al. (2020) and Grabowski et al. (2021a).

### 4.3.2 Numerical model and methodology

The interface shear test calculations were performed using the discrete model of 'Karlsruhe' sand. The parameters of the sand were given earlier in the Chapter 4.1 in the Table 4.2. The local material parameters for both types of particles, listed in Table 4.4, were determined using the triaxial compression test, also as shown in the Chapter 4.1. In the case of perfectly spherical particles with rotational resistance, the local variables were identical to those previously used in the case of the direct shear test presented in the Section 4.2. For the clumps, the calibration procedure based on the triaxial compression test was repeated, thus the variables were determined separately. Because clumped particles do not require rotational resistance due to their



geometrically irregular shape (Figure 4.34), these variables were different from those used for perfectly spherical particles. The sieve curve for both types of particles was the same, with particle sizes ranging from 0.25 mm to 0.75 mm and a medium grain diameter of  $d_{50}=0.5$  mm in both cases. However, the clumped particles were composed of four smaller spheres with diameters ranging from 0.5 to 0.6 times the diameter of the clump. The clumps had a convexity index '1' of 2.07, which is the ratio of the smallest sphere volume encompassing the cluster to the cluster volume. The convexity index '2' was 1.16, which is the ratio of the smallest convex volume encompassing the cluster to the cluster volume. The aspect ratio, defined as the ratio of the maximum diameter to the minimum diameter of the clump, was 1.50.

Table 4.4: Discrete material parameters for interface shear test.

| Parameter                                | Spheres with rotational resistance | Clumps     |
|--|------------------------------------|------------|
| interparticle friction angle $\mu_c$     | $18^\circ$                         | $26^\circ$ |
| local modulus of elasticity $E_c$        | 300 MPa                            | 300 MPa    |
| shear/normal local stiffness ratio $v_c$ | 0.3                                | 0.3        |
| limit rolling coefficient $\eta$         | 0.4                                | -          |
| rolling stiffness coefficient $\beta$    | 0.7                                | -          |

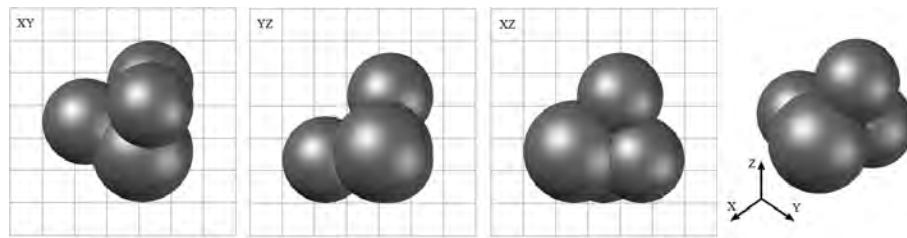


Figure 4.34: Asymmetric convex clump of 0.5 mm diameter in XYZ coordinate space, composed of 4 spheres used in discrete simulations (0.1 mm grid size) (Grabowski et al. (2021a), licensed under CC BY 4.0).

The numerical model setup shown in Figure 4.35 was created under full 3D conditions with the specimen depth reduced from 100 mm to 5 mm ( $10 \times d_{50}$ ) to shorten the computation time. The reduction of the specimen depth had a negligible effect on the numerical results as shown earlier (Figure 4.10 in Section 4.2). The other dimensions of the specimen were the same as those used in the experiments conducted by Tejchman and Wu (1995), with a height of 20 mm and a width of 100 mm. Similar to the direct shear test, a gap equal to the maximum grain diameter was left between the top frame and the rigid surface.

The standard interface shear test procedure was followed for all tests. The first step involved creating the granular assembly consisting of discrete particles within the upper frame of the shear box. Approximately 80 000 discrete elements were used in the case of spherical particles and 320 000 in the case of clumps of spheres. Next, a constant normal pressure  $\sigma_n$  was applied to the top frame. Once the desired void ratio of the sand mass was achieved and the kinetic energy of the assembly was negligible, the top frame filled with granular material was moved horizontally (inducing a horizontal displacement  $u$ ) at a constant velocity. The shear rate was small enough to consider the test as quasi-static (the inertial number  $I$  was kept below

10e-4 (Roux and Chevoir, 2005)). During the test, the rigid bottom surface was fixed, while the upper frame was free to move and smooth. The loss of sand during the shearing had a small effect on the void ratio and the volumetric strain (less than 1% of the particles leaked out of the shear box during the test). The frictional coefficient along these surfaces was  $\tan(\mu_s) = \tan(18^\circ) = 0.32$ .

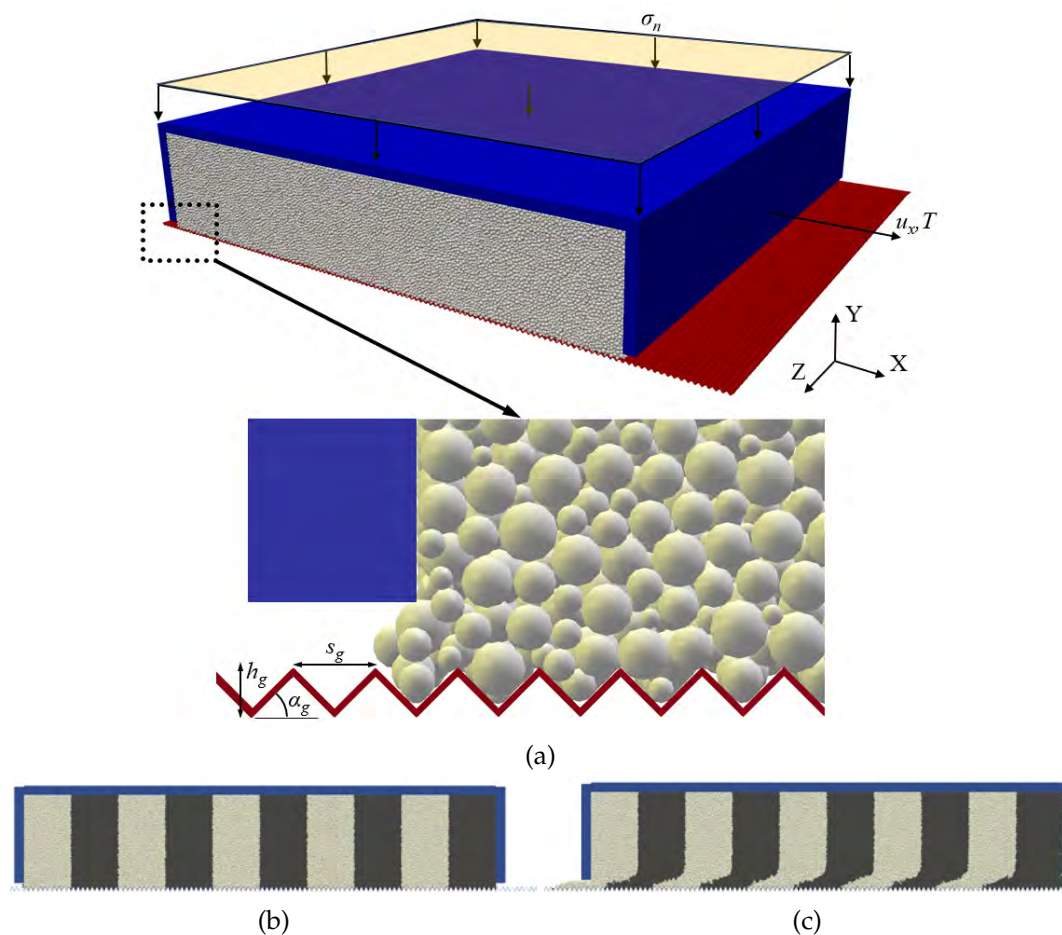


Figure 4.35: Interface shear test in DEM: a) numerical setup, b) sample at the initial state and c) deformed sample at the final state (Grabowski et al. (2020), licensed under CC BY 4.0).

In silo constructions, the surface can naturally exhibit randomness and complexity, as in the case of concrete silo walls, or regular and uniform, as seen in silo walls made from corrugated sheets. In the discrete simulations, the surface roughness has been simulated using a variety of methods. The primary approach was to generate the surface geometry using the overlapping spherical particles (Gu et al., 2017; Feng et al., 2018). Another common technique is the formation of regularly spaced grooves, resulting in saw-tooth surface profile (Jing et al., 2017). This approach was used in the discrete calculations presented in this section. The different geometries of the surfaces were composed of triangular asperities of varying height and inclination to the shearing direction (Figure 4.36). To describe the surface geometry the normalized surface roughness  $R_n = h_g/d_{50}$  was used (Uesugi and Kishida, 1986a), where  $h_g$  is the groove height and  $d_{50}$  is the mean grain diameter.

A series of interface shear tests were performed for both types of particles throughout the investigation, taking into consideration different surface roughness ( $R_n$  ranging from 0.01 to 2.0). In addition, the effect of the initial void ratio  $e_0$  of the samples (0.55 and 0.80) was analyzed. During the study, different groove spacing was also examined (e.g., every second groove, every fourth groove, etc.), but the results are beyond the scope of this thesis. This is because the effect of groove spacing on peak surface friction angle and interface shear zone thickness was found to be negligible within a certain range (very similar interface shear resistance and mesoscopic behavior were obtained for surfaces with groove spacing up to every fourth groove). Additionally, the influence of groove inclination was investigated. In contrast to groove spacing, the effect of groove inclination on interface efficiency was significant. However, the results for other inclinations are not presented here because they were not used in any other part of the thesis.

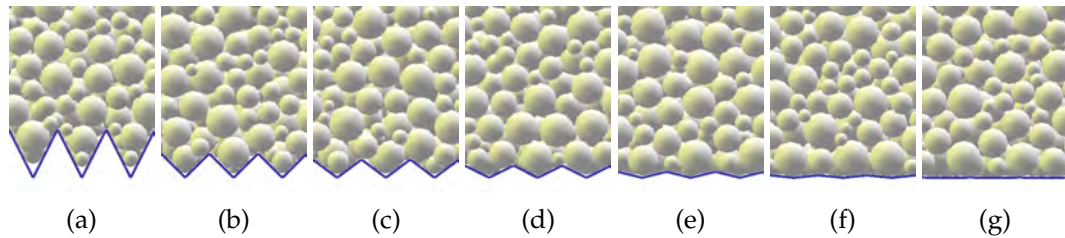


Figure 4.36: Rigid bottom surface sections with different normalized surface roughness  $R_n$ : a)  $R_n=2.0$ , b)  $R_n=1.0$ , c)  $R_n=0.75$ , d)  $R_n=0.5$ , e)  $R_n=0.25$ , f)  $R_n=0.1$  and g)  $R_n=0.01$  (Grabowski et al. (2020), licensed under CC BY 4.0).

### 4.3.3 Numerical results

In this section, the results of a series of interface shear tests obtained for both types of particles under various conditions are presented. First, the validation of the discrete model is performed based on the comparison between the numerical results and the laboratory experiments of Tejchman and Wu (1995). Second, the influence of the normalized roughness  $R_n$  and the initial void ratio  $e_0$  on the shear resistance and the volumetric strain of the specimen is presented. Then, the comprehensive analysis of the contact zone between the sand and the surface of different roughness, i.e. granular material deformation, the distribution of the sphere rotations, the void ratios and the force chains, and the stress distribution across the height of the specimen at the final stage of the shearing have been performed. In addition, as a result of the discrete analysis the boundary conditions for 2D continuum models were proposed based on the grain-level characteristics.

#### Effect of the surface roughness on the evolution of mobilized shear stress and volumetric strain

At the beginning, the effect of the surface geometry on the shear resistance (Figure 4.37) and the volumetric deformation (Figure 4.38) of the specimen was analyzed for both types of particles. The calculations were carried out on the initially dense specimen ( $e_0 = 0.55$ ) under vertical pressure applied to the upper frame  $\sigma_n = 100$

kPa. Figure 4.37 show the evolution of the surface friction angle  $\phi_s$  curve versus the total horizontal displacement  $u$ . In general, the peak value  $\phi_{s,max}$  and the residual value  $\phi_{s,res}$  of the effective surface friction angle increased with the roughness of the surface. The values of the  $\phi_s$  were extracted from the graphs and summarized in the Table 4.5. Additionally, the relationships between  $\phi_{s,max}$  and  $R_n$  as well as  $\phi_{s,res}$  and  $R_n$  were plotted in Figure 4.39. For both types of particles, there was an almost bilinear relationship between the normalized surface roughness and the surface friction angle, both for the maximum and residual values. This observation is in good agreement with the results of other studies (Hu and Pu, 2004; Jing et al., 2017; Su et al., 2018; Zhang and Evans, 2018). The peak values  $\phi_{s,max}$  were very similar for both clumps and spheres (Table 4.5). On the other hand, residual values of  $\phi_{s,res}$  were slightly lower for clumps with the normalized roughness parameter  $R_n \geq 0.25$  (e.g., they were lower by  $3^\circ$  for  $R_n \geq 0.5$  and by  $6^\circ$  for  $R_n = 0.25$ ). Further analysis revealed a limit to the surface friction angle when using spherical particles. Increasing the surface roughness  $R_n$  above a certain threshold (for spherical particles it was  $R_n=0.75$ ) did not significantly increase the interface shear resistance (Figure 4.37Aa-c). Any increase of  $R_n$  above this value resulted in a negligible changes in the surface friction angle. This is consistent with the literature which states that the shear resistance of the interface cannot exceed the shear resistance of the soil (Potyondy, 1961).

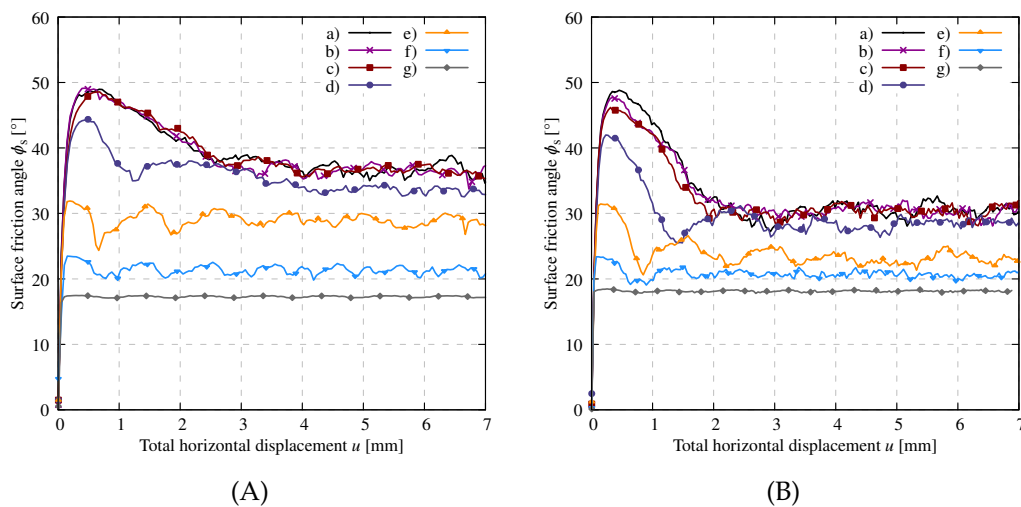


Figure 4.37: Mobilized surface friction angle  $\phi_s$  versus horizontal displacement  $u$  obtained for: A) spheres (Grabowski et al., 2020) and B) clumps (Grabowski et al., 2021a) for different normalized surface roughness  $R_n$ : a)  $R_n=2.0$ , b)  $R_n=1.0$ , c)  $R_n=0.75$ , d)  $R_n=0.50$ , e)  $R_n=0.25$ , f)  $R_n=0.10$  and g)  $R_n=0.01$  ( $e_0=0.55$  and  $\sigma_n=100$  kPa) (Adapted graphics licensed under CC BY 4.0; changes include font, line style and size adjustments).

Figure 4.38 shows the evolution of the volumetric strain  $\varepsilon_v$  versus the total horizontal displacement  $u$  for both types of particles. In addition, Table 4.5 also shows the value of the final volumetric strain  $\varepsilon_v$  for different surface roughness for both types of particles. The dilatancy of the granular material was significantly affected by the geometry of the profile and increased with increasing surface roughness (Figure 4.38). Only for the almost flat surface ( $R_n = 0.01$ ), no dilatancy and no contraction was captured within the granular specimen. The final volumetric strains were higher in the case of spherical particles compared to the clumps (e.g. they were

higher by 0.05 for  $R_n \geq 1.0$ ). The use of perfectly spherical particles usually results in an artificial dilatancy of the granular material (Zhao et al., 2018).

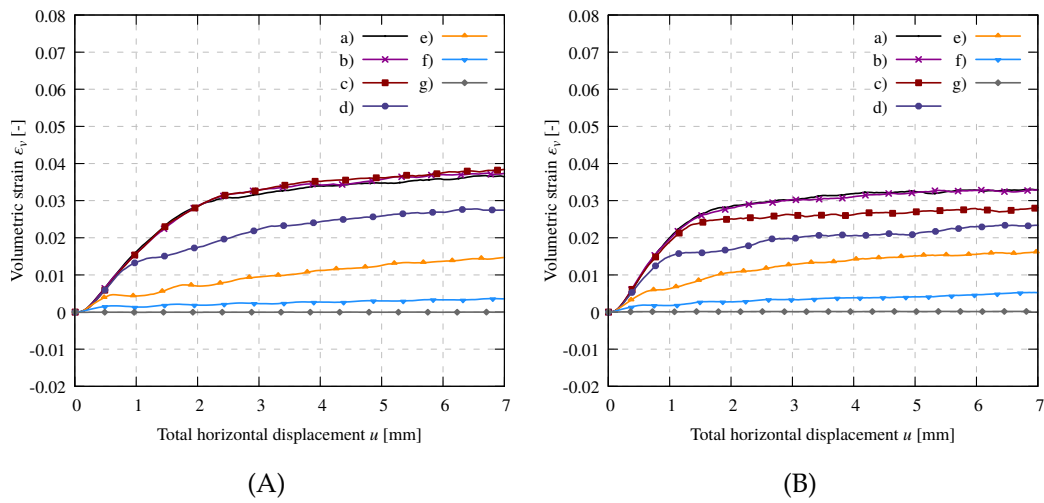


Figure 4.38: Volumetric strain  $\varepsilon_v$  versus horizontal displacement  $u$  obtained for: A) spheres (Grabowski et al., 2020) and B) clumps (Grabowski et al., 2021a) for different normalized surface roughness  $R_n$ : a)  $R_n=2.0$ , b)  $R_n=1.0$ , c)  $R_n=0.75$ , d)  $R_n=0.50$ , e)  $R_n=0.25$ , f)  $R_n=0.10$  and g)  $R_n=0.01$  ( $e_0=0.55$  and  $\sigma_n=100$  kPa) (Adapted graphics licensed under CC BY 4.0; changes include font, line style and size adjustments).

Table 4.5: Calculated values of maximum surface friction angle  $\phi_{s,max}$ , residual surface friction angle  $\phi_{s,res}$  and residual volumetric strain  $\varepsilon_v$  for different normalized surface roughness  $R_n$  using spheres and clumps (Grabowski et al. (2021a), licensed under CC BY 4.0).

| $R_n$ | $\phi_{s,max}$ |        | $\phi_{s,res}$ |        | $\varepsilon_v$ |        |
|-------|----------------|--------|----------------|--------|-----------------|--------|
|       | spheres        | clumps | spheres        | clumps | spheres         | clumps |
| 2.0   | 49°            | 49°    | 35°            | 32°    | 3.9%            | 3.3%   |
| 1.0   | 49°            | 47.5°  | 35°            | 32°    | 3.9%            | 3.27%  |
| 0.75  | 49°            | 45.5°  | 35°            | 32°    | 3.9%            | 2.8%   |
| 0.5   | 44°            | 42°    | 32°            | 29°    | 3.0%            | 2.4%   |
| 0.25  | 31.0°          | 31.5°  | 30°            | 24°    | 1.8%            | 1.6%   |
| 0.1   | 23.0°          | 23.5°  | 20°            | 21°    | 0.1%            | 0.5%   |
| 0.01  | 18.0°          | 18.0°  | 18.0°          | 18.0°  | 0.01%           | 0.01%  |

Based on the curves presented in Figures 4.37 and 4.38, the analyzed surfaces can be conventionally classified into two categories: smooth and rough, according to the surface roughness  $R_n$ . The analysis showed that the critical normalized roughness  $R_{n,crit}$  was approximately 0.25 for spheres. For clumps, it was difficult to clearly determine the exact value of the critical roughness, but it was within the range of 0.1 to 0.25. When  $R_n$  is below the critical value, the surface is considered smooth, and the shear failure mechanism is elastic-perfectly plastic. If the parameter is above the critical value, the interface is considered rough, and the granular material exhibits successive hardening and softening related to dilatancy. Similar value of  $R_{n,crit}$ , as in the case of clumps (Figure 4.37B), were obtained in experiments by Hu and Pu (2004) ( $R_{n,crit}=0.1$ ). In DEM calculations by Jing et al. (2017), the critical roughness was obtained for  $R_{n,crit}=0.375$ , which is slightly higher than in the case of spheres (Figure 4.37A).

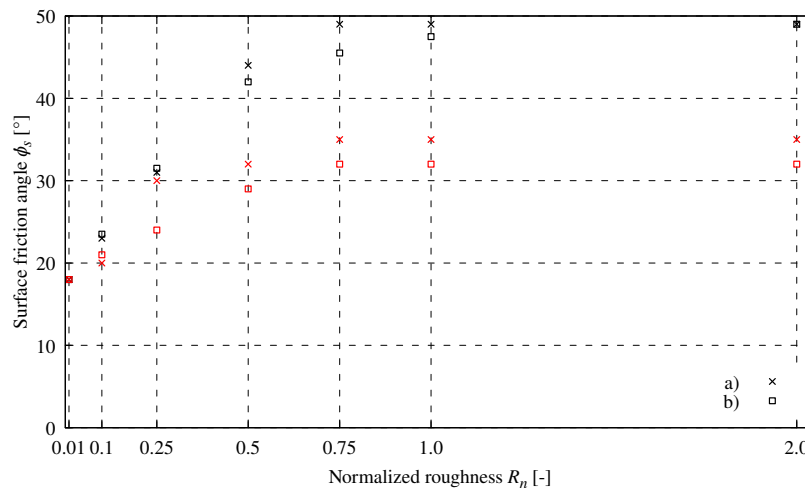


Figure 4.39: Relationship between maximum surface friction angle  $\phi_{s,max}$  and residual surface friction angle  $\phi_{s,res}$  for different normalized surface roughness  $R_n$  for: a) spheres and b) clumps (black color represents  $\phi_{s,max}$  and red color represents  $\phi_{s,res}$ ) (adapted from Grabowski et al. (2021a), licensed under CC BY 4.0. Graphic changes include color and size adjustments).

In addition, the discrete results were compared with the experimental results obtained by Tejchman and Wu (1995). In the mentioned study, three different surfaces with varying degrees of roughness, classified based on  $R_n$ , were used: smooth ( $0 \leq R_n \leq 0.1 \times d_{50}$ ), rough ( $0.1 \times d_{50} < R_n < 0.5 \times d_{50}$ ), and very rough ( $R_n \geq 0.5 \times d_{50}$ ). The smooth surface consisted of a flat steel plane. The rough surface was created by degradation of the element in a corrosion chamber. Finally, the very rough surface was achieved by randomly gluing grains of 'Karlsruhe' sand with a mean grain diameter equal to or greater than 0.5 mm to the surface.

The comparison between the experimental results and the discrete calculations is presented in Figures 4.40 and 4.41. Although the experimental interface roughness differed from the artificial monotonic saw-tooth profile used in the discrete analysis, there was satisfactory agreement between the DEM and laboratory results. This agreement was observed particularly in the shape of the surface friction and volumetric strain curves, as well as in the maximum value of the friction angles  $\phi_{s,max}$ . However, for the rough and very rough interfaces, the calculated residual surface friction angles  $\phi_{s,res}$  were much smaller than the experimental values. In addition, the calculated maximum value of the surface friction angle  $\phi_{s,max}$  occurred about 1.0 mm earlier than in the laboratory tests. These differences are due to a combination of factors. First, the calibration procedure was performed on triaxial compression tests, which do not account for the formation of the shear zone. Second, the stiffness of the shear box was not analyzed. Third, the assumed friction angle between the sand and the smooth steel surface differed from the experimental value. In the referenced experiments, the surface friction angle for smooth steel was between  $10^\circ$  and  $12^\circ$ . However, in the discrete model, it was assumed to be  $18^\circ$ , which is within the typical range for sand-smooth steel interfaces (Uesugi and Kishida, 1986a). These factors indicate that the numerical sand sample or the shear frame was too stiff. In the case of the volumetric strain  $\varepsilon_v$ , the values obtained in the discrete analysis were greater by a factor of 2.0 for spheres with rotational resistance and by a factor of 1.5

for clumps compared to the laboratory results. These discrepancies resulted from the experimental interface roughness and particle shapes not being faithfully reproduced in the DEM simulations.

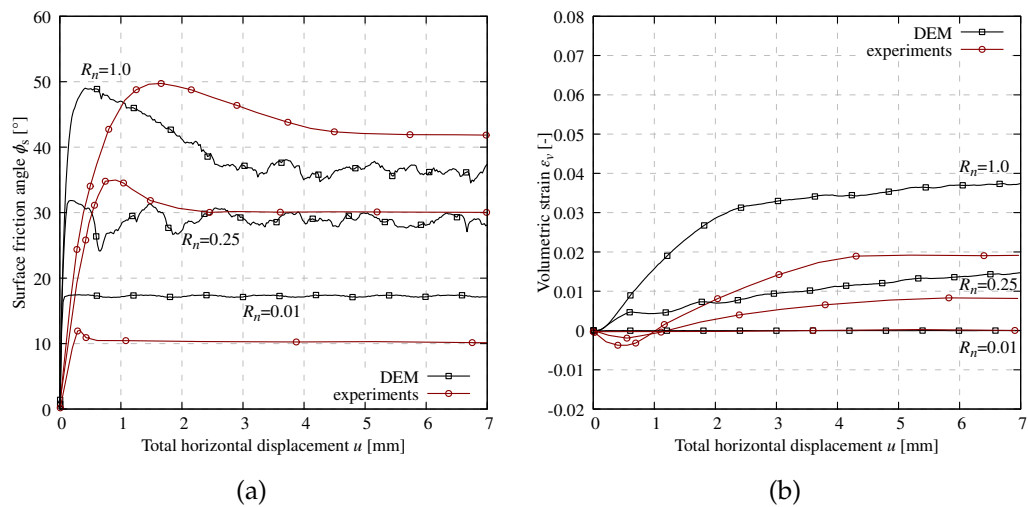


Figure 4.40: DEM results obtained for spheres of: a) mobilized surface friction angle  $\phi_s$  and b) volumetric strain  $\epsilon_v$  versus horizontal displacement  $u$  compared to experimental results by Tejchman and Wu (1995) for different normalized surface roughness  $R_n$ :  $R_n=1.0$ ,  $R_n=0.25$  and  $R_n=0.01$  ( $e_0=0.55$  and  $\sigma_n=100$  kPa) (adapted from Grabowski et al. (2020), licensed under CC BY 4.0. Graphic changes include color and size adjustments).

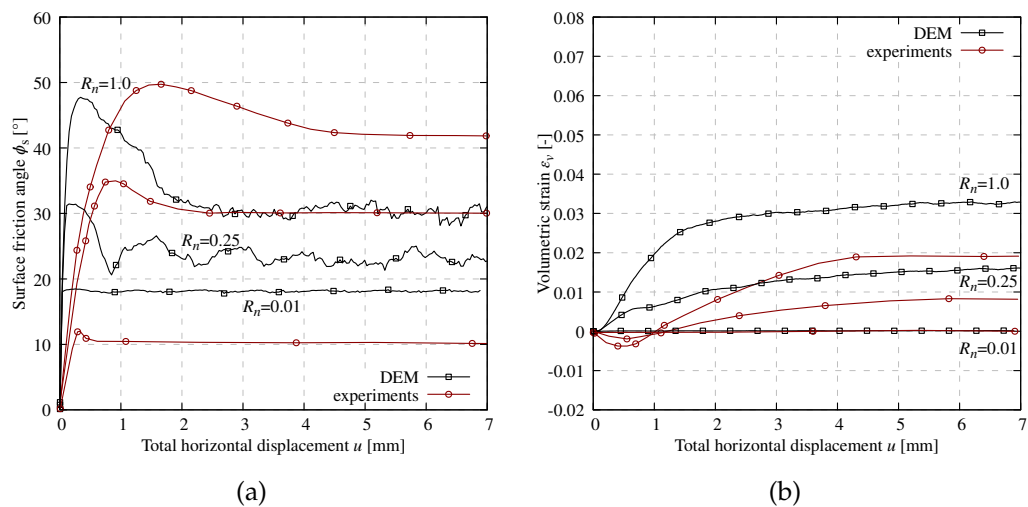


Figure 4.41: DEM results obtained for clumps of: a) mobilized surface friction angle  $\phi_s$  and b) volumetric strain  $\epsilon_v$  versus horizontal displacement  $u$  compared to experimental results by Tejchman and Wu (1995) for different normalized wall roughness  $R_n$ :  $R_n=1.0$ ,  $R_n=0.25$  and  $R_n=0.01$  ( $e_0=0.55$  and  $\sigma_n=100$  kPa) (adapted from Grabowski et al. (2021a), licensed under CC BY 4.0. Graphic changes include color and size adjustments).

#### Effect of the initial void ratio of the specimen on the evolution of mobilized shear stress and volumetric strain

In addition, the effect of initial void ratio  $e_0$  on the global response of the specimen was also investigated. Two different sand samples with initial void ratios of

$e_0=0.55$  (initially dense sand) and  $e_0=0.80$  (initially loose sand) were prepared under a constant vertical pressure  $\sigma_n=100$  kPa applied to the top frame of the direct shear apparatus. The normalized surface roughness was  $R_n=1.0$ . Figures 4.42 and 4.43 presents the comparison between the DEM results obtained for both types of particles and the experiments by Tejchman and Wu (1995). The evolution of the surface friction angle  $\phi_s$  and the volumetric strain  $\varepsilon_v$  curves are typical for sand behavior during shearing on a rough surface in a direct shear apparatus (Tejchman and Wu, 1995; Salazar et al., 2015). Initially, for both types of particles, the dense samples exhibited hardening, reaching the mobilized surface friction angle  $\phi_{s,max}=49.0^\circ$  at  $u = 0.5$  mm for spheres, and  $\phi_{s,max}=47.5^\circ$   $u = 0.4$  mm for clumps. Then, in both cases, the samples exhibited softening (Figure 4.42a and Figure 4.43a). The surface friction angle in the residual state for the initially dense sample was  $\phi_{s,res}=35^\circ$  (for  $u \geq 3$  mm) for spheres and  $\phi_{s,res}=32^\circ$  (for  $u \geq 2.5$  mm) for clumps. The initially loose sand yielded the surface friction angle  $\phi_{s,max}=42^\circ$  at the peak ( $u=1.5$  mm) for spheres and  $\phi_{s,max}=40^\circ$  at the peak ( $u=2.0$  mm) for clumps. The residual surface friction angle for the initially loose sample was similar to that of the initially dense sample. It was higher for spheres ( $\phi_{s,res} = 34^\circ$  for  $u \geq 3$  mm) than for clumps ( $\phi_{s,res} = 32^\circ$  for  $u \geq 2$  mm). The initially loose sample exhibited continuous contraction, while the initially dense sample dilated throughout the test (Figures 4.42b and 4.43b). The evolution of the curves was similar to the experiments, but there were some discrepancies. The largest difference was in the magnitude of the surface friction angle in the residual state. For spheres and clumps,  $\phi_{s,res}$  was approximately 24% lower than in the experiments. Both particle types showed a stiffer response than observed in the experiments. In contrast to the laboratory experiments, where little dilation occurred, only contraction was observed in the discrete model (Figures 4.42b and 4.43b).

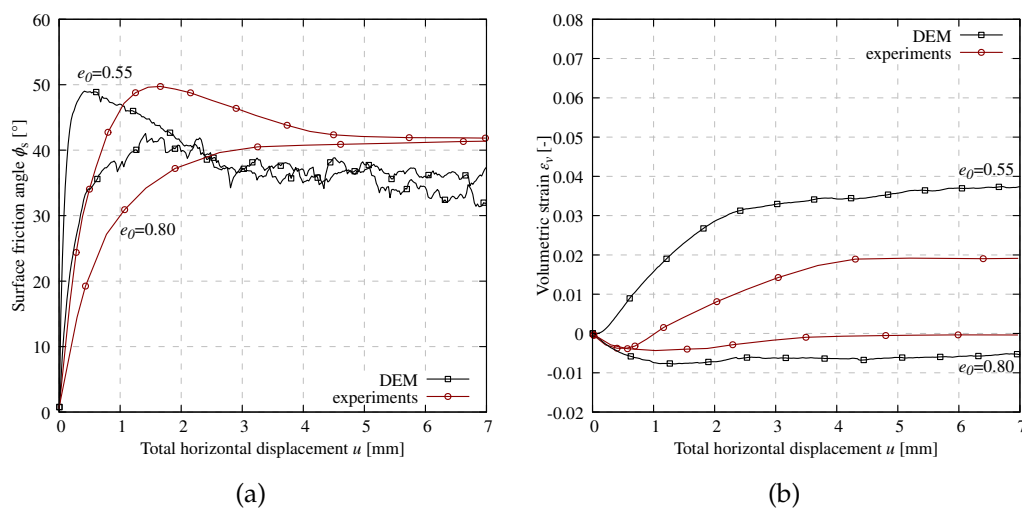


Figure 4.42: DEM results obtained for spheres of: a) mobilized surface friction angle  $\phi_s$  and b) volumetric strain  $\varepsilon_v$  versus horizontal displacement  $u$  compared to experimental results by Tejchman and Wu (1995) with two different initial void ratios of sand:  $e_0=0.55$  and  $e_0=0.80$  ( $\sigma_n=100$  kPa and  $R_n=1.0$ ) (adapted from Grabowski et al. (2020), licensed under CC BY 4.0. Graphic changes include color and size adjustments).



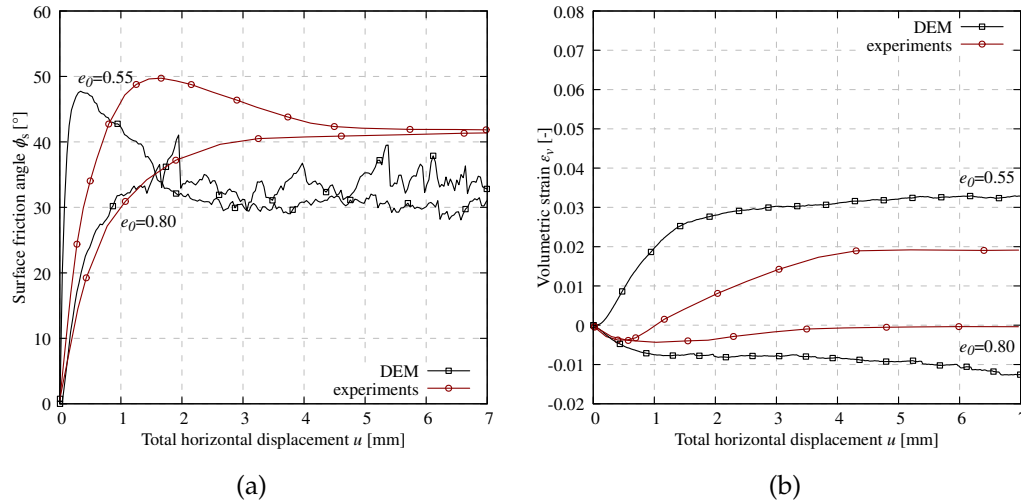


Figure 4.43: DEM results obtained for clumps of: a) mobilized surface friction angle  $\phi_s$  and b) volumetric strain  $\epsilon_v$  versus horizontal displacement  $u$  compared to experimental results by Tejchman and Wu (1995) with two different initial void ratios of sand:  $e_0=0.55$  and  $e_0=0.80$  ( $\sigma_n=100$  kPa and  $R_n=1.0$ ).

### Effect of the surface roughness on the mesoscopic behavior of the sand-surface interface

The research described in previous sections, has so far focused on the macroscopic behavior of the interface between cohesionless sand and surfaces of different roughness. In this section, the effect of the surface roughness on the mesoscopic behavior of the contact zone between the sand and the surface has been investigated. The numerical results for the grain-level characteristics, such as the final deformation of the sample, the distribution of the normal force chains, sphere rotations, and the void ratio distribution are presented. The presented results were obtained at the final state of shearing ( $u_x=7.0$  mm).

First, the influence of the surface roughness  $R_n$  on the deformation of the sand specimen was investigated (Figures 4.44 and 4.45). Similarly, as in the previous section, the  $R_n$  varied between 0.01 and 2.0. It can be observed that for the surfaces with  $R_n \leq 0.1$  for both types of particles, the entire sand mass behaved like a rigid body during the shearing (Figures 4.44f,g and 4.45f,g). In these cases, no shear zone occurred because the material slipped directly on the surface and the shear resistance was mainly influenced by the particle-on-surface friction. A thin shear zone was observed for the surface with  $R_n=0.25$ . The remaining cases (Figures 4.44a-d and 4.45a-d) were characterized by a different failure mechanism. In these cases, the sand grains in the area adjacent to the surface were partly locked between the grooves and partly followed the motion of the upper frame of the shear box. As a result, these surfaces were considered as rough.

In addition, the distribution of displacements  $u$  along the normalized height  $h/d_{50}$  in the center region of the sample was analyzed (Figure 4.46). For the roughest surfaces ( $R_n \geq 0.75$  for spheres and  $R_n \geq 1.0$  for clumps), the granular material locked in between the surface asperities exhibited zero horizontal displacements. The horizontal slip, expressed as the ratio of the final displacement of the particles directly at the surface to the total prescribed horizontal displacement for each

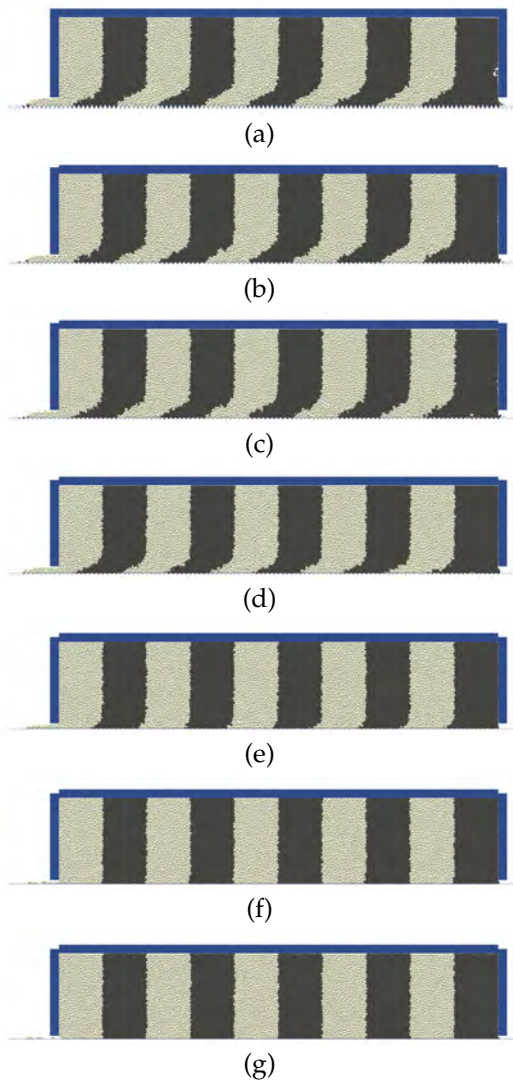


Figure 4.44: Front view of the sand specimen composed of spheres at the final state of the test ( $u_{tot}=7.0$  mm) for different normalized surface roughness parameter  $R_n$ : a)  $R_n=2.0$ , b)  $R_n=1.0$ , c)  $R_n=0.75$ , d)  $R_n=0.5$ , e)  $R_n=0.25$ , f)  $R_n=0.1$  and g)  $R_n=0.01$  ( $e_0=0.55$  and  $\sigma_n=100$  kPa).

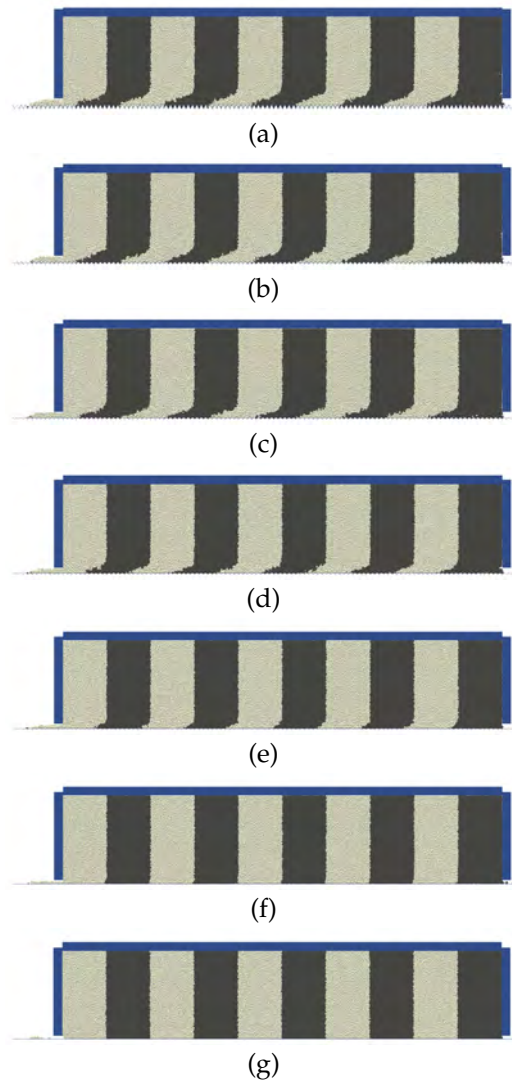


Figure 4.45: Front view of the sand specimen composed of clumps the final state of the test ( $u_{tot}=7.0$  mm) for different normalized surface roughness parameter  $R_n$ : a)  $R_n=2.0$ , b)  $R_n=1.0$ , c)  $R_n=0.75$ , d)  $R_n=0.5$ , e)  $R_n=0.25$ , f)  $R_n=0.1$  and g)  $R_n=0.01$  ( $e_0=0.55$  and  $\sigma_n=100$  kPa).

interface is listed in Table 4.6. This ratio was found to increase significantly with decreasing  $R_n$ , and was generally higher for clumped particles.

The thickness of the shear zone  $t_s$  for the rough surfaces was determined based on the horizontal displacements presented in Figure 4.46. It was equal to  $t_s=5-10 \times d_{50}$  for spheres and  $t_s=3-7 \times d_{50}$  for clumps. These values are consistent with other numerical and experimental studies. Slightly lower shear zone thicknesses for granular materials composed of spherical particles were obtained in discrete simulations by Chen et al. (2020) ( $t_s=4 \times d_{50}$ ) and Feng et al. (2018) ( $t_s=3-4 \times d_{50}$ ). Similar values, as for clumps, were observed in experiments conducted by Uesugi et al. (1988) and Hu and Pu (2004) (approximately  $t_s=5 \times d_{50}$ ), as well as by DeJong et al. (2006) (approximately  $t_s=5-7 \times d_{50}$ ). The distribution of the horizontal displacement was similar as in interface shear laboratory tests analyzing the photographic data (Uesugi et al., 1988) and using particle image velocimetry (PIV) (DeJong et al., 2003; DeJong et al., 2006; DeJong and Westgate, 2009), and DEM simulations by Feng et al. (2018).

Table 4.6: Horizontal slip along the rigid bottom surface.

| Normalized roughness $R_n$ | Value for spheres | Value for clumps |
|----------------------------|-------------------|------------------|
| 2.00                       | 0%                | 0%               |
| 1.00                       | 2%                | 7%               |
| 0.75                       | 3%                | 14%              |
| 0.50                       | 22%               | 35%              |
| 0.25                       | 70%               | 70%              |
| 0.10                       | 93%               | 95%              |
| 0.01                       | 99%               | 99%              |

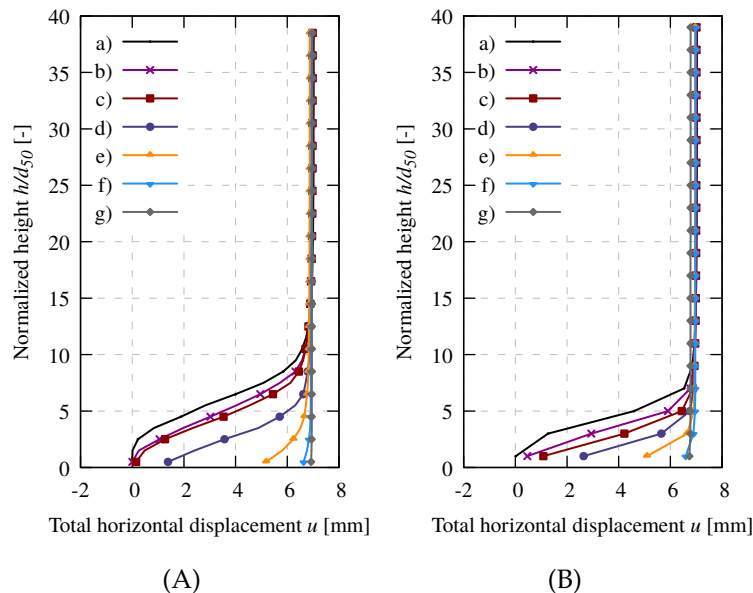


Figure 4.46: Distribution of horizontal grain displacement  $u$  across normalized specimen height  $h/d_{50}$  at the specimen mid-point at residual state for  $u_{tot}=7.0$  mm for: A) spheres (Grabowski et al., 2020) and B) clumps (Grabowski et al., 2021a) for different normalized surface roughness  $R_n$ : a)  $R_n=2.0$ , b)  $R_n=1.0$ , c)  $R_n=0.75$ , d)  $R_n=0.50$ , e)  $R_n=0.25$ , f)  $R_n=0.10$  and g)  $R_n=0.01$  ( $e_0=0.55$  and  $\sigma_n=100$  kPa) (Adapted graphics licensed under CC BY 4.0; changes include font, line style and size adjustments).

Figures 4.47-4.50 presents the distributions of particle rotations in the entire specimen. Red color represents clockwise rotation and blue color represents counterclockwise rotation. For both types of particles, the direction of the grain rotations in the localized region was mainly clockwise, according to the shear direction, with only a few loose spheres rotating in the opposite direction. In the case of clumps, more particles were observed rotating counterclockwise compared to perfect spheres with rotational resistance, as shown in the zoomed sections of Figures 4.47 and 4.48. For both types of particles, a clear horizontal shear zone appeared in the interface contact zone in the case of the rough surfaces. Based on the distribution of the particle rotations the thickness of the shear zone was estimated (the same procedure for estimation was used as the one presented in Chapter 4.2). Small differences between the two types of particles were observed in the thickness of the shear zone  $t_s$  and in the magnitude of rotations within the localized region. These variables increased with an increase of the  $R_n$ . For spherical particles, it was equal  $14 \times d_{50}$  ( $R_n \geq 0.75$ ),  $10 \times d_{50}$  ( $R_n=0.5$ ),  $6 \times d_{50}$  ( $R_n=0.25$ ). For clumps, the shear zone thickness was equal  $12 \times d_{50}$  ( $R_n=2.0$ ),  $11 \times d_{50}$  ( $R_n=1.0$ ),  $10 \times d_{50}$  ( $R_n=0.75$ ),  $8 \times d_{50}$  ( $R_n=0.5$ ) and  $6 \times d_{50}$  ( $R_n=0.25$ ). The thickness of the shear zone in sand composed of clumps was lower by 15-40% than for spheres for surfaces of roughness  $R_n \geq 0.5$ . The minor rotations related to the sliding of the grains located directly at the smooth surface can be observed for both types of particles (Figures 4.49f,g and 4.50f,g). The thickness of the shear zone measured with the particle rotation distribution was greater than that measured with the particle displacements by up to 70%. It appears that granular material also exhibits rotations outside the shear zone in the area adjacent to the shear zone.

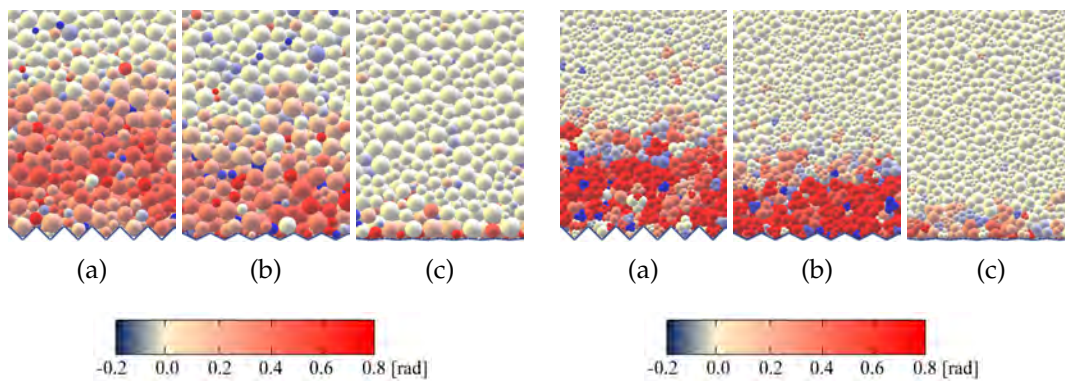


Figure 4.47: A zoom on the distribution of particle rotations  $\omega$  in sand specimen composed of spheres at the final state of the test ( $u_{tot}=7.0$  mm) for different normalized surface roughness  $R_n$ : a)  $R_n=1.0$ , b)  $R_n=0.5$  and c)  $R_n=0.1$  ( $e_0=0.55$  and  $\sigma_n=100$  kPa) (adapted from Grabowski et al. (2020), licensed under CC BY 4.0. Graphic changes include color and size adjustments).

Figure 4.48: A zoom on the distribution of particle rotations  $\omega$  in sand specimen composed of clumps at the final state of the test ( $u_{tot}=7.0$  mm) for different normalized surface roughness  $R_n$ : a)  $R_n=1.0$ , b)  $R_n=0.5$  and c)  $R_n=0.1$  ( $e_0=0.55$  and  $\sigma_n=100$  kPa) (adapted from Grabowski et al. (2021a), licensed under CC BY 4.0. Graphic changes include color and size adjustments).

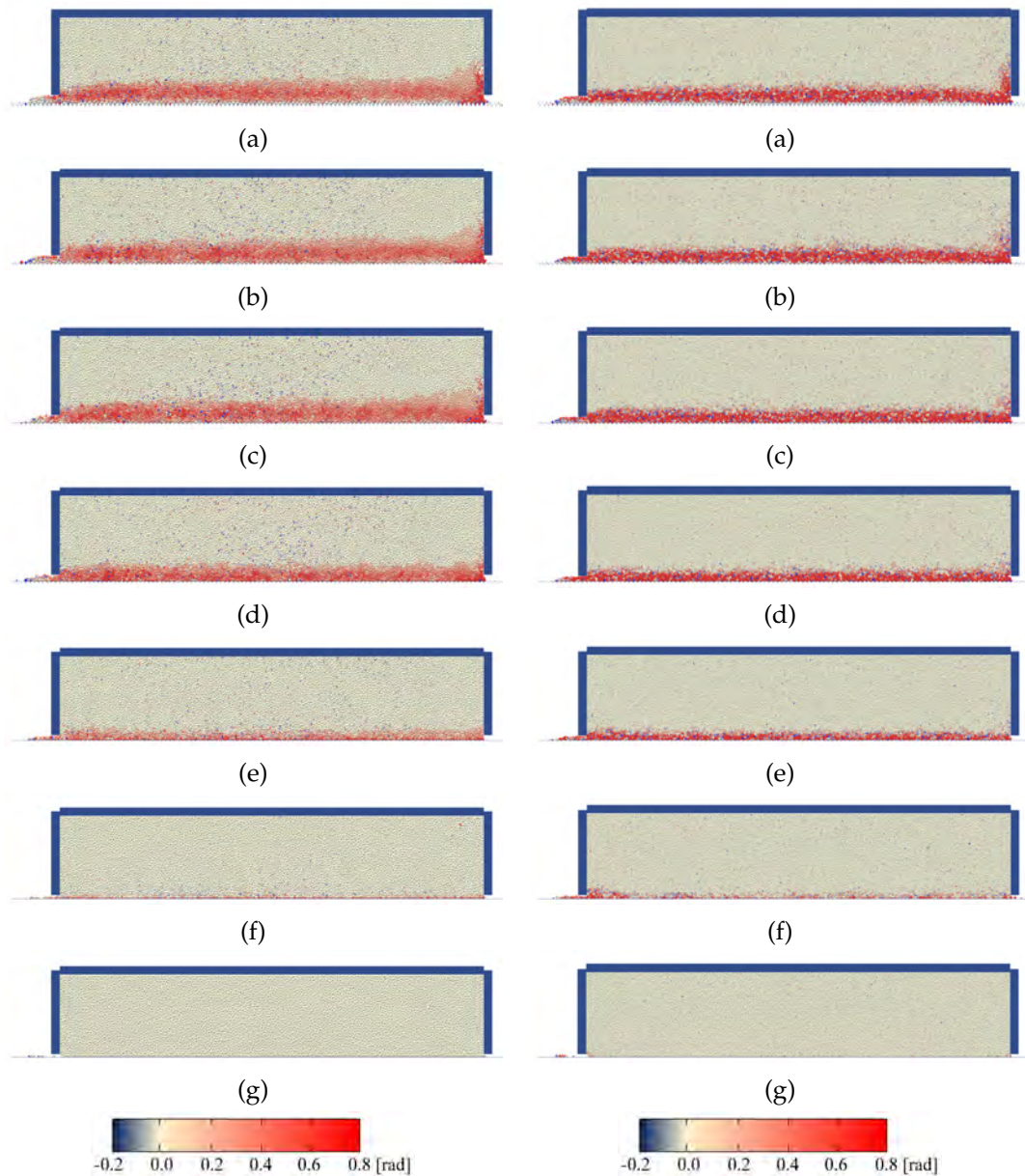


Figure 4.49: Distribution of particle rotations  $\omega$  in sand specimen composed of spheres at the final state of the test ( $u_{tot}=7.0$  mm) for different normalized surface roughness  $R_n$ : a)  $R_n=2.0$ , b)  $R_n=1.0$ , c)  $R_n=0.75$ , d)  $R_n=0.5$ , e)  $R_n=0.25$ , f)  $R_n=0.1$  and g)  $R_n=0.01$  ( $e_0=0.55$  and  $\sigma_n=100$  kPa).

Figure 4.50: Distribution of particle rotations  $\omega$  in sand specimen composed of clumps at the final state of the test ( $u_{tot}=7.0$  mm) for different normalized surface roughness  $R_n$ : a)  $R_n=2.0$ , b)  $R_n=1.0$ , c)  $R_n=0.75$ , d)  $R_n=0.5$ , e)  $R_n=0.25$ , f)  $R_n=0.1$  and g)  $R_n=0.01$  ( $e_0=0.55$  and  $\sigma_n=100$  kPa).

Based on the rotations of the spheres, the location of the interface shear zone can be determined (Figure 4.51). The magnitudes of these rotations  $\omega$  were calculated using the previously used REV cell (see Chapter 4.2 for details). The largest grain rotations were located slightly above the surface ( $h/d_{50} = 5 \div 6$  for spheres and  $h/d_{50} = 3 \div 5$  for clumps) for  $R_n \geq 0.75$  (Figures 4.51Aa-c and 4.51Ba-c). In these cases, the particle rotations at the rigid surface approached zero, meaning that the particles were blocked between the asperities during sand deformation. Maximum

residual grain rotation for  $R_n \geq 0.75$  was equal approximately 0.75 rad for spheres and 1.05 rad for clumps. For  $R_n < 0.75$  the highest grain rotations were directly located at the interface and diminished with the reduction of  $R_n$  (Figures 4.51Ad-g and 4.51Bd-g). No rotation was observed for particles located above the shear zone in the moving part of the shear box.

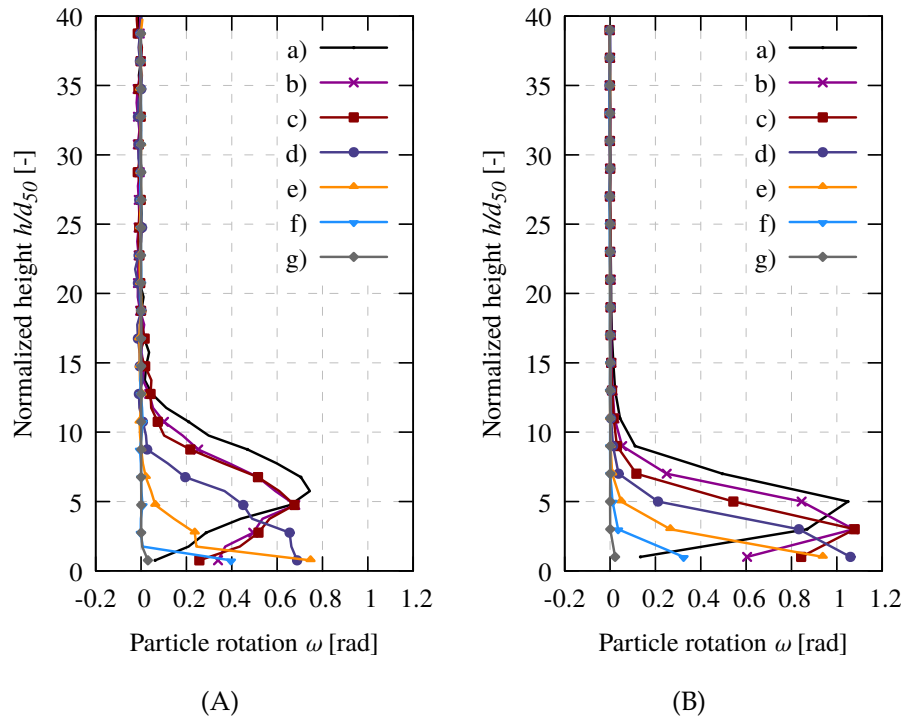


Figure 4.51: Distribution of grain rotation  $\omega$  across normalized specimen height  $h/d_{50}$  at the specimen mid-point at residual state for  $u_{tot}=7.0$  mm for: A) spheres (Grabowski et al., 2020) and B) clumps (Grabowski et al., 2021a) for different normalized roughness  $R_n$ : a)  $R_n=2.0$ , b)  $R_n=1.0$ , c)  $R_n=0.75$ , d)  $R_n=0.50$ , e)  $R_n=0.25$ , f)  $R_n=0.10$  and g)  $R_n=0.01$  ( $e_0=0.55$ , and  $\sigma_n=100$  kPa) (Adapted graphics licensed under CC BY 4.0; changes include font, line style and size adjustments).

In the next part, the void ratio  $e$  distribution shown in Figures 4.52 and 4.53 was examined (the procedure for  $e$  calculations was the same as in the Chapter 4.2). The distribution of porosity in the contact area between the sand and the rigid surface corresponded well with the distribution of particle rotations with respect to the formation of the shear zone. A uniform horizontal shear zone appears for both types of particles when  $R_n \geq 0.25$  (Figures 4.52a-e and 4.53a-e). The differences between the two particle types were observed mainly in the thickness of the shear zone. In these cases, it was observed that the significant dilation of the sand occurs mainly in the localized area. Above the shear zone, changes in porosity were negligible. In the remaining cases ( $R_n < 0.25$ ), no changes in void ratio were observed at all (Figures 4.52fg and 4.53f,g). This is in good agreement with the volumetric strain curves (Figure 4.38f,g), where little or no dilatancy occurred during shearing for these surfaces.

Similarly as in the case of particle rotations, the distribution of the void ratio  $e$  across the normalized height of the specimen, at the specimen mid-region at the residual state was investigated (Figure 4.54). For both types of particles, the void ratio increased in the shear zone at the interface with growing  $R_n$ . The maximum void

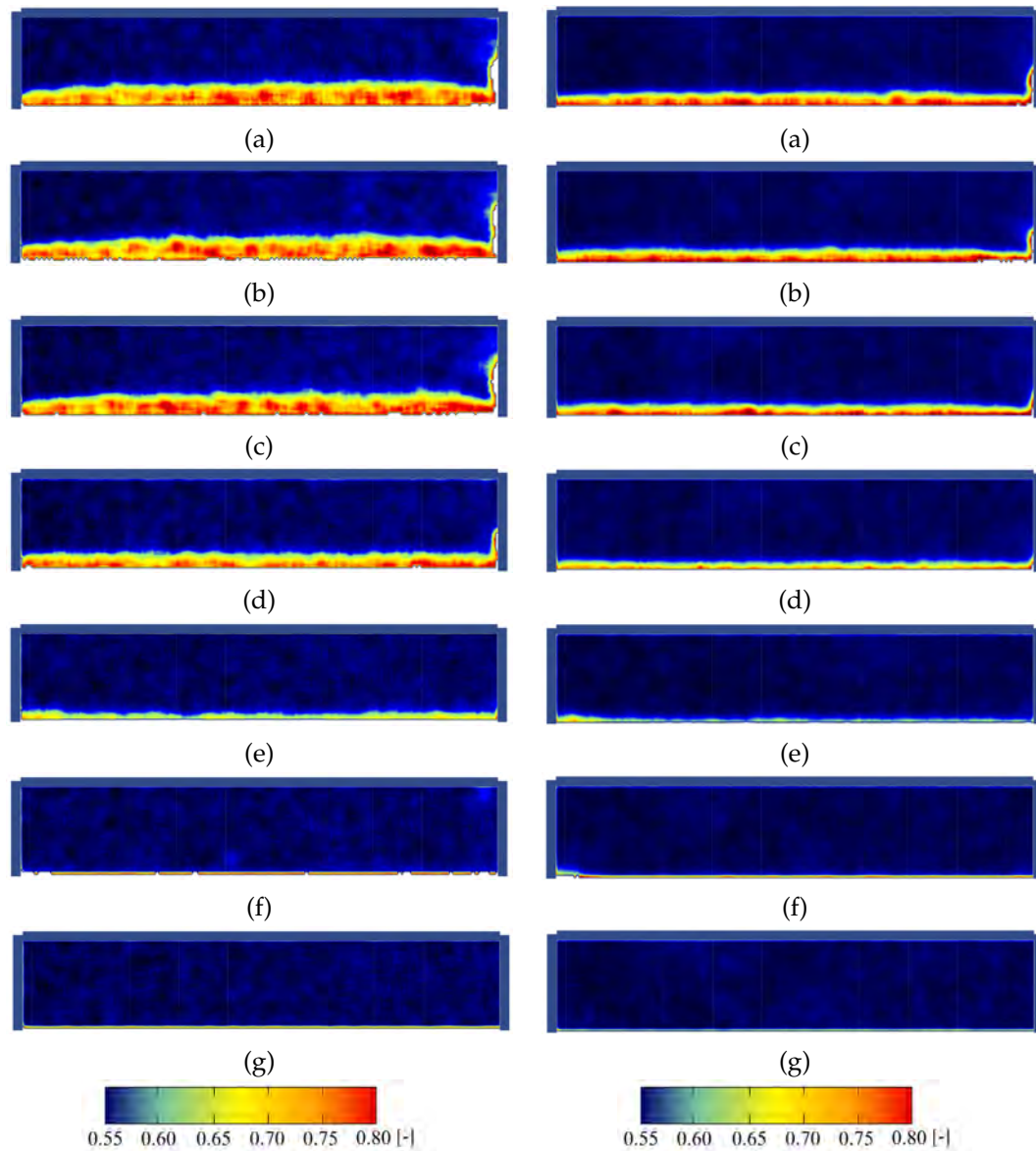


Figure 4.52: Distribution of void ratio  $e$  in sand specimen composed of spheres at the final state of the test ( $u_{tot}=7.0$  mm) for different normalized surface roughness  $R_n$ : a)  $R_n=2.0$ , b)  $R_n=1.0$ , c)  $R_n=0.75$ , d)  $R_n=0.5$ , e)  $R_n=0.25$ , f)  $R_n=0.1$  and g)  $R_n=0.01$  ( $e_0=0.55$  and  $\sigma_n=100$  kPa).

Figure 4.53: Distribution of void ratio  $e$  in sand specimen composed of clumps at the final state of the test ( $u_{tot}=7.0$  mm) for different normalized surface roughness  $R_n$ : a)  $R_n=2.0$ , b)  $R_n=1.0$ , c)  $R_n=0.75$ , d)  $R_n=0.5$ , e)  $R_n=0.25$ , f)  $R_n=0.1$  and g)  $R_n=0.01$  ( $e_0=0.55$  and  $\sigma_n=100$  kPa).

ratio in the dilatant surface shear zone at the residual state changed between  $e=0.55$  ( $R_n=0.01$ ) and  $e=0.85$  ( $R_n=2.0$ ) for both spheres and clumps. Above the shear zone, the void ratio remained constant and was equal to the initially prescribed value,  $e_0=0.55$ .

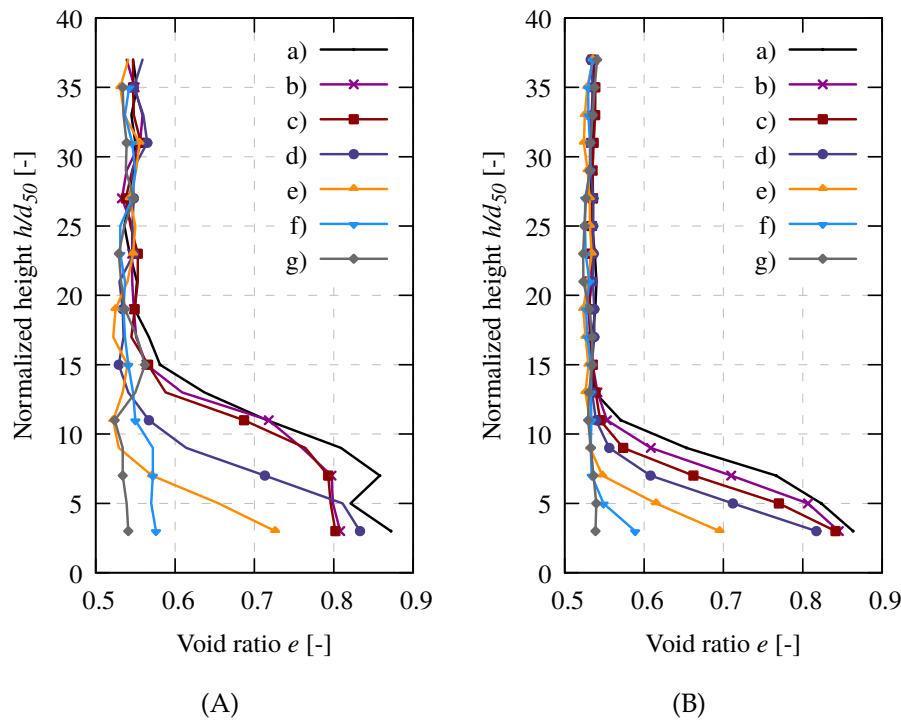


Figure 4.54: Distribution of void ratio  $e$  across normalized specimen height  $h/d_{50}$  at the specimen mid-point at residual state for  $u_{tot}=7.0$  mm for: A) spheres (Grabowski et al., 2020) and B) clumps (Grabowski et al., 2021a) for different normalized roughness  $R_n$ : a)  $R_n=2.0$ , b)  $R_n=1.0$ , c)  $R_n=0.75$ , d)  $R_n=0.50$ , e)  $R_n=0.25$ , f)  $R_n=0.10$  and g)  $R_n=0.01$  ( $e_0=0.55$  and  $\sigma_n=100$  kPa) (Adapted graphics licensed under CC BY 4.0; changes include font, line style and size adjustments).

Next, the distribution of the normal contact forces in the entire granular specimen at the residual state (front view) for the different normalized surface roughness  $R_n$  was investigated (Figures 4.55 and 4.56). The red lines represent forces above the mean values, with the thickness of the line corresponding to the magnitude of the normal force. The results of force chains evidently show that the nonuniformity of the contact forces might be pronounced during interface shearing, in particular, for initially dense sand and very rough and rough walls ( $R_n > 0.25$ ). Furthermore, the nonuniformity of these forces increases as  $R_n$  grows. This effect is more prominent for pure spheres with rotational resistance. More pronounced force chains observed for the surfaces with  $R_n \geq 0.5$  indicated significantly higher resistance of the interface (Figures 4.55a-d and 4.56a-d). In these cases, asperities created numerous contact points characterized by force chains that were much greater than the mean value. On the other hand, for relatively smooth surfaces ( $R_n=0.01$  and  $R_n=0.10$ ) the distribution of the contact forces appeared to be more uniform. This distribution indicated very low shear resistance of the interface, which is consistent with the mobilized surface friction angle curves. It is worth noting that the contact forces were higher at the left side wall where a passive state developed, in contrast to the active

state observed at the right side wall. Based on the distribution of normal forces in the specimen it is not possible to determine the path and thickness of the shear zone.

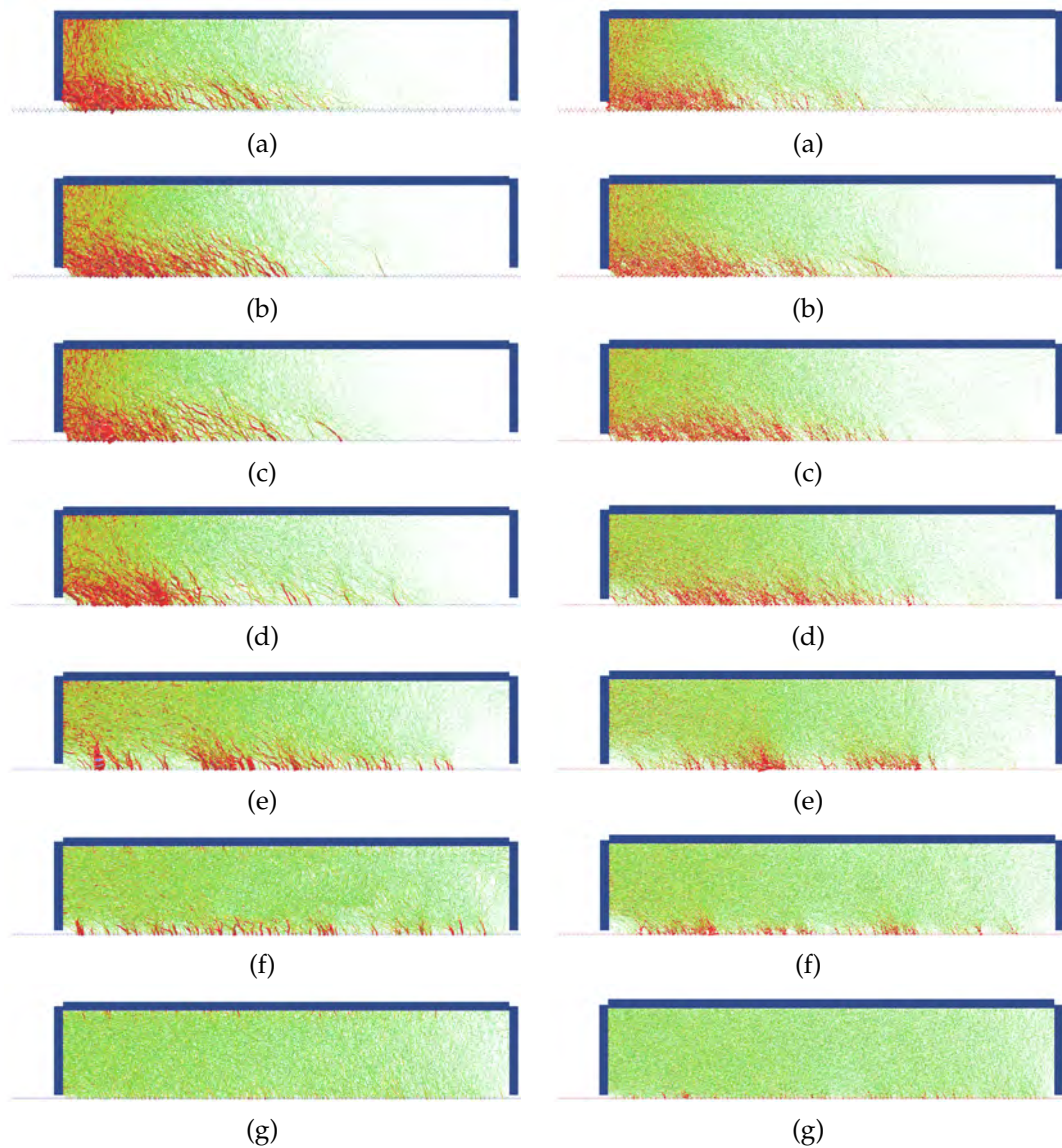


Figure 4.55: Distribution of normal force chains in sand specimen composed of spheres at the final state of the test ( $u_{tot}=7.0$  mm) for different normalized surface roughness  $R_n$ : a)  $R_n=2.0$ , b)  $R_n=1.0$ , c)  $R_n=0.75$ , d)  $R_n=0.5$ , e)  $R_n=0.25$ , f)  $R_n=0.1$  and g)  $R_n=0.01$  ( $e_0=0.55$  and  $\sigma_n=100$  kPa) (red color corresponds to normal contact forces higher than mean value, maximum value of forces is 0.05 N) (Grabowski et al. (2020), licensed under CC BY 4.0).

Figure 4.56: Distribution of normal force chains in sand specimen composed of clumps at the final state of the test ( $u_{tot}=7.0$  mm) for different normalized surface roughness  $R_n$ : a)  $R_n=2.0$ , b)  $R_n=1.0$ , c)  $R_n=0.75$ , d)  $R_n=0.5$ , e)  $R_n=0.25$ , f)  $R_n=0.1$  and g)  $R_n=0.01$  ( $e_0=0.55$  and  $\sigma_n=100$  kPa) (red color corresponds to normal contact forces higher than mean value, maximum value of forces is 0.05 N) (Grabowski et al. (2021a), licensed under CC BY 4.0).

In this paragraph, a polar distribution of contact forces in the x-y plane (mean

amplitude and orientation to the horizontal) at the beginning of the test (when the specimen was settled) and at the residual state for spheres and clumps was analyzed (Figures 4.57 and 4.58). Initially, the distribution of mean contact forces was nearly symmetrical. The vertical mean contact forces, with an orientation to the horizontal of  $90^\circ$ , dominated within the specimen. These forces were almost twice the horizontal contact forces due to the vertical pressure  $\sigma_n$  applied to the specimen. Generally, as the sand-structure interface shearing process proceeded, the direction of mean contact forces changed from a vertical to a diagonal. This behavior is consistent with the results of the other DEM studies (Salazar et al., 2015; Feng et al., 2018; Chen et al., 2020). Only in the case of the smooth surface with  $R_n=0.01$  the horizontal component of the forces transferred from the sand to the surface was significantly weaker than in the rest of the surfaces. (Figures 4.57g and 4.58g). Depending on the normalized interface roughness, the orientation of the mean contact forces to the horizontal at the residual state varied from  $135^\circ$  ( $R_n=0.01$ ) up to  $140^\circ$  ( $R_n=0.25-2.0$ ) for clumps and from  $125^\circ$  ( $R_n=0.01$ ) up to  $160^\circ$  ( $R_n=0.75-2.0$ ) for pure spheres with rotational resistance. For rough and very rough surfaces (Figures 4.57a-e and 4.58a-e), the final maximum diagonal contact forces were up to twice higher than the maximum initial vertical contact forces. In summary, the anisotropy of the interparticle forces increased with the increase of the surface roughness. The noticeable differences between clumps and spheres with rotational resistance regarding induced anisotropy of contact normal forces were also indicated in (Zhao et al., 2018) in a triaxial compression test. These differences grew with an increase in the aspect ratio of clumps.

Figures 4.59-4.62 present the distribution of the normal stresses  $\sigma_{ij}$  and shear stresses  $\sigma_{ji}$  across the normalized specimen height  $h/d_{50}$  at the specimen mid-point for the different normalized interface roughness parameter  $R_n$ . The values were calculated at the residual state for the horizontal displacement  $u_{tot}=7.0$  mm. In the following figures,  $\sigma_{11}$  is the horizontal normal stress,  $\sigma_{22}$  is the vertical normal stress,  $\sigma_{12}$  is the horizontal shear stress, and  $\sigma_{21}$  is the vertical shear stress. The stresses inside the granular material were calculated according to the Love-Webber equation presented previously in (Luding, 2004) (see Chapter 4.2 for the description).

The surface shear stresses  $\sigma_{12}$  and  $\sigma_{21}$  grew with increasing surface roughness. For both types of particles, the evolution of  $\sigma_{12}$  and  $\sigma_{21}$  was similar, however it was not perfectly symmetric (Figures 4.59 and 4.60). The magnitude of these stresses near the surface increased as the normalized roughness increased (Figures 4.59 and 4.60). The distribution of the vertical normal stress  $\sigma_{22}$  was constant across the specimen height and equal to the prescribed magnitude of load acting on the specimen throughout the test. In case of rough surfaces (e.g.  $R_n=1.0$ ) the peak values of  $\sigma_{11}$ ,  $\sigma_{12}$  and  $\sigma_{21}$  were observed inside the shear zone and slightly above the surface (approximately  $h/d_{50}=5-10$  for spheres and  $h/d_{50}=3-5$  for clumps) for both types of particles (Figures 4.61AB and 4.62AB). These values then decreased as they approached the surface. For the smooth surfaces, the distribution of all stresses exhibited an almost linear pattern, indicating negligible changes in the distribution of particle-surface interaction forces (Figures 4.61C and 4.62C). The distributions of stresses were in acceptable agreement with FEM results within micropolar continuum (Tejchman and Wu, 2010) and other DEM results (Kozicki et al., 2013).

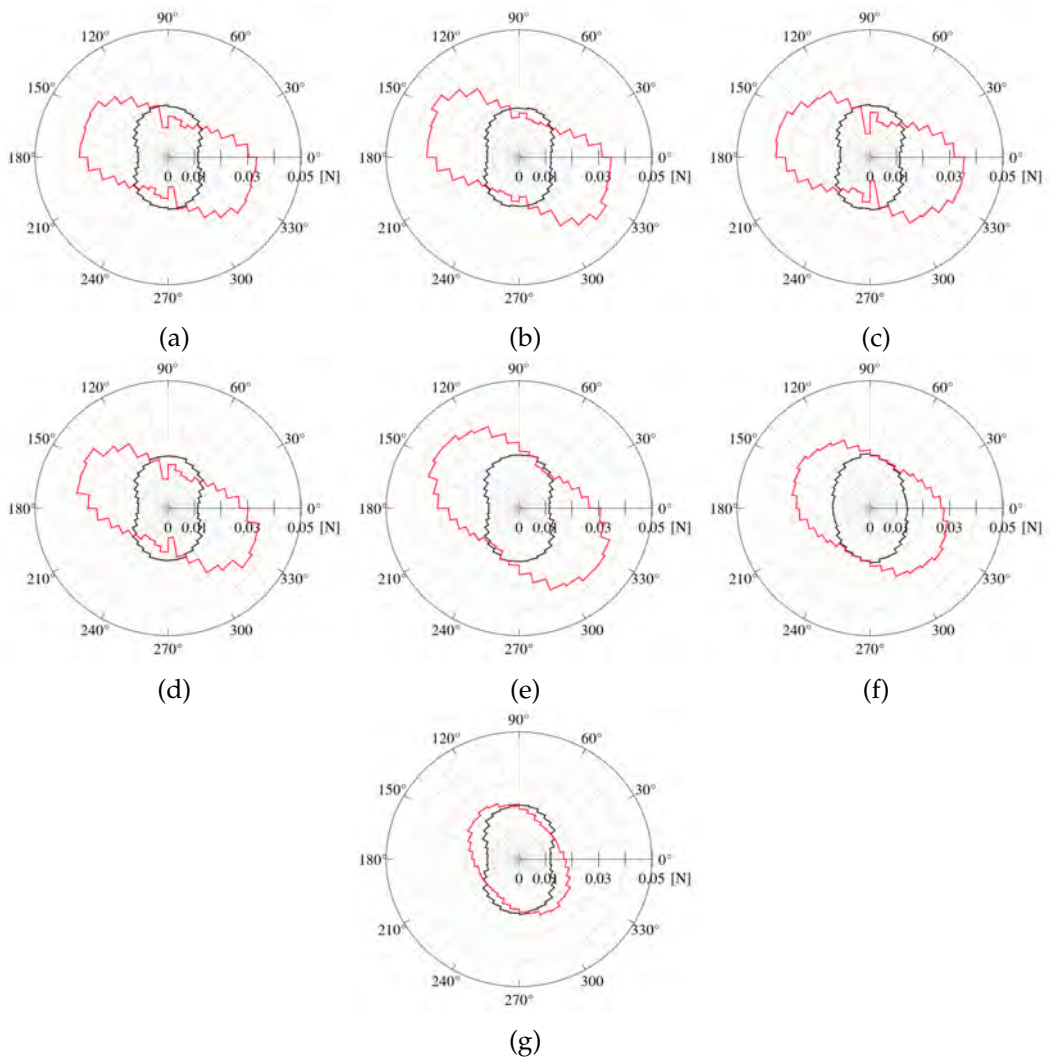


Figure 4.57: Polar mean contact force distribution in granular sand composed of spheres at the initial state (black line) and final state of the test ( $u_{tot}=7.0$  mm) (red line) for different normalized surface roughness  $R_n$ : a)  $R_n=2.0$ , b)  $R_n=1.0$ , c)  $R_n=0.75$ , d)  $R_n=0.5$ , e)  $R_n=0.25$ , f)  $R_n=0.1$  and g)  $R_n=0.01$  ( $e_0=0.55$  and  $\sigma_n=100$  kPa) (Grabowski et al. (2020), licensed under CC BY 4.0).

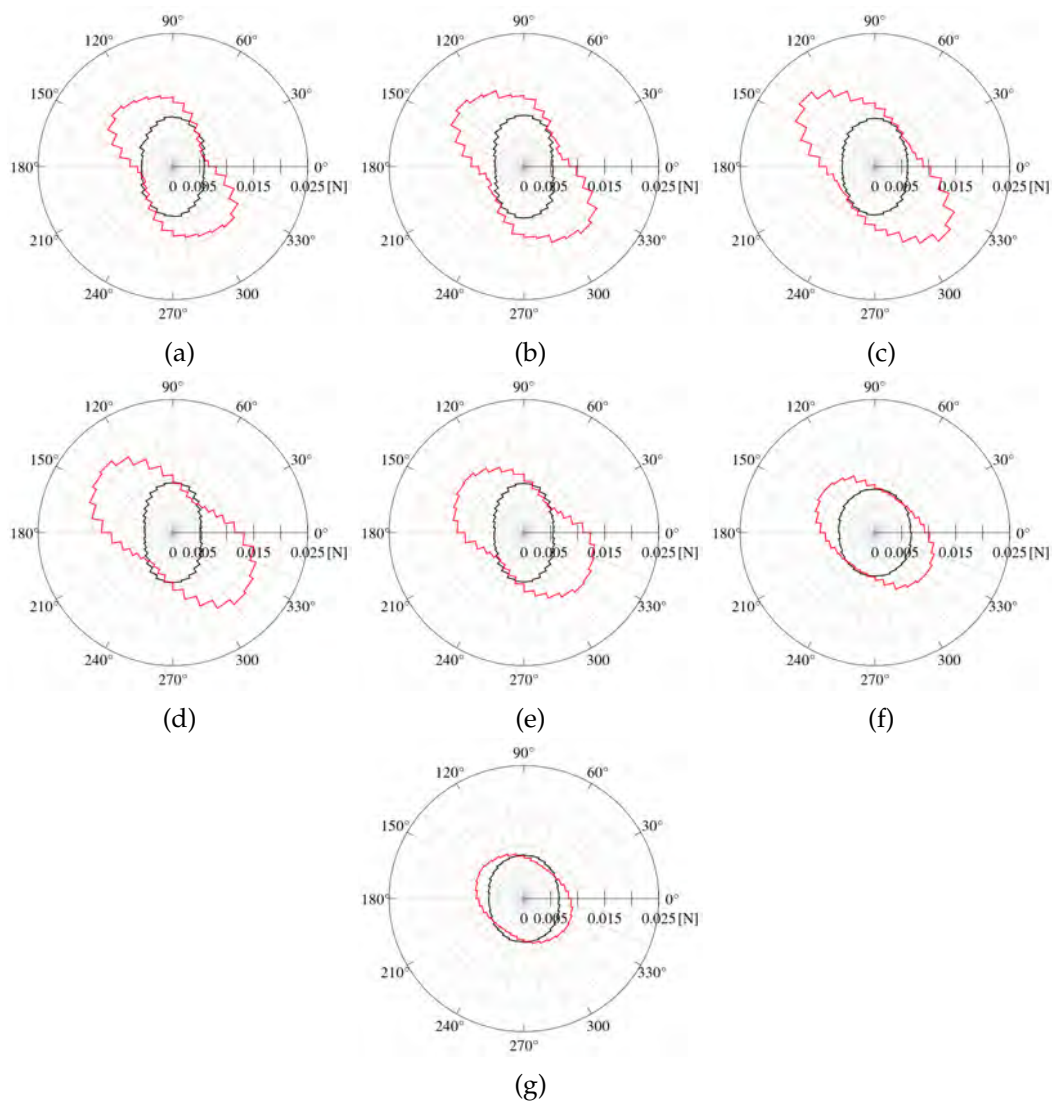


Figure 4.58: Polar mean contact force distribution in sand specimen composed of clumps at the initial state (black line) and final state of the test ( $u_{tot}=7.0$  mm) (red line) for different normalized surface roughness  $R_n$ : a)  $R_n=2.0$ , b)  $R_n=1.0$ , c)  $R_n=0.75$ , d)  $R_n=0.5$ , e)  $R_n=0.25$ , f)  $R_n=0.1$  and g)  $R_n=0.01$  ( $e_0=0.55$  and  $\sigma_n=100$  kPa) (Grabowski et al. (2021a), licensed under CC BY 4.0).

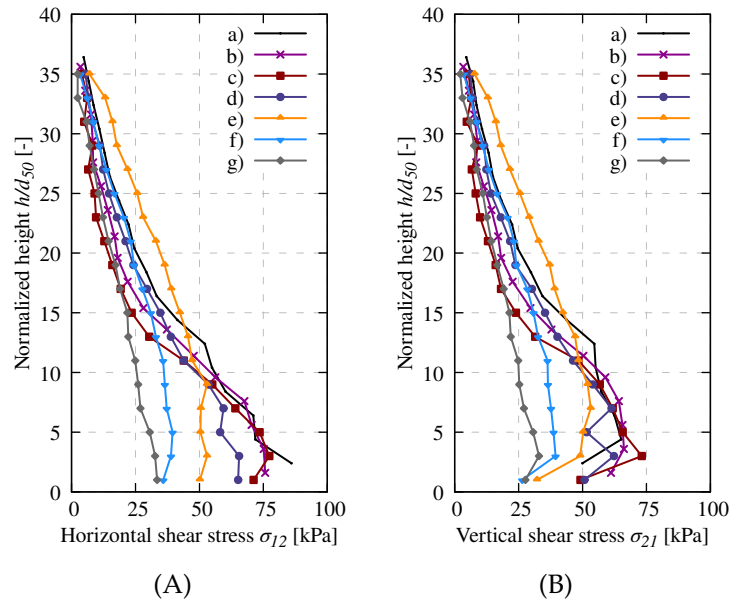


Figure 4.59: Distribution of: A) horizontal  $\sigma_{12}$  and B) vertical shear stress  $\sigma_{21}$  across normalized height  $h/d_{50}$  for spheres at residual state ( $u_{tot}=7.0$  mm) at specimen mid-point with different normalized surface roughness  $R_n$ : a)  $R_n=2.0$ , b)  $R_n=1.0$ , c)  $R_n=0.75$ , d)  $R_n=0.5$ , e)  $R_n=0.25$ , f)  $R_n=0.10$  and g)  $R_n=0.01$  ( $e_0=0.55$  and  $\sigma_n=100$  kPa) (adapted from Grabowski et al. (2020), licensed under CC BY 4.0. Graphic changes include color and size adjustments).

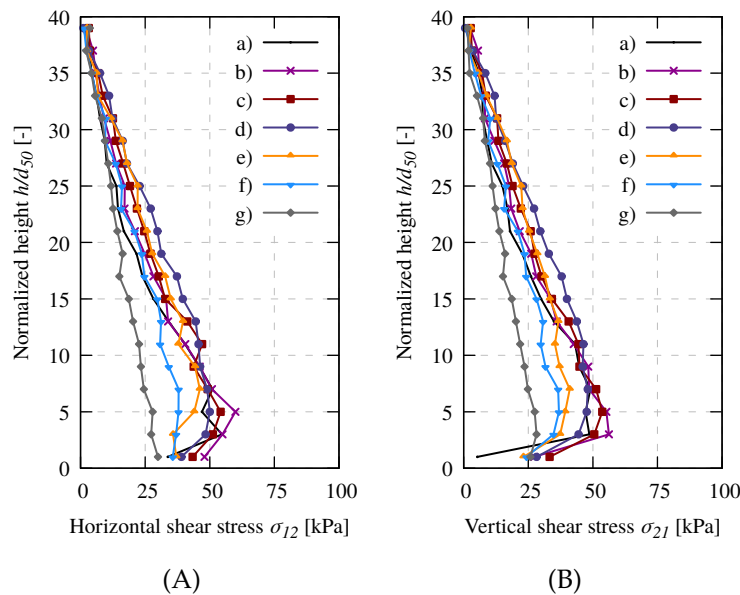


Figure 4.60: Distribution of: A) horizontal  $\sigma_{12}$  and B) vertical shear stress  $\sigma_{21}$  across normalized height  $h/d_{50}$  for clumps at residual state ( $u_{tot}=7.0$  mm) at specimen mid-point with different normalized surface roughness  $R_n$ : a)  $R_n=2.0$ , b)  $R_n=1.0$ , c)  $R_n=0.75$ , d)  $R_n=0.5$ , e)  $R_n=0.25$ , f)  $R_n=0.10$  and g)  $R_n=0.01$  ( $e_0=0.55$  and  $\sigma_n=100$  kPa) (adapted from Grabowski et al. (2021a), licensed under CC BY 4.0. Graphic changes include color and size adjustments).

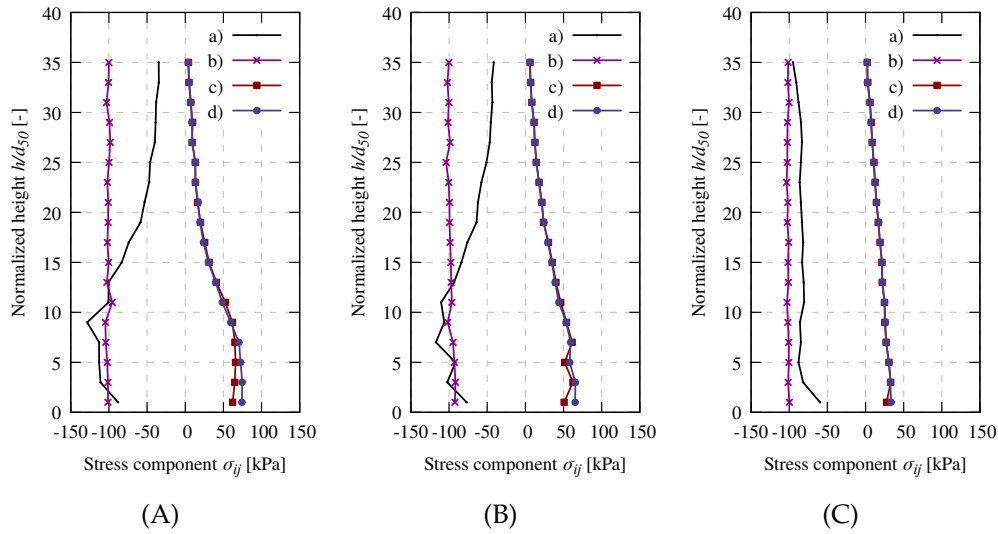


Figure 4.61: Distribution of stress components for spheres: a) horizontal normal stress  $\sigma_{11}$ , b) vertical normal stress  $\sigma_{22}$ , c) horizontal shear stress  $\sigma_{12}$  and d) vertical shear stress  $\sigma_{21}$  across normalized specimen height  $h/d_{50}$  at residual state ( $u_{tot}=7.0$  mm) at specimen mid-point with different normalized interface roughness  $R_n$ : A)  $R_n=1.0$ , B)  $R_n=0.50$  and C)  $R_n=0.01$  ( $e_0=0.55$  and  $\sigma_n=100$  kPa) (adapted from Grabowski et al. (2020), licensed under CC BY 4.0. Graphic changes include color and size adjustments).

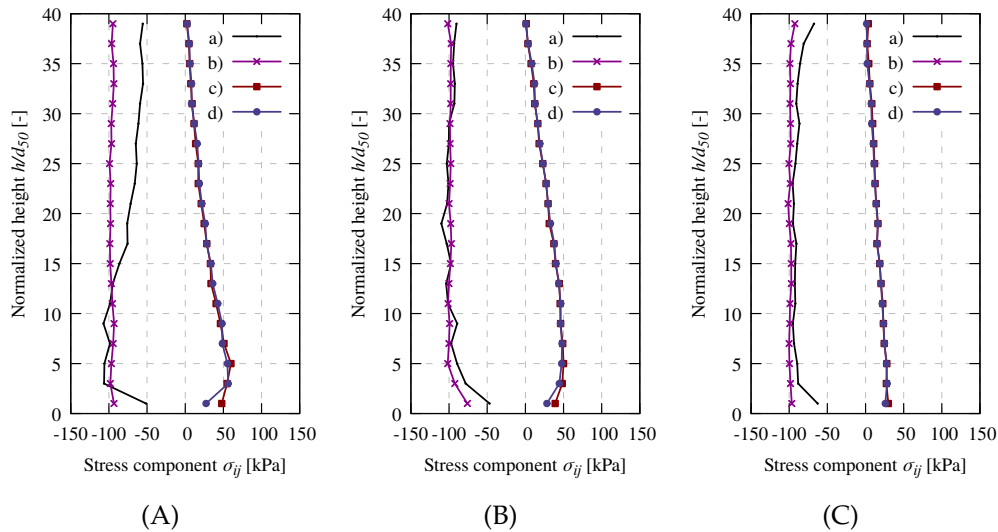


Figure 4.62: Distribution of stress components for clumps: a) horizontal normal stress  $\sigma_{11}$ , b) vertical normal stress  $\sigma_{22}$ , c) horizontal shear stress  $\sigma_{12}$  and d) vertical shear stress  $\sigma_{21}$  across normalized specimen height  $h/d_{50}$  at residual state ( $u_{tot}=7.0$  mm) at specimen mid-point with different normalized interface roughness  $R_n$ : A)  $R_n=1.0$ , B)  $R_n=0.50$  and C)  $R_n=0.01$  ( $e_0=0.55$  and  $\sigma_n=100$  kPa) (adapted from Grabowski et al. (2021a), licensed under CC BY 4.0. Graphic changes include color and size adjustments).

### Mesoscopic behavior of the sand-surface interface for initially loose specimen

After a detailed analysis of the interface shear test performed for the initially dense sand, the results of the interface shear test for the initially loose sample with  $e_0=0.80$  are presented in this section. As previously, these calculations were performed for both types of particles. In the analysis, the rough interface with normalized roughness  $R_n=1.0$  was chosen. During the test, the sand sample was subjected to the normal load of magnitude  $\sigma_n=100$  kPa. Similarly to the previous section, the presented results were obtained at the final state of shear ( $u_{tot}=7.0$  mm). The following figures present various characteristics of the specimen, including its deformation (Figures 4.63a and 4.64a), particle rotations (Figures 4.63b and 4.64b), void ratio (Figures 4.63c and 4.64c), force chains (Figures 4.63d and 4.64d) and the distribution of polar mean contact forces (Figures 4.65 and 4.66).

During the shearing, initially loose sand was locked in between the surface asperities and exhibited zero horizontal displacements (Figures 4.63a and 4.64a). The horizontal slip  $u$  along the surface for both types of particles was lower than 5% of the total prescribed displacement. Similarly to the initially dense samples, based on the particle rotations (Figures 4.63b and 4.64b) and void ratio distribution (Figures 4.63c and 4.64c), an almost horizontal shear zone along the bottom surface was observed. The grain rotations had nearly always the same positive sign (clockwise rotation). Due to the looser particle arrangement, more particles rotated in the counterclockwise direction as compared to the dense samples for both cases. For the spherical particles, the shear zone thickness, obtained based on the grain rotations was approximately 50% higher than in initially dense sample. For the clumps, the shear zone thickness was approximately 10% greater. The distribution of normal contact forces was similar for both types of particles. However, there were some differences in the magnitude of these forces, with greater forces observed for the clumps. This is because purely spherical particles exhibit a lower coordination number  $n$ , meaning they have fewer interactions between them compared to the clumped particles. Consequently, the lower number of interactions in initially loose sand resulted in greater magnitudes of interparticle contact forces compared to those in initially dense sand (for both spheres and clumps). Similarly to the previous results, the contact forces were higher at the left side wall where a passive state developed, in contrast to the active state observed at the right side wall (Figures 4.63d and 4.64d). The final orientation angle of mean contact forces to the horizontal was about  $115^\circ$  for spheres and  $120^\circ$  for clumps (Figures 4.63e and 4.64e). The final maximum diagonal contact forces were up 40% higher than the maximum initial vertical contact forces for both types of particles (Figures 4.65 and 4.66). The anisotropy of the contact forces was lower than in the initially dense sample.



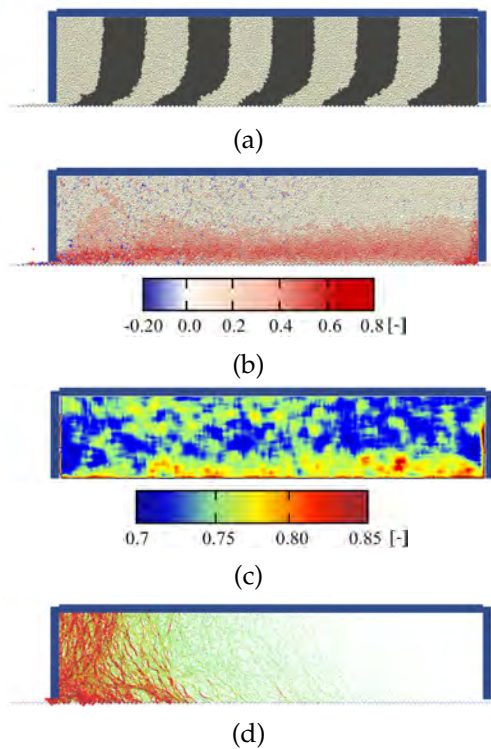


Figure 4.63: Discrete results obtained at the final state of the test ( $u_{tot}=7.0$  mm) for initially loose sand ( $e_0=0.80$ ) composed of spheres: a) front view of the specimen, b) particle rotations distribution (red color represents the clockwise rotations, blue color the counterclockwise rotations), c) void ratio distribution, and d) normal force chains distribution in the specimen (red color corresponds to normal contact forces higher than mean value, maximum value of forces is 0.05 N) ( $R_n=1.0$  and  $\sigma_n=100$  kPa) (Grabowski et al. (2020), licensed under CC BY 4.0).

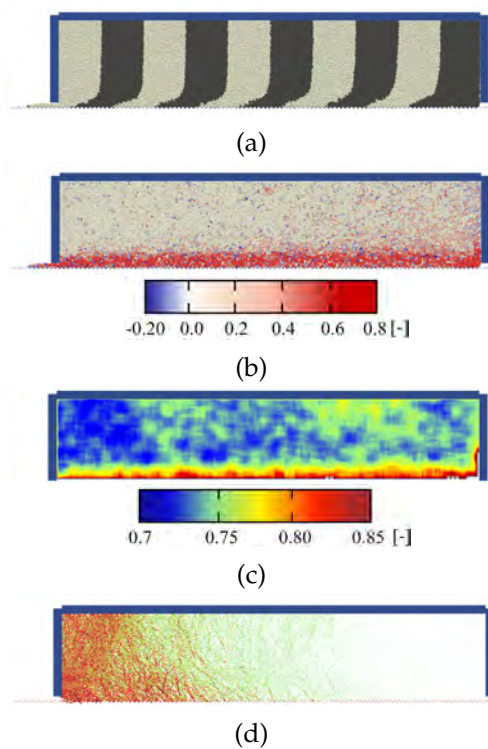


Figure 4.64: Discrete results obtained at the final state of the test ( $u_{tot}=7.0$  mm) for initially loose sand ( $e_0=0.80$ ) composed of clumps: a) front view of the specimen, b) particle rotations distribution (red color represents the clockwise rotations, blue color the counterclockwise rotations), c) void ratio distribution, and d) normal force chains distribution in the specimen (red color corresponds to normal contact forces higher than mean value, maximum value of forces is 0.05 N) ( $R_n=1.0$  and  $\sigma_n=100$  kPa) (Grabowski et al. (2021a), licensed under CC BY 4.0).

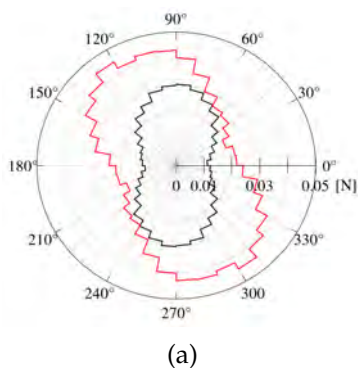


Figure 4.65: Polar mean contact force distribution in granular specimen at the initial state (black line) and final state of the test (red line) for initially loose sand ( $e_0=0.80$ ) composed of spheres ( $R_n=1.0$ ,  $\sigma_n=100$  kPa and  $d_{50}=0.5$  mm).

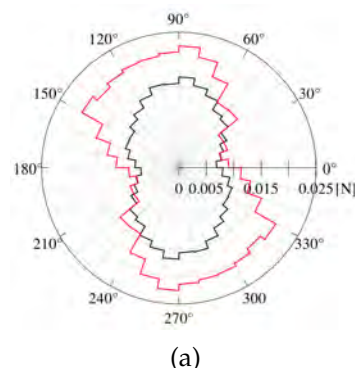


Figure 4.66: Polar mean contact force distribution in granular specimen at the initial state (black line) and final state of the test (red line) for initially loose sand ( $e_0=0.80$ ) composed of clumps ( $R_n=1.0$ ,  $\sigma_n=100$  kPa and  $d_{50}=0.5$  mm).

### Micropolar boundary conditions

The analysis presented earlier showed the significant effect of the surface roughness on the mechanical behavior of interfaces. The study presented both qualitative and quantitative results regarding the shear zone formation in the sand-structure contact zone obtained from discrete simulations. Unfortunately, DEM is often restricted to the study of small-scale phenomena and problems due to major software and hardware limitations. The analysis of large-scale systems using particle methods is often limited by these constraints. However, the discrete results can be valuable for simulating large soil-structure systems using the Finite Element Method. To accurately analyze granular material-structure system with FEM, including modeling of shear zone formation, a proper description of the contact along the interface is essential. DEM can provide insights into the mechanical behavior of the interface, thus allowing the description of boundary conditions for granular material confined by the structure.

As shown earlier the behavior of the interface between granular material and surface depends strictly on the roughness of the interface. In addition, the shear resistance and the deformation of bulk solids also depends on the applied pressure, initial density, the rotations, the shape and the mean diameter of grains (Tejchman and Wu, 2009; Ebrahimian and Bauer, 2011). To properly simulate the behavior of shear zones with the FEM constitutive models enhanced by a characteristic length must be used (Tejchman, 1989; Tejchman and Wu, 2009). In order to capture the properties of the granular material micro- and mesostructure, the micropolar (Ebrahimian and Bauer, 2011; Tejchman and Wu, 2010) or Cosserat (Tejchman and Wu, 1995; Mühlhaus and Vardoulakis, 1987) continuum approaches are frequently applied. Within these models, the nonlinear deformation of granular material, taking into account the formation of localization, is possible by adding an additional rotational degree of freedom to each point (Mühlhaus and Vardoulakis, 1987; Tejchman and Wu, 1995; Ebrahimian and Bauer, 2011). Particle rotations can be used as one of the boundary conditions for Finite Element Analysis (FEA) of interfaces between bulk solids and structures, along with other boundary conditions such as translational ones. Unfortunately, the determination of the individual grain characteristics, such as rotations are difficult to measure in the experiments. However, these local characteristics of grains are easy to determine with DEM, therefore, the discrete analysis presented earlier may be used to propose surface boundary conditions for micropolar continua.

Some micropolar boundary conditions have already been proposed to describe the interface roughness (Huang et al., 2003; Tejchman and Wu, 2010; Ebrahimian and Bauer, 2011). Tejchman and Wu (2010) presented 2D boundary conditions along the horizontal rigid interface including two ratios connected to the normalized interface roughness: 1) a ratio of the micropolar rotation multiplied by the mean grain diameter and the horizontal displacement, and 2) a ratio between the horizontal shear stress multiplied by the mean grain diameter and the horizontal couple stress. In the studies by Ebrahimian and Bauer (2011) and Huang et al. (2003), the boundary condition in the 2D analyses was assumed to be the ratio between the slip and the total imposed displacement at the interface was assumed instead of the ratio between



the horizontal shear stress multiplied by the mean grain diameter and the horizontal couple stress.

With the numerical simulations presented in this chapter, the following boundary conditions at the interface for the 2D continuum models were proposed. These ratios can only be applied to 2D continua, as the boundary condition for the twist in the contact plane between the bodies was not prescribed. The first boundary condition, is the ratio between surface grain rotation and surface grain slip  $A = \omega d_{50}/u$  (Figure 4.67). The second one, is the ratio between the horizontal slip and the total imposed displacement at the end of the shearing  $B = u/u_x$  (Table 4.6). The last ratio, is determined based on the interface grain tangential force  $t$  and interface grain moments  $m$  calculated along the surface asperities (Figure 4.68). These local variables were calculated in the center of the specimen at the residual state for the final horizontal displacement  $u_x=7.0$  mm for all studied surfaces. The contact moments were calculated by multiplying the tangential and normal forces by their distance from the contact point 'C' (where the sphere component of clump interacts with the asperity) to the gravity center of clump 'O'. Next, these interaction forces and moments were transformed into the global coordination system. Based on these interaction forces, the ratio  $C = t'd_{50}/m'$  was proposed as the third boundary conditions (Figure 4.69).

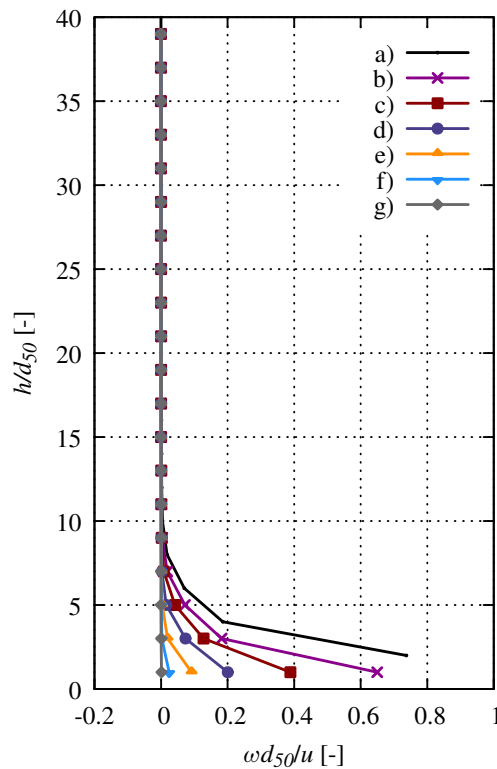


Figure 4.67: Evolution of ratio  $A = \omega d_{50}/u$  across the normalized specimen height  $h/d_{50}$  at the specimen center at the end of the test ( $u_x=7.0$ ) obtained for clumps for different normalized surface roughness  $R_n$ : a)  $R_n=2.0$ , b)  $R_n=1.0$ , c)  $R_n=0.75$ , d)  $R_n=0.50$ , e)  $R_n=0.25$ , f)  $R_n=0.10$  and g)  $R_n=0.01$  ( $e_0=0.55$  and  $\sigma_n=100$  kPa) (adapted from Grabowski et al. (2021a), licensed under CC BY 4.0. Graphic changes include color and size adjustments).

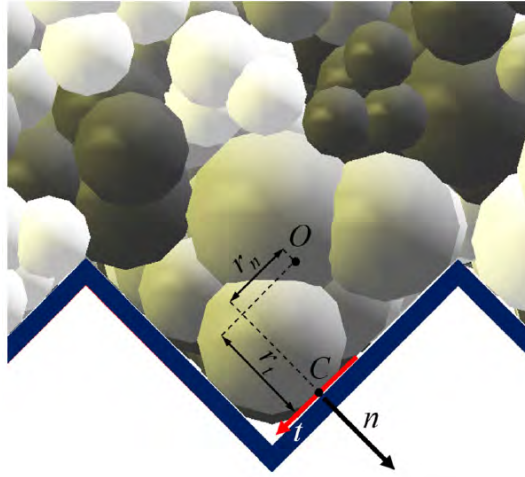


Figure 4.68: Normal and tangential interface forces  $n$  and  $t$  acting on surface grooves ('O' is the center of the clump, 'C' is the wall contact point, and  $r_n$  and  $r_t$  are the lever arms of the contact forces against point 'O') (Grabowski et al. (2021a), licensed under CC BY 4.0).

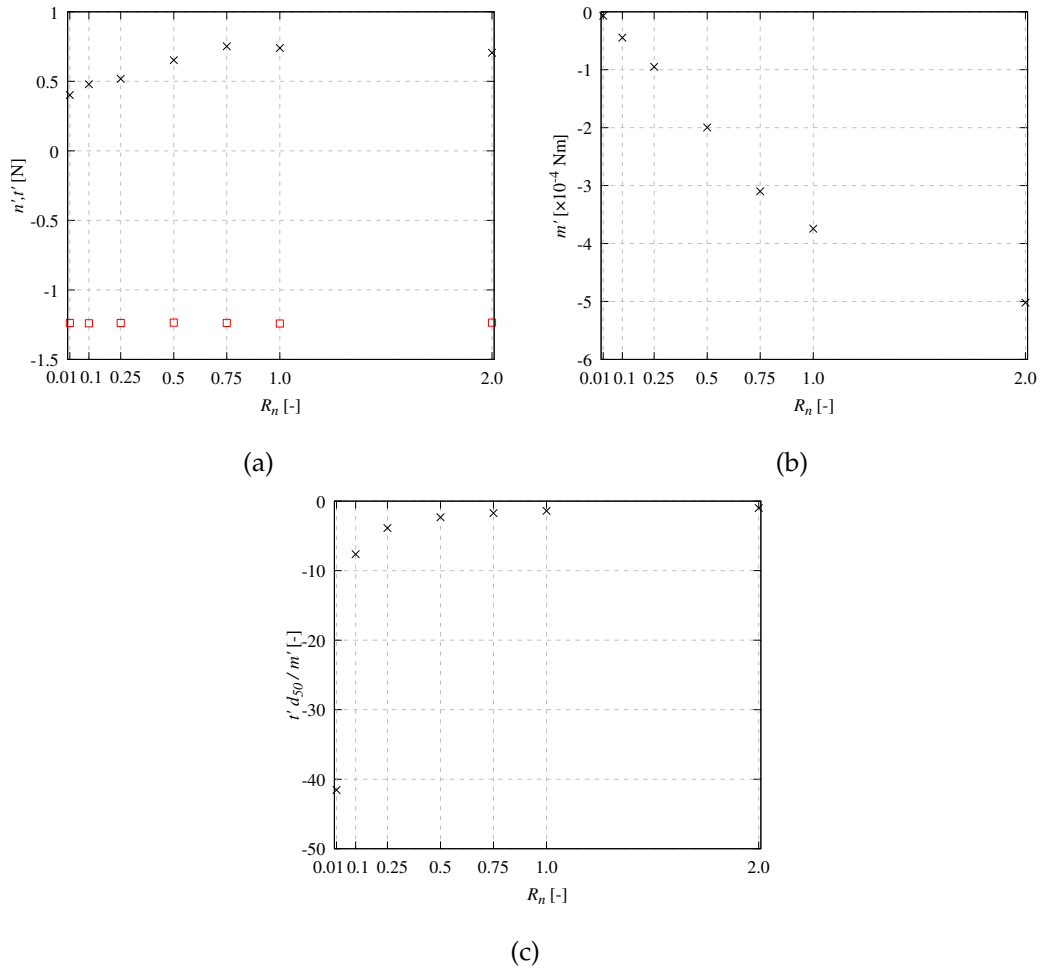


Figure 4.69: Relationship between: a) normal interface force  $n'$  in vertical direction (squares) and tangential interface force  $t'$  (crosses) in horizontal direction and tangential interface forces  $n$  and  $t$  acting on inclined surface grooves) (Grabowski et al. (2021a), licensed under CC BY 4.0).

The proposed ratios were calculated for clumped particles and can be approximated in the range  $0 \leq R_n \leq 1.0$  as:

$$A = \omega d_{50}/u \cong 0.5R_n \quad (4.2)$$

$$B = u/u_x \cong 1 - R_n \quad (4.3)$$

$$C = t'd_{50}/m' \cong 1/R_n \quad (4.4)$$

These ratios can be related to the normalized surface roughness  $R_n$  only. These boundary conditions may be prescribed along the interface nodes of FE mesh in simulations using micropolar continua. In the case of the particle rotation  $\omega$  it can be replaced by the micropolar Cosserat rotation  $\omega_c$  (Tejchman and Wu, 1995; Tejchman and Wu, 2010). In addition, the boundary conditions were calculated also for the spherical particles with rotational resistance. However, they differed slightly from the boundary conditions determined for clumps. Therefore, it seems that proposed ratios slightly depend on the particle shape. The influence of the particle shape on these boundary conditions could be also checked in DEM simulations by assuming, e.g. different particle shapes and different sieve curves.

#### 4.3.4 Summary

In this section, a detailed discrete analysis of the sand-structure interface behavior with varying surface roughness was conducted. The analysis investigated the influence of particle shape on interface resistance and shear localization by employing two types of particles: perfectly spherical particles with rotational resistance and asymmetric convex clumps composed of spheres. Additionally, interface boundary conditions for micropolar continua were proposed. The following major conclusions can be summarized from the simulations:

- Particles in the form of spheres with rotational resistance exhibited lower residual interface shear resistance, particle rotations, and slips, as well as a higher thickness of the interface shear zone, volume changes, and orientation of mean contact forces to the horizontal when compared to irregular convex clumped particles. The peak interface shear resistance was solely similar. The rolling resistance model was proven to be able to model localization phenomena. However, it has some drawbacks, such as additional artificial dilatancy occurring within the granular material.
- Surface roughness had a significant effect on the mobilized interface friction angle and the thickness of the shear zone at the interface. Interface shear resistance increased with the rise of surface roughness. Both the peak and residual interface friction angles increased proportionally with the surface roughness. The relationship between the peak or residual interface friction angle and normalized interface roughness exhibited a bilinear/parabolic trend. The residual surface friction angle was generally 3-7° higher for spheres with rotational resistance compared to clumps ( $R_n \geq 0.25$ ).

- The interface shear resistance is directly related to the thickness of the shear zone, which increases bilinearly with the rise of  $R_n$ . The thickness of the surface shear zone, calculated based on particle rotation, ranged between  $6 \times d_{50}$  and  $14 \times d_{50}$  for spheres and between  $6 \times d_{50}$  and  $12 \times d_{50}$  for clumps. Consequently, the shear zone thickness in sand composed of clumps was lower by 15-40% compared to spheres ( $R_n \geq 0.5$ ). For smooth surfaces ( $R_n \leq 0.1$ ), mostly slipping occurred at the surface, resulting in rotations of approximately one layer of particles ( $1 \times d_{50}$ ).
- For the roughest surfaces ( $R_n \geq 0.75$ ) the maximum particle rotation occurred slightly above the surface ( $3-5 \times d_{50}$ ). For these surfaces particle rotations approached zero at the surface. This was because they were trapped between the grooves. For surfaces with  $R_n \leq 0.5$ , the largest particle rotations occurred directly at the surface. The rotations for clumps were 30% higher than for spheres with rotational resistance ( $R_n \geq 0.25$ ).
- The normalized surface roughness exerted a significant effect on the contact forces within the granular specimen. The anisotropy of the force network increased proportionally with the increase of interface roughness. The distribution of forces at the final state of shearing was more uniform in the case of clumped particles. The orientation of mean contact forces at the residual state increased with the rise in surface roughness for both types of particles. For spherical particles, the angle to the horizontal ranged between  $135^\circ$  and  $140^\circ$ , while for clumps, it ranged between  $125^\circ$  and  $160^\circ$ .
- Three different ratios were proposed to describe the boundary conditions at the interface for the 2D continuum models (the boundary for the twist in the plane between the bodies was not proposed). The first ratio,  $A = \omega d_{50} / u \cong 0.5 R_n$ , combines particle rotation, multiplied by the mean grain diameter, divided by the horizontal slip along the surface. The second ratio,  $B = u / u_x \cong 1 - R_n$ , is the ratio between the horizontal slip and the total horizontal displacement. The third ratio,  $C = t' d_{50} / m' \cong 1 / R_n$ , is determined based on the interface grain tangential force, multiplied by the mean grain diameter, divided by the interface grain moment. These ratios were approximated to the normalized roughness of the surface. The magnitude of these ratios depends on the particle shape.

## 4.4 Interface shear test between sand and corrugated sinusoidal surfaces

### 4.4.1 Introduction

The study presented in the following section deals with numerical investigations of the interface between granular material and sinusoidal corrugated surface. Such interfaces are commonly encountered in steel silos supported by thin-walled columns around the silo perimeter (Wójcik et al., 2011; Kuczyńska et al., 2015). The interface behavior, which is influenced by the characteristics of both the opposing structure and the contacting granular material (see Section 4.3 for the analysis), is closely linked to the safety of these structures. During the deformation of the bulk solid, the contact zone is characterized by the formation of the localized zones in the region adjacent to the construction surface. The location of these zones plays an important role in estimating the shear resistance and loads transferred from the granular material to the structure Tejchman and Wu, 1995; Hu and Pu, 2004; Su et al., 2018. For this reason, a comprehensive understanding of the behavior of the bulk solid/corrugated wall contact zone is essential for accurate maintenance of bulk solids handling processes.

The key aspect of the interface between granular material and structure analysis is the friction between these two media. Although extensive research on the mechanism of the interface between granular material and various types of surfaces has been carried out (see Chapter 4.3 for the detailed description of these studies), relatively little attention has been paid to the behavior of interfaces between granular material and corrugated surfaces (Moore et al., 1984; Molenda et al., 2002; Wiącek et al., 2021; Wiącek et al., 2023).

In case of silo with corrugated walls supported by thin walled columns, the properties of the interface, such as the effective coefficient of friction against the corrugated wall, play a major role in the correct determination of the vertical loads acting on the silo structure (Molenda et al., 2002; Wiącek et al., 2021). The processes that occur in the contact zone present many challenges to engineers, and as a result, the theoretical approach is usually simplified. For example, the European Standard EN 1991-4 (2006) allows to determine the effective friction coefficient without taking into consideration the exact geometry of the corrugation. According to Eurocode, for corrugated wall surface, the this coefficient can be determined as:

$$\mu_{eff} = (1 - a_w) \tan(\phi_i) + a_w \mu_w \quad (4.5)$$

where:  $\mu_{eff}$  is the effective wall friction,  $\phi_i$  is the granular material internal friction angle,  $\mu_w$  is the wall friction coefficient and  $a_w$  is the wall contact factor (Figure 4.70).

The standard recommends that the designer either perform his own analysis of the contact regime between the bulk solid and the wall or assume the constant value  $a_w=0.2$  for the profiles similar to the one shown in Figure 4.70. However, this approach results in determining the coefficient of friction  $\mu_{eff}$  solely based on the frictional properties of the bulk material and the wall. Unfortunately, as the previous research (Molenda et al., 2002; Wiącek et al., 2021) has shown, this method can lead

to significant differences between the determined standard load values and the experimentally measured ones. This can seriously affect the safety of corrugated steel silos.

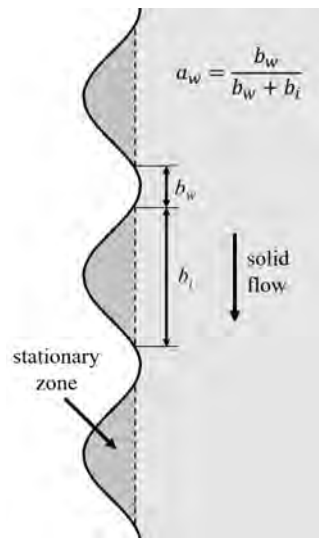


Figure 4.70: Dimension of profile for sinusoidal corrugated surfaces with the approximate location of shear plane (dashed line) according to EN 1991-4 (2006).

Current knowledge of the mechanical behavior of the interface between the corrugated silo walls and the bulk solid is relatively limited. The problems associated with the study of the mechanisms inside the contact zone are mainly caused by the discrete and nonlinear nature of bulk solids. Despite these limitations, previous studies have provided useful contributions to the mechanical description of the given problem. In laboratory experiments by Moore et al. (1984), a shear plane develops in the contact zone just below the peaks of the corrugation. Consequently, the interface friction coefficient is influenced by two components: grain-on-grain friction (shearing within the granular material) and grain-on-surface friction (sliding of the granular material against the metal surface). Similar mechanism of interface shearing was captured by Zhang et al. (1994), using a direct shear apparatus. A series of tests were performed to analyze the effect of the normal pressure applied to the granular sample and the moisture of the sample on the behavior of the contact zone. In the study, the friction coefficient of the interface was determined and ranged from 0.41 to 0.63 depending on the test conditions. It was found that this friction was mainly associated with grain-on-grain friction. Similar as in previous studies, the shear plane developed partially at the peaks of the corrugation and partially within the granular material. A specially modified direct shear apparatus was used by Molenda et al. (2002) to determine the effective coefficient of friction of wheat on smooth and corrugated steel surfaces. The dimensions of the test specimen were close to the real dimensions of the bulk solid-silo construction system. The study revealed that the effective coefficient of friction is significantly dependent on the corrugated wall geometry. In the case of short-period corrugated sheets, the coefficient was more related to grain-on-grain friction than in the case of long-period corrugated sheets. In the experiments by Wiącek et al. (2021) the influence of silo outlet size and filling method on pressure distribution and friction

mechanism in the interface was studied. This problem was investigated using a laboratory scale silo with sinusoidal corrugated walls. The location of the shear zone was approximated based on the photographic data analyzed using the Particle Image Velocimetry (PIV) technique. It was positioned 5 to 8 grain diameters below the corrugation peaks. The pressures exerted by the bulk solid on the corrugated silo walls did not agree with the pressures predicted by the Eurocode formula. In the study by Wiącek et al. (2023) the discrete analysis of the contact zone between wheat and corrugated sinusoidal surface was performed. The friction between these two domains was determined for different normal loads and shearing velocity.

Recent literature shows that the mechanism occurring in the interface zone between granular material and corrugated silo walls is an interesting problem for many civil and agricultural researchers and engineers. These studies show that many aspects related to the discussed problem are still understudied and need further research. Unfortunately, the discrete modeling of granular flow in silos with sinusoidal corrugated walls is beyond the capabilities of most current Discrete Element Method (DEM) codes. These codes are generally limited to handling hundreds of thousands or a few million particles, while typical granular materials stored in silo structures consist of billions of particles. To overcome this limitation, the formation of the shear zone in the contact area between granular material and sinusoidal corrugated surfaces has instead been investigated in reduced scale using a direct shear apparatus.

In addition, the appendix A presents the comprehensive laboratory analysis of the numerical tests performed. The experimental part was used to calibrate the numerical model and to validate the numerical results.

#### 4.4.2 Numerical model and methodology

The basic physical and mechanical properties of the sand obtained in comprehensive geotechnical laboratory analysis are presented in Appendix A (Table A.1). The local material parameters for the numerical model of the interface between sand and a sinusoidal corrugated surface in the direct shear test were determined using the experimental data presented in the Appendix A. The simulations of the interface shear test were performed using spherical particles with rotational resistance. The material parameters of the discrete model model were the same as before and are listed in the Table 4.7. The sieve curve was the same as in the experiments, with particle sizes ranging from 0.25 mm to 1.00 mm, with a mean grain diameter  $d_{50}=0.71$  mm.

Table 4.7: Discrete material parameters for interface shear test.

| Parameter                                  | Value   |
|--|---------|
| interparticle friction angle $\mu_c$       | 18°     |
| local modulus of elasticity $E_c$          | 300 MPa |
| shear/normal local stiffness ratio $\nu_c$ | 0.3     |
| limit rolling coefficient $\eta$           | 0.4     |
| rolling stiffness coefficient $\beta$      | 0.7     |

The numerical model setup (shown in Figure 4.71) was created under full 3D conditions, with the specimen depth reduced from 60 mm to 7 mm ( $10 \times d_{50}$ ) to shorten



the computation time. Specimen height and width were the same as in the experiments (Appendix A), with  $h=15$  mm and  $b=60$  mm, respectively. The gap equal to the maximum grain diameter was left between the lower and upper frame walls as in the experiment to prevent locking of particles at the bottom corners during shearing. The standard interface shear test procedure was followed for all tests. The first step involved creating the granular assembly consisting of approximately 60 000 distinct particles inside the upper shear box (the detailed procedure of the sample preparation was described in the Chapter 4.2). This was followed by applying a constant initial force, denoted by  $P$  to the upper box ( $P/A_c=\sigma_n$ , where  $A_c$  is the internal area of the shear box). Once the desired void ratio of the sand mass was achieved and the kinetic energy of the assembly was negligible, the interparticle friction angle was set to the prescribed value  $\mu_c=18^\circ$  and the upper frame moved horizontally  $u_x$  at a constant velocity. The horizontal velocity of the shear box was small enough to consider the test as quasi-static (the inertial number  $I$  was kept below  $10e-4$  (Roux and Chevoir, 2005)). During the test, the rigid bottom surface was fixed, while the upper frame was movable and smooth. The frictional coefficient along these surfaces was  $\tan(\mu_s)=\tan(16^\circ)=0.29$ .

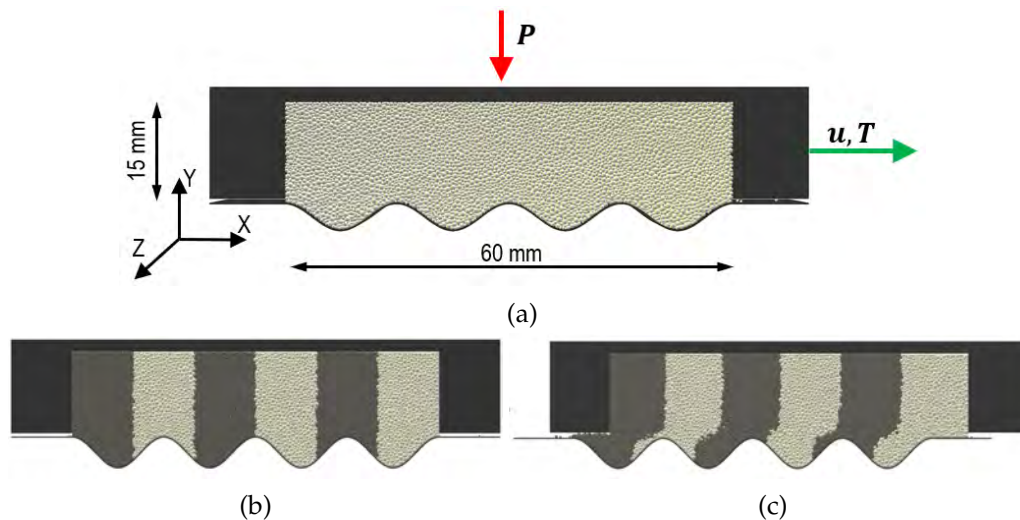


Figure 4.71: Interface shear test in DEM: a) numerical setup, b) sample at the initial state and c) deformed sample at the final state.

During the discrete analysis, as in the experiment, the influence of six surfaces was examined: a completely flat one (Figure 4.72a), and the rest based on the geometry of silo wall corrugations (Figure 4.72b-f). The sinusoidal corrugations had the same wavelength ( $l=15$  mm which equals approximately  $21 \times d_{50}$ ), but different depth  $d$  (distance between the hills) (Figure 4.72), which was varied from 0.8 mm (approx.  $1 \times d_{50}$ ) to 6.4 mm (approx.  $9 \times d_{50}$ ) with a step of 1.4 mm ( $2 \times d_{50}$ ). As a result, the range of the depth to wavelength ( $d/l$ ) coefficients for the profile was between 0.053 and 0.427, what fits in the typical scope of this ratio from thin-walled silos (where  $d/l$  varies between 0.11 and 0.24).

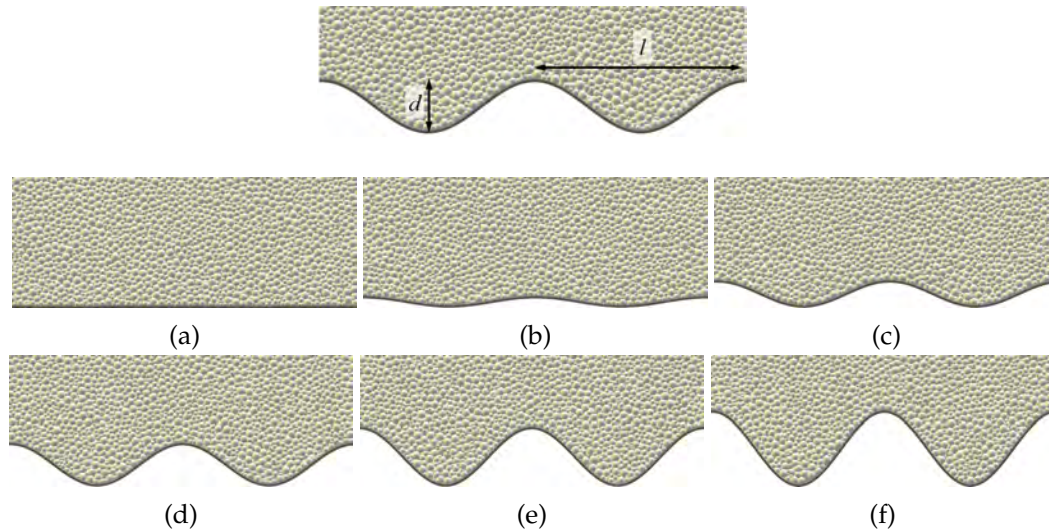


Figure 4.72: Rigid bottom corrugated sinusoidal surfaces with different corrugation coefficient  $d/l$ : a)  $d/l=0.000$ , b)  $d/l=0.053$ , c)  $d/l=0.147$ , d)  $d/l=0.240$ , e)  $d/l=0.333$  and f)  $d/l=0.428$  ( $d$  - corrugation depth and  $l$  - corrugation length).

#### 4.4.3 Numerical results

In this section, the results of simulations of the interface between sand and a sinusoidal corrugated surface in the direct shear test for sinusoidal corrugated surfaces of different depth to wavelength ratio  $d/l$  are presented. First of all, a comparison between the shear resistance and granular material deformation obtained with numerical simulations and with laboratory experiments is shown. Next, the effect of the different  $d/l$  ratio on the shear zone formation and on its mesoscopic characteristics is presented. The results include granular material deformation, the distribution of sphere rotations, void ratios, and force chains at the final stage of shearing. Finally, the interface shear zone evolution is presented based on two selected corrugated surfaces.

##### Evolution of mobilized shear stress and volumetric strain

At the beginning, the numerical model was calibrated, since the experimental data were no longer based on the 'Karlsruhe' sand. For the calibration, own experiments of the interface shear test were used (see Appendix A for description). Figures 4.73 and 4.74 present the comparison between evolution of the mobilized shear stress  $\tau$  and the volumetric strain  $\varepsilon_v$  versus the normalized displacement  $u/L$  obtained in discrete and experimental approach. A satisfactory agreement was obtained between the DEM results and the laboratory data, particularly with respect to the shape of the shear stress and volumetric strain curves, as well as the peak value of the shear resistance. Minor differences were observed in both cases, with the experimental specimens showing a slightly higher magnitude of shear stress in the residual phase compared to the numerical specimens.

The shear stress of the interface increased with increasing corrugation depth (Figure 4.73). For the flat surface ( $d/l=0.000$ ) and the one with corrugation coefficient  $d/l=0.053$ , the curves followed almost a bilinear pattern with negligible softening

of the granular material observed (Figure 4.73). In the remaining cases, when  $d/l$  varied from 0.147 to 0.427, a typical evolution of the frictional stress for medium-dense samples was obtained, similar to the studies by Uesugi and Kishida (1986a), Teichman and Wu (1995), Hu and Pu (2004). At the beginning of the test, the granular material exhibited hardening, which was initially related to contraction. The shear stress peaked at about  $u/L=0.035$  and then exhibited softening, again associated with dilatancy. The dilatancy of the granular material was also significantly affected by the geometry of the profile and increased with increasing corrugation depth (Figure 4.74). Only for the flat surface ( $d/l=0.000$ ) no dilatancy related to localization was observed. No contraction was captured either. The characteristic values calculated for the curves obtained in the numerical study are listed in the Table 4.8.

Based on the corrugation coefficient  $d/l$ , the analyzed surfaces can be classified into two categories: shallow and deep. The analysis showed that the critical value of the corrugation coefficient is approximately  $d/l=0.053$ . When this ratio is less than a critical value, the corrugated surface is considered shallow. The shear failure mechanism is then elastic-perfectly plastic. When the ratio is greater than a critical value, the interface is considered deep and the granular material exhibits successive hardening and softening due to dilatancy. Furthermore, the analysis showed that the shear resistance of the interface does not increase when the corrugation coefficient  $d/l$  is increased beyond a certain value. In particular, in our case, increasing this ratio above 0.333 (Figure 4.73) resulted in a negligible increase in interface shear stress.

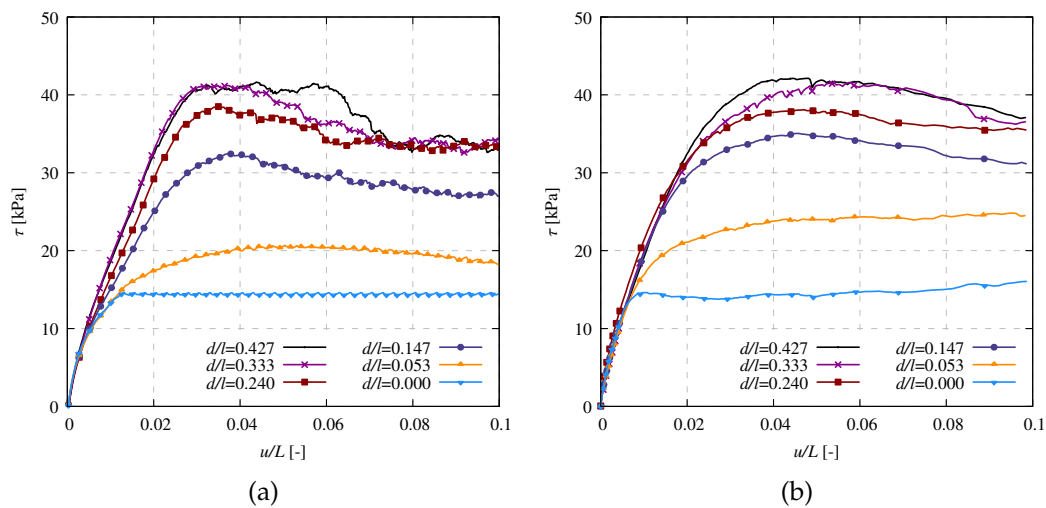


Figure 4.73: Mobilized shear stress  $\tau$  versus normalized horizontal displacement  $u/L$  for different corrugation coefficient  $d/l$  obtained with: a) DEM simulations and b) experimental analysis ( $e_0=0.63$  and  $\sigma_n=48$  kPa).

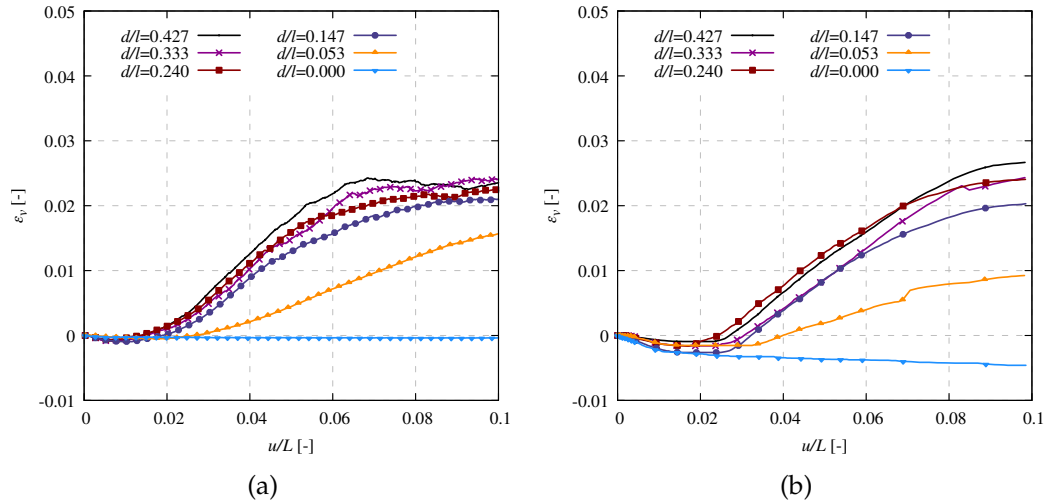


Figure 4.74: Volumetric strain  $\varepsilon_v$  versus normalized horizontal displacement  $u/L$  for different corrugation coefficient  $d/l$  obtained with: a) DEM simulations and b) experimental analysis ( $e_0=0.63$  and  $\sigma_n=48$  kPa).

Table 4.8: Calculated values of peak effective wall friction coefficient  $\mu_{eff,max}$ , effective wall friction coefficient  $\mu_{eff,res}$  and residual volumetric strain  $\varepsilon_v$  for different corrugation coefficient  $d/l$ .

| $d/l$ [-] | $\mu_{eff,max}$ [-] | $\mu_{eff,res}$ [-] | $\varepsilon_v$ [-] |
|-----------|---------------------|---------------------|---------------------|
| 0.000     | 0.290               | 0.290               | -0.0005             |
| 0.053     | 0.427               | 0.381               | 0.0157              |
| 0.147     | 0.674               | 0.558               | 0.0210              |
| 0.240     | 0.798               | 0.689               | 0.0224              |
| 0.333     | 0.861               | 0.724               | 0.0241              |
| 0.427     | 0.872               | 0.730               | 0.0235              |

### Friction of sand on corrugated sinusoidal surface

Based on the mobilized shear stress curves the friction between the sand and the corrugated sinusoidal surface was determined. The effective wall friction coefficient was calculated as:

$$\mu_{eff} = T/P \quad (4.6)$$

where  $T$  is the total horizontal force applied to the upper frame of the shear box and  $P$  is the normal force applied to the top plate during the test (dividing these forces by the contact area gives  $\tau$  and  $\sigma$ , respectively). The  $\mu_{eff}$  was calculated for the peak and the residual value of the shear resistance. Figure 4.75A presents the value of calculated effective wall friction coefficient. The magnitude of the  $\mu_{eff}$  was significantly influenced by the profile geometry, and increased with the increase of the corrugation coefficient. Equation 4.7, which is a transformation of the formula 4.5, was used to determine the wall contact factor  $a_w$ :

$$a_w = \frac{\mu_{eff} - \tan(\phi_i)}{\mu_w - \tan(\phi_i)} \quad (4.7)$$

where  $\phi_i$  represents the internal friction angle (in this case, it is the value of

$\phi_{i,max} = 42^\circ$ ), and  $\mu_w$  denotes the coefficient of friction against a flat surface (in this case, it corresponds to the assumed value for the flat surface with  $d/l=0.0$ , i.e.,  $\mu_w=0.290$ ). Figure 4.75B presents the calculated value of the wall contact factor  $a_w$  based on the peak and residual effective surface friction coefficients obtained in each test. The  $a_w=0.2$  recommended by EN 1991-4 (2006) is represented by a red line. The analysis reveals that as  $d/l$  increased, the wall contact factor decreased. These findings are consistent with those of other researchers (Zhang et al., 1994). The relationship between the wall contact factor  $a_w$  and the corrugation coefficient  $d/l$  was nonlinear throughout the entire studied range. This tendency correspond well to the relationship captured in experiments (Figure A.9 in Appendix A).

At the residual state the magnitude of  $a_w$  was higher than at the maximum state. In both cases, this parameter reached an asymptotic limit. At the maximum state, the limit was approximately  $a_w=0.139$ , and at the residual state, it was approximately  $a_w=0.349$  for surfaces with  $d/l \geq 0.333$ . For shallow surfaces, the coefficient of friction was much closer to that of grain-on-surface friction than to the internal friction angle of sand, reaching  $a_w=1.0$  for a flat surface. It is evident that the value of this factor is not constant for the tested surfaces, contrary to the recommendations of EN 1991-4 (2006). Moreover, in the typical range of wall profiles used in steel silos supported by thin-walled columns ( $0.11 \leq d/l \leq 0.24$ ),  $a_w$  does not equal 0.2 as proposed in the standard. In this range the minimum value of  $a_w$  was 0.224 ( $d/l=0.240$ ) at the peak state of shearing. In the mentioned range, the magnitude of  $a_w$  could be roughly estimated with a linear function  $f(x) = -2x + 0.7$ , where  $x$  is the corrugation coefficient  $d/l$  ( $x = d/l$ ) (the function is shown in Figure 4.75B as a blue dotted line).

It is important to remember that the proposed estimation function  $f(x)$  was formulated based on the study of the contact zone in the direct shear apparatus. Therefore, it does not yet provide an accurate estimation of the effective wall friction coefficient  $\mu_{eff}$  during flow in a silo, as obtained from the data of other researchers. However, the proposed function has been used to verify the loads applied to the corrugated sinusoidal surfaces/walls in other studies available in the literature. In the study conducted by Wiącek et al. (2023), using  $a_w=0.2$ , as recommended by the standard, provided a reasonably accurate estimate of  $\mu_{eff}$  for a profile with a corrugation coefficient  $d/l=0.191$ . Using the value  $a_w=0.32$  calculated with the proposed function  $f(x)$ , would lead to an underestimation of the wall pressures. On the other hand, in the experiments performed by Wójcik et al. (2017), the use of  $a_w=0.2$ , according to the standard formula, resulted in an overestimation of the shear wall pressures by up to 35%. Calculations of the wall contact factor  $a_w$  using the proposed function  $f(x)$  for a corrugation coefficient of  $d/l=0.237$ , as in the experiments, would provide a more realistic value of  $a_w$  ( $f(0.237) = -2 \cdot 0.237 + 0.7 = 0.23$ ). Therefore, a more detailed analysis taking into account factors such as particle types and sizes, different wall pressure magnitudes, and different void ratios of the granular material is required to improve the accuracy of the estimation function.

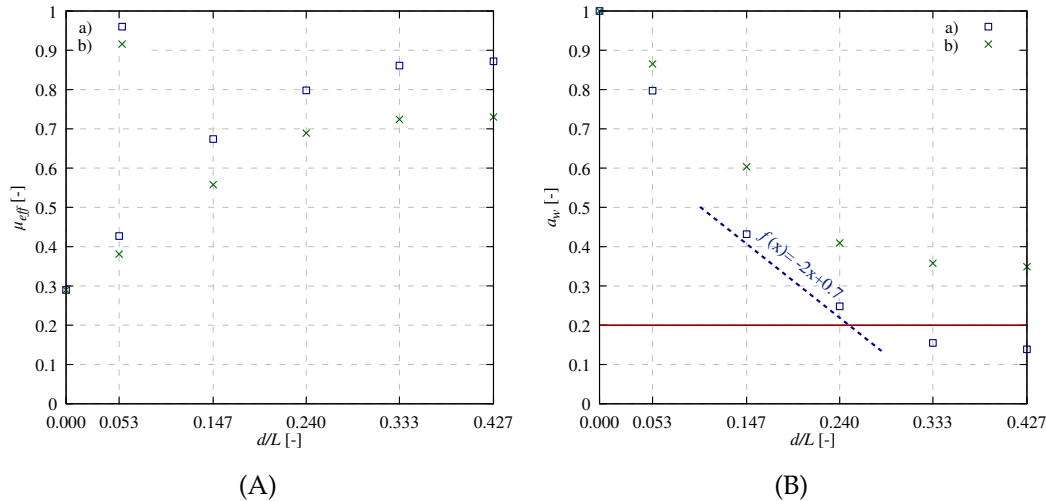


Figure 4.75: Calculated: A) effective friction coefficient  $\mu_{eff}$  and B) wall contact factor  $a_w$  versus normalized horizontal displacement  $u/L$  at the: a) peak and b) residual state for different corrugation coefficient  $d/l$  obtained with DEM (red line represents the  $a_w=0.2$  recommended by EN 1991-4 (2006)).

### Effect of the corrugations geometry on the mesoscopic behavior of the sand-surface interface

The research, described in previous section, has so far focused on the macroscopic behavior of the interface between sand and sinusoidal corrugated surfaces of various geometries. In this section, the effect of the corrugation coefficient on the mesoscopic behavior of the bulk solid-corrugated surface regime has been investigated.

First, the effect of the  $d/l$  ratio on the deformation of the sand sample was studied (Figure 4.76). The deformation of the granular material was found to be strictly dependent on the geometry of the surface. Based on the sand deformation, the first two surfaces were considered to be shallow ( $d/l \leq 0.053$ ). It can be seen that for these surfaces almost the entire sand mass behaved like a rigid body during the shearing (Figures 4.76a, b). In these cases, no shear zone occurred because the material slipped directly on the surface and the shear resistance was mainly influenced by the particle-surface friction. The remaining cases (Figures 4.76c-f) were characterized by a different failure mechanism and could therefore be considered as deep. In these cases, sand grains were partly locked in the valleys and partly followed the motion of the shear box. The granular material locked in the valleys in the area adjacent to the surfaces showed zero horizontal displacement. The stationary zone occurred in a similar way as in the case of mass flow during discharge of silo constructions with sinusoidal corrugated walls. It was observed that with increasing corrugation coefficient, the shearing began to occur inside the granular material, with the shear zone localized at the level of the surface peaks. Therefore, the shear resistance of the interface was a combination of both grain-to-grain and grain-to-surface friction.

Figure 4.77 presents the distributions of particle rotations in the entire specimen at the final state of the test. It is clear that for the flat surface, the grains either did not rotate at all (Figure 4.77a) or showed negligible rotation in the case of a surface with a corrugation coefficient of  $d/l=0.053$  (Figure 4.77b). In these cases, the granular material slipped directly at the moving surface, with the shear resistance being

mainly a result of the friction between the granular material and the surface. It can be seen that with the increase of the corrugations depth, the shear zone was more firmed and clear and occur between the peaks of the corrugations. The thickness of the shear zone between was approximately  $5 \times d_{50}$  based on the distribution of the sphere rotations (the same procedure for estimation was used as the one presented in Section 4.2). The shear zone thickness was in good agreement with the experiments where  $t_s$  varied between  $4 \times d_{50}$  and  $5 \times d_{50}$ . Within the localization, the grain rotations almost always had the same positive sign (clockwise rotation).

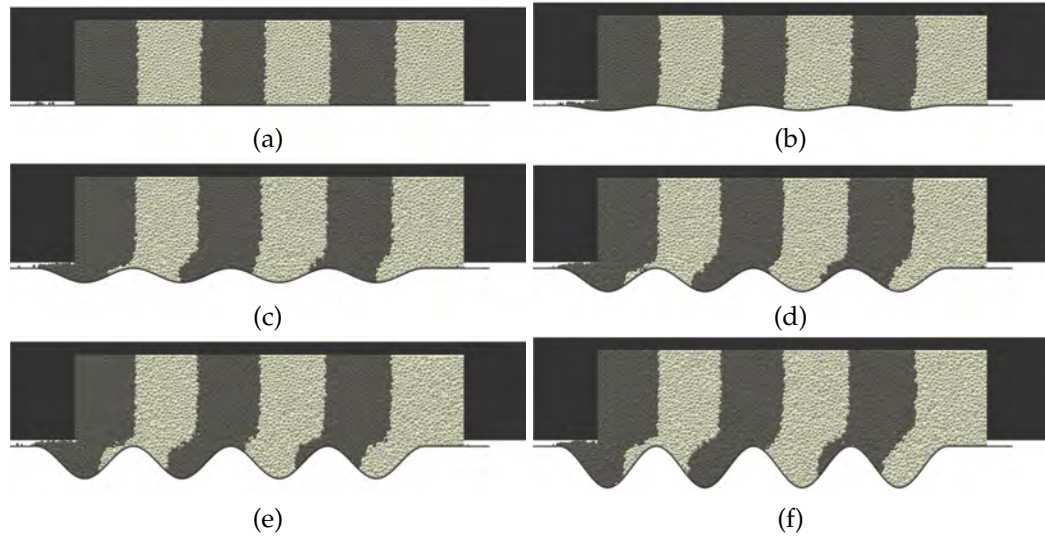


Figure 4.76: Front view of the sand specimen composed at the final state of the test ( $u/L=0.1$ ) for different corrugation coefficient  $d/l$ : a)  $d/l=0.000$ , b)  $d/l=0.053$ , c)  $d/l=0.147$ , d)  $d/l=0.240$ , e)  $d/l=0.333$  and f)  $d/l=0.427$  ( $e_0=0.63$  and  $\sigma_n=48$  kPa).

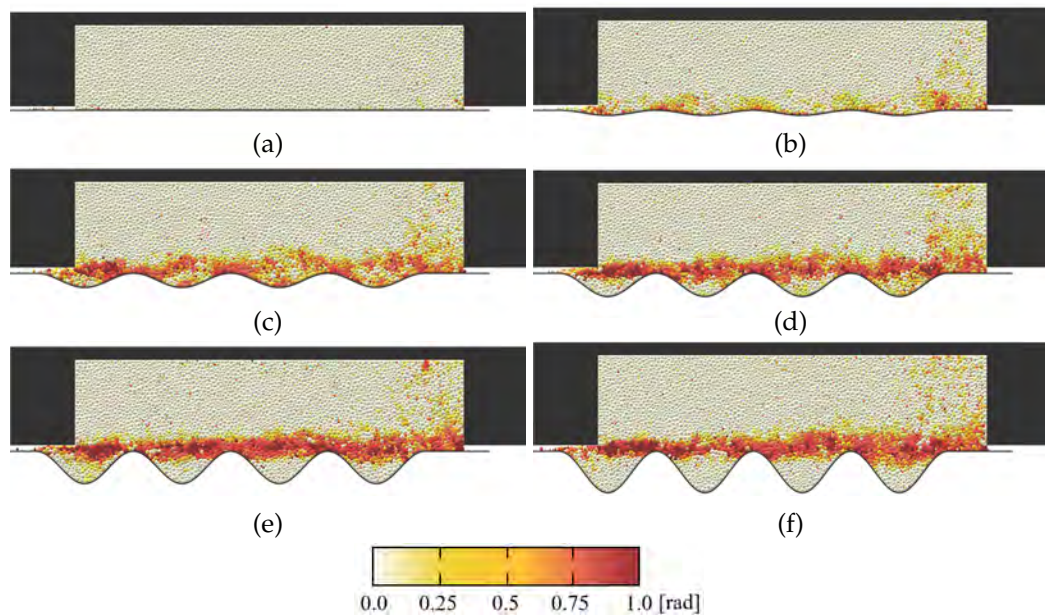


Figure 4.77: Distribution of particle rotations  $\omega$  in sand specimen at the final state of the test ( $u/L=0.1$ ) for different corrugation coefficient  $d/l$ : a)  $d/l=0.000$ , b)  $d/l=0.053$ , c)  $d/l=0.147$ , d)  $d/l=0.240$ , e)  $d/l=0.333$  and f)  $d/l=0.427$  ( $e_0=0.63$  and  $\sigma_n=48$  kPa).

Next, the distribution of the void ratio in the entire specimen at the end of the shearing was studied (Figure 4.78). This parameter shows that in the case of the flat surface ( $d/l=0.000$ ), granular material exhibited no dilation along the entire surface (Figure 4.78a). In the case of a surface with  $d/l=0.053$  (Figure 4.78b), dilatant zones occurred directly at the surface in the shallow valleys. In the remaining cases, the shear plane was located slightly below the corrugation peaks (Figure 4.78c-f). The shear zone developed between the grains locked in the valleys and the granular mass located in the upper shear box frame. Within the localized area, significant dilation occurred, particularly in the region between the surface peaks. At the corrugation peaks, negligible changes in porosity were observed, thus the grains slipped on the corrugated surfaces. As a result, the shear resistance of the sample depended on both the grain-to-grain and grain-to-surface friction components. In all cases, there was some loosening of the granular material associated with the movement of the shear box.

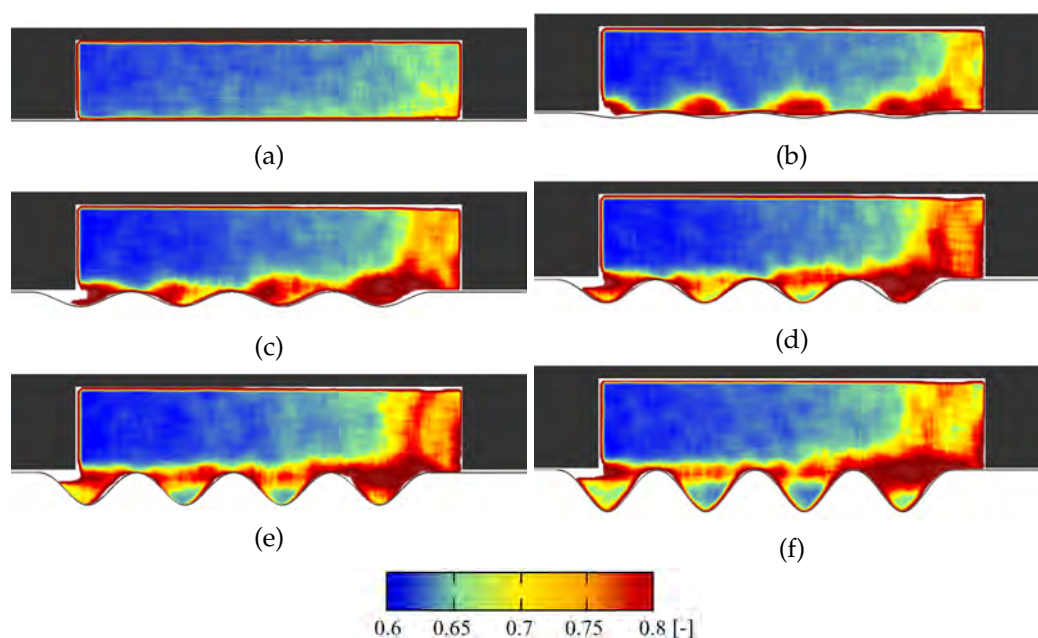


Figure 4.78: Distribution of void ratio  $e$  in sand specimen at the final state of the test ( $u/L=0.1$ ) for different corrugation coefficient  $d/l$ : a)  $d/l=0.000$ , b)  $d/l=0.053$ , c)  $d/l=0.147$ , d)  $d/l=0.240$ , e)  $d/l=0.333$  and f)  $d/l=0.427$  ( $e_0=0.63$  and  $\sigma_n=48$  kPa).

Afterwards, the distribution of the normal force chains in the entire sand sample was examined (Figure 4.79). The corrugation depth had a significant effect on the distribution of forces between the particles. In the case of the contact zone between the sand and the flat surface (Figure 4.79a) the distribution of forces was almost uniform within the sample at the end of the shearing. Some minor changes were observed near the boundary conditions, such as an increase in forces on the advancing side of the specimen (left side of the sample) and a slight decrease on the receding side of the specimen (right side of the sample). In the remaining cases, the distribution of forces between the particles was strongly non-uniform (Figure 4.79b-f). The orientation of the force chains was diagonal to the shear zone. A significant increase in the forces magnitude was observed between the peaks of the corrugation. The forces appear to originate from the corrugation peaks and oppose the movement of

the top box. Columns of particles are formed, indicating the shear resistance of the interface. The shear zone itself is barely visible based on the distribution of force chains. Similar to the flat surface case, a significant increase in force magnitude was observed near the advancing side of the shear box and a significant decrease in force magnitude was observed on the receding side.

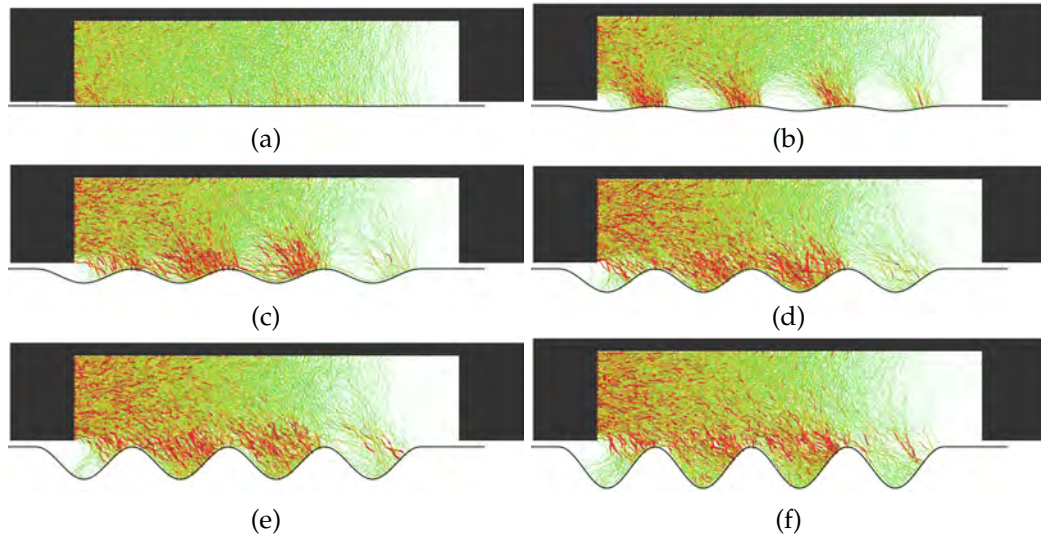


Figure 4.79: Distribution of normal force chains in sand specimen at the final state of the test ( $u/L=0.1$ ) for different corrugation coefficient  $d/l$ : a)  $d/l=0.000$ , b)  $d/l=0.053$ , c)  $d/l=0.147$ , d)  $d/l=0.240$ , e)  $d/l=0.333$  and f)  $d/l=0.428$  ( $e_0=0.63$  and  $\sigma_n=48$  kPa) (red color corresponds to the force chain above the mean value).

Finally, the strains within the granular material were calculated with Digital Image Correlation (DIC) technique by analyzing the displacement fields, as presented in Figures 4.80-4.82 (for a brief description of the DIC method and DIC analysis parameters, see Appendix A). Figure 4.80 shows the horizontal strains  $\varepsilon_{xx}$  corresponding to each type of corrugated surface. Observations show that the flat surface (Figure 4.80a) did not cause any significant deformation of the granular material, while minor changes were observed in the case of a surface with a corrugation coefficient of  $d/l=0.053$  (Figure 4.80b). In the latter case, the changes in the granular material structure were located directly at the surface, therefore the shear resistance depended mostly on grain-on-surface friction. In the remaining cases, when  $d/l=0.147$  or above (Figure 4.80c-f), an evident shear zone can be seen which is located above the surface. It is clear that the shearing takes place partially within the material and partially at the peaks of the surface, thus, the shearing resistance is dependent on both the grain-on-grain and grain-on-surface friction angle. Based on the calculations of the horizontal strains for these cases (Figures 4.80c-f) some interesting conclusions may be drawn. The observed shear zone consisted of alternating regions of contracting and dilating sand. Although the material sheared globally in one direction related to the movement of the upper shear box, local deformation inside the shear zone occurred in both directions. It is hypothesized that this behavior is due to the successive formation and collapse of particle columns during shearing of the granular material (Rechenmacher, 2006; Chupin et al., 2011). Similar local deformations were also observed in laboratory studies by Oda and Kazama (1998),

and in the DEM analysis by Nitka et al. (2015). These studies showed that this mechanism is related to the void ratio distribution within the localized area. Along the shear zone, large voids occurred almost periodically, creating localized regions of contraction and dilation, similar to the strain fields.

The calculated vertical strain fields  $\varepsilon_{yy}$  presented in Figure 4.81 correspond well with the results for shear strains  $\varepsilon_{xy}$  presented in Figure 4.82. Based on these strain fields, the interfaces with  $d/l=0.000$  and  $d/l=0.053$  can be classified as shallow because they showed negligible changes in sand structure during shearing. In the other cases, when  $d/l=0.147$  or above (Figures 4.81c-f and 4.82c-f), an obvious shear zone was observed. The most pronounced and clear zones were obtained for surfaces with a corrugation coefficient of  $d/l=0.240$  or above. In these cases, the majority of shearing took place within the granular material, with minimal interaction at the surface. No significant deformation was visible on the top of the hills, due to the sliding of the particles on the surface. In these cases, the shear zone divided the material into two quasi-rigid bodies, one located above the localization and the other locked below in the surface valleys.

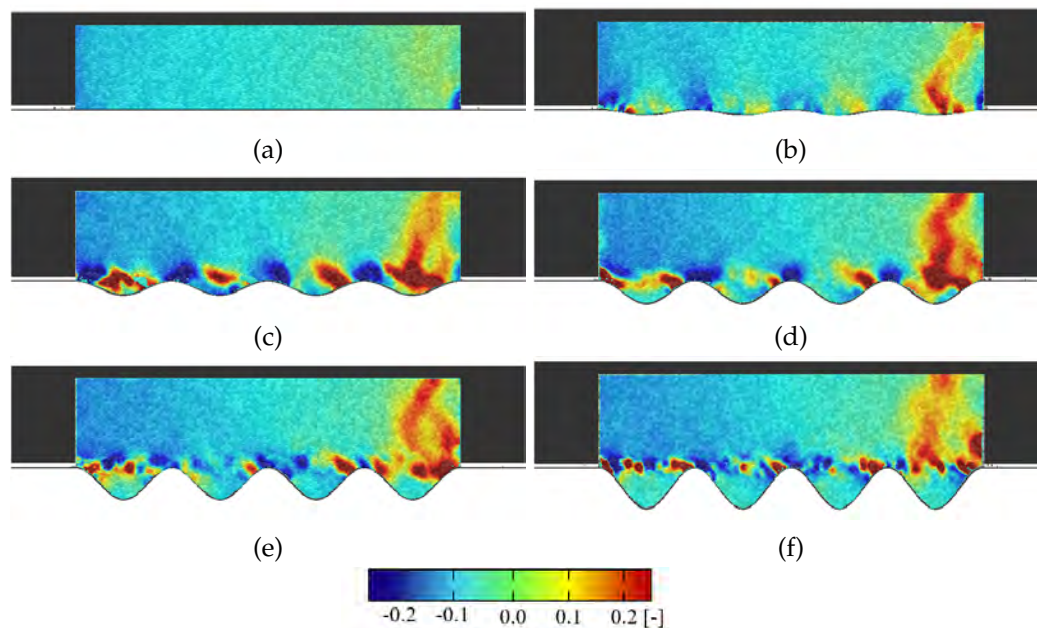


Figure 4.80: Distribution of the horizontal strain  $\varepsilon_{xx}$  in sand specimen at the final state of the test ( $u/L=0.1$ ) obtained with DIC analysis for different corrugation coefficient  $d/l$ : a)  $d/l=0.000$ , b)  $d/l=0.053$ , c)  $d/l=0.147$ , d)  $d/l=0.240$ , e)  $d/l=0.333$  and f)  $d/l=0.427$  ( $e_0=0.63$  and  $\sigma_n=48$  kPa).

The formation of the interface shear zone obtained with in discrete analysis was compared to the experimental results (Appendix A). Figures 4.83 and 4.84 present the distribution of the horizontal  $\varepsilon_{xx}$ , vertical  $\varepsilon_{yy}$  and shear  $\varepsilon_{xy}$  strains for two exemplary interfaces with corrugation coefficient  $d/l=0.053$  and the other with  $d/l=0.333$ . In both cases, the deformation of the sand near the surface was in good agreement with the real experiments. Similarly as in the laboratory tests, in the case of the shallow interface some minor changes during the shearing were observed directly at the corrugated surface (Figure 4.83). The characteristic shear behavior observed during the laboratory analysis, such as alternating regions of horizontal strains of

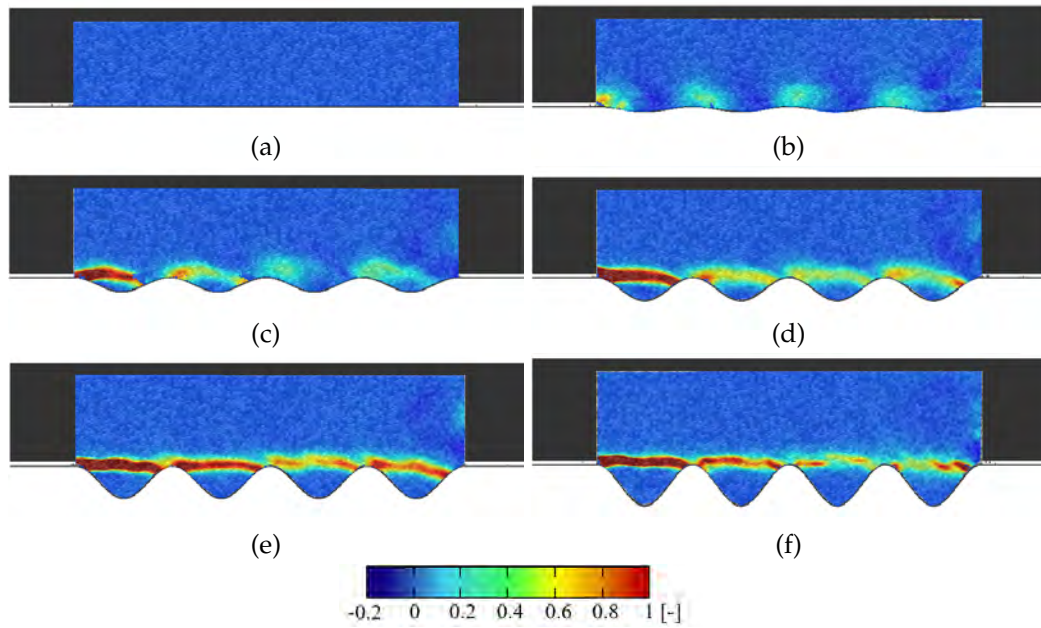


Figure 4.81: Distribution of the vertical strain  $\varepsilon_{yy}$  in sand specimen at the final state of the test ( $u/L=0.1$ ) obtained with DIC analysis for different corrugation coefficient  $d/l$ : a)  $d/l=0.000$ , b)  $d/l=0.053$ , c)  $d/l=0.147$ , d)  $d/l=0.240$ , e)  $d/l=0.333$  and f)  $d/l=0.427$  ( $e_0=0.63$  and  $\sigma_n=48$  kPa).

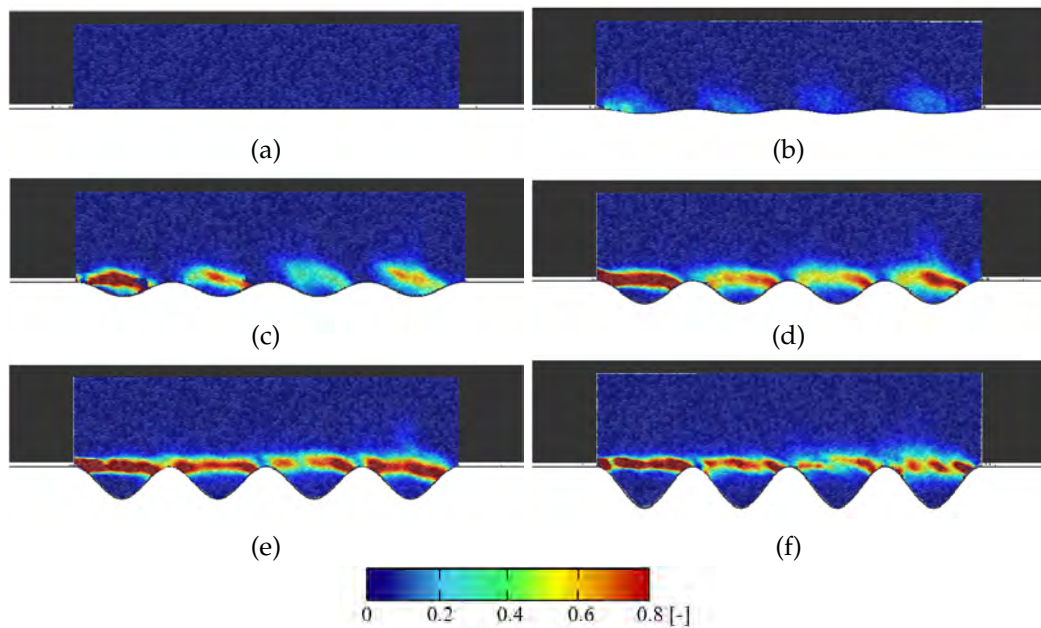


Figure 4.82: Distribution of the shear strain  $\varepsilon_{xy}$  in sand specimen at the final state of the test ( $u/L=0.1$ ) obtained with DIC analysis for different corrugation coefficient  $d/l$ : a)  $d/l=0.000$ , b)  $d/l=0.053$ , c)  $d/l=0.147$ , d)  $d/l=0.240$ , e)  $d/l=0.333$  and f)  $d/l=0.427$  ( $e_0=0.63$  and  $\sigma_n=48$  kPa).

opposite signs (Figure 4.83A) and the large vertical strain concentrated at the top of the peaks (Figure 4.83B), were captured in the numerical analysis. The real shape and location of the shear zone was also accurately captured for the deep interface ( $d/l=0.333$ ). Laboratory analysis showed that although the material was globally

sheared in one direction due to the movement of the upper shear box, local deformation within the shear zone occurred in both directions (Figure 4.84A). In comparison to the experiments, it can be seen that in both numerical and laboratory analysis the shear zone was located approximately slightly below or at the corrugation peak (Figure 4.84BC). There were slight differences in the shape of the interface localization. Those obtained numerically were more uniform compared to those obtained experimentally. Moreover, the latter consisted of smaller shear zones. Additionally, the thickness of the shear zone  $t_s$  was analyzed. In all studied cases, the shear zone thickness was approximately  $t_s=3.2$  mm ( $4\text{-}5\times d_{50}$ ), which was in good agreement with the experimental study (see Appendix A).

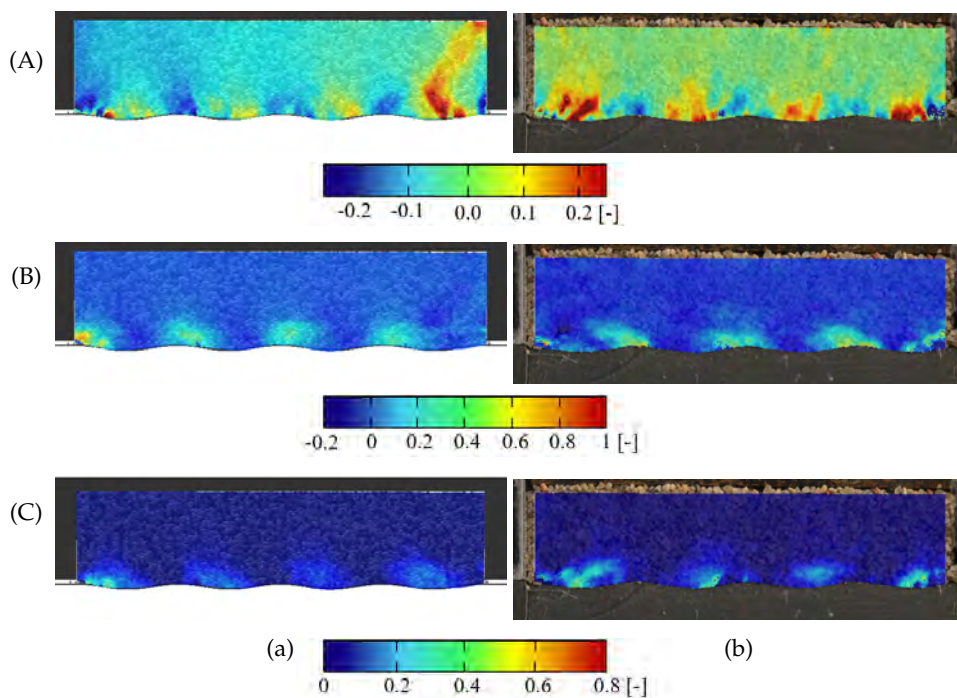


Figure 4.83: Distribution of the: A) horizontal strain  $\varepsilon_{xx}$ , B) vertical strain  $\varepsilon_{yy}$  and C) shear strain  $\varepsilon_{xy}$  in sand specimen at the final state of the test ( $u/L=0.1$ ) obtained with DIC method in: a) discrete analysis and b) experiments (Appendix A, Grabowski et al. (2023)) for the surface with corrugation coefficient  $d/l=0.053$  ( $e_0=0.63$  and  $\sigma_n=48$  kPa).

Next, the grain-on-grain component and grain-on-surface friction component were studied based on the distribution of shear strain  $\varepsilon_{xy}$  at the final state of the test for surfaces with  $d/l \geq 0.147$ . The remaining surfaces ( $d/l=0.000$  and  $d/l=0.053$ ) were not analyzed because negligible shear strain occurred in these cases, and it was assumed that in these instances, the sand slipped on the surface without forming pronounced shear zone. The analyzed area of the images was limited to the internal waves within a region of 45 mm in length to minimize the boundary effects of the shear frames (Figure 4.85). In each of the studied case, the localization zone was clearly visible, allowing for the approximate determination of the wall contact factor  $a_w$  components  $b_i$  and  $b_w$  according to EN 1991-4 (2006). Based on the figures, it can be seen that with the increase of the corrugation coefficient  $d/l$ , the area of the interface subjected to the grain-on-grain friction increased and was equal  $b_i=30.5$  mm for  $d/l=0.147$ ,  $b_i=35.9$  mm for  $d/l=0.240$ ,  $b_i=40.2$  mm for  $d/l=0.333$  and  $b_i=40.5$

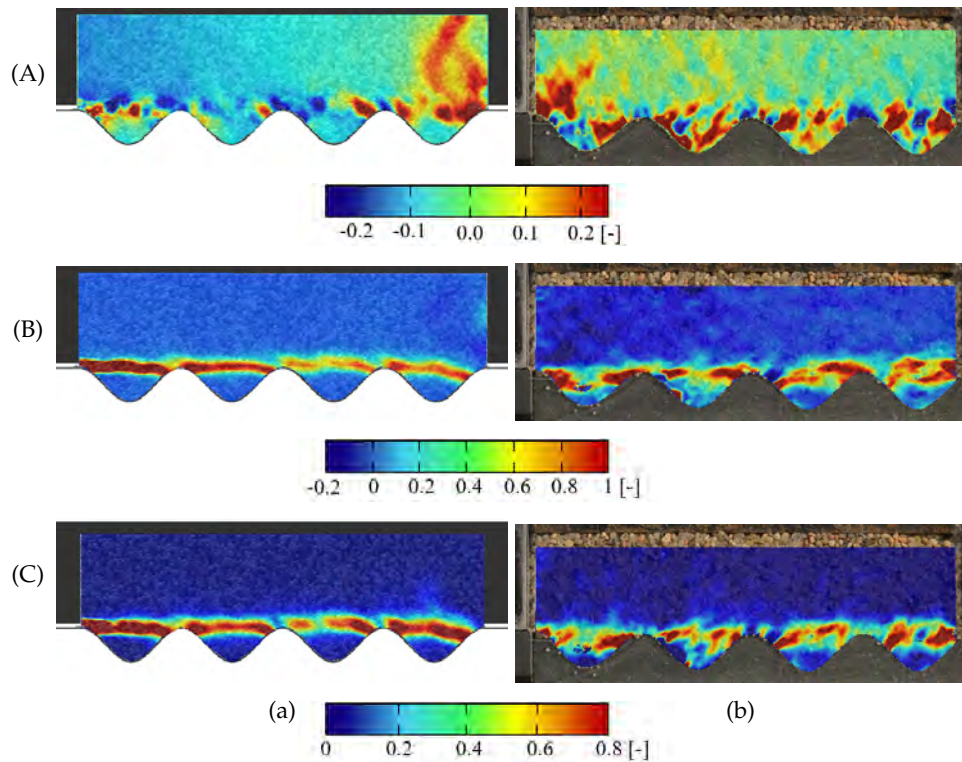


Figure 4.84: Distribution of the: A) horizontal strain  $\varepsilon_{xx}$ , B) vertical strain  $\varepsilon_{yy}$  and C) shear strain  $\varepsilon_{xy}$  in sand specimen at the final state of the test ( $u/L=0.1$ ) obtained with DIC method in: a) discrete analysis and b) in experiments (Appendix A, Grabowski et al. (2023)) for the surface with corrugation coefficient  $d/l=0.333$  ( $e_0=0.63$  and  $\sigma_n=48$  kPa).

mm for  $d/l=0.427$ . On the contrary, the area of the interface subjected to the grain-on-surface friction diminished with the increase of the  $d/l$  and the  $b_w$  component was equal 14.5 mm for  $d/l=0.147$ , 9.1 mm for  $d/l=0.240$ , 4.7 mm for  $d/l=0.333$  and 4.5 mm for  $d/l=0.427$ . As a result, the magnitudes of  $a_w$  calculated based on the visual measurement of the distribution of the shear strain  $\varepsilon_{xy}$  at the residual state were lower than those calculated using Equation 4.7 (Figure 4.70). The range of  $a_w$  calculated with the DIC method in DEM simulations was slightly lower than in experiments (Table 4.9).

Table 4.9: Comparison between experimental and numerical values of the wall contact factor  $a_w$  in the residual state calculated with the Equation 1.7 and with the DIC technique.

| corrugation<br>coefficient $d/l$ | wall contact factor $a_w$ [-] |       |       |       |
|----------------------------------|-------------------------------|-------|-------|-------|
|                                  | Equation 1.7                  |       | DIC   |       |
|                                  | DEM                           | LAB.  | DEM   | LAB.  |
| 0.147                            | 0.603                         | 0.477 | 0.322 | 0.333 |
| 0.240                            | 0.410                         | 0.369 | 0.202 | 0.238 |
| 0.333                            | 0.358                         | 0.324 | 0.104 | 0.227 |
| 0.427                            | 0.349                         | 0.287 | 0.100 | 0.133 |

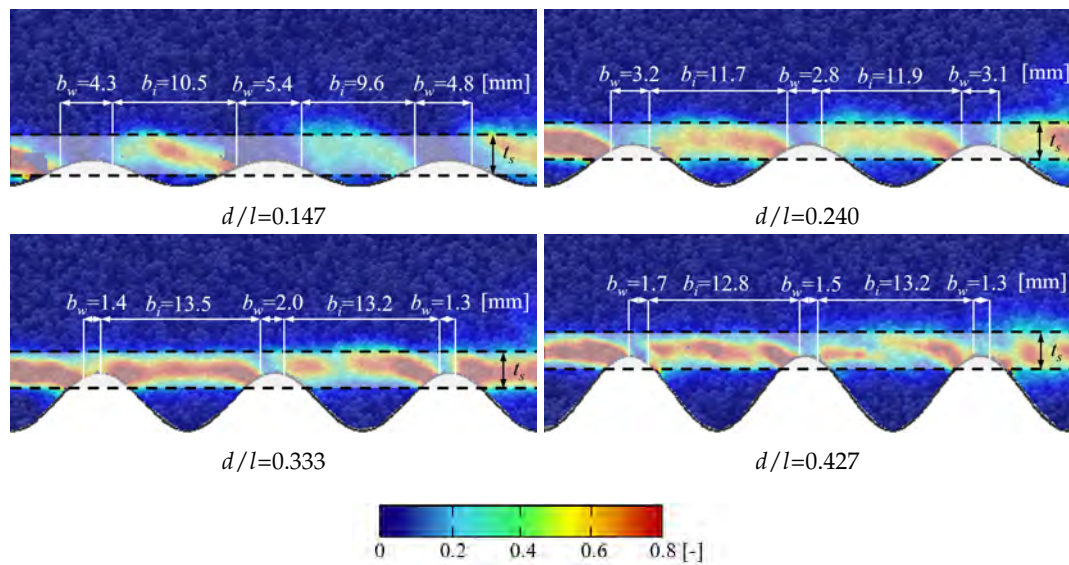


Figure 4.85: Highlight of the shear zone based on shear strain  $\varepsilon_{xy}$  distribution at the final state ( $u/L=0.1$ ) obtained with discrete analysis for different corrugation coefficient  $d/l$ .

### Evolution of the interface shear zone

Up to now, previous sections have focused on studying the effect of corrugation depth on the mesostructural behavior of the sand-surface interface. The cumulative results at the final shear state for various corrugated surfaces were presented. This section focuses on the evolution of the interface shear zone during the laboratory test with the strain fields obtained within the granular material. The DIC analysis was conducted at different stages of the tests, from the initial step ( $u/L=0$ ) up to the final state of the test ( $u/L=0.1$ ) with an incremental step of  $du/L=0.02$ . Two tests with different profiles were chosen to study the shear zone evolution: shallow interface with  $d/l=0.053$  and deep interface with  $d/l=0.333$ . They were chosen because of their different behavior as shown in the previous section.

At the beginning, the evolution of the shear zone in the interface between sand and shallow surface was analyzed. The distribution of horizontal  $\varepsilon_{xx}$ , vertical  $\varepsilon_{yy}$ , and shear strains  $\varepsilon_{xy}$  at consecutive stages of the test is presented in the following figures (Figures 4.86-4.88). In the initial phase of the test, the deformation of the sand near the surface was barely visible by means of the calculated strains (e.g. Figure 4.87a-c). As the shearing proceeded, some minor deformations were started to be visible directly at the surface ( $u/L \geq 0.6$ ). At the top of the corrugations, during the test the sand moved towards the surface. This caused minor local dilation of the sand observed also on the volumetric changes curve (Figure 4.74a). In contrast, in the valleys, the granular material moved in the upper direction, causing local compaction of the sand (Figure 4.87d-f).

Next, the evolution of the shear localization for the surface with  $d/l=0.333$  (Figures 4.89-4.91) was examined. The strain fields show that the initiation points of the shear zone were localized near the boundaries of the shear frame (Figure 4.90c and Figure 4.91c). As shearing progressed, the shear zone began to occur along the

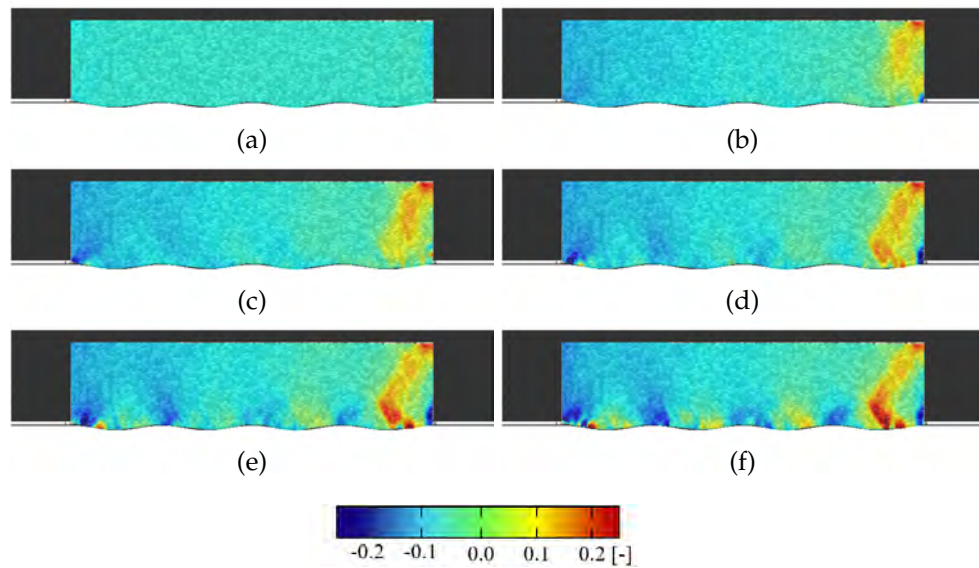


Figure 4.86: Distribution of the horizontal strain  $\epsilon_{xx}$  for: a)  $u/L=0$ , b)  $u/L=0.02$ , c)  $u/L=0.04$ , d)  $u/L=0.06$ , e)  $u/L=0.08$ , and f)  $u/L=0.1$  obtained with DIC analysis for corrugation coefficient  $d/l=0.053$  ( $e_0=0.63$  and  $\sigma_n=48$  kPa).

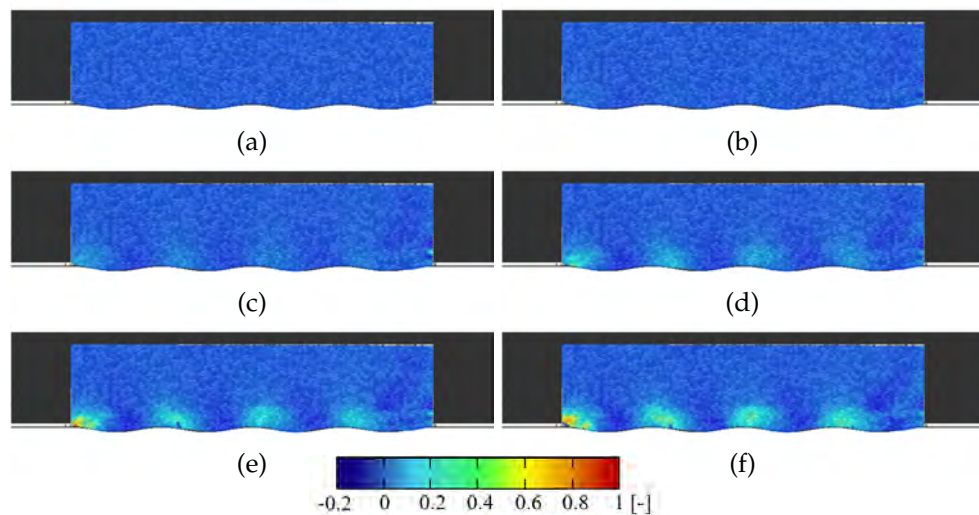


Figure 4.87: Distribution of the vertical strain  $\epsilon_{yy}$  for: a)  $u/L=0$ , b)  $u/L=0.02$ , c)  $u/L=0.04$ , d)  $u/L=0.06$ , e)  $u/L=0.08$ , and f)  $u/L=0.1$  obtained with DIC analysis for corrugation coefficient  $d/l=0.053$  ( $e_0=0.63$  and  $\sigma_n=48$  kPa).

entire length of the contact zone between the surface and the sand (Figure 4.90d-f). The shear zone was composed of smaller zones that formed between the hills of the surface. Interesting mechanism was observed within the horizontal strains  $\epsilon_{xx}$  distribution. The localization zone comprised successive regions exhibiting strains of opposite sign, with alternating patterns of contraction and expansion observed throughout the shear zone. Similar behavior was observed in the laboratory tests (see Appendix A).

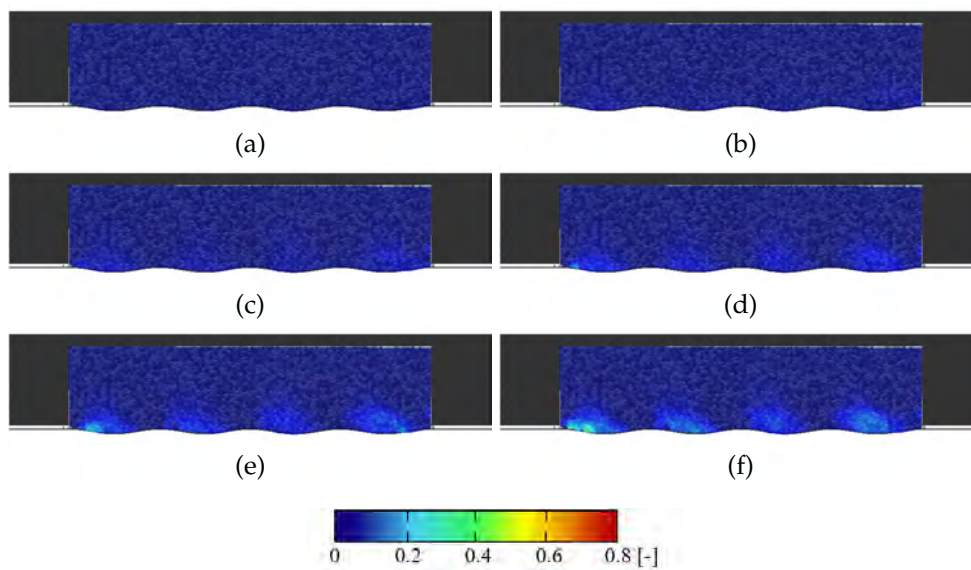


Figure 4.88: Distribution of the shear strain  $\varepsilon_{xy}$  for: a)  $u/L=0$ , b)  $u/L=0.02$ , c)  $u/L=0.04$ , d)  $u/L=0.06$ , e)  $u/L=0.08$ , and f)  $u/L=0.1$  obtained with DIC analysis for corrugation coefficient  $d/l=0.053$  ( $e_0=0.63$  and  $\sigma_n=48$  kPa).

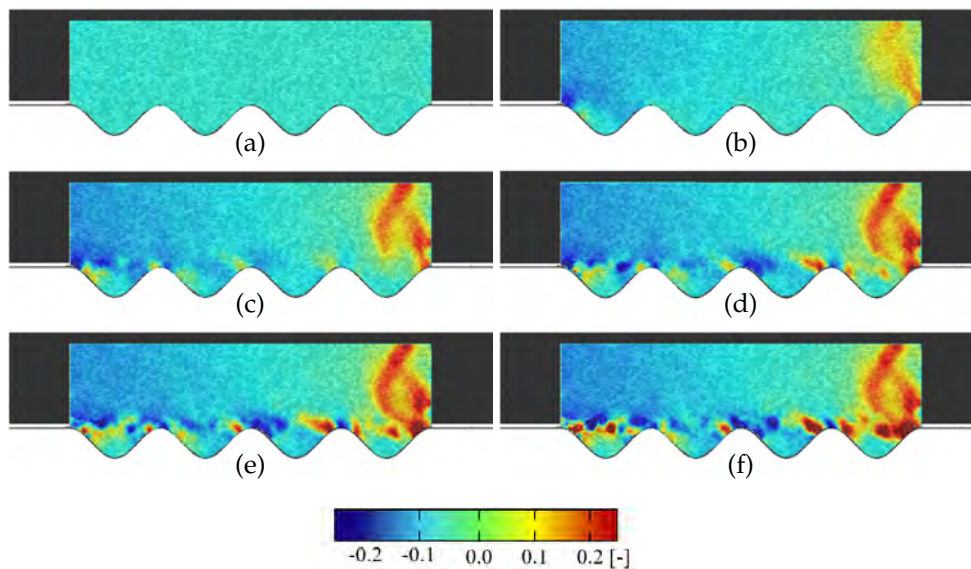


Figure 4.89: Distribution of the horizontal strain  $\varepsilon_{xx}$  for: a)  $u/L=0$ , b)  $u/L=0.02$ , c)  $u/L=0.04$ , d)  $u/L=0.06$ , e)  $u/L=0.08$ , and f)  $u/L=0.1$  obtained with DIC analysis for corrugation coefficient  $d/l=0.333$  ( $e_0=0.63$  and  $\sigma_n=48$  kPa).

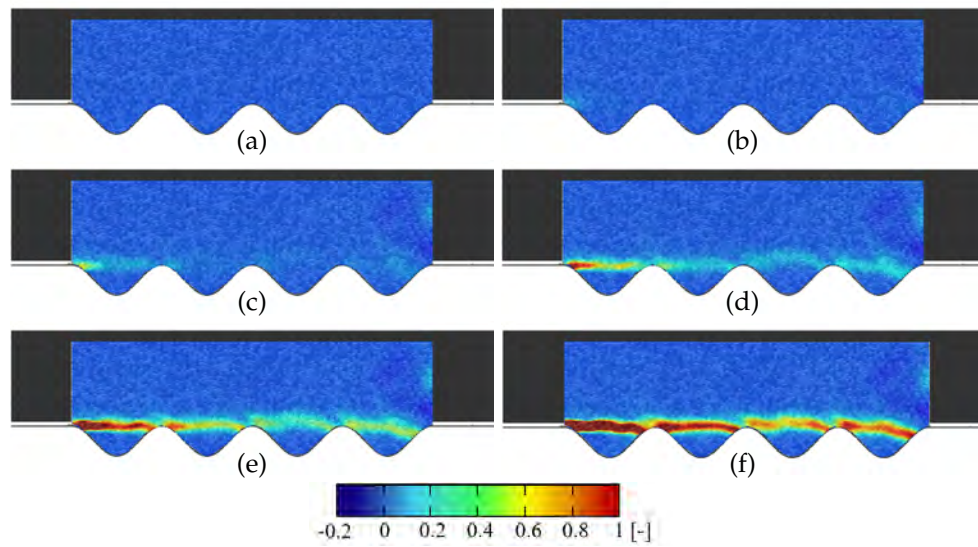


Figure 4.90: Distribution of the vertical strain  $\varepsilon_{yy}$  for: a)  $u/L=0$ , b)  $u/L=0.02$ , c)  $u/L=0.04$ , d)  $u/L=0.06$ , e)  $u/L=0.08$ , and f)  $u/L=0.1$  obtained with DIC analysis for corrugation coefficient  $d/l=0.333$  ( $e_0=0.63$  and  $\sigma_n=48$  kPa).

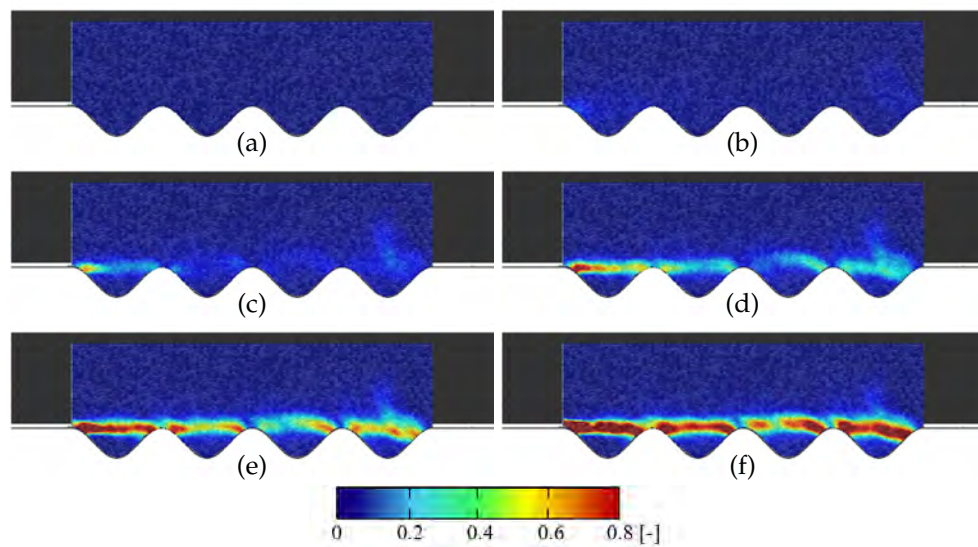


Figure 4.91: Distribution of the shear strain  $\varepsilon_{xy}$  for: a)  $u/L=0$ , b)  $u/L=0.02$ , c)  $u/L=0.04$ , d)  $u/L=0.06$ , e)  $u/L=0.08$ , and f)  $u/L=0.1$  obtained with DIC analysis for corrugation coefficient  $d/l=0.333$  ( $e_0=0.63$  and  $\sigma_n=48$  kPa).

#### 4.4.4 Summary

In the section, the influence of the surface geometry on the behavior of the contact zone between the sand and sinusoidal corrugated surfaces was studied. The following conclusions were drawn from the investigation:

- The geometry of the sinusoidal corrugated surface had a large influence on the effective friction coefficient  $\mu_{eff}$  and the shear behavior of the sand. Both, the coefficient and the volumetric changes increased as the corrugation coefficient  $d/l$  of the surface increased. In the case of surfaces, which were considered as deep, sand initially exhibited hardening, related to contractancy and later to dilatancy, in contrast to shallow surfaces, where granular material showed only contraction throughout the test.
- The wall contact factor  $a_w$  was significantly influenced by the geometry of the surface and grew with the decrease of corrugation coefficient  $d/l$ . For the peak value of effective friction coefficient  $a_w$  was in the range between  $a_w=1.0$  ( $d/l=0.000$ ) and  $a_w=0.1387$  ( $d/l=0.427$ ). For the residual value of effective friction coefficient  $a_w$  was in the range between  $a_w=1.0$  ( $d/l=0.000$ ) and  $a_w=0.3488$  ( $d/l=0.427$ ). The values of  $a_w$  obtained from discrete element method correspond well with the experimental results. The  $a_w=0.2$  recommended by EN 1991-4 (2006) results in pressure levels with a safety margin for the typical corrugated profiles.
- The mesoscopic behavior allowed the study of the wall contact factor  $a_w$  for deep interfaces, which was estimated from the shear strain distribution  $e_{xy}$ . Contrary to the value recommended by EN 1991-4 (2006),  $a_w$  was not constant. However, this method of determining  $a_w$  provides qualitative rather than quantitative results, as these values differ from those determined using the equation.
- The Discrete Element Method provided valuable insights into the mesoscopic behavior of the sand-corrugated surface interface. The geometry of the corrugation had a significant influence on the formation of the interface contact zone. For the shallow surfaces, instead of the shear zone, slipping occurred directly at the surface. In this case, the shear resistance mostly depended on the grain-on-surface friction. On the other hand, for the deep surfaces, the shear plane occurred above the valleys within the material and at the peaks of the corrugation. In this case, the shear resistance was related to both the grain-on-grain and grain-on-surface friction angles.



## Chapter 5

# Modeling of granular flow in laboratory-scale silo with DEM

### 5.1 Introduction

This chapter presents the numerical results for the confined flow of cohesionless sand in a model silo with parallel walls using Discrete Element Method. Two types of flows have been studied. In the first part of the chapter, calculations of the quasi-static granular flow are shown. In the second part, simulations of confined gravitational flow are presented. The investigation focused on quantifying the effect of wall roughness on the flow mechanism, with particular attention to the formation of shear zones. These zones should be considered during silo discharge as they are an inherent property of all deforming granular materials and may indicate complex flow patterns and affect the wall pressure distribution (Michalowski, 1984; Wójcik and Tejchman, 2009; Tejchman, 2013).

There are many experimental and numerical analyses of granular flow in silos in the literature. First of all, the initiation and development of shear zones have been studied in numerous laboratory experiments (Cutress and Pulfer, 1967; Nedderman and Laohakul, 1980; Michalowski, 1987; Tejchman, 1989; Niedostatkiewicz et al., 2011; Grudzien et al., 2012), which were mostly performed in laboratory-scale silos. The mechanism of strain localization was studied mainly on the basis of the description of the deformation of the granular material during the flow. The formation of localized zones has been imaged with colored layers of granular material (Takahashi and Yanai, 1973; Stazhevskii, 1982; Tejchman, 1989), X-rays (Cutress and Pulfer, 1967; Michalowski, 1984; Michalowski, 1987; Michalowski, 1990; Drescher, 1992; Drescher, 1998), electrical capacitance tomography (ECT) (Grudzien et al., 2012), and particle image velocimetry (PIV) (Slominski et al., 2007). These studies have provided valuable insights into the formation and evolution of the shear zones, including information on their thickness, location and orientation.

In the past, the confined granular flow in silos were also reasonably described by continuum methods, in particular using FEM. Various constitutive models were used to analyze the mechanism of granular material deformation, such as elastoplastic (Lade, 1977; Desrues and Chambon, 1989; Vardoulakis et al., 1992) and hypoplastic models (Mühlhaus, 1990; Tejchman and Wu, 1995; Bauer, 1996). These models have the ability to analyze various aspects of granular flow mechanics, such as flow patterns, shear zone formation and the determination of pressures exerted



on the silo structure. These methods take into account important features of granular media, such as incremental nonlinearity, dependence on pressure level, density and direction of strain rate (Tejchman, 2013). In the case of granular flows, where bulk solid undergoes large deformations, the models have been extended by a characteristic length of the microstructure to properly capture the properties of the shear localization (Tejchman, 2004; Wójcik and Tejchman, 2009; Krzyżanowski et al., 2021).

Although both experimental and continuum approaches have provided important information on the formation of the shear zone during granular flow, these methods have their weaknesses. They are usually unable to provide insight into the mesoscopic properties of granular materials, limiting the fundamental understanding and application of the results due to the lack of grain-level information. This limitation can be overcome by numerical simulations performed with discrete or meshless methods, such as DEM (González-Montellano et al., 2011; Gallego et al., 2019), MPM (Więckowski, 2004; Krzyżanowski et al., 2021; Krzyżanowski et al., 2021), and Cellular Automaton (Tejchman, 2013). These methods can simulate large deformations of granular media, providing insights into the particle-level features of granular flow. Among these, DEM allows the behavior of granular materials to be mimicked by assuming the local contact properties of individual grains. While this approach has been widely used to study shear zone formation in various soil mechanics problems (Iwashita and Oda, 1998; Oda and Iwashita, 2000; Zhang and Thornton, 2007; Kozicki et al., 2013; Nitka et al., 2015; Liu et al., 2019; Leśniewska et al., 2020), a comprehensive study of these zones during granular flow in a silo using DEM has not yet been performed.

As shown earlier, the discrete model is capable of modeling the behavior of sand during selected soil mechanics laboratory tests by taking into account both internal and interface shear zones. The objective of this study is to present the ability of the DEM to study the formation of the shear localization in a cohesionless sand during confined flow under various boundary conditions. During the numerical investigation, several quasi-static granular flows were performed using different roughness of silo walls and different initial densities of sand. In addition, in the case of the gravitational flow the effect of three types of outlets, i.e. symmetric outlet and two asymmetric outlets of different width on flow mechanism was investigated. In both cases, the emphasis was on the formation and evolution of both internal and wall shear zones during sand flow.

Some of the results presented in this chapter are already covered in the paper published in the *Computers and Geotechnics* journal (Grabowski et al., 2021b).

## 5.2 Numerical model and methodology

Similarly, as in the simulations of the preliminary soil mechanics tests, the 'Karlsruhe' sand was used (the parameters of 'Karlsruhe' sand were given in Table 4.2 Chapter 4.1). To calibrate granular material for the discrete simulations of laboratory scale silo flow the procedure based on triaxial compression test described in Chapter 4.1 was used. Although, there exist comprehensive analysis of the triaxial compression laboratory test for 'Karlsruhe' sand of different initial void ratio in the range of high and medium pressures of 50–1000 kPa (Kolymbas and Wu, 1990; Wu, 1992), in



the range of low mean pressures of e.g. 5 kPa or lower that dominate in a prefilled model silo of a height of 0.5 m, the laboratory triaxial compression test results are lacking. Therefore, the calibration tests were performed with initially dense sand (initial void ratio  $e_0=0.60$ ) and initially loose sand (initial void ratio  $e_0=0.80$ ) for the lateral pressure of  $\sigma_0=5$  kPa (equivalent to the mean pressure in a pre-filled model silo) with the parameters listed in Table 5.1. Compared to the parameters used in the soil mechanics test, the repeated calibration resulted in a significantly lower value of the local modulus of elasticity  $E_c$  ( $E_c=10$  MPa instead of  $E_c=300$  MPa), a lower value of the rolling stiffness coefficient  $\beta$  ( $\beta=0.2$  instead of  $\beta=0.7$ ), and a higher value of the interparticle friction angle  $\mu_c$  ( $\mu_c=25^\circ$  instead of  $\mu=18^\circ$ ). The values of the shear/normal stiffness ratio  $v_c$  and the limit rolling coefficient  $\eta$  were the same as those used in the previous simulations. The wall friction angle between the particles and the flat wall was assumed to be  $\mu_w=18^\circ$ .

Table 5.1: Discrete material parameters for the quasi-static silo flow.

| Parameter                             | Value      |
|---------------------------------------|------------|
| interparticle friction angle $\mu_c$  | $25^\circ$ |
| local modulus of elasticity $E_c$     | 10 MPa     |
| shear/normal stiffness ratio $v_c$    | 0.3        |
| limit rolling coefficient $\eta$      | 0.4        |
| rolling stiffness coefficient $\beta$ | 0.2        |

A satisfactory qualitative agreement with typical triaxial compression test results was obtained for both initially dense and initially loose sand specimens. The first specimen exhibited hardening, initially characterized by low contraction, followed later by softening due to the dilatancy of the material (Figure 5.1a). The second sample was characterized by continuous hardening related to the continuous contractancy 5.1b). Based on the macroscopic response the following variables of the initially dense sand specimen were calculated: the dilatancy angle  $\psi=40^\circ$ , contractancy angle  $\psi=-15^\circ$ , the global elastic modulus  $E=3.0$  MPa. The global elastic modulus was approximately equal to the value by the Terzaghi formula for oedometric unloading  $E=(1+e_0)p/C_s \approx 3$  MPa (with the mean silo pressure  $p=5$  kPa and the swelling index  $C_s=0.003$ , Tejchman (2013)). The global peak mobilized internal friction angle was  $\phi_{i,max} = 47.5^\circ$  for the normal strain of  $\varepsilon_1=4\%$  and the residual peak internal friction angle was  $\phi_{i,res}=35^\circ$  for  $\varepsilon_1=30\%$ .

The geometry of the laboratory-scale silo used in the discrete analysis is shown in Figure 5.2. The silo had a height  $h_s=0.5$  m, a width  $b_s=0.2$  m, and a depth  $d_s=0.0075$  m (equal to  $5 \times d_{50}$ ). The depth of the silo was reduced by a factor of 80 compared to the experimental setup of Tejchman (1989). The effect of reducing the granular sample depth on the results was found to be negligible, as demonstrated in the DEM simulations of the direct shear test presented in Chapter 4.2. However, compared to the simulations of direct and interface shear tests, the depth was reduced once again by a factor of 2, making the discrete model a quasi-3D representation. It should be noted that this approach influenced the results, causing fluctuations in the forces acting on the silo structure. In the numerical analysis, the silo walls were considered as non-deformable rigid structures, in agreement with the experimental conditions.

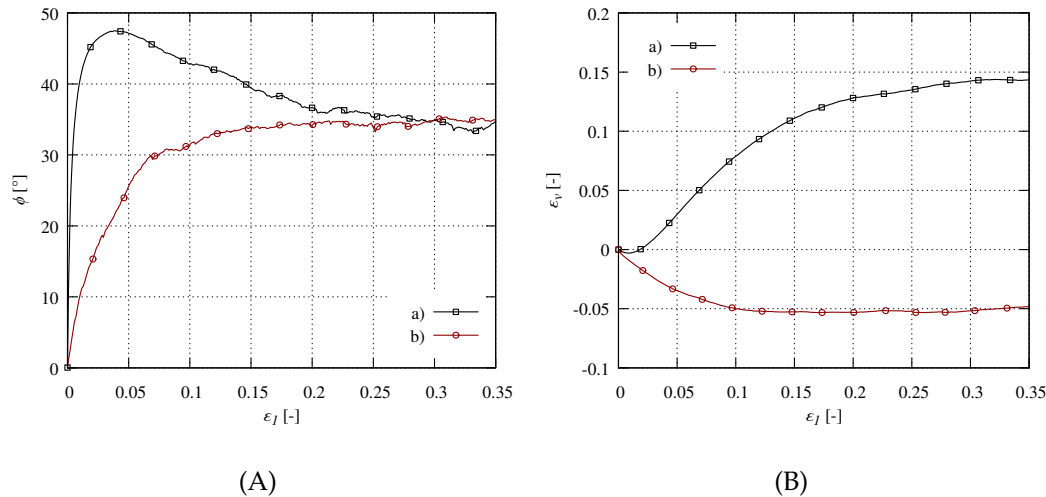


Figure 5.1: Triaxial compression test results of a: A) mobilized internal friction angle  $\phi_i$  and B) volumetric strain  $\epsilon_v$  versus vertical normal strain  $\epsilon_1$  for sand specimens composed of spheres with rotational resistance for two different initial void ratios of sand: a)  $e_0=0.60$  and b)  $e_0=0.80$  ( $\sigma_0=5$  kPa and  $d_{50}=5.0$  mm) (Grabowski et al., 2021b).

During the preparation phase, the silo was filled with sand composed of approximately 200 000 spherical particles with rotational resistance. The packing was done progressively by distributed gravitational filling using 6 layers of sand. Each upper layer of granular material was added after the kinetic energy of the particles in the silo decreased to a negligible level. The mean grain diameter of the particles was  $d_{50}=1.5$  mm, varying linearly in the range  $d_{min}=0.5$  mm and  $d_{max}=2.5$  mm. The mean grain diameter was scaled to three times the value used in the laboratory analysis by Teichman (1989), where  $d_{50}=0.5$  mm. While using the real diameter was technically possible, it would significantly increase the computational time. When the silo was completely filled with sand and the kinetic energy of the discrete material became negligible, the numerical model was ready to simulate confined granular flow. During the study, two types of flow were examined: quasi-static (Figure 5.2a) and gravitational granular flow (Figure 5.2b). In the first case, after the silo was filled, the bottom plate moved vertically, initiating quasi-static flow. In the second case, after the preparation phase, the outlet located at the bottom surface was opened inducing gravitational flow until the entire silo was empty. In both cases the upper boundary (sand surface) was left unconstrained.

In reality, the topography of the silo walls varies depending on the silo structure. In the current analysis, the side walls of the silo had artificially created roughness in the form of regularly spaced triangular grooves, similar to those used in the preliminary analysis of the interface shear test. These asperities varied in height and spacing, but had the same inclination (Figure 5.3). Similar to the preliminary calculations, the wall roughness was characterized by the non-dimensional parameter of normalized roughness  $R_n=h_g/d_{50}$ . Other types of rough surfaces used in discrete simulations have been described earlier (see Chapter 4.3).

During the analysis, several granular flow tests were conducted on different sand samples under different boundary conditions. At the beginning, the tests were performed on initially dense sand with different roughness levels of the silo side walls

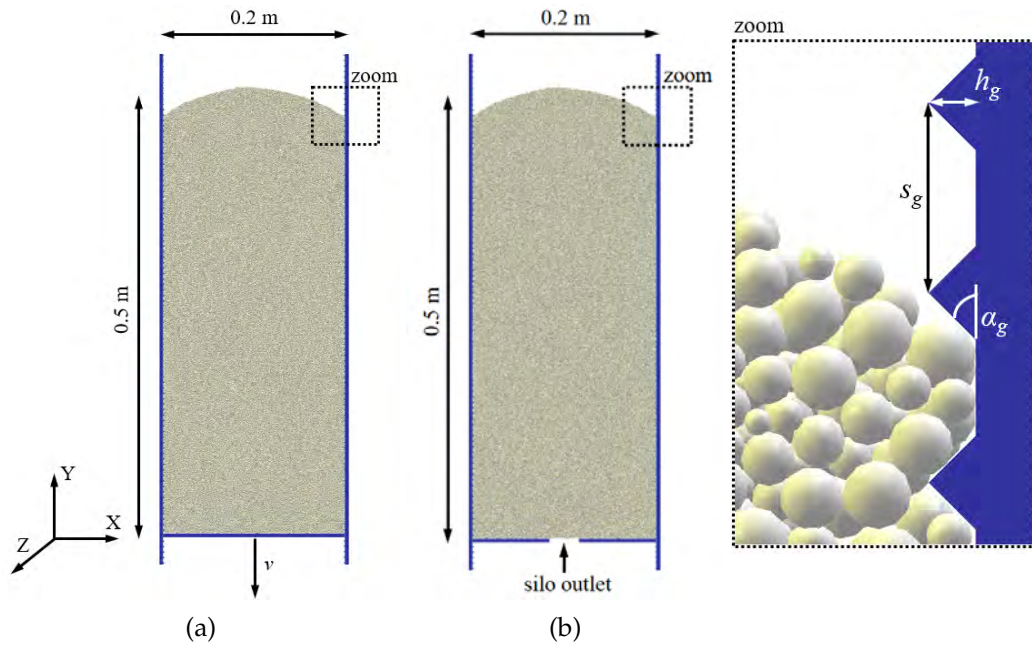


Figure 5.2: DEM model setup of silo with parallel walls (height  $h_s=0.5$  m and width  $b_s=0.2$  m) with: a) constant outlet velocity applied along entire bottom and b) bottom outlet of various width and location ( $h_g$  - groove height,  $\alpha_g$  - groove inclination and  $s_g$  - groove spacing) (Grabowski et al., 2021b).

(Figure 5.3). The slope of the grooves, denoted by  $\alpha_g$ , was set to  $\alpha_g=45^\circ$  for all cases. The distance between the asperities, denoted as  $s_g$ , was set to  $s_g=4 \times d_{50}$  for the silo with very rough walls ( $R_n=1.0$ ),  $s_g=d_{50}$  for the silo with rough walls ( $R_n=0.25$ ), and  $s_g=0.04 \times d_{50}$  for the silo with smooth walls ( $R_n=0.01$ ). Additionally, silo with wall roughness  $R_n=0.5$  was analyzed in the discrete analysis, but it showed similar results as the silo with very rough walls ( $R_n=1.0$ ). As demonstrated in the preliminary analysis and in other studies (Pincus et al., 1995; Hu and Pu, 2004; Su et al., 2018), typically, increasing the surface roughness above 0.4-0.5 leads to insignificant changes in the effective wall friction angle. The calculations of gravitational flow were performed for the walls with roughness  $R_n=1.0$  and  $R_n=0.01$  only. In the second part of the analysis, the effect of the initial porosity of the granular sample was investigated for both types of flow. The calculations were performed for the initially dense sand with void ratio  $e_0=0.60$  (as in the experiment by Teichman (1989)) and for the initially loose sample with void ratio  $e_0=0.76$  in a silo with very rough walls ( $R_n=1.0$ ). In the case of numerical simulations of silo structures, the experimental value of void ratio equal to  $e_0=0.85$  was difficult to obtain. A higher value of the void ratio could be achieved by using irregularly shaped particles instead of perfectly spherical ones, but this would result in a larger mean grain size diameter (which would make the grain level analysis of the shear localizations impossible) or significantly longer simulation time.

Finally, for gravitational flow, different cases involving different silo outlet locations and sizes were investigated. In the first case (type '1'), the outlet of width  $b=30$  mm ( $=20 \times d_{50}$ ) was located symmetrically in respect to the vertical axis of the silo (Figure 5.4a). In the second case (type '2'), the outlet of width  $b=30$  mm ( $=20 \times d_{50}$ ) was located at the right wall (Figure 5.4b). In the last case (type '3'), the outlet of width  $b=60$  mm ( $=40 \times d_{50}$ ) was also located at the right wall (Figure 5.4c).

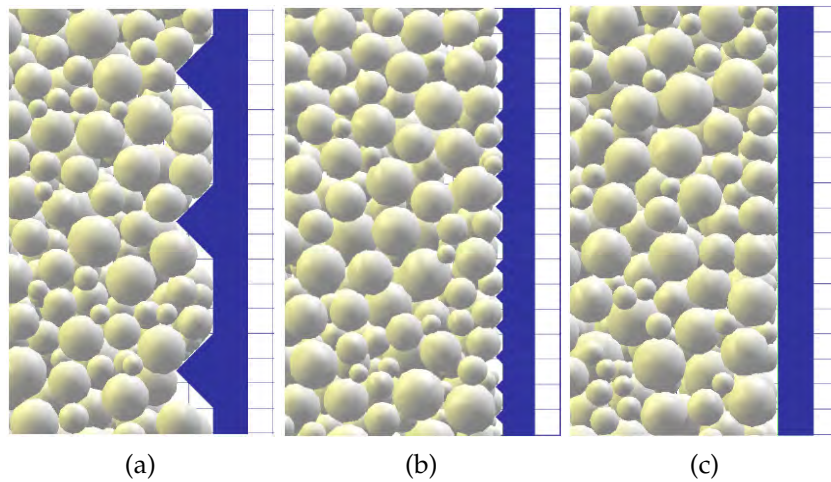


Figure 5.3: Rigid silo walls with different normalized surface roughness parameter  $R_n = h_g / d_{50}$ : a)  $R_n = 1.0$ , b)  $R_n = 0.25$  and c)  $R_n = 0.01$  (Grabowski et al., 2021b).

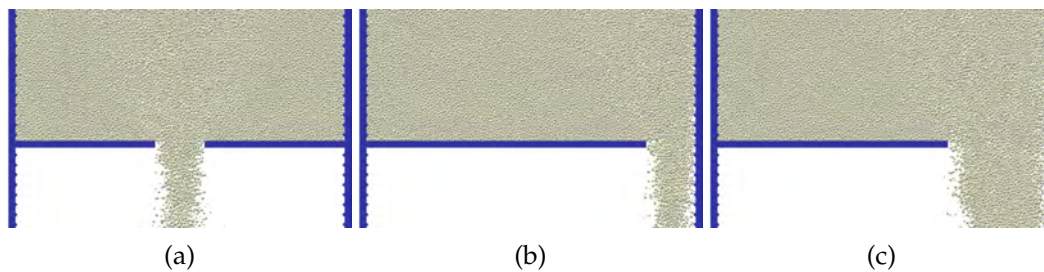


Figure 5.4: The size and the location of silo outlets used in discrete calculations: a) type '1' - symmetric outlet with a width of  $b = 30$  mm, b) type '2' - asymmetric outlet with a width of  $b = 30$  mm, c) type '3' - asymmetric outlet with a width of  $b = 60$  mm.

## 5.3 Numerical results

### 5.3.1 Quasi-static flow in silo

In the first section, the numerical results for the confined quasi-static flow in silo with parallel walls and slowly movable bottom are presented. The main aim of the investigation was to study the internal and wall shear zones under precisely controlled constraints. During the analysis, the roughness of the walls and initial void ratio were varied. The focus was on the initiation, formation and propagation of shear zones during granular flow modeled in discrete simulations. In addition, the forces exerted on side walls and bottom plate were calculated. These results were used to calibrate and validate the numerical model based on the results comparison with the experiments by Tejchman (2013).

At the beginning, a comparison between the numerical results and the laboratory experiments of Tejchman (2013) was presented, taking into account the forces exerted on the bottom and side walls during the flow. Next, a comprehensive analysis of the influence of silo wall roughness on the flow mechanism and the mesostructural behavior of dense granular material is presented. Finally, a detailed analysis of quasi-static flow in silos filled with initially loose sand is presented.

### Evolution of forces exerted on walls

To validate the accuracy of the numerical model, the resultant forces acting on the silo walls were measured as in the experiments by Tejchman (2013). The following values were measured during the flow: the resultant vertical wall friction force  $T$ , the resultant horizontal wall force  $N$ , and the resultant vertical bottom force  $P$ . The magnitude of these forces was determined based on the interactions between the particles and the silo that occurred during each time step of the simulation. To calculate  $P$ , the vertical component of the normal force from each particle-bottom wall interaction was summed. To calculate  $T$ , the vertical components of the normal and tangential force from each particle-side wall interaction were added. Finally, to calculate  $N$ , the horizontal components of normal and tangential force from each particle-side wall interaction were summed. Figures 5.5 and 5.6 show the calculated evolution of these forces normalized by the total sand weight  $G$ . During the test, the sum of the vertical forces exerted on both walls and the bottom of the silo was constant and equal to the total weight of the sand ( $G=2T+P$ ). These forces were related to the vertical displacement  $u$  of the bottom plate measured during the flow. First, the flow of the initially dense sample with void ratio  $e_0=0.60$  was analyzed in silos with very rough, rough and smooth walls. Then, the granular flow within the silo with very rough walls filled with initially loose sand with void ratio  $e_0=0.76$  was studied. Additionally, the evolution of the resultant mobilized wall friction angle  $\phi_w=\arctan(T/N)$  was calculated for each flow. For comparison, the experimental forces measured by Tejchman (2013) were also normalized by the sand weight.

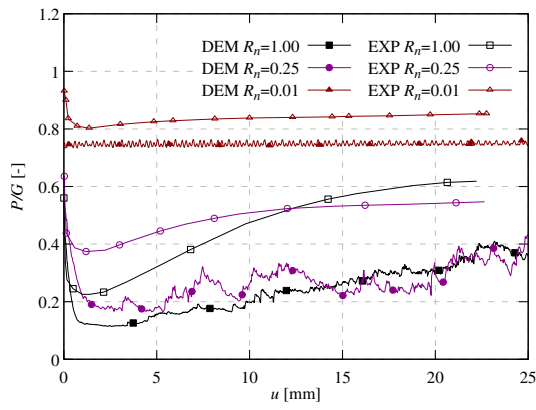
At the beginning, the values of the normalized resultant forces acting on the walls at the end of the filling between the numerical and experimental results were compared (Table 5.2). Before the discharge, the greatest differences between the numerical and laboratory outcomes regarding the  $P$ ,  $T$ , and  $N$  forces were observed for the silo with smooth walls. However, in this case the mobilized wall friction angle  $\phi_w$  was almost the same as in the experiment (the value of  $18^\circ$  was imposed to the walls). For the silo with very rough and rough walls, some noticeable differences were observed for the resultant horizontal wall force  $N$  and the mobilized wall friction angle  $\phi_w$ . For these silos, negligible discrepancies were observed in the initial magnitude of forces  $P$  and  $T$ . It is worth noting that in the studies by Wójcik and Tejchman (2009) and Krzyżanowski et al. (2021), similar differences were observed for the resultant horizontal wall force  $N$  acting on silo walls in analyses using the FEM and MPM, respectively. The magnitude of  $N$  throughout the flow in these studies was significantly higher than in the experiments.

Then, the evolution of the resultant forces during the quasi-static flow was analyzed. As presented in Figures 5.5-5.7, a satisfactory qualitative agreement with the experimental results was obtained. While some discrepancies were observed, e.g. in the magnitude of the forces after filling or in the force changes during flow, the numerical curves showed a similar evolution to the experimental ones. The initial decrease of the vertical force  $P$  and the initial increase of the vertical force  $T$  were similar to those obtained in experimental studies. The changes of these forces during the flow became stronger with the increase of the roughness of the walls  $R_n$  (Figure 5.5a,b) and with the decrease of the initial void ratio of the sand  $e_0$  (Figure 5.6a,b). In the case of initially dense sand, the resultant forces  $P$  and  $T$  reached their minimum

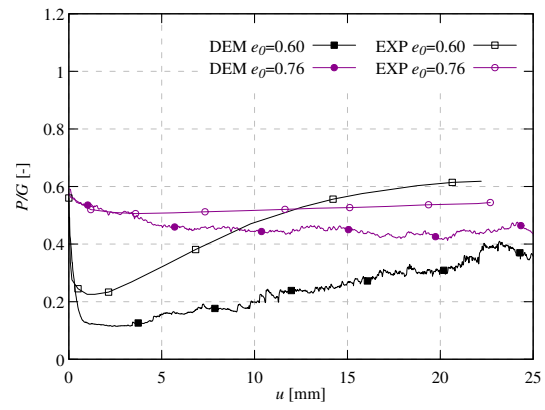
Table 5.2: Experimental (Tejchman, 2013) and numerical values of the normalized resultant vertical bottom force  $P_{min}$ , the resultant vertical wall friction force  $T$ , the resultant horizontal wall force  $N$ , and the resultant mobilized wall friction angle  $\phi_w$  for initially dense sand during flow.

| Normalized force | Very rough walls |      | Rough walls |      | Smooth walls |      |
|------------------|------------------|------|-------------|------|--------------|------|
|                  | DEM              | Exp. | DEM         | Exp. | DEM          | Exp. |
| $P/G$ [-]        | 0.50             | 0.56 | 0.56        | 0.64 | 0.75         | 0.95 |
| $T/G$ [-]        | 0.25             | 0.25 | 0.22        | 0.20 | 0.12         | 0.06 |
| $N/G$ [-]        | 0.35             | 0.26 | 0.35        | 0.26 | 0.38         | 0.26 |
| $\phi_w$ [°]     | 36               | 42   | 30          | 35   | 18           | 17   |

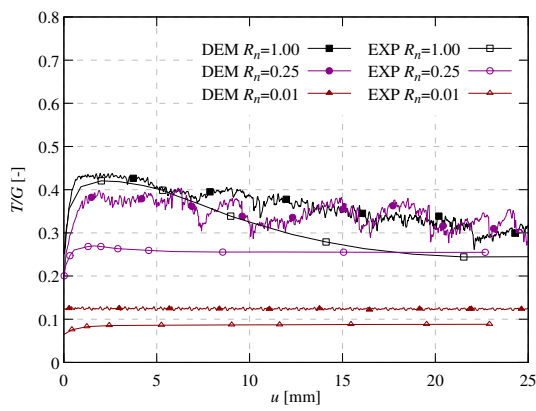
and maximum values, respectively, shortly after the start of the flow. Then, the  $P$  force increased and the  $T$  force decreased with the movement of the bottom plate in the case of the silo with very rough and rough walls (Figure 5.5a,b). At the end of the test, these forces reached an asymptote. This respective increase and decrease in the softening part of the flow was stronger for the silo filled with initially dense sand, due to the occurrence of high dilatancy. On the other hand, in the case of the silo with rough walls filled with initially loose sand the softening was weaker than for the silo with initially dense sand (Figure 5.6a,b). The resultant horizontal force acting on walls  $N$  in the case of the silo with very rough and rough walls increased as the flow progressed. The calculated maximum values of the  $N$  force obtained in the numerical analysis in the cases of the silo filled with initially dense sand were too high comparing to the experiments (Figure 5.5c). Similar discrepancies in the curves were observed in the numerical analysis using FEM (Wójcik and Tejchman, 2009) and MPM (Krzyżanowski et al., 2021) methods. In the case of the silo filled with initially dense sand, the maximum values of  $N$  were too high for all type of walls. However, the tendency of growing the  $N$  force after the start of the discharge was in agreement with the experimental results. In the case of the silo with initially loose sand, the magnitude of  $N$  was lower than in the experiments (Figure 5.6c). The overall evolution of the maximum mobilized wall friction angle  $\phi_w$  was in good accordance with experiments. In general, in the case of the  $\phi_w$ , it increased with the rise of the wall roughness and with the decrease of the initial void ratio (Figure 5.7). In case of these graphs, beside minor discrepancies observed between the initial value of the resultant wall friction angle, slight changes were observed in the case of the maximum value of the resultant wall friction angle  $\phi_{w,max}$  (Figure 5.7a). The numerical results of  $\phi_{w,max}$  for very rough wall was slightly lower ( $\phi_{w,max}=44^\circ$  versus  $\phi_{w,max}=48^\circ$ ) than the one obtained by Tejchman (2013) in the experiments. In the remaining cases the maximum value of the wall friction angle obtained with DEM was similar as in the experiments. The magnitude of residual resultant friction angle  $\phi_{w,res}$  for silo filled with initially dense sand agreed well with experimental value. On the other hand, the  $\phi_{w,res}$  for the silo filled with initially loose sample obtained in numerical analysis was slightly higher ( $\phi_{w,res}=37^\circ$  versus  $\phi_{w,res}=32^\circ$ ) than in the experiments (Figure 5.7b). In all cases an asymptote of function was reached at the end of the test. In general, the evolution of the numerical functions agreed well with the evolution of experimental functions.



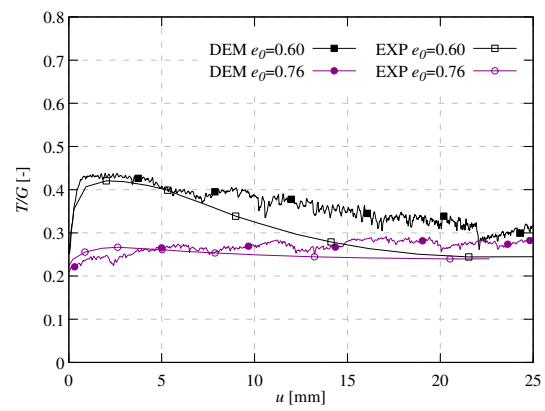
(a)



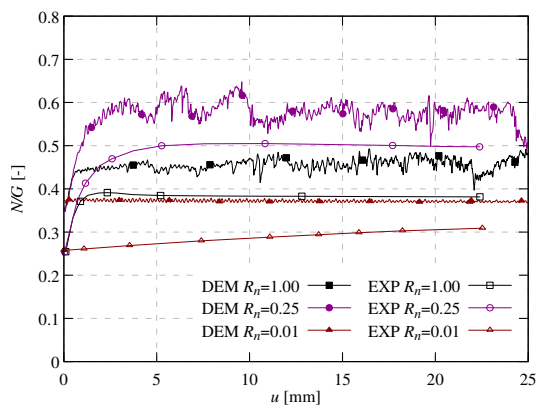
(a)



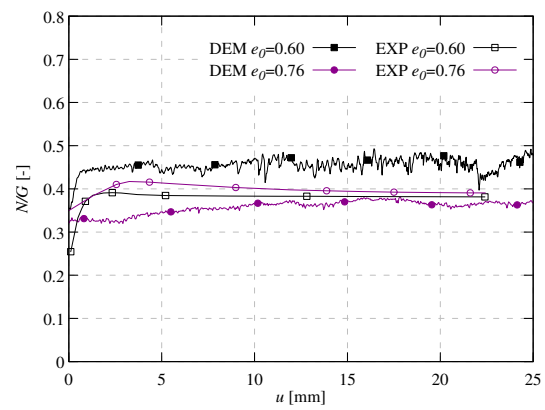
(b)



(b)



(c)



(c)

Figure 5.5: Experimental (Tejchman, 2013) (empty dots) and numerical (full dots) evolution of: a) normalized resultant bottom force  $P/G$ , b) normalized resultant wall friction force  $T/G$  and c) normalized resultant wall normal force  $N/G$  after bottom displacement  $u$  for initially dense sand ( $e_0=0.60$ ) with different normalized roughness  $R_n$  ( $G$ -sand weight).

Figure 5.6: Experimental (Tejchman, 2013) (empty dots) and numerical (full dots) evolution of: a) normalized resultant bottom force  $P/G$ , b) normalized resultant wall friction force  $T/G$  and c) normalized resultant wall normal force  $N/G$  after bottom displacement  $u$  with very rough wall for different initial void ratio  $e_0$  of the sample ( $G$ -sand weight).

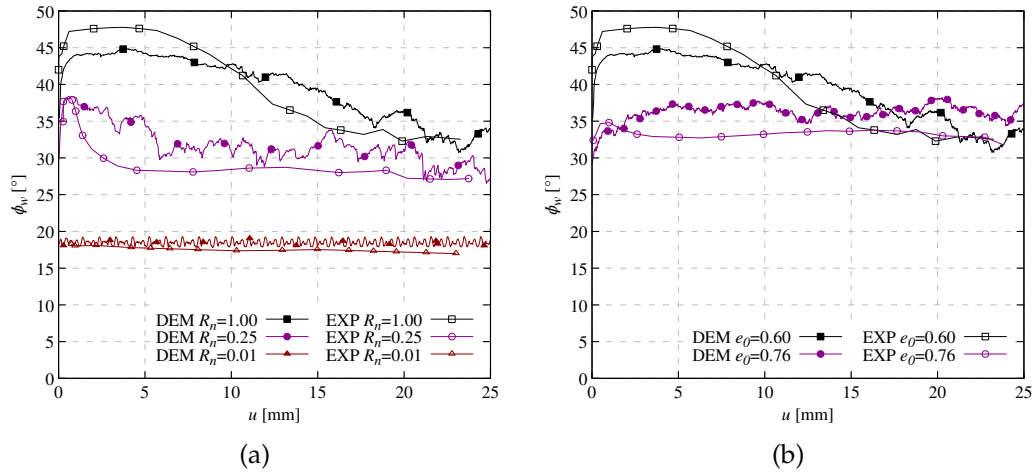


Figure 5.7: Experimental (Tejchman, 2013) (empty dots) and numerical (full dots) evolution of resultant mobilized wall friction angle  $\phi_w$  after bottom displacement  $u$  for: a) initially dense sand ( $e_0=0.60$ ) with different normalized roughness  $R_n$ , and b) very rough wall ( $R_n=1.0$ ) for different initial void ratio  $e_0$  of the sample.

Finally, the numerical and experimental results of the resultant force exerted on the bottom plate  $P$  obtained in the residual phase of the flow were compared to the theoretical silo formula by Drescher (1991) and a standard silo formula by EN 1991-4 (2006). Both of these theoretical formulas are based on the slice method by Janssen. According to this method, the force  $P$  was calculated as:

$$P = \bar{\sigma}_z b_s d_s = \frac{\gamma b_s}{K \tan \phi_w} (1 - e^{-\frac{K \tan \phi_w}{b_s} h_s}) b_s d_s \quad (5.1)$$

where  $\bar{\sigma}_z$  is the mean vertical normal stress,  $b_s$  is the width of the silo (in this case  $b_s = 0.2$  m),  $d_s$  is the silo depth (in this case  $d_s = 0.6$  m),  $\gamma$  is the volumetric weight of sand,  $K$  is the lateral pressure coefficient of bulk solid calculated as  $K = \sigma_n / \bar{\sigma}_z$  (where  $\sigma_n$  is the horizontal wall pressure) and  $h_s$  is the silo height (in this case  $h_s = 0.5$  m). The lateral pressure ratio  $K$  was calculated with formula:

$$K = \frac{\sin \phi_i \sin [\arcsin \frac{\sin \phi_w}{\sin \phi_i} + \phi_w]}{1 - \sin \phi_i \cos [\arcsin \frac{\sin \phi_w}{\sin \phi_i} + \phi_w]} / \tan \phi_w \quad (5.2)$$

where  $\phi_i$  is the effective internal friction angle, which was equal  $\phi_i = 35^\circ$ . The following experimental wall friction angles in the residual phase were used to calculate the lateral pressure coefficient  $K$ :  $32^\circ$  for the very rough walls,  $27^\circ$  for the rough walls and  $17^\circ$  for the smooth walls. The corresponding values of  $K$  were obtained for each type of silo walls filled with initially dense sand:  $K=0.83$  for the silo with very rough walls,  $K=1.21$  for the silo with rough walls, and  $K=1.73$  for the silo with smooth walls. The bulk density of  $\gamma = 16$  kN/m<sup>3</sup> was assumed. In the calculations using EN 1991-4 2006 approach the lateral pressure ratio was calculated as  $K = 0.45 \times 1.4 = 0.63$ . The residual wall friction coefficients, calculated as  $\mu_{eff} = \tan \phi_w$ , were assumed  $\mu_{eff} = 0.31$  for smooth walls,  $\mu_{eff} = 0.51$  for rough walls, and  $\mu_{eff} = 0.62$  for very rough walls. Experimental values of force  $P$  were obtained from laboratory tests by Tejchman (2013) for silos with smooth ( $P = 760$

N), rough ( $P = 480$  N), and very rough walls ( $P = 530$  N). From the discrete calculations performed in this chapter, the value of  $P$  was found to be  $P = 650$  N for silo with smooth walls,  $P = 370$  N for silo with rough walls, and  $P = 320$  N for silo with very rough walls.

Table 5.3 presents a comparison between the resultant bottom force  $P$  at the residual state obtained using experimental, numerical and theoretical approaches. Major differences were observed between the outcomes obtained with different methods. Primarily, significant differences occurred between the values calculated with the Drescher formula and the numerical ones, particularly in the case of rough and very rough walls. These discrepancies occurred mainly due to the greater mean grain diameter  $d_{50}$  used in the DEM simulations. From Figure 5.5 it can be deduced that the asymptotic limit of the normal bottom force  $P$  was not reached after displacement of  $u=30$  mm. Using real size of particles ( $d_{50}=0.5$  mm instead of  $d_{50}=1.5$  mm) would lead to an increase of the dilatancy angle, resulting in a higher magnitude of  $P$  calculated in the residual phase. Significant differences were also observed between the numerical values and the ones calculated according to EN 1991-4 2006 approach, particularly in the case of the silo with rough and very rough walls. On the other hand, very good agreement was obtained for the silo with smooth walls. The experimental results were in good agreement with the both theoretical approaches in the case of the silo with rough and very rough walls. Contrary, for smooth walls, a normal bottom force  $P$  captured within experiments was significantly higher than in any other approach. In general, the differences between theoretical approaches and experimental and numerical analyses are due to the fact that theoretical formulas do not take into account the real deformation in the bulk solid. For example, the silos with very rough walls showed a plastic state both in the experiments and in the discrete calculations. Finally, it should be noted that the granular flow in silo constructions is always influenced by the size effect, which is mainly caused by the different pressure levels and the ratio between the silo width/diameter and the mean size of the bulk solid grain (Tejchman, 2013). Therefore, by reducing the size of a silo, the nominal wall stresses in the structure become higher. This is due to the fact that both the mobilized friction and the dilatancy of the granular material increase with decreasing pressure. On the other hand, as the ratio of mean grain diameter to silo width/diameter decreases, the nominal wall stresses decrease because the shear/rolling resistance and the thickness of the wall shear zones decrease with decreasing  $d_{50}$ .

Table 5.3: Experimental and numerical values of the resultant vertical bottom force  $P$  in the residual state for initially dense sand during flow as compared to the theoretical silo formula by Drescher (1991) and standard formula by EN 1991-4 (2006).

|                            | $P$ [N]<br>smooth walls | $P$ [N]<br>rough walls | $P$ [N]<br>very rough walls |
|----------------------------|-------------------------|------------------------|-----------------------------|
| Experiments                | 760                     | 480                    | 530                         |
| DEM                        | 650                     | 370                    | 320                         |
| Formula by Drescher (1992) | 533                     | 490                    | 537                         |
| Formula by EN 1991-4       | 655                     | 508                    | 446                         |



### Distribution of wall stresses

In addition to the resultant forces acting on the side and bottom walls presented in the previous section, the distributions of wall stresses along these vertical walls were also calculated. Figures 5.8 to 5.11 show the distribution of wall horizontal stress  $\sigma_{11}$  and wall shear stress  $\sigma_{21}$  along the silo height for different roughness of the silo walls and different initial void ratios of the sand. The stresses within the granular material were calculated according to the formula presented in the previous chapter (see Chapter 4.3 for explanation). The stresses were calculated at the end of the filling (referred to in the figure as the "initial state"), for the maximum horizontal wall force  $N_{max}$  (referred to in the figure as the "maximum state"), and at the end of the flow when the displacement of the bottom  $u=30$  mm was reached (referred to in the figure as the "residual state").

In the initial phase of the flow, the typical distribution of bulk solid in a silo was observed for cases with very rough and rough walls (see Figure 5.8, 5.9, and 5.11). The stresses increased linearly from the top of the sand in direct proportion to the silo height, and then remained constant approximately 10-15 cm above the silo bottom until the bottom plate was reached. Near the bottom of the silo, the stresses even slightly decreased. Only in the case of the silo with smooth walls an almost hydrostatic distribution of both wall stresses was obtained (Figure 5.10). During flow, the distribution of wall stresses exerted on the silo walls strongly depended on the wall roughness and the initial void ratio of the sand. The most pronounced changes occurred for the silo with very rough walls filled with initially dense sand (Figure 5.8). The smallest changes were observed for the silo with smooth walls and initially dense sand (Figure 5.10) as well as for the silo with very rough walls and initially loose sand (Figure 5.11). Both the magnitude of the wall horizontal stress  $\sigma_{11}$  and the wall shear stress  $\sigma_{21}$  increased during the test with increasing  $R_n$  and decreasing  $e_0$ . In each case, the distribution of stresses exerted on the silo walls showed significant fluctuations in all three studied time steps. The greatest fluctuations were observed in the case of the very rough and rough walls. Similar evolution of the curves was obtained by Wójcik and Tejchman (2009) and Krzyżanowski et al. (2021) on the base of numerical analyses performed with FEM and MPM. The values of  $\sigma_{11}$  calculated using the hypoplastic constitutive model by Wójcik and Tejchman (2009) were similar to those calculated using discrete model in case of the silo with very rough walls filled with initially dense sand (the remaining cases were not studied with FEM). On the other hand, the values calculated using MPM in the study carried out by Krzyżanowski et al. (2021) were generally higher than those calculated in the discrete analysis. The occurrence of the peaks (curve in the residual state in Figure 5.8) and the drops (curve in the maximum state in Figure 5.8) in the stresses can be attributed to the formation of the internal shear zones (Wójcik and Tejchman, 2009; Tejchman, 2013). However, it should be noted that the quasi-three-dimensional model, along with the greater mean grain diameter of the particles than the one used in the experiments, could partially contributed to the magnitude of these extreme values.



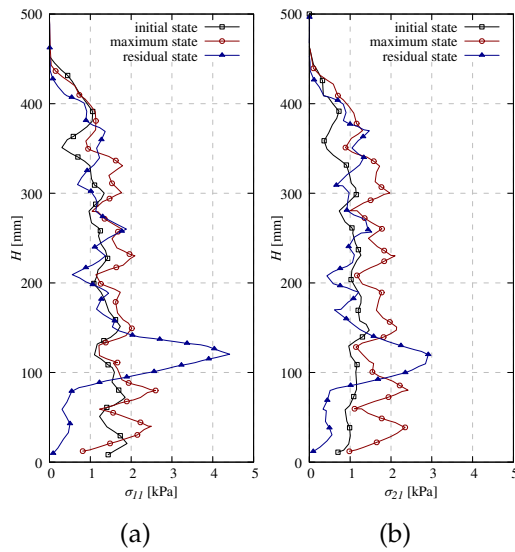


Figure 5.8: Distribution of: a) wall horizontal stress  $\sigma_{11}$  and b) wall shear stress  $\sigma_{21}$  in silo with very rough walls ( $R_n=1.0$ ) for initially dense sand ( $e_0 = 0.60$ ) at initial state, maximum state and residual state of quasi-static flow (Grabowski et al., 2021a).

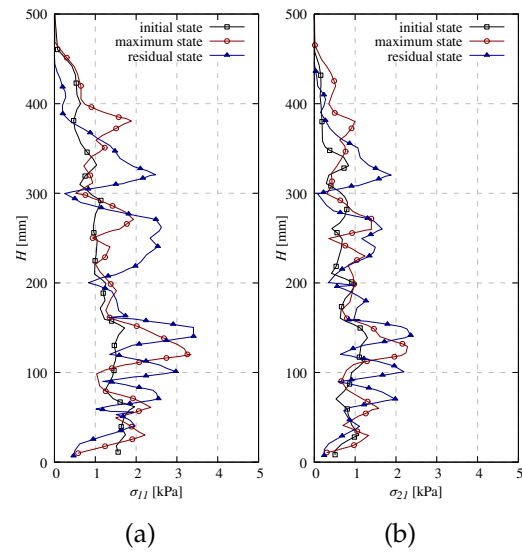


Figure 5.9: Distribution of: a) wall horizontal stress  $\sigma_{11}$  and b) wall shear stress  $\sigma_{21}$  in silo with rough walls ( $R_n=0.25$ ) for initially dense sand ( $e_0 = 0.60$ ) at initial state, maximum state and residual state of quasi-static flow (Grabowski et al., 2021a).

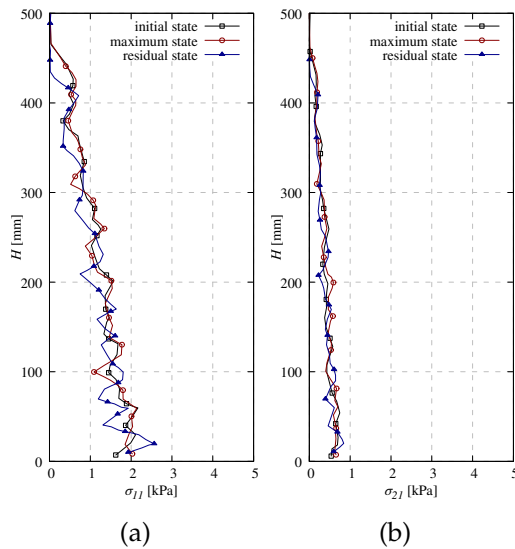


Figure 5.10: Distribution of: a) wall horizontal stress  $\sigma_{11}$  and b) wall shear stress  $\sigma_{21}$  in silo with smooth walls ( $R_n=0.01$ ) for initially dense sand ( $e_0 = 0.60$ ) at initial state, maximum state and residual state of quasi-static flow (Grabowski et al., 2021a).

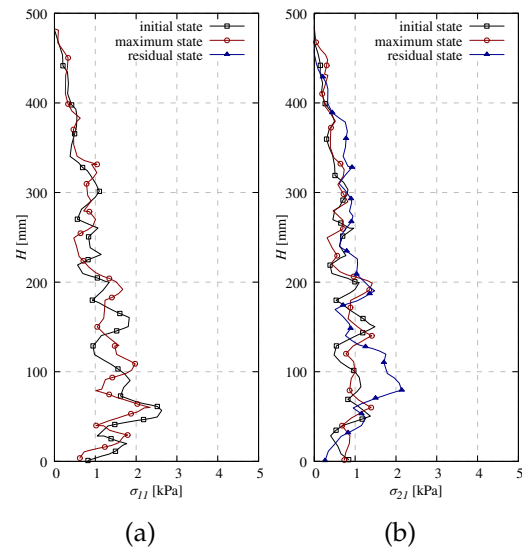


Figure 5.11: Distribution of: a) wall horizontal stress  $\sigma_{11}$  and b) wall shear stress  $\sigma_{21}$  in silo with very rough walls ( $R_n=1.0$ ) for initially loose sand ( $e_0 = 0.76$ ) at initial state, maximum state and residual state of quasi-static flow (Grabowski et al., 2021a).



### Effect of wall roughness on mesoscopic behavior inside the granular material during silo flow

In this section, the focus shifts from studying the forces and stresses exerted by sand on silo walls to examining the effect of wall roughness and the initial void ratio of the samples on the mesoscopic behavior of the bulk material. The discrete results for the grain-level characteristics, such as the deformations of the sand, the distribution of the normal force chains, sphere rotations, and the void ratio distribution are presented.

Initially, the sand displacements obtained with the aid of colored layers in quasi-static flow for different normalized roughness of the silo walls were analyzed (Figures 5.12-5.14). This method is one of the basic approaches used to analyze the deformation of granular material during confined flow (Tejchman, 2013; Slominski et al., 2007). In addition, the distribution of particle displacements across the silo width at three cross-sections along the silo height was calculated (Figure 5.15). During the flow, the clear wall shear zones occurred for the case of the silo with very rough walls (Figure 5.12). In this case, although the geometry of the set up was symmetric, the granular flow and, consequently, the distribution of particle displacements was strongly asymmetric (Figure 5.15). In this case, a characteristic step-like profiles of the granular material were observed (Figure 5.12c,d), which were caused by the occurrence of the internal shear zones. In the case of the silo with rough walls, no step-like profiles occurred during the flow (Figure 5.13c,d). Thus, only the vertical shear zones directly at the walls were present. For the silo with smooth walls, negligible deformation of the sand was observed at the walls. Neither vertical wall shear zones nor internal shear zones were observed (Figure 5.14). The entire sand mass moved as a quasi-rigid body during the flow. In general, similar to the experiments (Tejchman, 2013), the extent of the deformed granular material near the walls and, consequently, the thickness of the shear localization decreased with decreasing wall roughness.

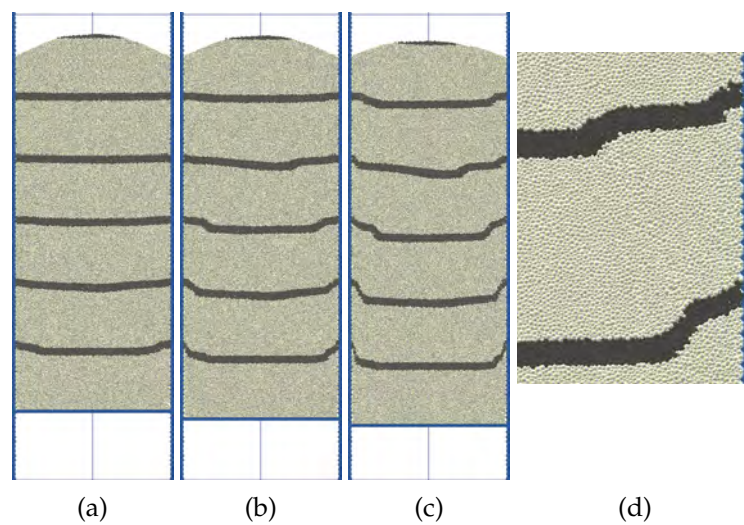


Figure 5.12: Displacements in sand after bottom displacement  $u$  in initially dense sand ( $e_0 = 0.60$ ) with normalized wall roughness  $R_n = 1.0$ : a)  $u = 10$  mm, b)  $u = 20$  mm, c)  $u = 30$  mm and d) zoomed view of (c) showing detailed displacements at the right wall (Grabowski et al., 2021b).

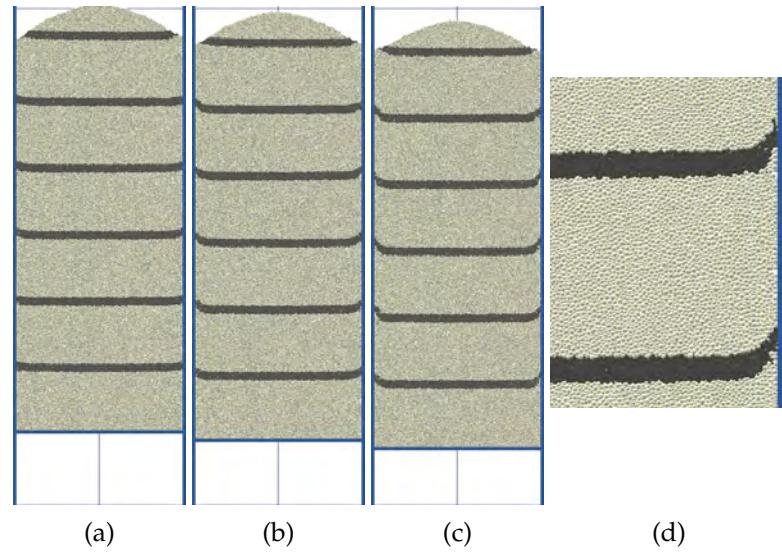


Figure 5.13: Displacements in sand after bottom displacement  $u$  in initially dense sand ( $e_0 = 0.60$ ) with normalized wall roughness  $R_n = 0.25$ : a)  $u = 10$  mm, b)  $u = 20$  mm, c)  $u = 30$  mm and d) zoomed view of (c) showing detailed displacements at the right wall (Grabowski et al., 2021b).

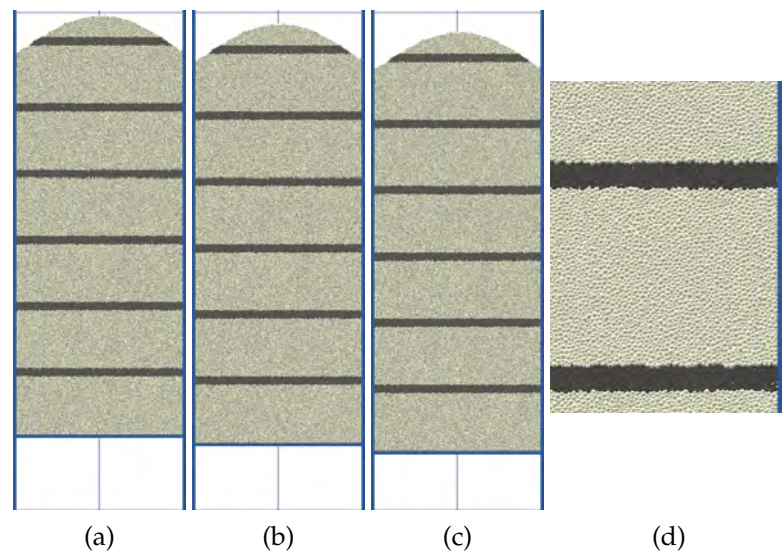


Figure 5.14: Displacements in sand after bottom displacement  $u$  in initially dense sand ( $e_0 = 0.60$ ) with normalized wall roughness  $R_n = 0.01$ : a)  $u = 10$  mm, b)  $u = 20$  mm, c)  $u = 30$  mm and d) zoomed view of (c) showing detailed displacements at the right wall (Grabowski et al., 2021b).

Following the displacements, the distribution of grain rotations and the void ratio within the sand were calculated (Figures 5.16-5.23). The changes in porosity within the granular sample and the increase in grain rotations are typical indicators of shear zone formation (Cutress and Pulfer, 1967; Desrues et al., 1996; Hall et al., 2010). The values of void ratio  $e$  were calculated similarly as in previous chapter from a cubic REV cell of the size  $5d_{50} \times 5d_{50} \times 5d_{50}$  being moved by  $d_{50}$ . The calculated grain rotations and increasing void ratios were very high with very rough

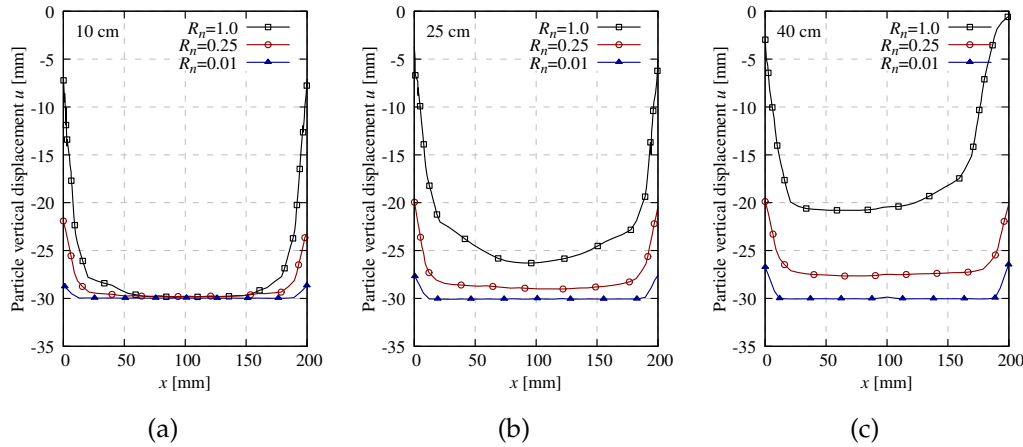


Figure 5.15: Distribution of particle displacements  $u$  across silo width at cross-section located: a) 10 cm, b) 25 cm and c) 40 cm above silo bottom after bottom displacement  $u = 30$  mm from DEM for initially dense sand ( $e_0 = 0.60$ ) with different normalized wall roughness  $R_n$  (Grabowski et al., 2021b).

walls, high with rough walls and extremely low with smooth walls (Figures 5.18–5.23). Based on grain rotations and increasing void ratio, internal curvilinear dilatant shear zones were detected. They clearly appeared during the flow of the initially dense sand with in the silo with very rough (Figures 5.18 and 5.21) as in the numerical FE analysis by Wójcik and Tejchman (2009). They were less visible with rough walls (Figure 5.19) and invisible with smooth walls (Figure 5.20). The shear zones appeared as dilatant parabolic ones in the sand interior and caused the flow nonuniformity. They occurred at the joint between bottom and vertical walls and propagated upward to the free boundary. At places of wall grooves, they branched into a vertical and parabolic one. For the silo with very rough walls, the highest rotations occurred in the vertical shear zone near the wall and in the curvilinear shear zones inside the sand. In the case of the vertical shear zone, the rotations did not occurred directly at the wall but slightly away from it (Figure 5.16). On the other hand, for the silo with rough walls, the highest rotations occurred exactly at the walls. The void ratio reached a residual value of about  $e = 0.85$  at walls and inside of sand (for very rough walls only) (Figure 5.17). The initially dense sand was always subjected to global dilatancy (increasing with the growing wall roughness) during flow and finally moved almost as a rigid body (as in the experiment by Tejchman (1989) and Tejchman (2013) and in numerical analysis using MPM by Krzyżanowski et al. (2021)).

Based on the particle rotations, the thickness of the shear localization was calculated (similarly as in the Chapter 4). In DEM, the mean thickness of the wall shear zone was about  $t_s = 30$  mm ( $=20 \times d_{50}$ ) for  $R_n = 1.0$  and  $t_s = 20$  mm ( $=13 \times d_{50}$ ) for  $R_n = 0.25$  (Table 5.4). In case of smooth wall ( $R_n = 0.01$ ) no shear zone was established and sand only slipped on the wall. For  $R_n = 1.0$  and  $R_n = 0.25$ , the numerical values of  $t_s$  (with  $d_{50} = 1.5$  mm) were slightly higher than the experimental outcomes (Tejchman, 1989; Tejchman, 2013) due to a 3-time higher value of  $d_{50}$  used in discrete tests. In the experiments, the thickness of the wall shear zones was 15–20 mm ( $=(30–40) \times d_{50}$ ) (initially dense sand,  $d_{50} = 0.5$  mm) for silo with very rough walls and 5 mm ( $=10 \times d_{50}$ ) for silo with rough walls (initially dense sand,  $d_{50} = 0.5$  mm).

Table 5.4: Thickness of the wall shear zones  $t_s$  at the mid-height of the silo obtained in DEM simulations ( $d_{50}=1.5$  mm) compared to the experiments ( $d_{50}=0.5$  mm) and ( $d_{50}=1.0$  mm) (Grabowski et al., 2021b).

| Wall roughness/<br>sand void ratio       | $t_s$<br>DEM<br>( $d_{50}=1.5$ mm) | $t_s$<br>exp.<br>( $d_{50}=0.5$ mm)                         | $t_s$<br>exp.<br>( $d_{50}=1.0$ mm) |
|--|------------------------------------|---|-------------------------------------|
| very rough wall/<br>initially dense sand | 30 mm<br>( $20 \times d_{50}$ )    | 15 to 20 mm<br>( $30 \times d_{50}$ to $40 \times d_{50}$ ) | 22 mm<br>( $22 \times d_{50}$ )     |
| very rough wall/<br>initially loose sand | 30 mm<br>( $20 \times d_{50}$ )    | 20 mm<br>( $40 \times d_{50}$ )                             | 25 mm<br>( $25 \times d_{50}$ )     |
| rough wall/<br>initially dense sand      | 20 mm<br>( $13 \times d_{50}$ )    | 5 mm<br>( $10 \times d_{50}$ )                              |                                     |
| smooth wall/<br>initially dense sand     | 1.5 mm<br>( $1 \times d_{50}$ )    | 0.5 mm<br>( $1 \times d_{50}$ )                             |                                     |

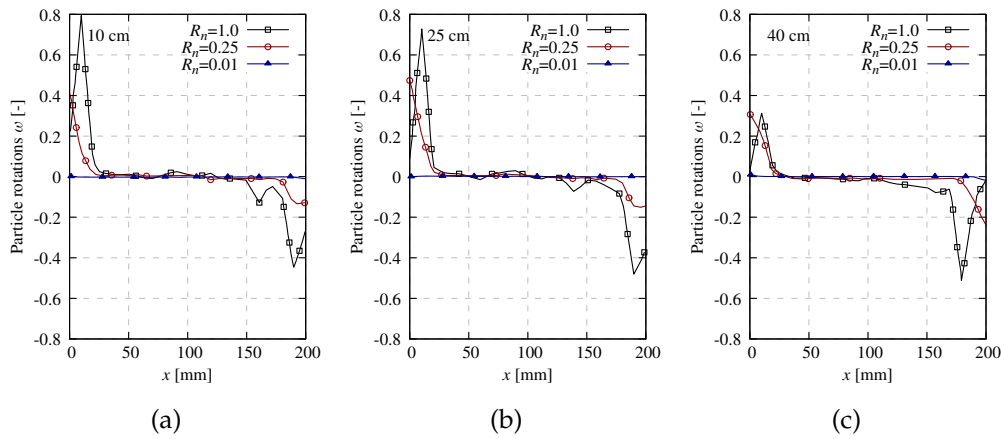


Figure 5.16: Distribution of particle rotations  $\omega$  across silo width at cross-section located: a) 10 cm, b) 25 cm and c) 40 cm above silo bottom after bottom displacement  $u = 30$  mm from DEM for initially dense sand ( $e_0 = 0.60$ ) with different normalized wall roughness  $R_n$  (Grabowski et al., 2021b).

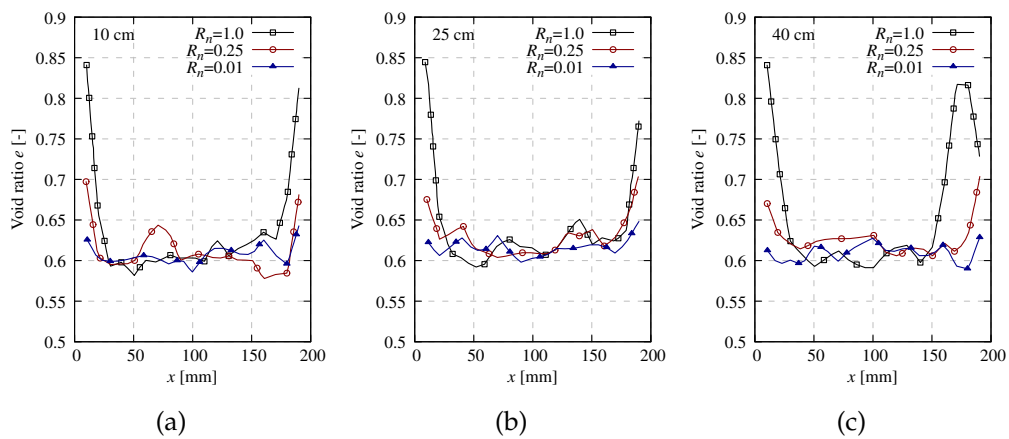


Figure 5.17: Distribution of void ratio  $e$  across silo width at cross-section located: a) 10 cm, b) 25 cm and c) 40 cm above silo bottom after bottom displacement  $u = 30$  mm from DEM for initially dense sand ( $e_0 = 0.60$ ) with different normalized wall roughness  $R_n$  (Grabowski et al., 2021b).

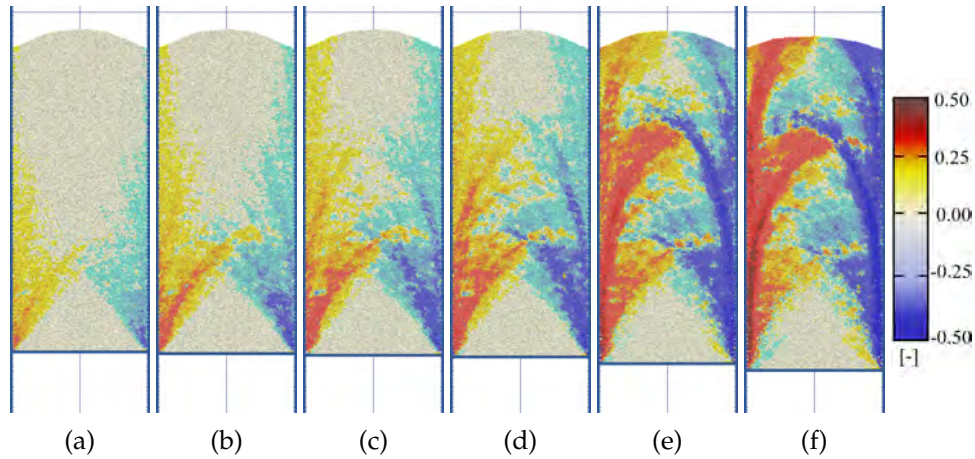


Figure 5.18: Distribution of particle rotations after bottom displacement  $u$  in initially dense sand ( $e_0 = 0.60$ ) with normalized wall roughness  $R_n = 1.00$ : a)  $u = 2.5$  mm, b)  $u = 5.0$  mm, c)  $u = 7.5$  mm, d)  $u = 10.0$  mm, e)  $u = 20.0$  mm and f)  $u = 30.0$  mm (Grabowski et al., 2021b).

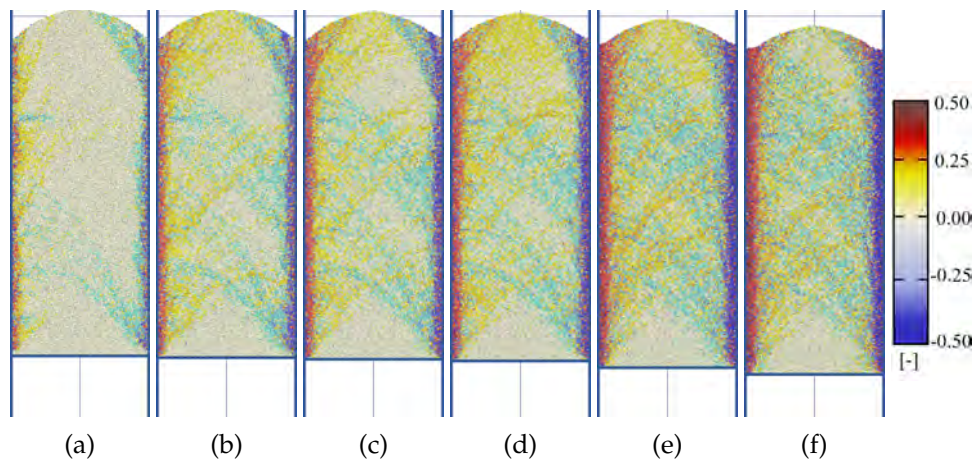


Figure 5.19: Distribution of particle rotations after bottom displacement  $u$  in initially dense sand ( $e_0 = 0.60$ ) with normalized wall roughness  $R_n = 0.25$ : a)  $u = 2.5$  mm, b)  $u = 5.0$  mm, c)  $u = 7.5$  mm, d)  $u = 10.0$  mm, e)  $u = 20.0$  mm and f)  $u = 30.0$  mm (Grabowski et al., 2021b).

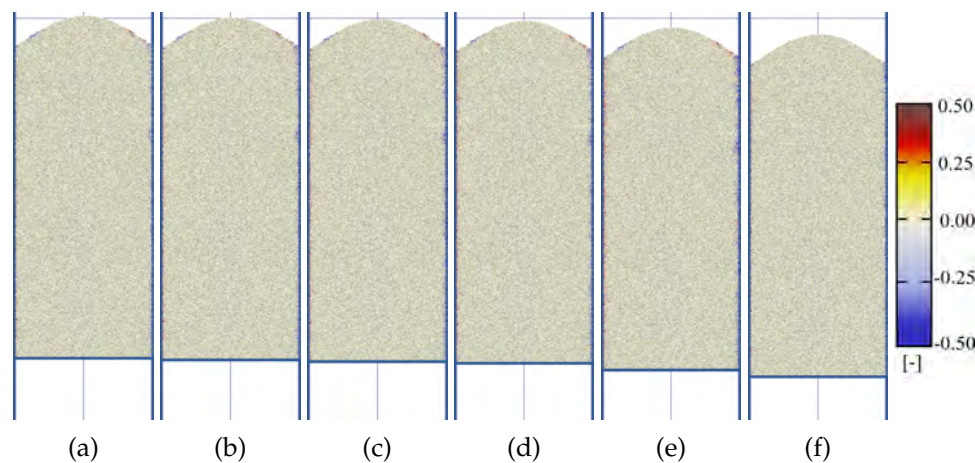


Figure 5.20: Distribution of particle rotations after bottom displacement  $u$  in initially dense sand ( $e_0 = 0.60$ ) with normalized wall roughness  $R_n = 0.01$ : a)  $u = 2.5$  mm, b)  $u = 5.0$  mm, c)  $u = 7.5$  mm, d)  $u = 10.0$  mm, e)  $u = 20.0$  mm and f)  $u = 30.0$  mm (Grabowski et al., 2021b).

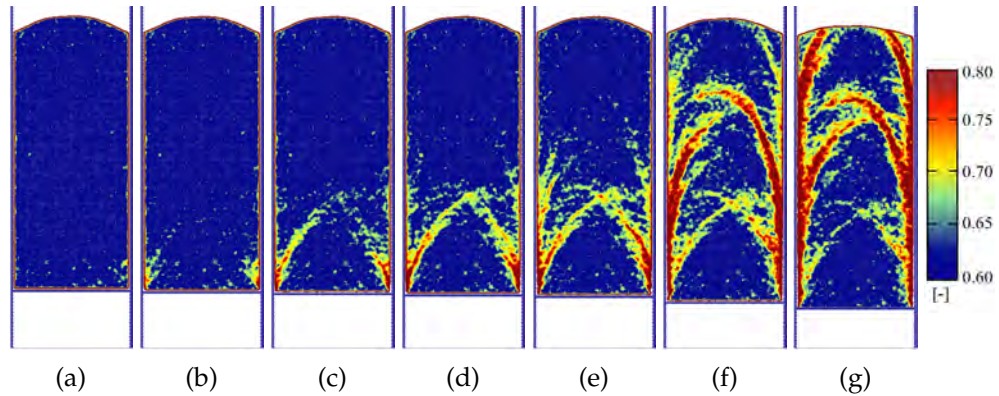


Figure 5.21: Distribution of void ratio after bottom displacement  $u$  in initially dense sand ( $e_0 = 0.60$ ) with normalized wall roughness  $R_n = 1.00$ : a)  $u = 0.0$  mm, b)  $u = 2.5$  mm, c)  $u = 5.0$  mm, d)  $u = 7.5$  mm, e)  $u = 10.0$  mm, f)  $u = 20.0$  mm and g)  $u = 30.0$  mm (Grabowski et al., 2021b).

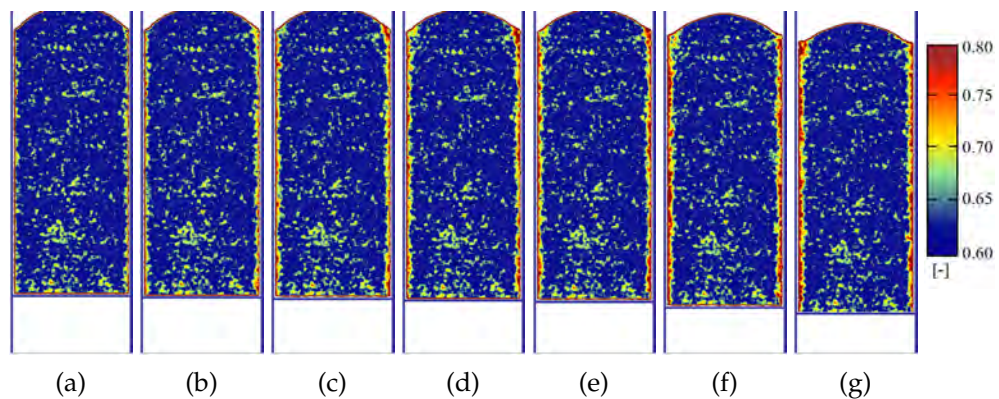


Figure 5.22: Distribution of void ratio after bottom displacement  $u$  in initially dense sand ( $e_0 = 0.60$ ) with normalized wall roughness  $R_n = 0.25$ : a)  $u = 0.0$  mm, b)  $u = 2.5$  mm, c)  $u = 5.0$  mm, d)  $u = 7.5$  mm, e)  $u = 10.0$  mm, f)  $u = 20.0$  mm and g)  $u = 30.0$  mm (Grabowski et al., 2021b).

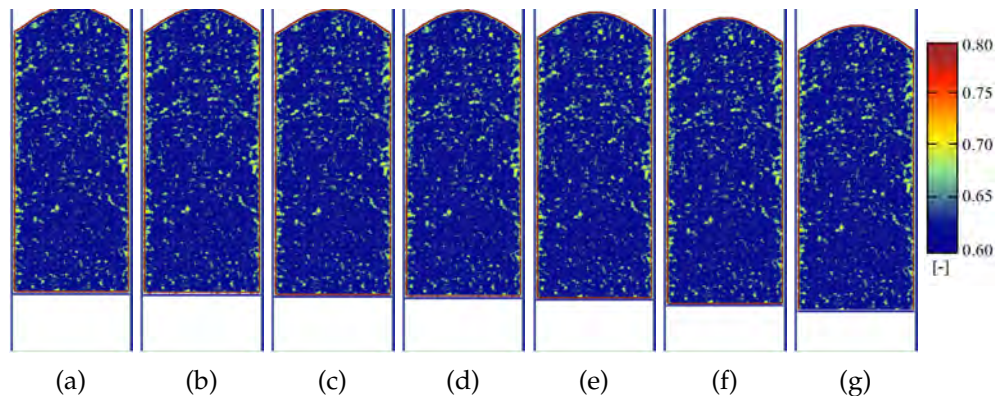


Figure 5.23: Distribution of void ratio after bottom displacement  $u$  in initially dense sand ( $e_0 = 0.60$ ) with normalized wall roughness  $R_n = 0.01$ : a)  $u = 0.0$  mm, b)  $u = 2.5$  mm, c)  $u = 5.0$  mm, d)  $u = 7.5$  mm, e)  $u = 10.0$  mm, f)  $u = 20.0$  mm and g)  $u = 30.0$  mm (Grabowski et al., 2021b).

The distribution of normal contact forces (Figures 5.24-5.26) corresponded well to the distribution of grain rotations in the sand interior (Figures 5.18-5.20). The nonuniformity and the anisotropy of the normal contact forces diminished with decreasing wall roughness. Strong normal contact force chains had a parabolic shape with very rough walls and rough walls (Figures 5.24 and 5.25) and a vertical one with smooth walls (Figure 5.26). The inclination of contact normal forces to the horizontal at the walls increased with growing  $R_n$ .

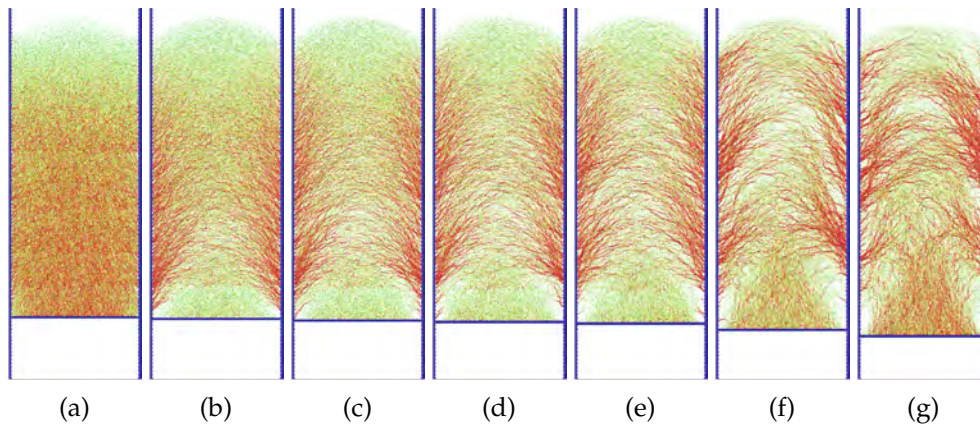


Figure 5.24: Distribution of normal force chains after bottom displacement  $u$  in initially dense sand ( $e_0 = 0.60$ ) with normalized wall roughness  $R_n = 1.00$ : a)  $u = 0.0$  mm, b)  $u = 2.5$  mm, c)  $u = 5.0$  mm, d)  $u = 7.5$  mm, e)  $u = 10.0$  mm, f)  $u = 20.0$  mm and g)  $u = 30.0$  mm (Grabowski et al., 2021b).

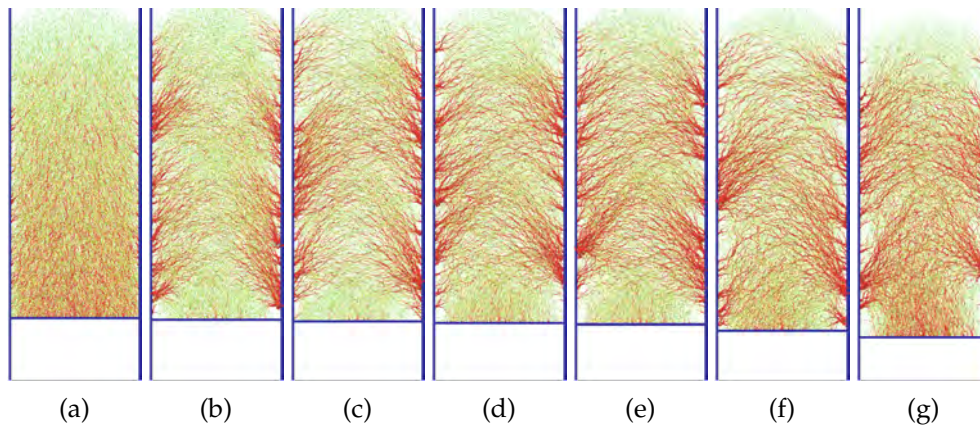


Figure 5.25: Distribution of normal force chains after bottom displacement  $u$  in initially dense sand ( $e_0 = 0.60$ ) with normalized wall roughness  $R_n = 0.25$ : a)  $u = 0.0$  mm, b)  $u = 2.5$  mm, c)  $u = 5.0$  mm, d)  $u = 7.5$  mm, e)  $u = 10.0$  mm, f)  $u = 20.0$  mm and g)  $u = 30.0$  mm (Grabowski et al., 2021b).

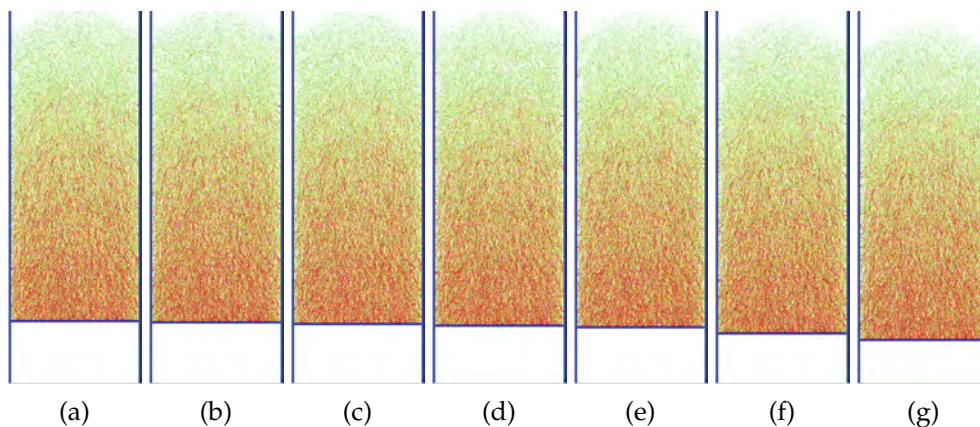


Figure 5.26: Distribution of normal force chains after bottom displacement  $u$  in initially dense sand ( $e_0 = 0.60$ ) with normalized wall roughness  $R_n = 0.01$ : a)  $u = 0.0$  mm, b)  $u = 2.5$  mm, c)  $u = 5.0$  mm, d)  $u = 7.5$  mm, e)  $u = 10.0$  mm, f)  $u = 20.0$  mm and g)  $u = 30.0$  mm (Grabowski et al., 2021b).

Figure 5.27 presents the polar distribution of all normal and tangential contact forces in the  $x$ - $y$  plane (mean amplitude and orientation to the normal direction to the left wall) at the end of filling of the silo (black line) and after bottom displacement of  $u = 30$  mm (red line). The contact forces were solely calculated for the left-half of the silo for the sake of clarity. After filling (black lines in Figure 5.27), the dominated mean contact force orientation was about  $70^\circ$  for very rough walls,  $80^\circ$  for rough walls and  $90^\circ$  for smooth walls due to gravity and wall friction. After the bottom displacement of  $u = 30$  mm, for very rough and rough walls, the dominated mean orientation against the normal to the wall diminished down to  $35^\circ$  and  $45^\circ$ , respectively (Figures 5.27a and 5.27b). For smooth walls, the mean orientation of the contact forces remained almost unchanged (Figure 5.27c). Thus, with the higher wall roughness, the contact forces at the walls changed from almost vertical ones to diagonal ones.

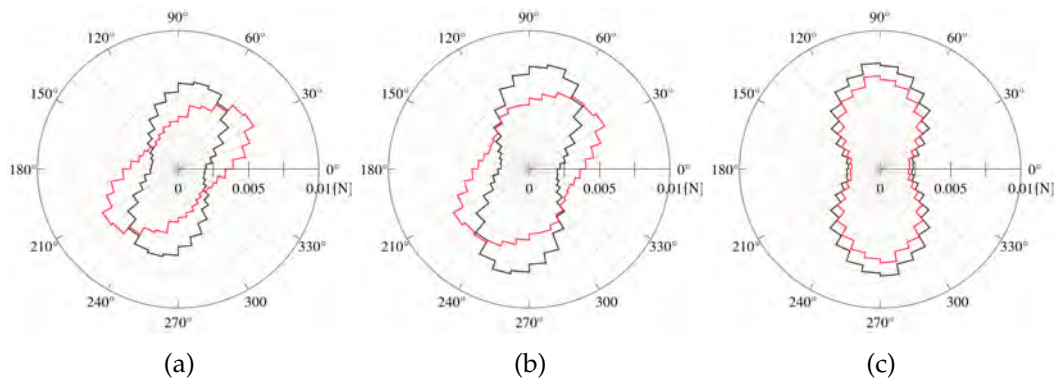


Figure 5.27: Polar mean contact force distribution in sand specimen at the end of filling (black line) and after bottom displacement of  $u = 30$  mm (red line) with different normalized roughness  $R_n$ : a)  $R_n=1.0$ , b)  $R_n=0.25$  and c)  $R_n=0.01$  ( $e_0 = 0.60$ ) (Grabowski et al., 2021b).

### Mesoscopic behavior inside the granular material during silo flow for initially loose specimen

During the study, the grain-level characteristics were also calculated for the initially loose sample ( $e_0=0.76$ ) during the flow in the silo with very rough walls ( $R_n=1.0$ ). It can be observed that contrary to the silo with very rough walls filled with initially dense sand the flow was more uniform (Figure 5.28). No step-like profiles were observed which were characteristic for the previous case. Major contractant shear zones occurred directly at the side walls of the silo (Figures 5.29 and 5.30). The thickness of the shear zones was  $t_s = 30$  mm ( $=20 \times d_{50}$ ) and it was similar to the thickness in initially dense sand. Based on rotations, the internal shear zones were significantly weaker than those in initially dense sand (Figure 5.29). Additionally, these zones were almost linear, forming a sand cone with an angle of repose at about  $40^\circ$  inclination to the bottom. The initial distribution of void ratio in initially loose sand was more nonuniform than the void ratio distribution of the initially dense specimens (Figure 5.30). A slight loosening of the sand was observed directly at the vertical walls, with a final void ratio of  $e=0.85$  (Figure 5.30f,g). A lower void ratio of about  $e=0.75$  was observed within the center of the wall shear zones where the

granular material slightly contracted. Significant difference is visible in the distribution of normal contact force chains. Compare to initially dense specimens, the normal contact force chains were more uniformly distributed in initially loose sand (Figure 5.31). Contrary to the results obtained for initially dense specimen, no significant concentration points of forces at the walls occurred. The forces within the wall shear zones were inclined and nearly vertical in the silo mid-region. Substantial vertical forces greater, than in the initially dense sand were exerted on the bottom plate during the flow. This behavior was also observed on the evolution of the  $P/G$  curve (Figure 5.6a). The mean contact force orientation was more vertical (Figure 5.32) than in initially dense sand (Figure 5.27a). The dominated orientation of contact forces was about  $75^\circ$  during filling and about  $60\text{-}70^\circ$  after bottom displacement of  $u=30$  mm was (higher than in initially dense sand).

In conclusion, the behavior of the initially loose sand in the silo with rough walls during quasi-static flow was more uniform compared to the flow of initially dense sand. This flow was characterized by smaller rotations of the sand particles and less evident changes in the void ratio. The distribution of contact forces was more homogeneous, but due to the lower amount of interactions between the particles (lower coordination number), these forces exhibit higher values. The less intense behavior, leading to smaller mesostructural changes, is consistent with the lower shear resistance and mobilization of the granular material observed on the curves of resultant forces acting on the walls and mobilized wall friction angle.

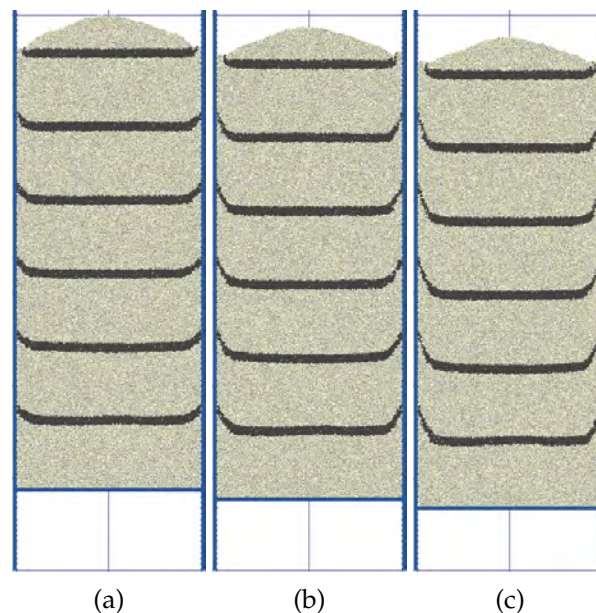


Figure 5.28: Displacements in sand after bottom displacement  $u$  in initially loose sand ( $e_0 = 0.76$ ) with normalized wall roughness  $R_n = 1.0$ : a)  $u = 10$  mm, b)  $u = 20$  mm and c)  $u = 30$  mm (Grabowski et al., 2021b).

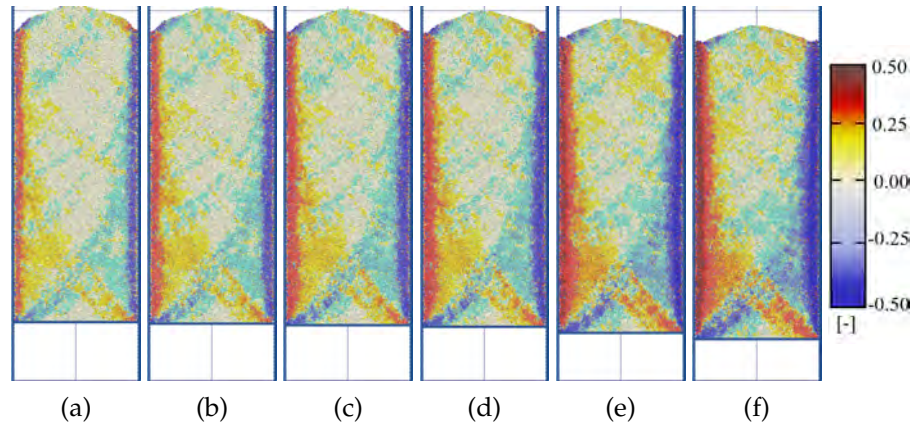


Figure 5.29: Distribution of particle rotations after bottom displacement  $u$  in initially loose sand ( $e_0 = 0.76$ ) with normalized wall roughness  $R_n = 1.00$ : a)  $u = 2.5$  mm, b)  $u = 5.0$  mm, c)  $u = 7.5$  mm, d)  $u = 10.0$  mm, e)  $u = 20.0$  mm and f)  $u = 30.0$  mm (Grabowski et al., 2021b).

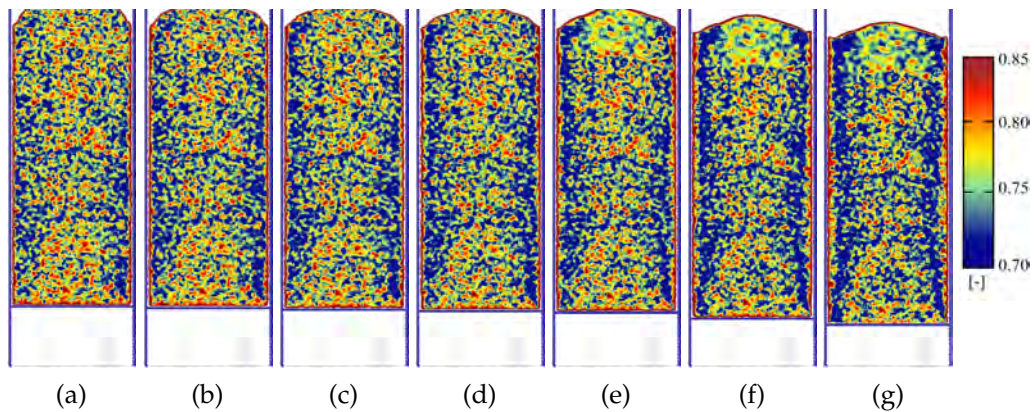


Figure 5.30: Distribution of void ratio after bottom displacement  $u$  in initially loose sand ( $e_0 = 0.76$ ) with normalized wall roughness  $R_n = 1.00$ : a)  $u = 0.0$  mm, b)  $u = 2.5$  mm, c)  $u = 5.0$  mm, d)  $u = 7.5$  mm, e)  $u = 10.0$  mm, f)  $u = 20.0$  mm and g)  $u = 30.0$  mm (Grabowski et al., 2021b).

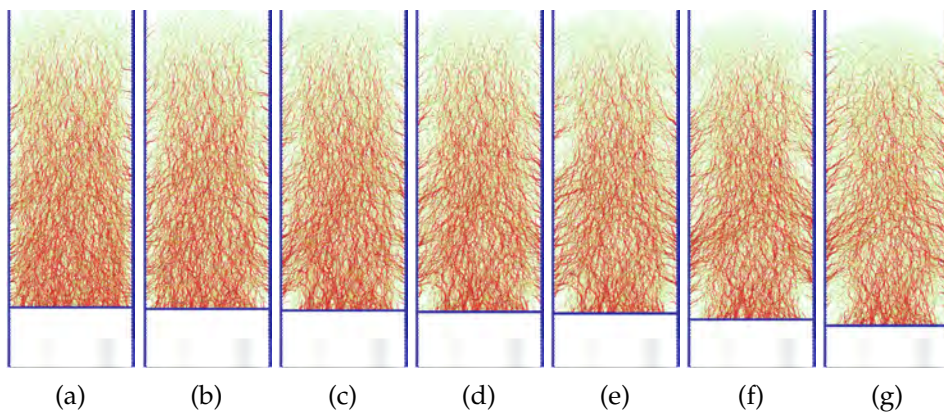


Figure 5.31: Distribution of normal force chains after bottom displacement  $u$  in initially loose sand ( $e_0 = 0.76$ ) with normalized wall roughness  $R_n = 1.00$ : a)  $u = 0.0$  mm, b)  $u = 2.5$  mm, c)  $u = 5.0$  mm, d)  $u = 7.5$  mm, e)  $u = 10.0$  mm, f)  $u = 20.0$  mm and g)  $u = 30.0$  mm (Grabowski et al., 2021b).

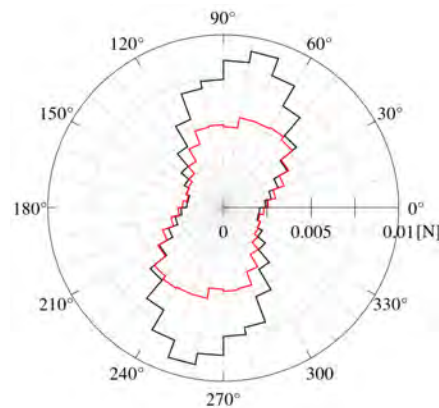


Figure 5.32: Polar mean contact force distribution in sand specimen at the end of filling (black line) and after bottom displacement of  $u = 30$  mm (red line) for initially loose specimen ( $e_0 = 0.76$ ) with normalized roughness  $R_n=1.0$  (Grabowski et al., 2021b).

### 5.3.2 Gravitational flow in silo

In the second part of this chapter, the numerical results for the confined gravitational flow in silo with parallel walls are presented. The investigation focused on quantifying the effect of wall roughness, as well as the geometry and location of the outlet, on the flow mechanism, with particular attention to the formation of shear zones. During the numerical investigation, several tests were performed with two types of silo walls (smooth and very rough) and three types of silo outlets (symmetric outlet and two asymmetric outlets of different width). In addition, the influence of the initial density of the sand on the discharge was studied (initially medium-dense and loose sand were tested).

#### Evolution of forces exerted on walls

Similarly as in the case of a quasi-static flow in silo presented in previous section, the resultant forces acting on the silo walls during flow were calculated. Again, these forces were normalized by the weight of the sand. Figures 5.33-5.38 show these normalized resultant forces as a function of discharge time. Before the flow started, the kinematic energy of the discrete particles accumulated during filling was dissipated. This settlement process is visible on each curve as a 0.5 second constant magnitude of the calculated force, during which the kinematic energy of the system became negligible. The forces shown in the following graphs were calculated on the left wall of the silo.

The calculated resultant forces  $P$ ,  $T$  and  $N$  showed satisfactory agreement with the general knowledge about the evolution of wall forces during the typical flow in the silo. Due to the lack of corresponding experimental and numerical analysis, these outcomes were not quantitatively compared with other results. The relationship between the initial magnitude of the forces in the analyzed cases was similar to that obtained in the simulations of quasi-static flow presented earlier. Therefore, these forces were also similar to those measured in the experiments by Tejchman (2013). The initial value of the  $P$  increased with the decrease of the wall roughness



(Figures 5.33a-5.35a) and with the increase of initial void ratio (Figures 5.36a-5.38a). The initial value of the vertical wall force  $T$  increased with the increase of  $R_n$  (Figures 5.33b-5.35b) and with the decrease of the  $e_0$  (Figures 5.36b-5.38b). The initial value of the horizontal wall force  $N$  increased with the decrease of the initial void ratio of the sand (Figures 5.36c-5.38c) and was independent of wall roughness (Figures 5.33c-5.35c). During the discharge, it was found that in the case of the silo with rough walls, there was a decrease in the vertical bottom force  $P$  (Figures 5.33a-5.35a) and an increase in the vertical wall friction force  $T$  (Figures 5.33b-5.35b) shortly after the start of the flow. In these cases, the force  $T$  increased at the beginning of the discharge until it reached its maximum value. The initial drop in the force exerted on the bottom wall  $P$  was related to the opening of the silo outlet, which caused an immediate lack of support for part of the material. Such tendency was previously reported by Tejchman (2013), Gallego et al. (2015), and Wójcik et al. (2017). The resultant horizontal wall force  $N$  in the case of the silo with rough walls was found to significantly decrease in the initial phase of the flow. It appeared that due to the small size of the outlet, the sand did not mobilize instantly as in the case of the quasi-static flow presented in the previous chapter (see Chapter 5.3.1).

During the emptying of silos with smooth walls, a gradual decrease of the resultant vertical bottom force  $P$  (Figures 5.33a-5.35a) and the resultant vertical wall friction force  $T$  (Figures 5.33b-5.35b) related to the outflow of sand from the silo was observed. As for the resultant horizontal wall force  $N$  (Figures 5.33c-5.35c), it increased slightly after the start of the discharge, then oscillated around a constant value and finally gradually decreased as the flow progressed. The evolution of the resultant forces in the case of initially loose samples was similar to the evolution of the forces in the case of dense samples. The main difference was observed in the case of the horizontal wall force  $N$ , which showed higher values during the flow for the silo filled with initially loose sand (Figures 5.36c-5.38c).

It should be noted that significant fluctuations in the magnitude of the resultant forces were observed during each flow. These fluctuations were mainly caused by the artificial harmonic nature of the wall roughness and due to the quasi-three-dimensional conditions of the flow. While the amplitude of the curves recorded during the numerical simulations of gravitational flow was significant, fluctuations in the forces or pressures acting on the silo side and bottom walls are typical for granular flow (Balevičius et al., 2012; Wang et al., 2015; Wójcik et al., 2017; Gandia et al., 2021). These fluctuations could be reduced by increasing the number of particles packed in the silo, characterized by a smaller mean grain diameter.

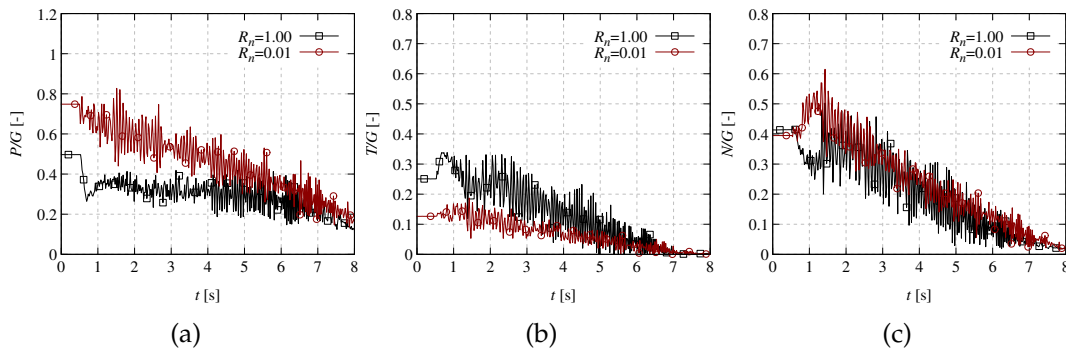


Figure 5.33: Evolution of: a) normalized resultant bottom force  $P/G$ , b) normalized resultant wall friction force  $T/G$  and c) normalized resultant wall normal force  $N/G$  during the discharge of a silo with the outlet of type '1' and a different normalized wall roughness  $R_n$  ( $e_0=0.60$ ) (G-sand weight).

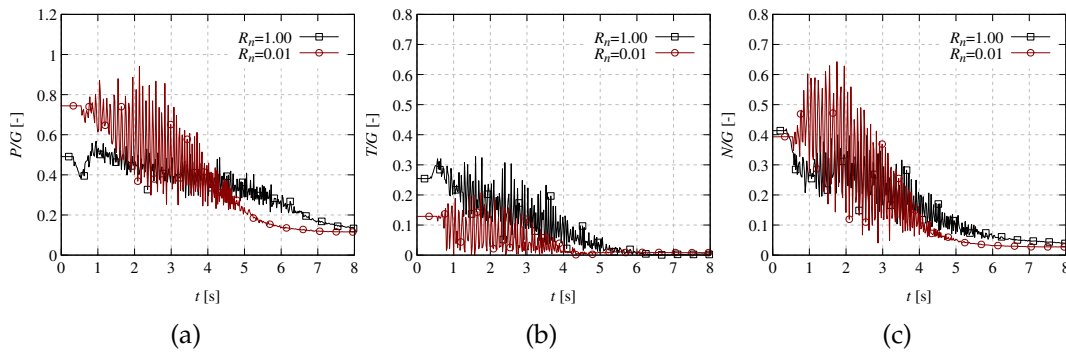


Figure 5.34: Evolution of: a) normalized resultant bottom force  $P/G$ , b) normalized resultant wall friction force  $T/G$  and c) normalized resultant wall normal force  $N/G$  during the discharge of a silo with the outlet of type '2' and a different normalized wall roughness  $R_n$  ( $e_0=0.60$ ) (G-sand weight).

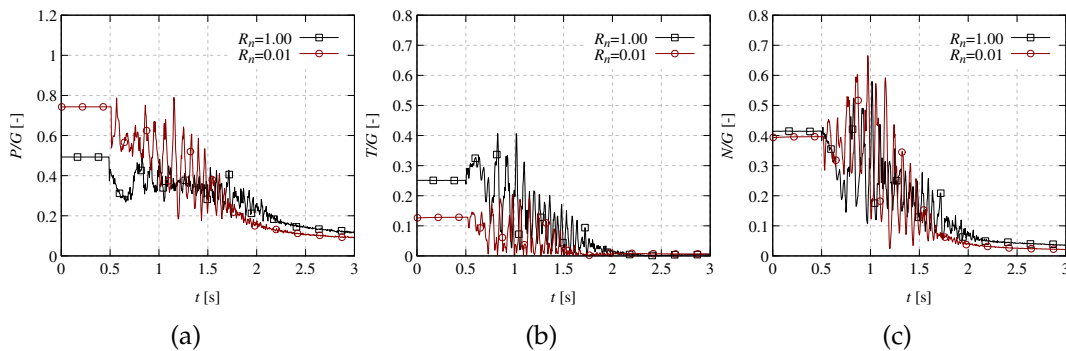


Figure 5.35: Evolution of: a) normalized resultant bottom force  $P/G$ , b) normalized resultant wall friction force  $T/G$  and c) normalized resultant wall normal force  $N/G$  during the discharge of a silo with the outlet of type '3' and a different normalized wall roughness  $R_n$  ( $e_0=0.60$ ) (G-sand weight).

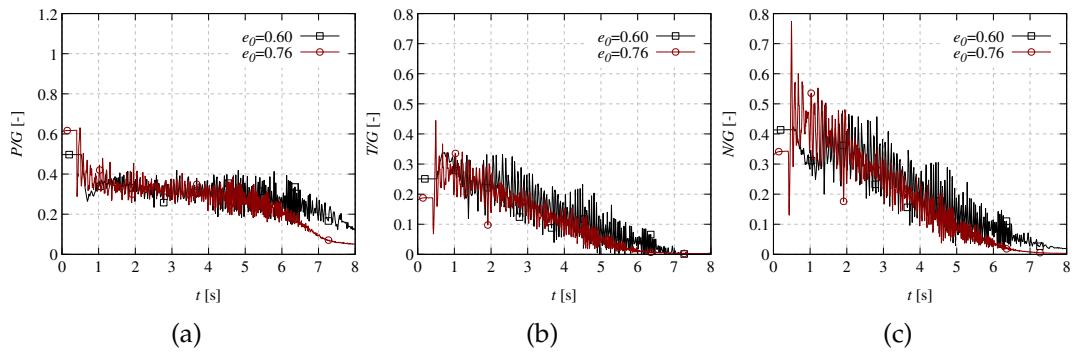


Figure 5.36: Evolution of: a) normalized resultant bottom force  $P/G$ , b) normalized resultant wall friction force  $T/G$  and c) normalized resultant wall normal force  $N/G$  during the discharge of a silo with the outlet of type '1' and a different initial void ratio of sand ( $R_{n1}=1.00$ ) (G-sand weight).

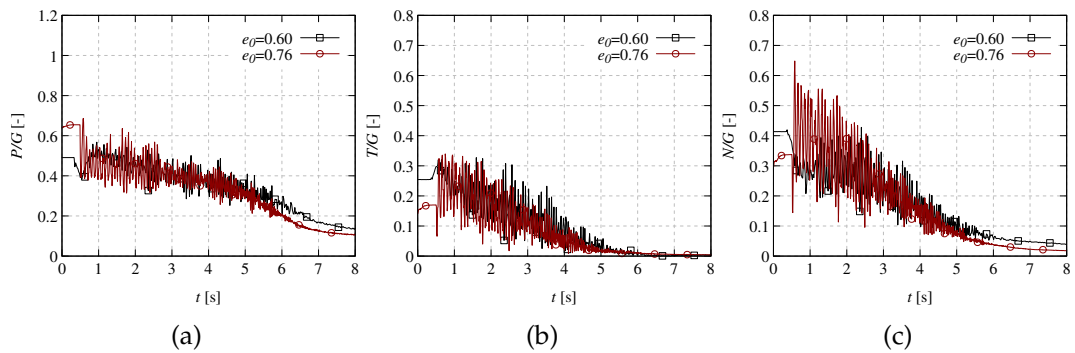


Figure 5.37: Evolution of: a) normalized resultant bottom force  $P/G$ , b) normalized resultant wall friction force  $T/G$  and c) normalized resultant wall normal force  $N/G$  during the discharge of a silo with the outlet of type '2' and a different initial void ratio of sand ( $R_{n1}=1.00$ ) (G-sand weight).

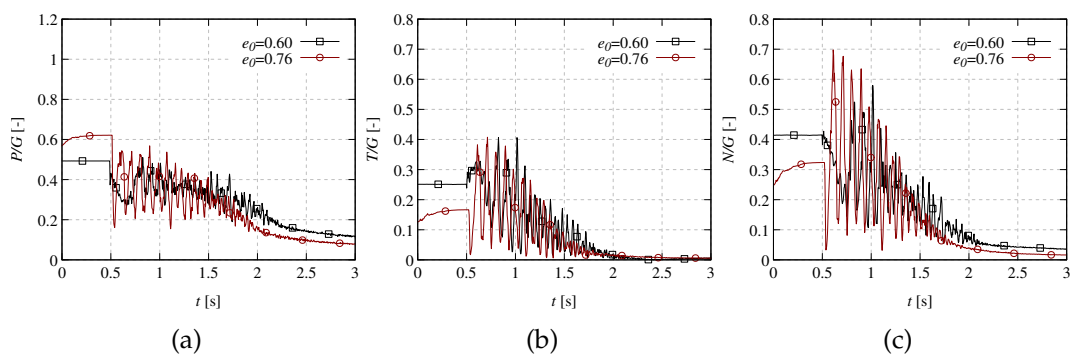


Figure 5.38: Evolution of: a) normalized resultant bottom force  $P/G$ , b) normalized resultant wall friction force  $T/G$  and c) normalized resultant wall normal force  $N/G$  during the discharge of a silo with the outlet of type '3' and a different initial void ratio of sand ( $R_{n1}=1.00$ ) (G-sand weight).

### Effect of wall roughness on flow mechanism in silo

In addition to the calculation of the forces acting on the laboratory-scale silo, the discrete model also allowed for an examination of the mesostructural behavior of the sand during gravitational flow. In this section, the effect of the wall roughness on the flow mechanism of initially medium-dense sand ( $e_0=0.60$ ) was investigated. The following calculations were performed for two types of walls ( $R_n=0.01$  and  $R_n=1.0$ ) and for three types of outlets presented in the introduction section (Figure 5.4). The numerical results for the grain-level characteristics, such as the deformations of the sand, the distributions of the particle rotations, the void ratio and the normal force chain network are presented. In the following paragraphs, the studied variables shown in the figures have been calculated for different stages of the test. Due to the different time of discharge for different types of outlets, these stages have been registered in relation to the amount of sand that flowed out of the silo during the discharge. For example, "1%" indicates that 1% of the initial mass of sand stored in the silo has already flowed out of the silo.

Initially, the effect of the wall roughness on the deformation of the sand during the flow was studied. In the figures below, the displacements profiles obtained with the aid of colored sand layers for silos with very rough and smooth walls are presented for all types of outlets (Figures 5.39-5.41). As it can be seen, the influence of the wall roughness on the flow mechanism and shear propagation was significant. Different types of flow were observed for silos with symmetric outlet. In the case of a silo with very rough walls, although a funnel flow was observed in the initial part of the discharge, the flow in the silo was qualified as a mixed flow as it changed during the flow (Figure 5.39A). As the flow progressed, a characteristic step-like profiles of the granular material were observed (Figure 5.39Ac-e). These profiles show that although a symmetrical outlet was used, the flow was highly asymmetrical and nonuniform. On the other hand, mass flow was observed in the case of the silo with smooth walls (Figure 5.39B). In this instance, the flow exhibited an almost symmetrical pattern, and no step-like profiles within the sand were observed. Major deformations were captured only in the area adjacent to the outlet (within 8 cm above the bottom plates). Above that region, the sand mass behaved like a quasi-rigid body. The profile of the sand mass unconstrained surface remained similar throughout the entire flow (Figure 5.39Ba-f). The result for the silos with asymmetric outlet of width  $b=30$  mm (type '2') showed also the significant effect of the roughness of the walls (Figure 5.40). The flow pattern obtained in both cases were different. In case of a silo with rough walls, the funnel flow was observed. The width of the funnel zone reached almost the half of the silo width (about  $60 \times d_{50}$ ) at the mid-height of the silo (Figure 5.40Ab-e). The shape of the upper surface changed during the discharge. In the smooth walled silo, the mixed flow was obtained, with the upper part of the material exhibiting mass flow. However, the width of the moving zone was wider than in the previous case and reached approximately 60% of the silo width (Figure 5.40Bb-d). The shape of the upper surface changed during the discharge, but not as clearly as in the silo with rough walls. In the case of the silo with smooth walls, the material located directly at the right wall of the structure slipped on the smooth surface, contrary to the first case, where groups of particles were locked between the grooves of the rough wall. For the silo with asymmetric outlet of type '3' the



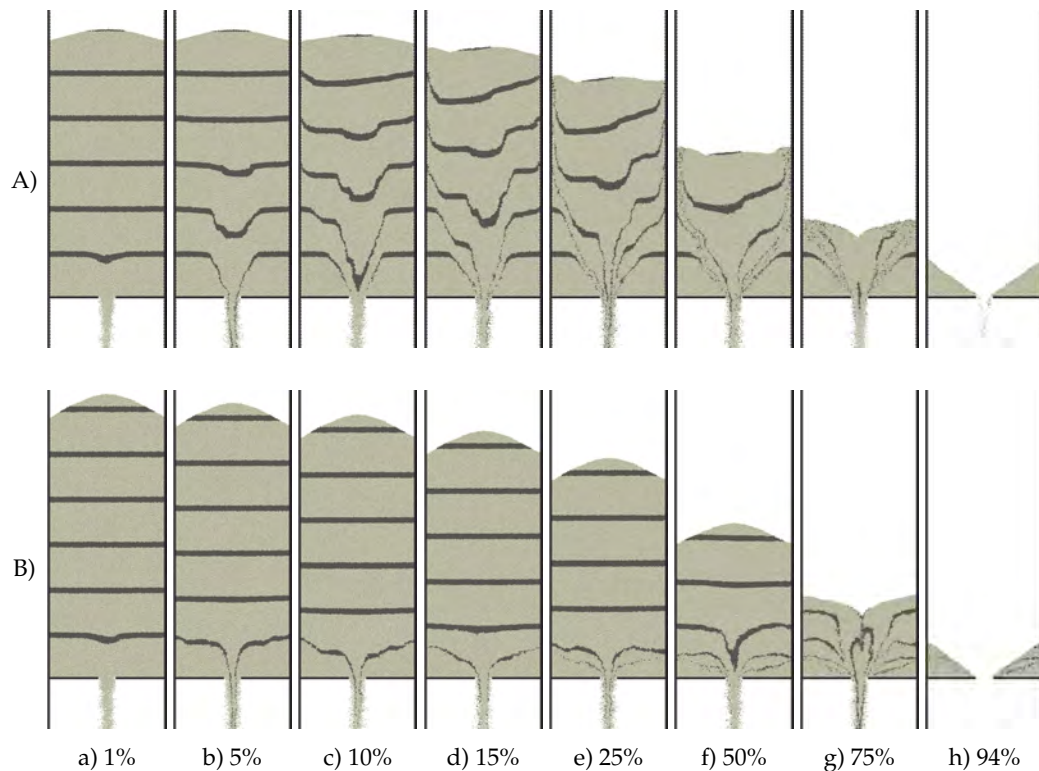


Figure 5.39: Sand deformation at different stages of discharge for silo filled with initially medium-dense sand ( $e_0 = 0.60$ ) with symmetric outlet of type '1' for different normalized roughness  $R_n$  of the walls: A)  $R_n = 1.00$  and B)  $R_n = 0.01$  (the percentages indicate the amount of sand that has flowed out of the silo).

difference between two types of walls was less evident (Figure 5.41). In case of the silo with very rough walls, particles were locked between the grooves during the discharge (Figure 5.41Ad-e). On the contrary, in case of the silo with smooth walls the mass flow was observed, with the upper part of specimen behaving like a quasi-rigid body. The step-like profiles of the sand were observed in both cases. For both silos, the location of the outlet caused the flow to be asymmetric and highly irregular.

Subsequently, the distribution of particle rotations during discharge was studied (Figures 5.42-5.44). In the presented figures, the shades of red indicate the clockwise rotation, while shades of blue indicate the counterclockwise rotation. The results show that both the roughness of the walls and the geometry and location of the outlet played a key role in the behavior of the sand during the flow.

In the case of the symmetric outlet of type '1', the most significant difference was observed between silos with different wall roughness (Figure 5.42). The numerical results show that during the flow in the silo with rough walls several shear zones occurred, characterized by high clockwise and counterclockwise particle rotations (Figure 5.42A). At the beginning of the discharge, two shear zones appeared in the region of the outlet (Figure 5.42Aa). As the flow progressed, these zones propagated in an almost vertical manner towards the upper surface of the sand (Figure 5.42Ab). At this stage, these vertical localizations separated the stationary zones of sand near the walls from the flowing mass in the center of the silo. These zones approached

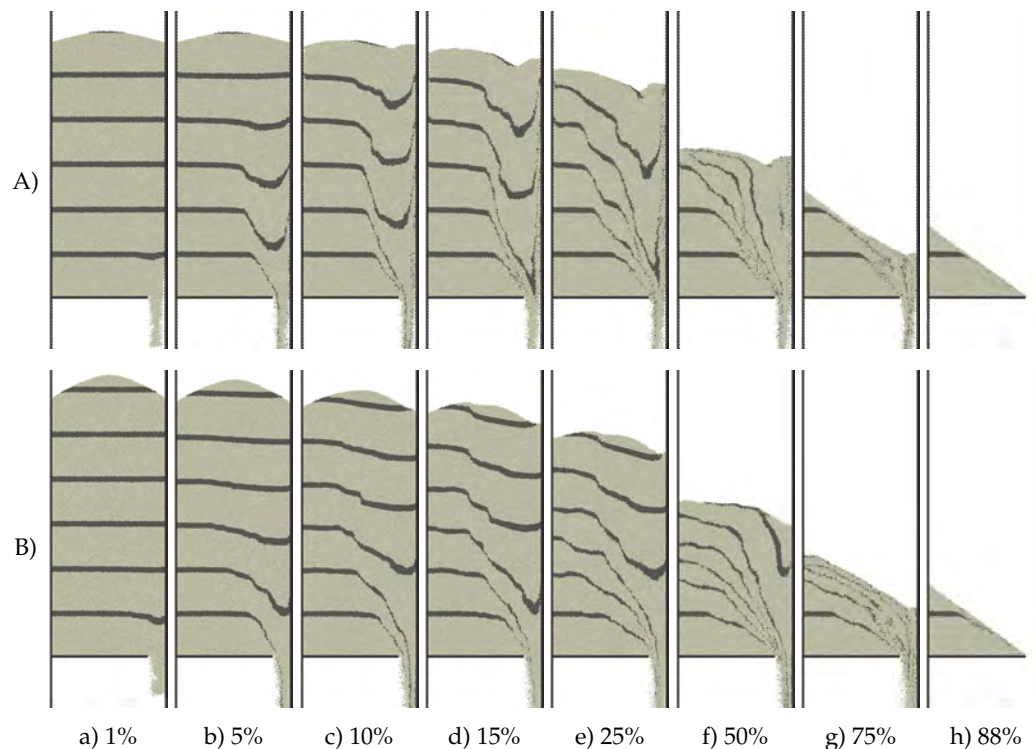


Figure 5.40: Sand deformation at different stages of discharge for silo filled with initially medium-dense sand ( $e_0 = 0.60$ ) with asymmetric outlet of type '2' for different normalized roughness  $R_n$  of the walls: A)  $R_n = 1.00$  and B)  $R_n = 0.01$  (the percentages indicate the amount of sand that has flowed out of the silo).

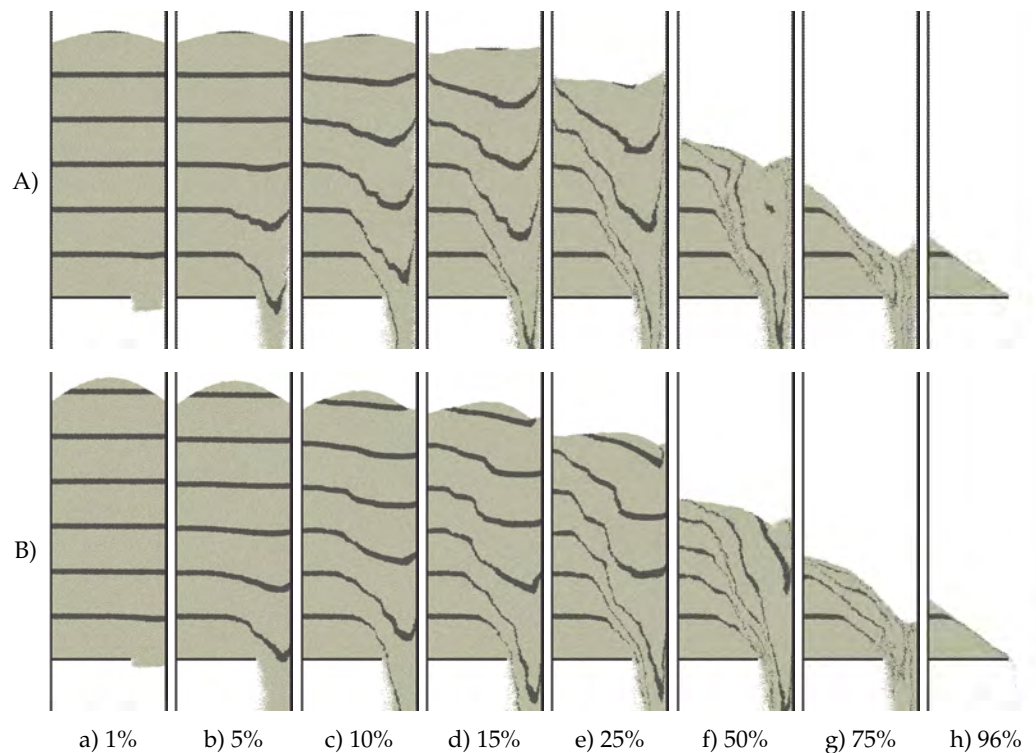


Figure 5.41: Sand deformation at different stages of discharge for silo filled with initially medium-dense sand ( $e_0 = 0.60$ ) with asymmetric outlet of type '3' for different normalized roughness  $R_n$  of the walls: A)  $R_n = 1.00$  and B)  $R_n = 0.01$  (the percentages indicate the amount of sand that has flowed out of the silo).

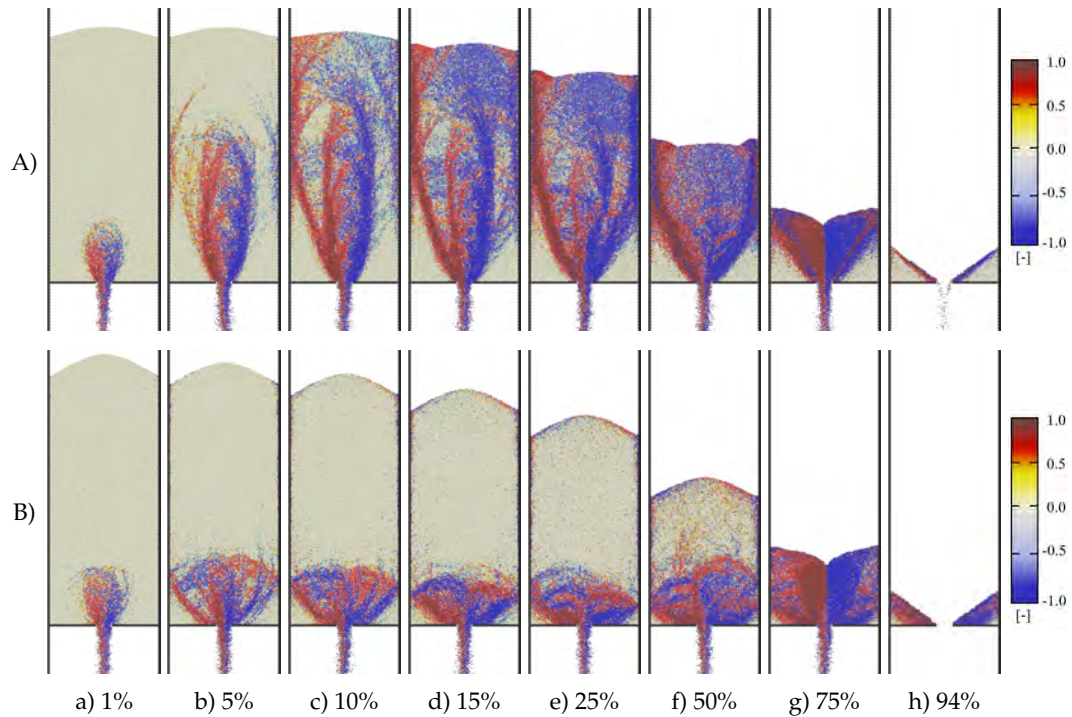


Figure 5.42: Distribution of particle rotations at different stages of discharge for silo filled with initially medium-dense sand ( $e_0 = 0.60$ ) with symmetric outlet of type '1' for different normalized roughness  $R_n$  of the walls: A)  $R_n = 1.00$  and B)  $R_n = 0.01$  (the percentages indicate the amount of sand that has flowed out of the silo).

each other around the symmetry axis slightly above the mid-height of the silo (Figure 5.42Ac-d). As the discharge proceeded, these zones did not remain stationary and moved downward toward the outlet. Simultaneously, another pair of inclined shear zones was initiated and reached the side walls (Figure 5.42Ac). These zones then propagated along the rough walls. From this time on, mainly mass flow was observed (Figure 5.42Ad-h). As a result, the flow was classified as mixed flow. The direction of particle rotations within the wall shear zones was a result of significant roughness, and consequently friction of the wall. The particle rotations in the left part of the silo were mainly clockwise, in contrast to the right part where the rotations were counterclockwise. On the other hand, mass flow was observed in the silo with symmetric outlet and smooth walls. Similar to the previous case, shear zones were initiated near the edges of the outlet at the beginning of the discharge (Figure 5.42Ba). As the flow progressed, these zones reached the nearby walls (Figure 5.42Bb). From then on, the rotations were concentrated mainly in the region adjacent to the outlet. At the same time, narrow zones of significantly weaker particle rotations were observed at the smooth walls (Figure 5.42Bc-f).

The roughness of the walls also had a notable effect on the flow in the silo with the eccentric outlet of type '2'. In this case, the difference between the two types of walls was significant. In the silo with rough walls, two shear zones were initially created, forming a flow zone approximately half the width of the silo, measured at the silo mid-height (Figure 5.43Ab). As the discharge continued, these primary shear zones reached the top surface. Then, the flowing core widened and, as a result, the flow type changed from funnel to nearly mass flow (Figure 5.43Ad).

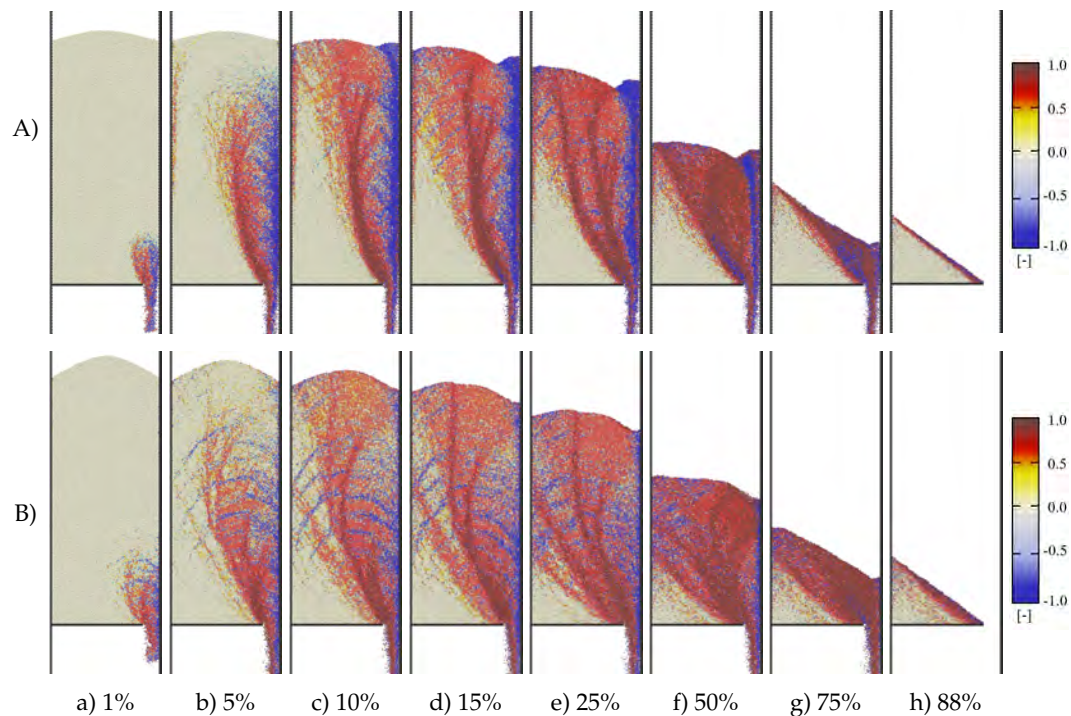


Figure 5.43: Distribution of particle rotations at different stages of discharge for silo filled with initially medium-dense sand ( $e_0 = 0.60$ ) with asymmetric outlet of type '2' for different normalized roughness  $R_n$  of the walls: A)  $R_n = 1.00$  and B)  $R_n = 0.01$  (the percentages indicate the amount of sand that has flowed out of the silo).

At this point, barely noticeable shear zones characterized by counterclockwise rotations (blue color) began to appear. In the silo with smooth walls with outlet of type '2', several shear zones were observed during the discharge, characterized by a greater curvature (Figure 5.43B). In contrast to the silo with rough walls, the flow zone was wider, reaching the left wall earlier. In this case, alternating areas of rotations with opposite signs, represented by red and blue colors, were observed (Figure 5.43Bb-d). These nearly parabolic shear zones were initiated in multiple points in the mid-height region of the silo and propagated through the entire silo width, reaching walls on the opposite side of the flow. It appears that the sand in the stagnant zone in the lower left corner provided support for the temporary suspension of the granular material. As a result, the sand in the flow channel was divided into segments of flowing granular material. Despite the walls of the silo being smooth, a similar mechanism to the arching effect was observed, which was caused by friction and interlocking of the particles. It is worth noting that in this case (silo with smooth walls and outlet of type '2') the curves of the resultant normal bottom force  $P$  and the resultant wall friction force  $T$  exhibited the highest oscillations (Figure 5.34a,c). This can be attributed to a cyclical formation and subsequent collapse of these parabolic arches. In addition, major linear shear zone, characterized by a clockwise rotations, divided the stationary region, located in the bottom left corner of the silo, from the moving zone. The orientation of this zone to the horizontal diminished during the discharge, tending finally to the natural angle of repose of sand (Figure 5.43Bc-h).

In the case of the silo with a wider outlet of type '3', a difference between the results obtained for two types of walls was less pronounced. In both cases, several

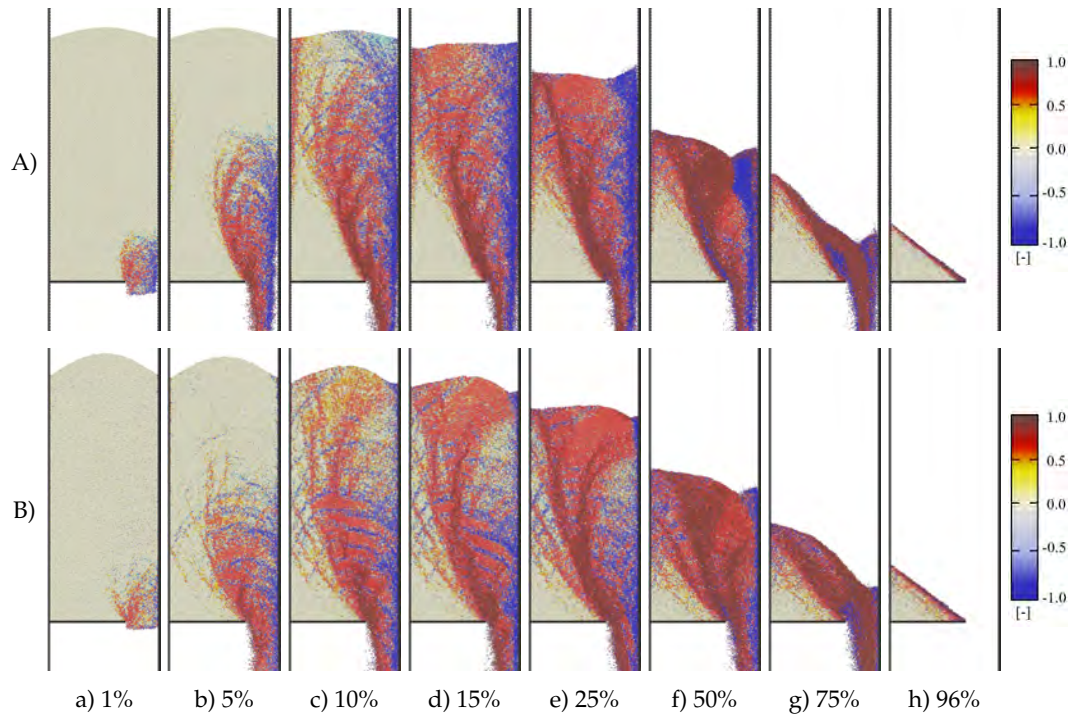


Figure 5.44: Distribution of particle rotations at different stages of discharge for silo filled with initially medium-dense sand ( $e_0 = 0.60$ ) with asymmetric outlet of type '3' for different normalized roughness  $R_n$  of the walls: A)  $R_n = 1.00$  and B)  $R_n = 0.01$  (the percentages indicate the amount of sand that has flowed out of the silo).

curvilinear shear zones occurred during the flow, regardless of the roughness of the walls. At the beginning of the flow, two shear zones appeared in the region of the outlet (Figure 5.44Aa). As the flow progressed, the shear zone propagated toward the left of the silo, separating the stationary region of sand located in the lower left corner of the silo from the flowing core (Figure 5.44Ab-d). At the same time, near the right wall, the shear zone propagated along the rough walls. In the upper part of the silo, subsequent parabolic localizations formed within the sand. In this case, the particles were partially locked between the grooves, causing changes in the shape of the top surface at the advanced stage of the flow (Figure 5.44Ade). The mechanism of flow observed in the silo with smooth walls was similar, with the difference that the thickness of the shear zone located at the right wall was smaller. Similar to the silo with outlet type '2', although the walls were smooth, some parabolic shear zones characterized by counterclockwise rotations (blue color) were observed (Figure 5.44Bb-e). Similar trajectories of parabolic shear zones were observed by Michalowski (1990) and Wójcik and Tejchman (2009) in a hopper silo with smooth walls. However, in the studied case of the rectangular silo, this behavior was caused by the stagnant zone formed during the flow instead of a hopper. Based on all the presented cases, it is clear that the stair-like flow profiles shown previously (Figures 5.39-5.41) are caused by the propagation of the shear zones.

Next, the distribution of the void ratio in the entire silo during the discharge was analyzed (Figures 5.45-5.47). The mechanism of the flow presented in these figures correspond well with the results for the distribution of grain rotations presented earlier. However, the results of the void ratio distribution were more diffused than

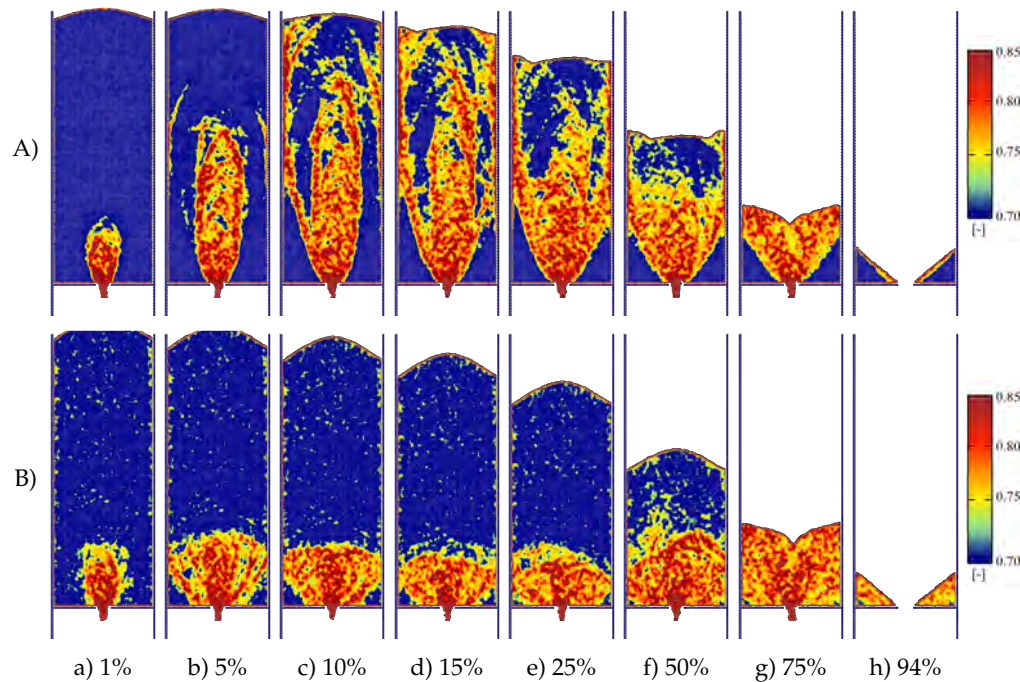


Figure 5.45: Distribution of void ratio at different stages of discharge for silo filled with initially medium-dense sand ( $e_0 = 0.60$ ) with symmetric outlet of type '1' for different normalized roughness  $R_n$  of the walls: A)  $R_n = 1.00$  and B)  $R_n = 0.01$  (the percentages indicate the amount of sand that has flowed out of the silo).

the results for the particle displacements and rotations. This was due to the fact that the latter values were shown for each distinct body, in contrast to the void ratio, which was calculated using the REV cell. Initially, the flow was concentrated in the region adjacent to the outlet, where a relatively uniform void ratio distribution was observed. As the discharge advanced, multiple dilatant zones were initiated at the boundaries of the outlet, which propagated in two distinct directions: toward the material (Figures 5.45A and 5.46A) or toward the walls (Figure 5.45B). It can be seen that the trajectory of the zones of increasing void ratio covered well the trajectory of the zones of high particle rotations. However, the changes in porosity near the walls were not so evident as the increase of the particle rotations. One of the reasons for this is that it is more difficult to calculate the void volume at the boundaries of the granular material near the walls with triangular asperities. In general, the flow in the case of the silos with smooth walls was wider than in the silos with rough walls. This was due to the friction between the sand and the walls. The asymmetric location of the outlet of the flow enhanced the nonuniformity and irregularity of the flow. The maximum void ratio calculated within the shear zones was approximately  $e=0.85$  in each case. At the end of the flow, the volume of the sand remaining on the bottom wall was greater for the silo with rough walls (Figures 5.45g-5.47g). This was attributed to the rough walls absorbing greater vertical forces, resulting in a higher angle of repose of the stagnant zone. In addition, the flow zone at the end of the discharge was thicker in the smooth wall silo compared to the rough wall silo. In the case of the silo with asymmetric outlet, almost the entire sand loosened during the flow (Figure 5.47h).

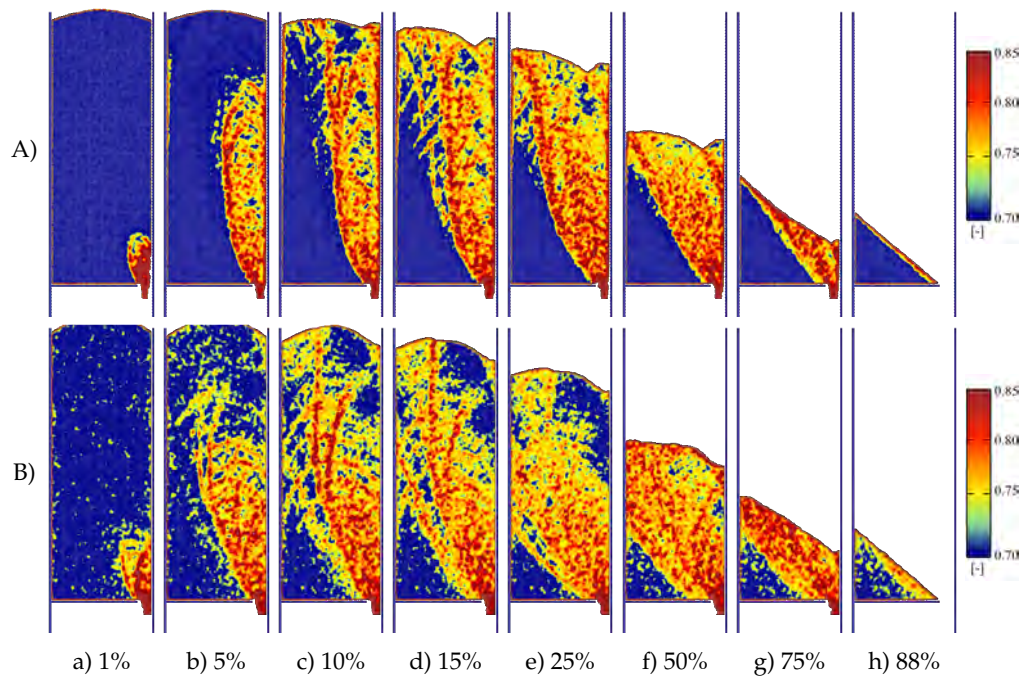


Figure 5.46: Distribution of void ratio at different stages of discharge for silo filled with initially medium-dense sand ( $e_0 = 0.60$ ) with asymmetric outlet of type '2' for different normalized roughness  $R_n$  of the walls: A)  $R_n = 1.00$  and B)  $R_n = 0.01$  (the percentages indicate the amount of sand that has flowed out of the silo).

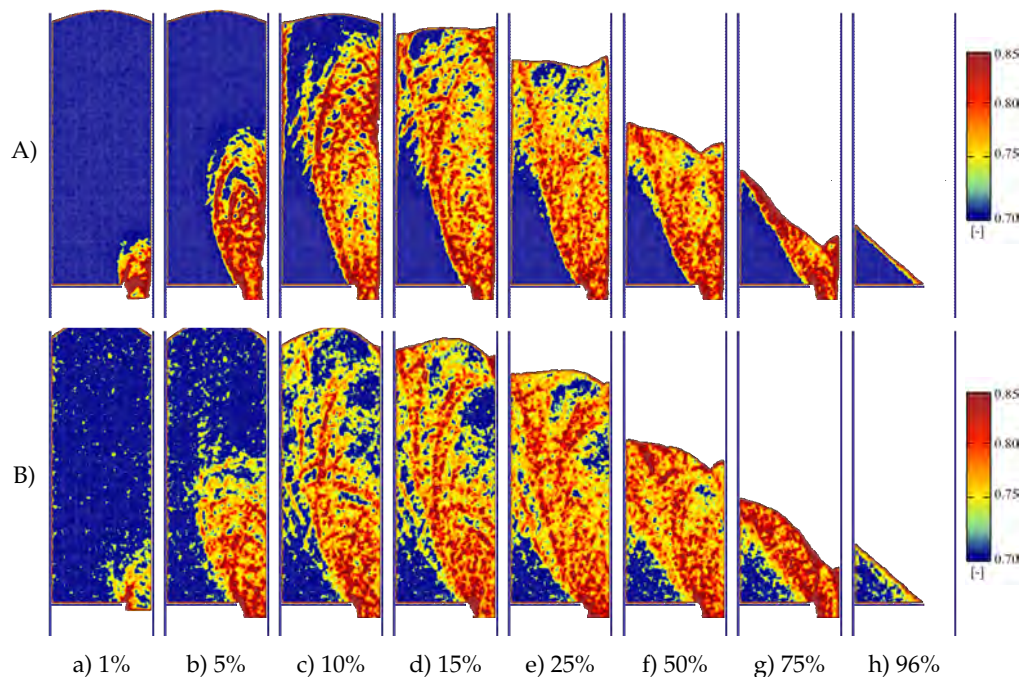


Figure 5.47: Distribution of void ratio at different stages of discharge for silo filled with initially medium-dense sand ( $e_0 = 0.60$ ) with asymmetric outlet of type '3' for different normalized roughness  $R_n$  of the walls: A)  $R_n = 1.00$  and B)  $R_n = 0.01$  (the percentages indicate the amount of sand that has flowed out of the silo).

Finally, the distribution of normal force chains during the discharge was studied (Figures 5.48-5.50). In the presented figures, the red color corresponds to the forces above the mean value, which was set to 0.02 N. The results demonstrate that these force networks were significantly influenced by the roughness of the walls. The most pronounced difference was observed in the case of the silo with an outlet of type '1', which highlighted a significant advantage of DEM. For the silo with rough walls, although the outlet was symmetrically located, the distribution of the normal force chains was strongly nonuniform and asymmetric due to the naturally heterogeneous assembly of the distinct particles. In this case, a significant increase in the value of the forces was observed not only in the region adjacent to the outlet, but also near the walls (Figures 5.48Ab-d). The grooves along the walls provided support for blocked particles, creating parabolic force chains. It can be observed that within the shear zones, numerous interactions between the particles were repeatedly broken and re-established. The local concentration of forces exerted on the silo walls appears to be random, both in location and size. Based on the force chains distribution, it is difficult to determine the trajectory and characteristics of the propagating shear zones. However, a comparison of the force network with the particle rotation distribution revealed that the vertical wall shear zones were characterized by the occurrence of major diagonal normal force chains. In the case of the silo with smooth walls, the normal forces were concentrated on the bottom wall near the joint with the vertical walls (Figure 5.48B). Contrary to the previous case, no significant changes in the force network were noted in the upper part of the sand. As a result, no random force concentration was observed on the vertical walls. This is in good agreement with previous results indicating the presence of mass flow. A slight asymmetry of the force chains was observed (Figure 5.48Bb). In both silo with rough and smooth walls, as the sand level decreased, the intensity and the number of the normal forces decreased.

The roughness of the walls also had a significant effect on the flow in the silo with an eccentric outlet (types '2' and '3'). It can be observed that during the discharge, the magnitude of the vertical normal forces was greater for the silo with smooth walls. This was due to the roughness of the wall, which implied that the sand was not supported by the wall grooves. Consequently, the greater vertical forces were exerted on the bottom plate than in the case of the silo with rough walls. It is noteworthy that parabolic force chains were observed in the flow zone of the silos with smooth walls (Figure 5.49Bc and Figure 5.50Bc). In all studied cases, the sand outside the flow zone is characterized by regions of pronounced normal forces, which were greater at the left side of the silo. In contrast, the funnel zone was characterized by weaker contact forces between the particles. In some parts of the zone, there was even a lack of contact forces (represented in the figures by white spaces), implying that the interactions between the particles have disappeared and the individual particles are falling freely towards the outlet. This highlights another advantage of DEM, i.e., its ability to handle the transition between the solid state (e.g., sand in the stagnant zone), quasi-fluid state (e.g., sand in the flow zone), and free-fall state (e.g., sand below the outlet) of granular materials.

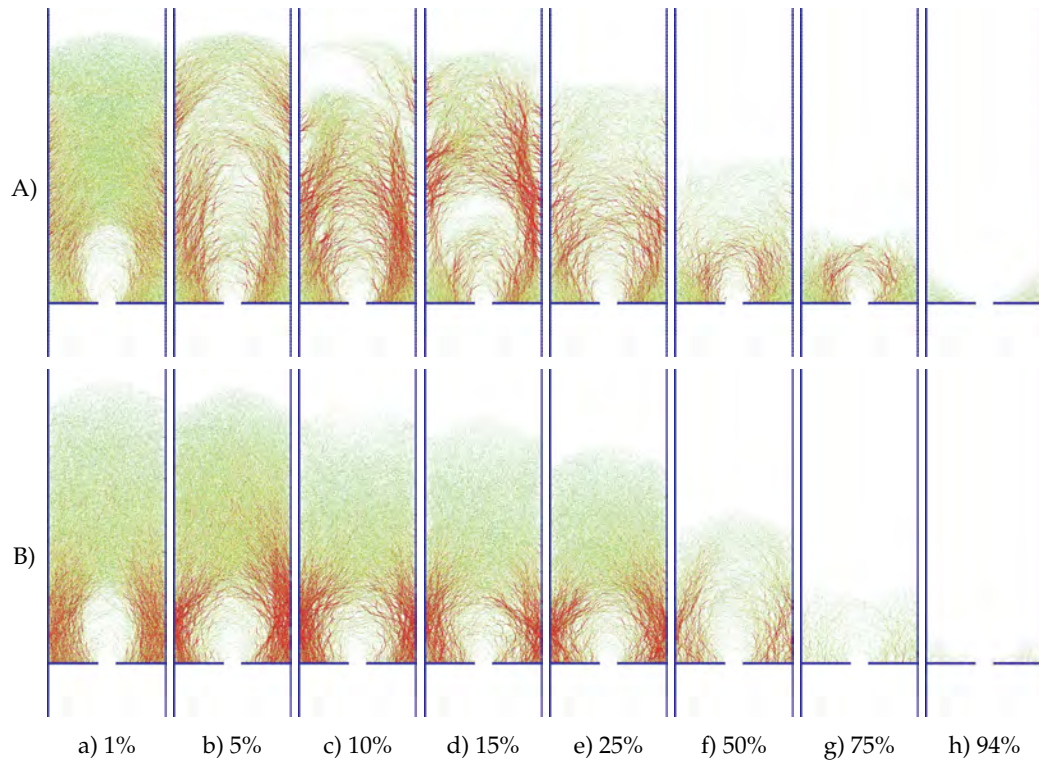


Figure 5.48: Distribution of normal force chains at different stages of discharge for silo filled with initially medium-dense sand ( $e_0 = 0.60$ ) with symmetric outlet of type '1' for different normalized roughness  $R_n$  of the walls: A)  $R_n = 1.00$  and B)  $R_n = 0.01$  (the percentages indicate the amount of sand that has flowed out of the silo).

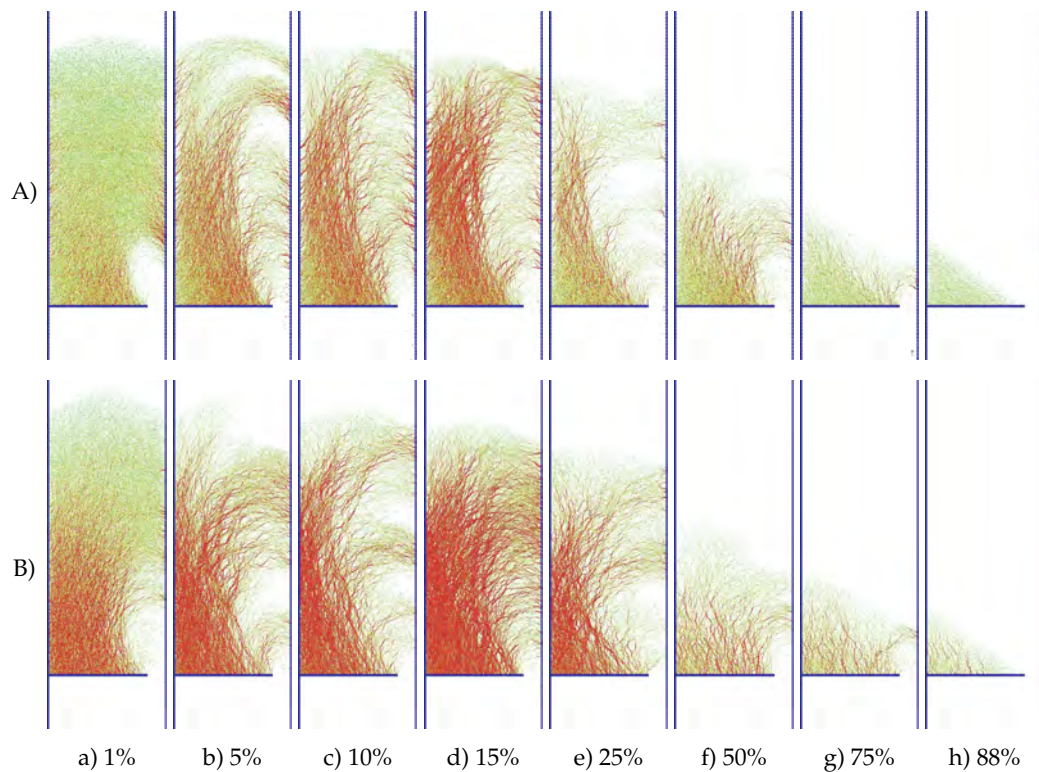


Figure 5.49: Distribution of normal force chains at different stages of discharge for silo filled with initially medium-dense sand ( $e_0 = 0.60$ ) with asymmetric outlet of type '2' for different normalized roughness  $R_n$  of the walls: A)  $R_n = 1.00$  and B)  $R_n = 0.01$  (the percentages indicate the amount of sand that has flowed out of the silo).

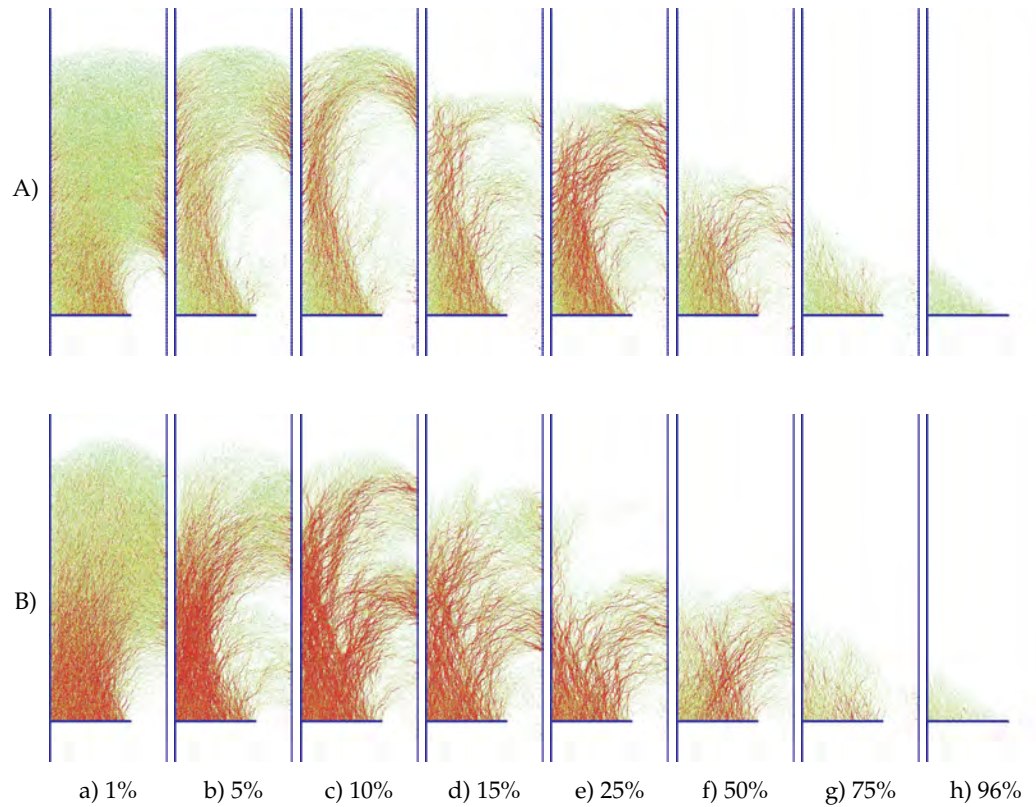


Figure 5.50: Distribution of normal force chains at different stages of discharge for silo filled with initially medium-dense sand ( $e_0 = 0.60$ ) with asymmetric outlet of type '3' for different normalized roughness  $R_n$  of the walls: A)  $R_n = 1.00$  and B)  $R_n = 0.01$  (the percentages indicate the amount of sand that has flowed out of the silo).

### Mesoscopic behavior of initially loose sand during flow in a silo with rough walls

Following the analysis of the flow of initially dense sand, the results of the grain-level behavior of initially loose sand ( $e_0=0.76$ ) for different locations and sizes of the outlet in the silo with rough walls ( $R_n=1.0$ ) are presented (Figures 5.51-5.54). At the beginning, the sand displacements obtained with the aid of colored sand layers were analyzed (Figure 5.51). In all studied cases, groups of particles were found to be locked between the grooves of the rough wall during the discharge. However, in contrast to the results for initially dense sand, no pronounced step-like profiles were observed. This implies that localized areas occurred primarily in the form of straight vertical shear zones at both walls. The flow of loose sand exhibited greater uniformity compared to the flow of dense sand. In all cases, mass flow was observed during discharge, resulting in slight changes in the shape of the top surface during flow.

The distribution of the particle rotations confirms the conclusions drawn from the displacement profiles. During the flow of initially loose sand, pronounced particle rotations were observed, with the majority occurring directly at the silo side walls. The mean thickness of these wall shear zones, determined from the particle rotations, was approximately  $t_s=25$  mm ( $=16-18 \times d_{50}$ ), which is consistent with the results for the initially dense sand. Based on rotations, the internal shear zones were significantly weaker and barely visible compared to those captured in initially dense sand (Figure 5.52).

Next, the void ratio distribution during flow was analyzed (Figure 5.53). In contrast to silos filled with initially dense sand, the initial distribution of sand porosity in the loose samples exhibited high nonuniformity (Figure 5.53a). Moreover, in these cases, the boundaries between the filling layers were noticeable at the beginning of the discharge. This was due to the method of preparation of the initial loose sample, where the damping was set at a higher value ( $\lambda_{d,prep}=0.3$ ) in comparison to the value set during the discharge ( $\lambda_d=0.01$ ), in order to obtain a looser sample. This reduced the kinetic energy of the particles during filling, resulting in a higher void ratios and increased heterogeneity of sand. Furthermore, the filling process also caused some loosening of the sand near the rough walls, especially between the wall grooves. Now, as for the flow, slight loosening of granular material was observed near the silo walls, which is consistent with the location of the shear zones. Significant loosening occurred in the flowing core near the outlet, in contrast to the sand located in the upper part of the silo, where material compaction was observed.

With regard to the distribution of normal force chains, the mean value of the forces was once again set to 0.02 N (Figure 5.54). The initially loose sample exhibited a greater mean normal force magnitude than the flow of the initially dense sand. This was due to the lower coordination number of the specimen. Similarly to the initially dense sand, numerous force chains were repeatedly broken and re-established within the vertical shear zones during discharge. Some minor curved force chains were also captured. In the initially loose material, the force network exhibited greater uniformity, i.e., there were no random significant concentrated loads generated on the walls as observed in the case of the silo with initially dense sand.

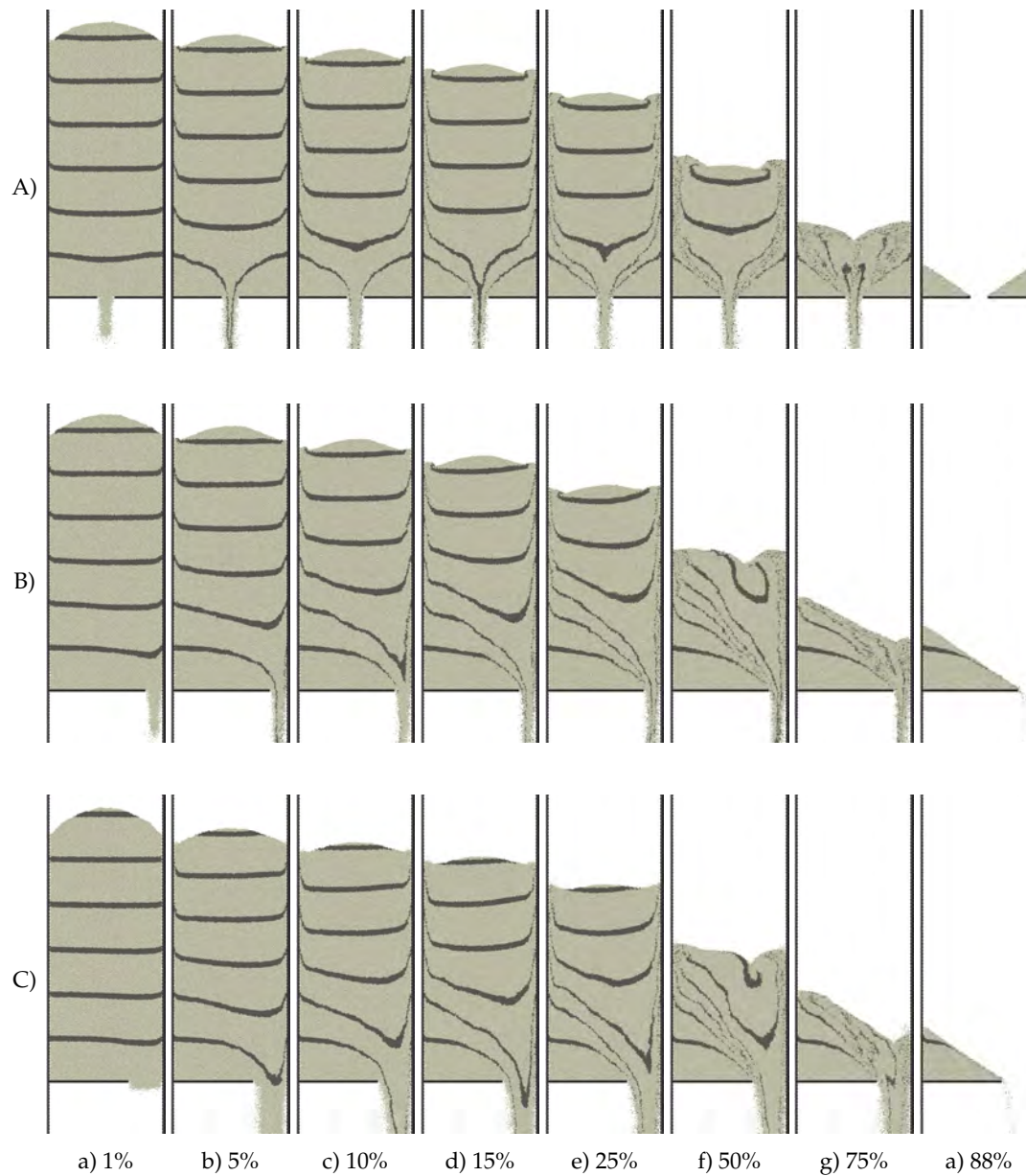


Figure 5.51: Sand deformation for initially loose sand ( $e_0 = 0.76$ ) during flow in silo with rough walls ( $R_n = 1.00$ ) with: A) symmetric outlet of type '1', B) asymmetric outlet of type '2' and C) asymmetric outlet of type '3' (percentages indicate the amount of sand that flow out of the silo).

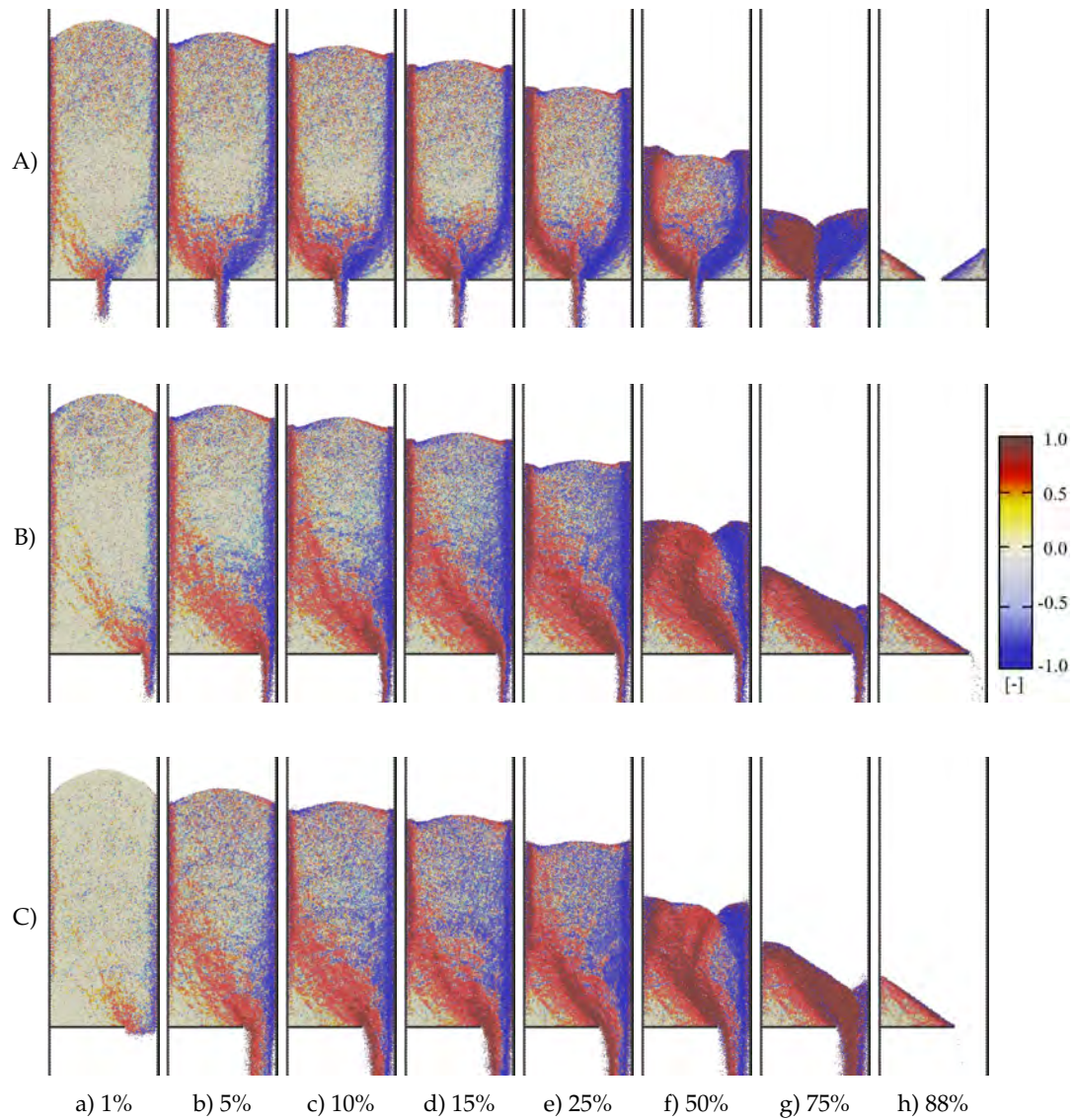


Figure 5.52: Distribution of particle rotations for initially loose sand ( $e_0 = 0.76$ ) during flow in silo with rough walls ( $R_n = 1.00$ ) with: A) symmetric outlet of type '1', B) asymmetric outlet of type '2' and C) asymmetric outlet of type '3' (percentages indicate the amount of sand that flow out of the silo).

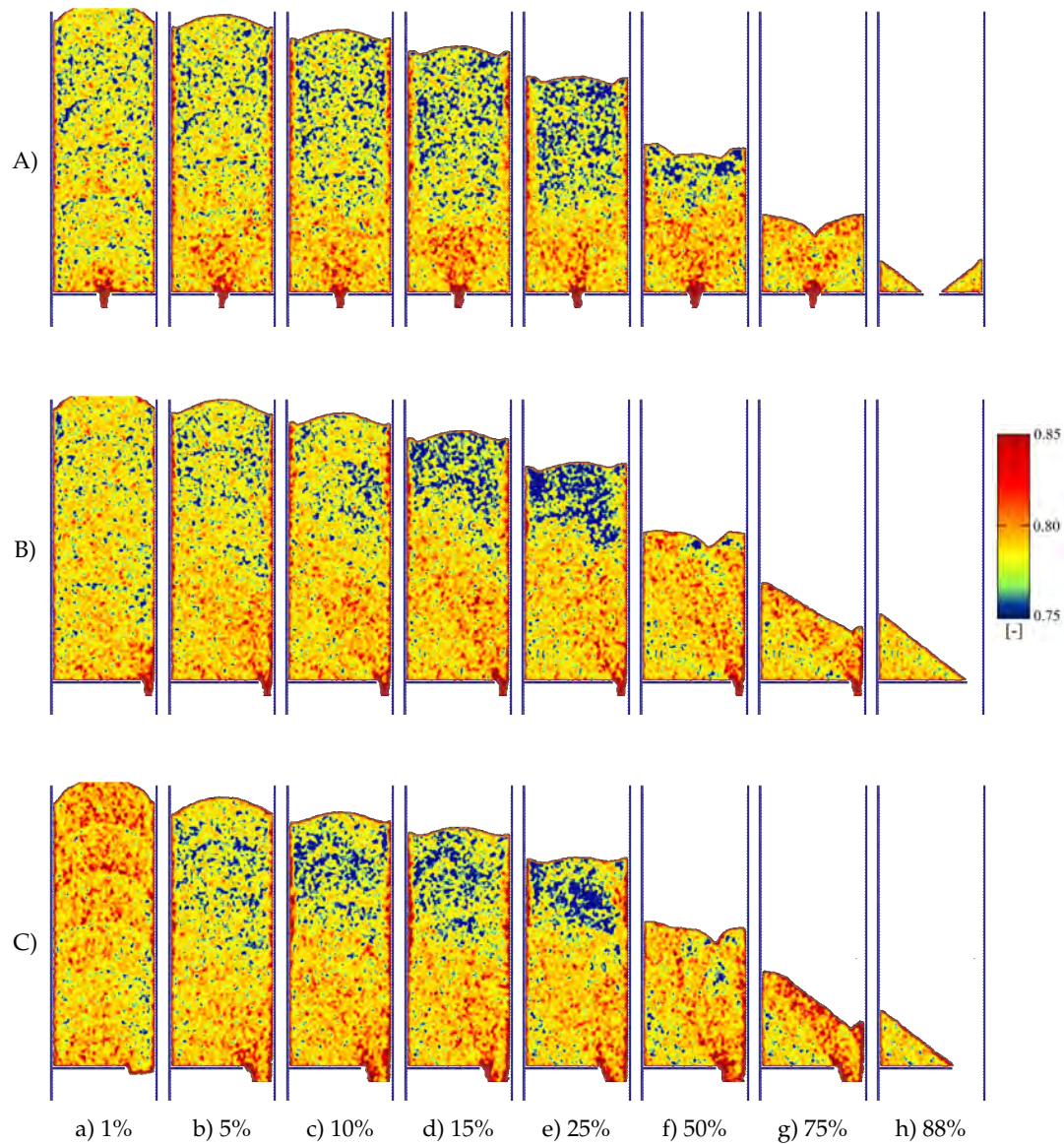


Figure 5.53: Distribution of void ratio for initially loose sand ( $e_0 = 0.76$ ) during flow in silo with rough walls ( $R_n = 1.00$ ) with: A) symmetric outlet of type '1', B) asymmetric outlet of type '2' and C) asymmetric outlet of type '3' (percentages indicate the amount of sand that flow out of the silo).

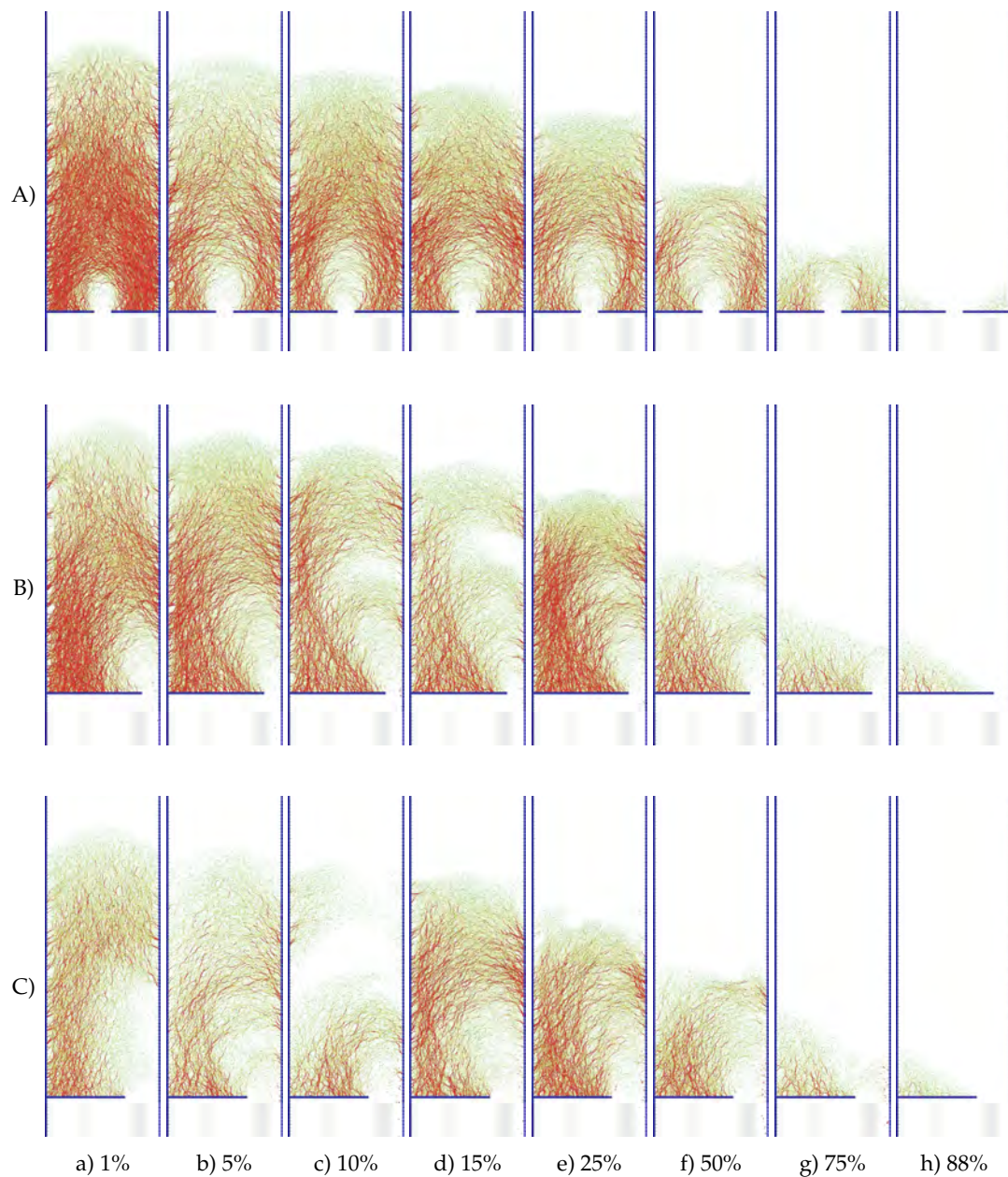


Figure 5.54: Distribution of normal force chains for initially loose sand ( $e_0 = 0.76$ ) during flow in silo with rough walls ( $R_n = 1.00$ ) with: A) symmetric outlet of type '1', B) asymmetric outlet of type '2' and C) asymmetric outlet of type '3' (percentages indicate the amount of sand that flow out of the silo).

### Distribution of wall stresses

Finally, the distribution of the horizontal  $\sigma_{11}$  and vertical  $\sigma_{21}$  stresses acting on the walls during the discharge is presented. These stresses were calculated according to the Love-Webber formula used earlier in the thesis (see Chapter 4.3 for explanation). Figures 5.55-5.63 show the stresses along the left and right walls of the silo at three stages of the tests. The first, referred to as the initial state in the figures, is the distribution of stresses after filling. The second, referred to as the maximum state, shows the stress distribution at the time of the highest  $T$  and  $N$  values (depending on the case, the maximum stresses were calculated after 1% to 10% of the sand had flowed out of the silo). The last one, referred to as the residual phase, shows the stresses after the peak of the  $T$  and  $N$  forces, when half of the silo was already empty.

The changes in the distribution of wall stresses during the discharge was significantly affected by a flow pattern of moving granular material and depended on the initial void ratio of sand and the roughness of the walls. For the symmetric flow (outlet of type '1') the highest wall horizontal stresses occurred in the silo with smooth walls filled with initially dense sand (Figure 5.56). In this case, the maximum horizontal wall stress of  $\sigma_{11,max}=5.3$  kPa was exerted on the bottom of left wall. A strong increase of the stresses was also observed in the case of the silo with rough walls ( $R_n=1.0$ ) filled with initially loose sand ( $e_0=0.76$ ), reaching  $\sigma_{11,max}=5.0$  kPa at the right wall (Figure 5.61). In both these cases, the flow of sand caused the increase of the  $\sigma_{11}$  above the effective transition point located at the border of the stagnant zone. Below that point, the horizontal stress decreased, reaching almost zero at the connection with the bottom wall. In both these cases the mass flow was observed. On the other hand, the lowest increase of the horizontal stress was observed during the symmetric flow (outlet of type '1') in the silo with rough walls ( $R_n=1.0$ ) (Figure 5.55). However, in this case, the shear stresses acting on walls during the discharge were obviously higher than in the silo with smooth walls, particularly in the initial phase of the flow. Similar evolution and magnitudes of both horizontal ( $\sigma_{11,max} = 2.0$  kPa) and shear stresses ( $\sigma_{12,max}=1.5$  kPa) were calculated by Krzyżanowski et al. (2021) using MPM at the end of filling for the same geometry of the silo (except for the outlet size, which was 80 mm wide). At the maximum state, these stresses obtained in DEM (Figure 5.55) exhibited significantly lower fluctuations than the ones calculated using MPM. However, this was partly due to the wider silo outlet, which introduced additional dynamics in the MPM study. For the symmetric silo with smooth walls (Figure 5.56), the calculated stresses were in accordance with the state of the earth pressure at rest with the small value of the shear wall pressures. This was due to the small contact friction angle, both material and geometric, applied to the silo walls.

During the flow in the silo with asymmetric outlets (outlet of type '2' and '3') with rough walls ( $R_n=1.0$ ), a significant asymmetry in the distribution of the stresses exerted on both walls was observed (Figures 5.57, 5.59, 5.62, and 5.63). In these cases, only slight increase in the stresses exerted on the wall opposite to the flow (the wall on the left side of the silo) were observed during the discharge. This was due to the stagnant zone observed on the this side of the silo. On the other hand, there was a notable drop in both the horizontal and shear stresses exerted on the right wall during discharge, occurring between the outlet level and a height of approximately 20 cm above the silo outlet. This was caused by the significant loosening of the sand in



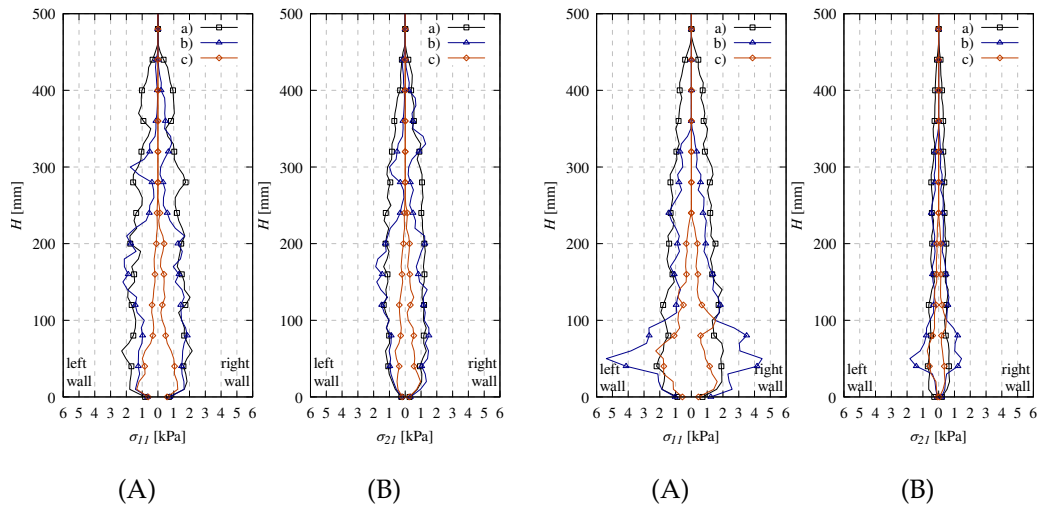


Figure 5.55: Calculated distribution of: A) wall horizontal stresses  $\sigma_{11}$  and B) wall shear stresses  $\sigma_{21}$  during the flow in silo at the: a) initial state, b) maximum state and c) in the residual phase (type '1',  $e_0=0.60$ ,  $R_n=1.00$ ).

Figure 5.56: Calculated distribution of: A) wall horizontal stresses  $\sigma_{11}$  and B) wall shear stresses  $\sigma_{21}$  during the flow in silo at the: a) initial state, b) maximum state and c) in the residual phase (type '1',  $e_0=0.60$ ,  $R_n=0.01$ ).

the region of the outlet (see the void ratio distribution during the flow presented in the previous section, e.g. Figure 5.46), where a significant amount of the particles located at the wall backed up and flowed out of the silo. During the eccentric flow, the maximum horizontal and shear wall stresses acting on the walls were obtained for the silo with rough walls ( $R_n=1.0$ ) and with the outlet of type '3', filled with initially dense sand ( $e_0=0.60$ ) (Figure 5.59). The stresses exerted on the left wall were respectively  $\sigma_{11,max}=2.9$  kPa and  $\sigma_{21,max}=2.4$  kPa, and the stresses exerted on the right wall were respectively  $\sigma_{11,max}=4.4$  kPa and  $\sigma_{21,max}=2.9$  kPa. The great magnitude of these forces was partially caused by the dynamics of the system. During the discharge of the silo with the biggest outlet, part of the particles randomly bounced and hit the silo walls.

In the case of asymmetric flow (outlet of type '2' and '3') in the silo with smooth walls ( $R_n=0.01$ ) filled with initially dense sand ( $e_0=0.60$ ) the shear wall stresses were smaller compare to the stresses in the silos with rough walls. In general, the stress acting on the bottom part of the right wall, decreased as the eccentricity of the outlet increased, which is consistent with other studies (Guaita et al., 2003; Krzyżanowski et al., 2021). On the other hand, such agreement was not found in the case of the horizontal stress acting on the wall opposite to the flow. Similarly as in the case of the eccentric flow in the silo with rough walls, the drop in the magnitude of horizontal stresses observed in the region adjacent to the outlet was connected to the loosening of granular material in the flow zone (Figures 5.58 and 5.60). The highest horizontal stresses were calculated for the silo with the smaller eccentric outlet and were respectively  $\sigma_{11,max}=3.4$  kPa in the case of the left wall and  $\sigma_{11,max}=3.0$  kPa in the case of the right wall.

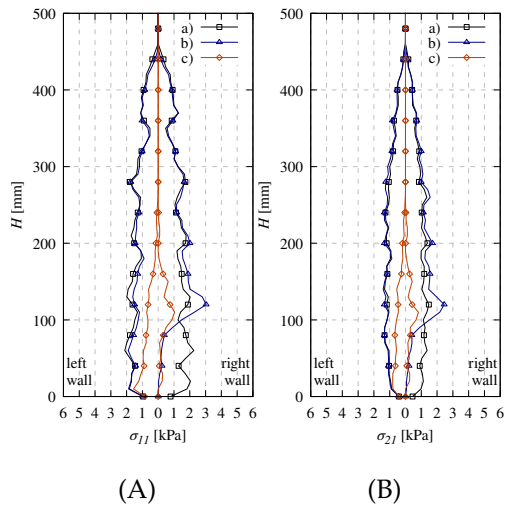


Figure 5.57: Calculated distribution of: A) wall horizontal stresses  $\sigma_{11}$  and B) wall shear stresses  $\sigma_{21}$  during the flow in silo at the: a) initial state, b) maximum state and c) in the residual phase (type '2',  $e_0=0.60$ ,  $R_n=1.00$ ).

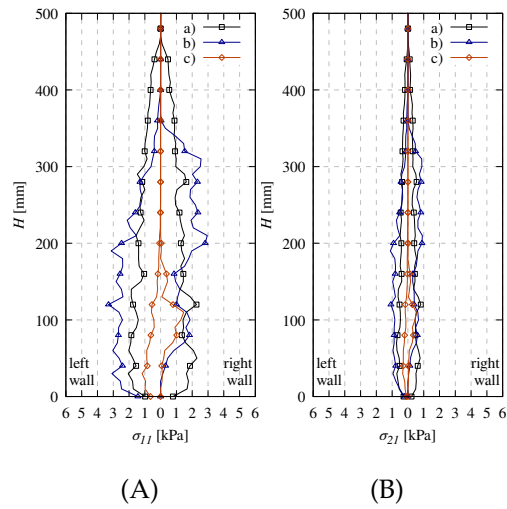


Figure 5.58: Calculated distribution of: A) wall horizontal stresses  $\sigma_{11}$  and B) wall shear stresses  $\sigma_{21}$  during the flow in silo at the: a) initial state, b) maximum state and c) in the residual phase (type '2',  $e_0=0.60$ ,  $R_n=0.01$ ).

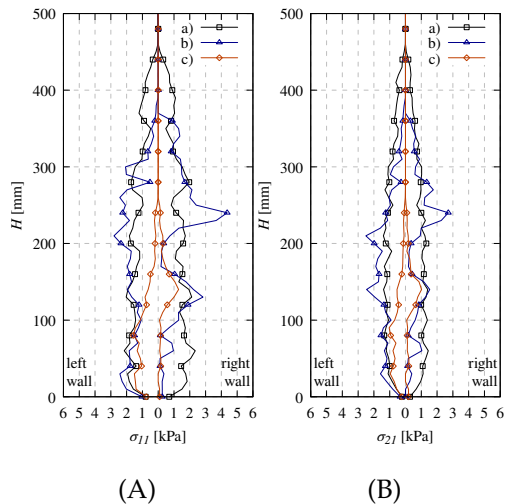


Figure 5.59: Calculated distribution of: A) wall horizontal stresses  $\sigma_{11}$  and B) wall shear stresses  $\sigma_{21}$  during the flow in silo at the: a) initial state, b) maximum state and c) in the residual phase (type '3',  $e_0 = 0.60$ ,  $R_n = 1.0$ )

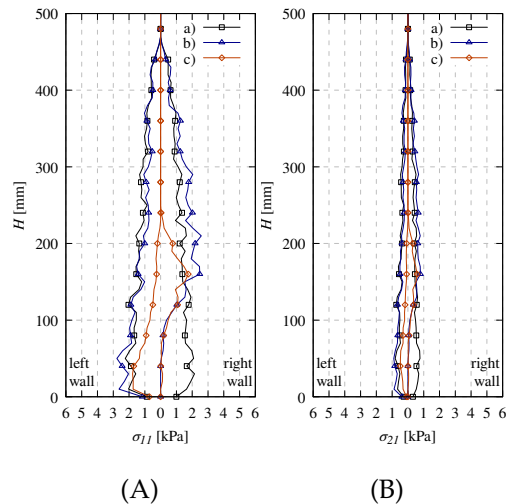


Figure 5.60: Calculated distribution of: A) wall horizontal stresses  $\sigma_{11}$  and B) wall shear stresses  $\sigma_{21}$  during the flow in silo at the: a) initial state, b) maximum state and c) in the residual phase (type '3',  $e_0 = 0.60$ ,  $R_n = 0.01$ )

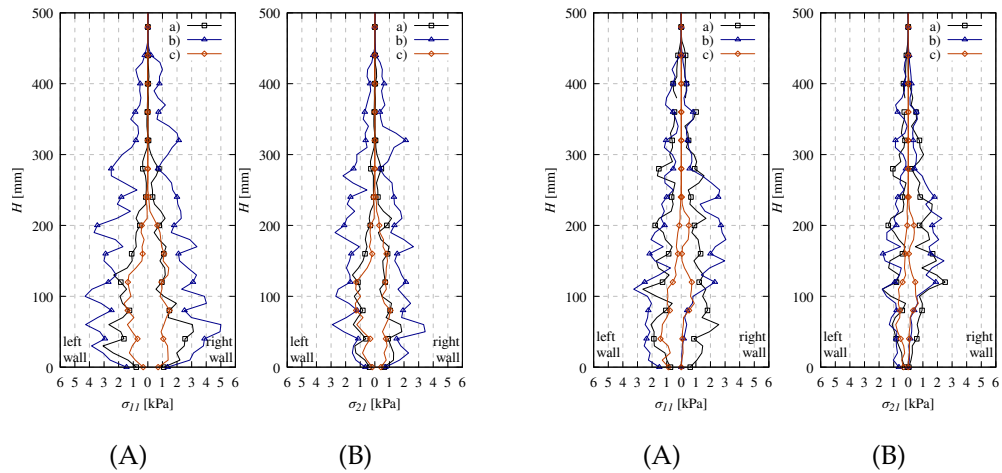


Figure 5.61: Calculated distribution of: A) wall horizontal stresses  $\sigma_{11}$  and B) wall shear stresses  $\sigma_{21}$  during the flow in silo at the: a) initial state, b) maximum state and c) in the residual phase (type '1',  $e_0 = 0.76$ ,  $R_{fl} = 1.0$ )

Figure 5.62: Calculated distribution of: A) wall horizontal stresses  $\sigma_{11}$  and B) wall shear stresses  $\sigma_{21}$  during the flow in silo at the: a) initial state, b) maximum state and c) in the residual phase (type '2',  $e_0 = 0.76$ ,  $R_{fl} = 1.0$ )

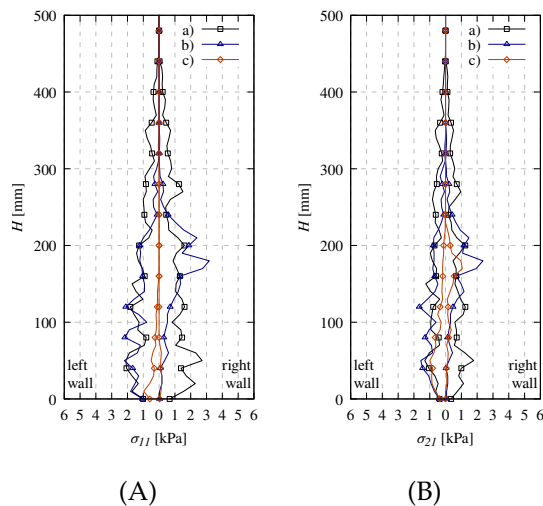


Figure 5.63: Calculated distribution of: A) wall horizontal stresses  $\sigma_{11}$  and B) wall shear stresses  $\sigma_{21}$  during the flow in silo at the: a) initial state, b) maximum state and c) in the residual phase (type '3',  $e_0 = 0.76$ ,  $R_{fl} = 1.0$ )



## 5.4 Summary

In this section, a detailed discrete analysis of quasi-static flow with controlled bottom velocity and gravitational flow of cohesionless sand in a laboratory-scale silo with parallel walls was presented. During the study, the influence of wall roughness and initial void ratio of the sand on the shear localization was studied. In addition, the effect of the size and location of the silo outlet was analyzed. The following main conclusions can be drawn from the simulations:

- The DEM showed the potential to model the confined granular flow in silo. Discrete results were consistent with the experimental results available in the literature. The DEM model realistically captured the nonlinear behavior of sand, including the formation of shear localization, both in the form of curvilinear internal and vertical wall shear zones. The significant advantage of the discrete method was its ability to capture both meso- and macroscopic behavior of sand.
- The silo wall roughness and the initial void ratio of the sand significantly affected the resultant forces acting on both the bottom and side walls of the silo. The evolution of the curves was in good agreement with the laboratory data. However, noticeable differences occurred in the magnitude of the forces obtained numerically, experimentally, and theoretically. The numerical results differed from the experimental ones due to certain simplifications assumed in the discrete model, such as a greater mean grain diameter and an artificially uniform geometry of the walls. The discrepancies with the theoretical results were due to the fact that the formulas did not take into account the complex deformation of the sand.
- In general, the maximum horizontal wall stresses occurred in silos with smooth walls and initially loose sand, while the maximum wall shear stresses occurred in silos with very rough walls and initially dense sand. The stresses were influenced by the location and size of the outlet. In the case of an asymmetrical outlet, a significant increase in stress was observed at the wall where the flow occurred, both in initially dense and loose sand. Near the outlet at the same wall, the magnitude of the forces tended to zero. The stress distribution in the silo with symmetrical outlet was more uniform, due to the fact that in this case the funnel flow occurred in the initial phase of the flow.
- The geometry of both internal shear zones and granular flow was affected by the roughness of the walls and the initial void ratio of the sand. Curvilinear localizations were most clearly observed during quasi-static flow in a silo with very rough walls filled with initially dense sand. Slightly weaker internal shear zones were observed in the case of initially dense sand in silos with rough walls. Finally, some weak curvilinear shear zones were noticeable in silos with very rough walls filled with initially loose sand. Within the localized zones, an increase in both particle rotations and void ratio was observed. These variables increased with increasing wall roughness and decreasing initial void ratio.



- The shear localization and the pattern of granular flow was also influenced by the location and size of the outlet. The internal shear zones within the initially dense sand were observed in the silo with rough walls for all types of studied outlets. In addition, in the case of asymmetric outlets, the internal shear zones were also captured in the silo with smooth walls. In the case of the initially loose sand, the shear localization occurred along the vertical walls, with barely noticeable internal curvilinear shear zones. In the case of silo with smooth walls and symmetric outlet barely visible internal shear zones occurred in the region adjacent to the outlet.
- As the wall roughness increased, the inhomogeneity of the normal contact forces increased. For quasi-static flow of initially dense sand in rough and very rough wall silos, the force chains showed a parabolic shape. With increasing wall roughness and decreasing initial sand density, the average orientation of the contact forces to the horizontal decreased. In a silo with rough and very rough walls, for both types of flow, numerous contacts characterized by a significant normal force are repeatedly broken and re-established during discharge. At the onset of these force chains, there is a concentration of loads exerted on the walls.
- The internal shear zone tended to initiate at multiple points along the wall. In addition, in the case of a silo with very rough walls and initially dense sand, the shear localizations exhibited an almost periodic pattern. The presence of internal shear zones contributed to the nonuniform distribution of sand density within the sample and the irregular distribution of wall pressures during flow. The higher oscillations of the resultant forces exerted on the silo structure can be attributed to the occurrence of parabolic shear zones.

## Chapter 6

# Conclusions and future research directions

### 6.1 Conclusions

This concluding chapter presents a summary of the findings from the thesis, and presents general conclusions drawn from the comprehensive study of these phenomena. Detailed conclusions related to the various aspects analyzed in the study of shear zone phenomena in granular materials during confined silo flow are provided in the Chapters 4 and 5. The following general conclusions can be drawn:

#### Soil mechanics tests:

- Discrete Element Method presented the potential to realistically model the shear localization within granular material by using numerical models composed of perfectly spherical particles with rotational resistance, and irregularly shaped clumps composed of spheres during typical soil mechanics tests. Discrete results produced trends which are consistent with those observed in physical experiments, by taking into consideration different modeling conditions, such as initial void ratio and the load applied to the sand specimen.
- Discrete Element Method allowed to capture the mesoscopic phenomena within the deforming granular material. The formation of the shear zone is characterized by pronounced particle rotations, increase of porosity and the increase of normal forces between the particles. Moreover, the shearing resulted in change of the forces orientation. These grain-level characteristics depend on the shape of the particles. For the clumped particles the shear zone thickness was smaller and the particle rotations were higher comparing to the spheres with rotational resistance. Therefore, the shear zone thickness depend on the particle shape. The changes in the void ratio during the shearing were similar for both types of particles.
- The location and thickness of the shear zone significantly influence the forces and loads exerted by the granular media on the surrounding structures. Surface pressures increase with the size of asperities, such as the height of grooves or the depth of corrugations. Loads from the granular material to the structure are transferred through columns of particles within the interface shear zone, which are repeatedly broken and re-established. The reorganization of

the particle chains causes the random local concentration of loads acting on the surface during the test.

- Mesoscopic characteristics obtained in discrete analysis were used to describe the boundary conditions at the interface between granular material and the structure. These ratios can only be applied to 2D continuum models of such interactions, as the boundary condition for the twist in the contact plane between the bodies was not prescribed. The proposed boundary conditions depend on the shape of the particles.
- Characteristic phenomena for silo constructions made of corrugated steel sheets were captured in the interface study of the contact zone between the sand and the sinusoidal surfaces. During the tests, the stationary zones located in the valleys were separated from the moving zones by the shear localizations. The extent of shear localization within the granular material and on the corrugated surface, and consequently the wall contact factor, can be determined from the overall strength of the interface. In addition, this extent can be qualitatively estimated from measurements of the strains occurring at the boundary of the granular material-structure system.

#### **Confined granular flow in silo:**

- Discrete Element Method presented the potential to realistically model the shear localization within granular material during silo flow by using discrete model composed of spherical particles with rotational resistance. Numerical results produced trends which are consistent with those observed in physical experiments, by taking into consideration different test conditions, such as initial void ratio, roughness of the walls and size and location of the silo outlet.
- The discrete model captured both vertical wall shear zones and internal curvilinear shear zones within the granular material. The geometry of the internal shear zones was influenced by the roughness of the walls, the initial void ratio of the sand, and the size and location of the silo outlet. Vertical wall shear zones occurred primarily in silos with rough and very rough walls, regardless of the initial void ratio. Internal curvilinear shear zones were observed in quasi-static flow of initially dense sand in rough and very rough wall silos and in gravitational flow in rough wall silos, regardless of the outlet location. In addition, in the case of asymmetric outlets, internal shear zones were also captured in silos with smooth walls.
- Discrete Element Method allowed to capture the mesoscopic phenomena within the sand during the quasi-static and gravitational confined granular flow in laboratory-scale silo. The formation of both wall and internal shear zones is characterized by pronounced particle rotations and an increase in the sand void ratio. In some cases, particularly during the flow of initially dense sand in a silo with rough walls, the inhomogeneity of the force chain network increases. In these instances, the force chains tend to form parabolic arcs with multiple onset points on both sides of the silo.

- The flow pattern is closely related to the trajectory and location of shear zones. The propagation of internal shear zones contribute to the non-uniform distribution of sand mass within the sample. As a result, the formation of these zones has a significant influence on the forces and loads exerted on the silo structure. Therefore, accurate modeling of shear zone formation is crucial, as it profoundly affect the distribution of loads acting on the structure.

## 6.2 Future research directions

Several research gaps remain in the field of silo construction. The following research steps are planned in the future:

- The study of shear zone formation within granular material during confined silo flow will be further improved and extended. Some numerical procedures used during the study, such as the preparation process of initially loose samples, require improvement. In the presented research certain simplifications were employed, such as geometry of the silo walls and particle shapes. Among many, future studies should consider using other types of materials (e.g., wheat) composed of non-spherical (e.g., clumped or polyhedral) particles during the flow analysis. In addition, the accuracy of the discrete model can be enhanced by the application of other contact laws, including nonlinear ones. Finally, as computational efficiency increases, the scale of the problems under study can be expanded. Simultaneously, the investigated problems can also be scaled by using continuum approaches and by implementing proposed boundary conditions.
- The study of the contact zone between the granular material and corrugated silo walls will be continued and extended. In silos with corrugated walls supported by thin-walled columns, the properties of this interface play a major role in the correct determination of the vertical loads acting on the silo structure. Discrete and experimental study on this subject are carried out within the PRELUDIUM 21 project entitled "Experimental and numerical (DEM) analysis of the contact zone between granular material and corrugated surface during silo flow", financed by the National Science Centre, Poland (NCN) (UMO-2022/45/N/ST8/03567).
- Discrete study of the self-excited dynamic-acoustic effects in silos during granular flow. This type of phenomenon can cause dynamic interactions between the granular material and the surrounding structure, leading to resonant behavior of the system. As a result, silo structures may exhibit characteristic acoustic phenomena known as "silo music" or even dynamic failures. Despite extensive research, this phenomenon is not yet fully understood. The Discrete Element Method appears to be the appropriate tool for studying this subject, by taking into account the interaction between granular material composed of distinct grains and flexible silo walls.

## Appendix A

# Experimental analysis of interface behavior between sand and corrugated surfaces

The Appendix A documents own experimental analysis of interface behavior between sand and corrugated sinusoidal surfaces performed by A. Grabowski, M. Nitka, J. Konkol, and M. Wójcik, which is currently under review. The author of the thesis participated in all the conducted laboratory tests and performed the entire DIC analysis.

### A.1 Introduction

The study presented in the following section deals with experimental investigations of the interface between granular material and a sinusoidal corrugated surface. As presented earlier (see Chapter 4.4 for the full introduction), the current understanding of the mechanical processes occurring in the bulk solid-corrugated wall regime is relatively limited. The available literature (Moore et al., 1984; Molenda et al., 2002; Wiącek et al., 2021; Wiącek et al., 2023) shows that the addressed issue is an interesting problem for many civil and agricultural researchers and engineers. These studies show that many mechanical aspects of such interfaces are still understudied and need further research.

The investigation presented in the following appendix focuses on the analysis of grain level events using a direct shear apparatus commonly employed in soil mechanics. In the study, a custom-built shear box was used. During the analysis, the silo corrugated steel walls were mimicked by 3D printed corrugated sinusoidal surfaces made of PLA material. The Digital Image Correlation (DIC) technique provided insights into the formation of the shear zone in the granular material-corrugated surface contact zone.

### A.2 Experimental methods and materials

#### A.2.1 Shear apparatus and granular material

In this study, all tests were conducted using a direct shear apparatus. This device is widely used in soil mechanics to determine the frictional properties of soils (Tejchman and Wu, 1995; DeJong et al., 2003; Hu and Pu, 2004; Su et al., 2018; Zhao and



Zhao, 2019). In the laboratory analysis, the digital shear machine Matest Shearlab S276 was used. The apparatus and shear box were modified to provide photographic data for Digital Image Correlation (DIC) analysis of the interface shear behavior (Figure A.1). To obtain photographs of specimen deformation, the front and back walls of the shear box, parallel to the shear direction, were made transparent by using 8 mm thick Perspex. Other parts of the shear box, such as the bottom and top loading frames, were custom made using PLA thermoplastic material (Figure A.2a). These parts were constructed with 3D printing technology. The overall modification of the apparatus allowed for an accurate and detailed analysis of the bulk solid-corrugated surface regime behavior during the test, while maintaining the integrity of the experimental setup. To verify the accuracy of the 3D printed direct shear device, the results of the direct shear test of sand using the modified device were compared to the results obtained using a typical brass shear box (Figure A.3).

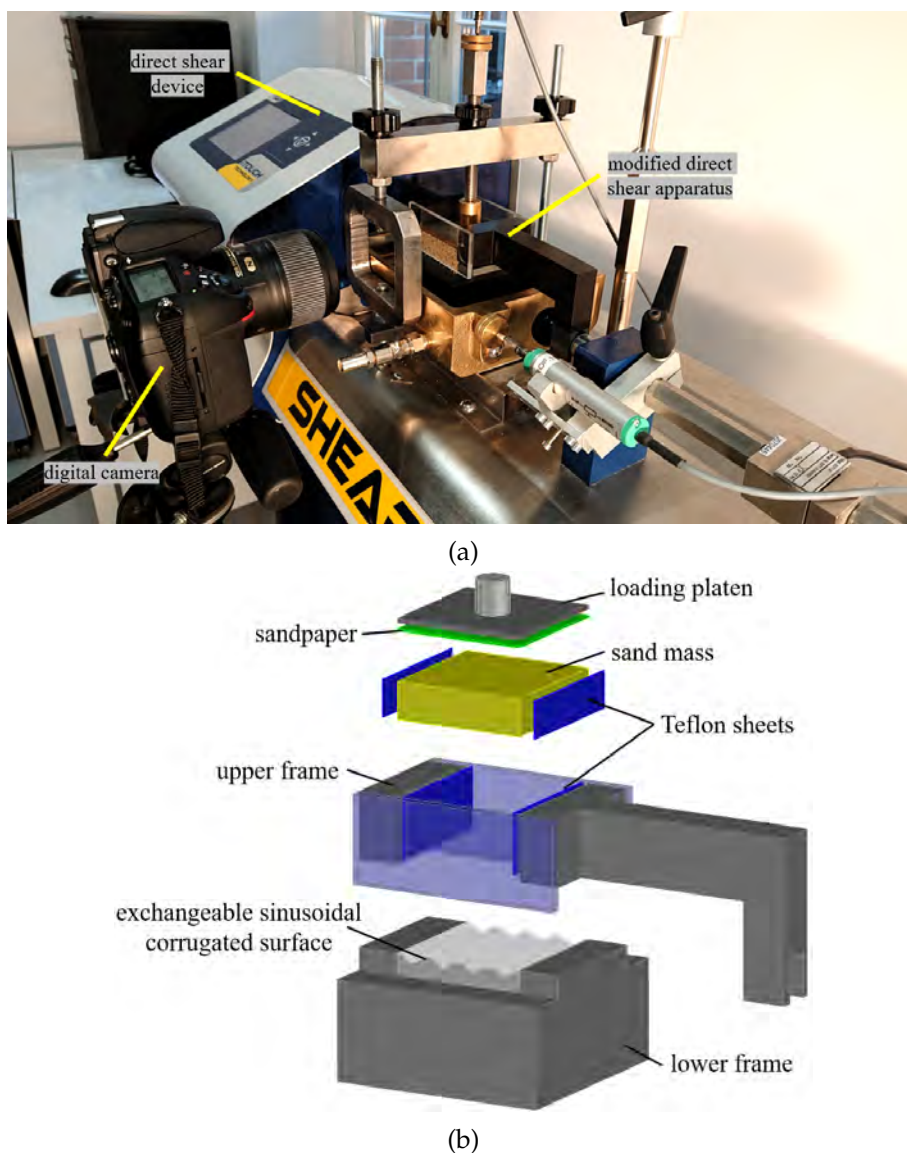


Figure A.1: Experimental setup: a) photograph of the experimental setup with a sand sample prepared for the shear test and b) computer visualization of individual parts of the modified box of the direct shear apparatus (Grabowski et al. (2023), CC BY 4.0).

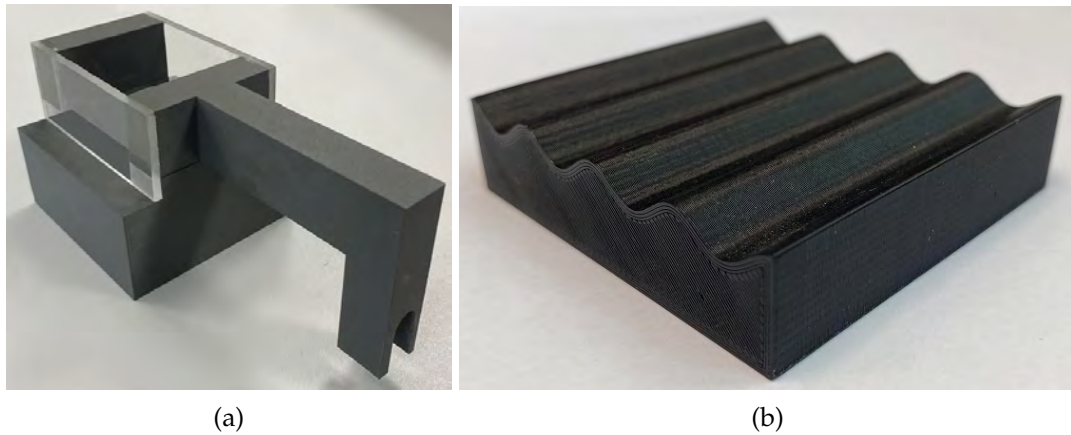


Figure A.2: Photograph of: a) a PLA-printed shear box, and b) an exemplary PLA-printed sinusoidal corrugated surface used during the investigation.

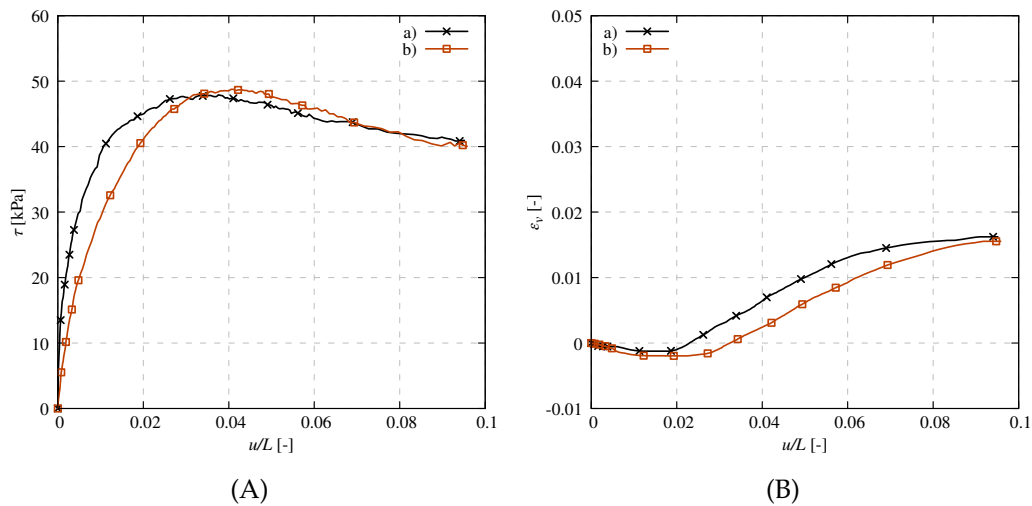


Figure A.3: Evolution of: A) mobilized shear stress  $\tau$  and B) volumetric strain  $\varepsilon_v$  versus normalized horizontal displacement  $u/L$  for sample composed of cohesionless sand obtained in direct shear test for: a) brass shear box and b) PLA printed shear box ( $e_0=0.63$  and  $\sigma_n=48$  kPa).

In addition to the shear box, 3D printing technology allowed for the creation of sinusoidal corrugated surfaces with various geometries (the example of the 3D-printed surface is shown in Figure A.2b). In the study, six different surface profiles were examined: one completely flat and the rest based on the geometry of sinusoidal corrugations of the silo wall. The corrugations had different depths, i.e., the distance between the crests of the profile (Figure A.4), ranging from 0.8 mm to 6.4 mm with a step of 1.4 mm. All corrugations had the same wavelength equal to  $l=15$  mm. As a result, the depth to wavelength ratio  $d/l$ , referred to as the corrugation coefficient in the appendix for clarity, ranged from 0 to 0.427. The study extended the analyzed range of the corrugation coefficient beyond the typical values for silos with sinusoidal corrugated sheeting, which usually cover the range of 0.11 to 0.24 (Molenda et al., 2002). However, the size of the corrugations was reduced due to the limitations of the shear apparatus, which was only able to handle a 60 by 60 mm sample. The profiles used in the tests were approximately 5 times smaller than the full-size

silo corrugated sheet. The ratio between the corrugation depth and the mean grain size varied from 1.13 (for a corrugation coefficient  $d/l=0.053$ ) to 9.01 (for a ratio of  $d/l=0.427$ ).

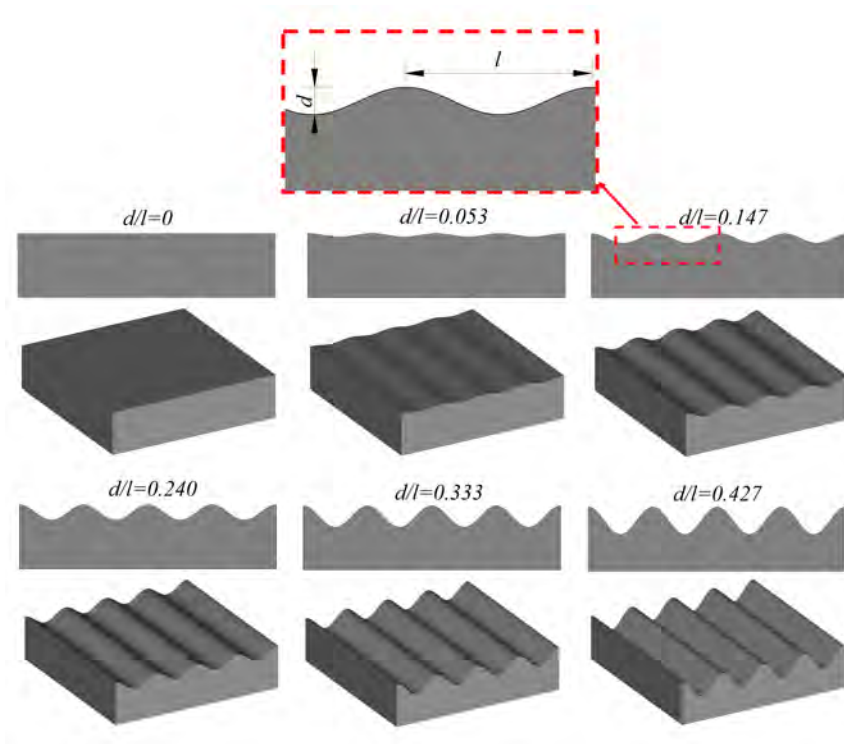


Figure A.4: Cross-sections (3D STL models) of sinusoidal corrugated surfaces used in experiments with different corrugation coefficients  $d/l$  (Grabowski et al. (2023), CC BY 4.0).

A medium-dense quartz sand with grain sizes between 0.25 mm and 1 mm with a mean grain diameter of  $d_{50}=0.71$  mm was selected for the experimental study (Figure A.5). The sand contained 10% particles in the range of 0.25 mm to 0.5 mm, while the remaining 90% of the grains were in the range of 0.5 mm to 1.0 mm. Table A.1 summarizes the basic physical and mechanical properties of the sand obtained from extensive laboratory geotechnical analysis. These parameters are typical for similar sand types, for example Bareither et al. (2008). Figure A.3 presents exemplary results of mobilized shear stress and volumetric strain for the studied sand sample obtained during shearing in a direct shear test apparatus (without interface). The comparison shows the macroscopic response of the sand during the shear test performed with a typical brass shear box and the PLA printed shear box used in the present study. The initial void ratio was  $e_0=0.63$ , and the vertical pressure applied to the top platen was  $\sigma_n=48$  kPa. The evolution of the two curves obtained with the 3D printed shear box showed good agreement with the results for the brass shear box, both in terms of maximum and critical values of the curves. The most noticeable difference was observed in the stiffness of the sand response, which was higher when using the metal shear box compared to the PLA printed one. This was due to the different stiffness and weight of the shear boxes. In the direct shear test, the sand exhibited typical behavior expected for a cohesionless, medium-dense sand sample undergoing shearing, initially showing hardening associated with contractancy, followed by the softening associated with dilatancy.



Figure A.5: Exemplary photograph of dry cohesionless sand used in the experiments.

Table A.1: Properties of dry cohesionless sand used in the experiments (Grabowski et al. (2023), CC BY 4.0).

| Parameter   | Value           | Units                  |
|---|-----------------|------------------------|
| Relative density $D_r$                                  | $55 \pm 5$      | %                      |
| Specific gravity $G_s$                                  | $2.64 \pm 0.02$ | -                      |
| Dry bulk density $\rho_d$                               | $1.64 \pm 0.02$ | $\text{g}/\text{cm}^3$ |
| Void ratio $e$  | $0.63 \pm 0.03$ | -                      |
| Minimal void ratio $e_{min}$                            | 0.49            | -                      |
| Maximal void ratio $e_{max}$                            | 0.74            | -                      |
| Maximal angle of internal friction $\phi'_{max}$        | 41.7            | $^\circ$               |
| Constant volume angle of internal friction $\phi'_{cv}$ | 35.3            | $^\circ$               |

While various types of sand are commonly used in interface shear test analyses (Uesugi and Kishida, 1986a; Uesugi et al., 1988; Tejchman, 1989; DeJong et al., 2003), typical granular materials for studying the addressed interfaces rather include other types of materials such as organic ones, e.g. bean seeds, pea seeds, and wheat grains (Wiącek et al., 2021). Unfortunately, some aspects of the selected methods exclude use of other these types of materials. There are several reasons that stand behind the choice of the sand for this study. The first is that the cohesionless sand is characterized by an easily adjustable sieve curve. As a result, this granular material allowed for the sufficiently small grain size distribution to capture its mesoscopic behavior during deformation. Furthermore, the selected sand allowed to avoid boundary effects in direct shear tests according to EN 1991-4 (2006). To prevent this, the Eurocode recommends that the initial vertical size of the specimen should be 30 times the maximum particle diameter of the material being tested. Finally, the fact that the obtained results will be used to calibrate numerical models for future investigations, e.g. DEM, was another important aspect considered in the selection of the material. For these reasons, the cohesionless sand was deemed the right choice for the laboratory analysis of the bulk solid corrugated wall regime, with the thought that in the future the experimental setup can be adapted to other types of granular materials stored in silos.

### A.2.2 Interface shear test procedure

The standard procedure for direct shear tests was applied in all experiments conducted in this study. Initially, the dry sand sample was prepared directly in the modified shear box. During the preparation, the material was tamped in three layers of equal height to obtain the desired value of the initial porosity. The thickness of the sand mass above the corrugation hills was about 20 mm, which is about  $30 \times d_{50}$ . As a result, the same mass of dry sand was used for each layer. Next, the upper surface of the sand sample was flattened and the initial void ratio was measured. The internal dimensions of the frame containing the sand specimen were 60 mm ( $85 \times D_{50}$ ) by 60 mm ( $85 \times D_{50}$ ). The contact area between the corrugated surface and the sand depended on the geometry of the profiles. Once the specimen was prepared, the prescribed nominal gravity load of 48 kPa was applied to the top platen. During the shearing phase, the rigid bottom surface moved horizontally to the right-hand position at a displacement rate of 0.6 mm/min to ensure quasi-static conditions. Using this displacement rate allowed the study to be conducted effectively with negligible effect on the test results. During the test, the upper frame was fixed while the platen could move vertically. By using a sufficiently thin platen, wedging between the loading platen and the upper frame was prevented (Matsushima et al., 2006). To avoid additional friction during shearing, the contact surfaces between the upper and lower frames were lubricated throughout all tests. In addition, to eliminate grain-on-surface friction, the internal walls were covered with Teflon sheets (Figure A.1). During shearing, the horizontal displacement of the lower frame and the vertical displacement of the upper platen were continuously measured. The horizontal force applied to the lower frame was also measured. The test was completed when a normalized displacement of  $u/L=0.1$  was reached, where  $u$  is the displacement of the bottom surface and  $L$  is the length of the specimen. This corresponded to a total displacement of the lower frame of  $u_{tot}=6.0$  mm. Exemplary pictures of the sample before the test ( $u/L=0.0$ ) and at the final stage of the test ( $u/L=0.1$ ) are shown in Figure A.6. A total of 30 tests were performed during the experimental analysis. Each surface geometry was examined in a series of at least three tests for each case.



Figure A.6: Front view of the sand sample: a) prepared for the interface shear test and b) at the final state of the test for exemplary surface with corrugation coefficient  $d/l=0.147$ .

### A.2.3 Digital Image Correlation (DIC)

A wide range of digital imaging techniques, such as photogrammetry (Uesugi et al., 1988; White et al., 2003), particle image velocimetry (PIV) (White et al., 2003; DeJong et al., 2006; DeJong and Westgate, 2009; Wiącek et al., 2021) and digital image correlation (DIC) (Rechenmacher, 2006; Réthoré et al., 2007; Alhakim et al., 2023) have



been developed to study the deformation of soils and granular materials. These methods allow the observation and measurement of the grain-scale behavior of bulk materials, including the formation and propagation of shear zones (Slominski et al., 2007; Leśniewska et al., 2023). In the presented study, the DIC technique (Peters and Ranson, 1982) was employed to study the behavior of sand-corrugated sinusoidal surface regime. For this purpose, the open source 2D DIC Matlab module Ncorr was employed (Blaber et al., 2015). This software enables the calculation of displacements and strains in solids through computer processing of 2D images. Ncorr is based on a DIC subset approach, i.e. the algorithm divides speckled images into smaller areas called subsets. This technique calculates the deformation of a body by tracking and matching the subset of pixels between the reference and deformed images. In addition, the step size is specified, which defines the number of pixels in the subset that will be used to calculate the displacement fields. In the analysis presented in this section, the subset window size was specified as 30 pixels and the step size was set to 2 pixels (Figure A.7). In the DIC analysis of bulk materials, which are characterized by a random distribution of individual grains of different sizes and shades, a naturally occurring speckled pattern is formed without the need for an artificial pattern (Stanier et al., 2016). The images of the cohesionless during interface shearing were taken with the Nikon Z5 digital camera equipped with the Nikor 24-50/4-6.3 lens. The camera was mounted directly in front of the direct shear apparatus, 12 cm from the shear box. The images taken during the tests were 1800 pixels by 650 pixels, resulting in a resolution of 25 pixels by 25 pixels for the mean grain size. A total of approximately 100 photographs were taken at intervals of 0.06 mm of lower frame horizontal displacement during each test.

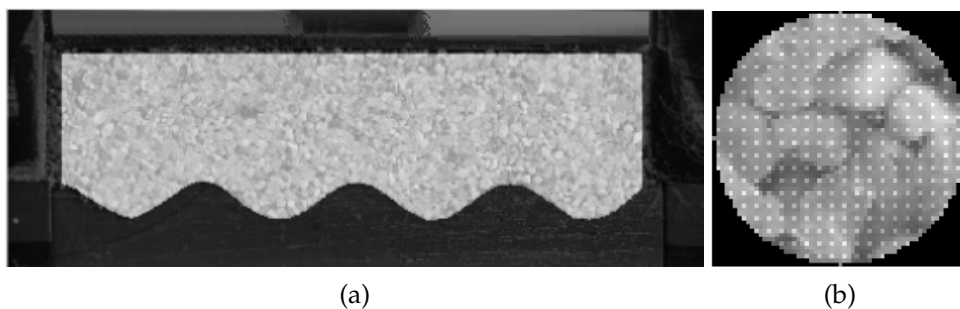


Figure A.7: DIC analysis: a) view of the sample with defined region of interest and b) close up view of the speckle pattern in a subset window (from the Ncorr software) (Grabowski et al. (2023), CC BY 4.0).

### A.3 Experimental results

In this section, the results of a series of laboratory tests of the interface between cohesionless sand and a corrugated sinusoidal surface in the modified direct shear test are presented. First of all, the influence of the corrugation geometry on the shear resistance and granular deformation was examined. Next, the effect of the different corrugation coefficient  $d/l$  ratio on the shear zone formation and on its mesoscopic

characteristics is presented. The results include displacements and strain distributions within the granular material at the final stage of shearing. In addition, the evolution of the interface shear zone during shearing was studied for selected cases.

### A.3.1 Evolution of mobilized shear stress and volumetric strain

Figure A.8 presents the evolution of the mobilized shear stress  $\tau$  and the volumetric strain  $\varepsilon_v$  versus the normalized displacement  $u/L$  obtained in the experiments. The shear resistance of the interface increased with increasing corrugation coefficient (Figure A.8a). For the flat surface ( $d/l=0.000$ ) and that with a corrugation coefficient of  $d/l=0.053$ , the curves were characterized by an almost bilinear pattern, with no softening of the granular material observed. In the other cases, when  $d/l$  varied from 0.147 to 0.427, a characteristic evolution of the shear stress for medium dense specimens was observed. Similar trends were reported in the studies of Ue-sugi and Kishida (1986a), Tejchman and Wu (1995), and Hu and Pu (2004). In the latter cases, in the first phase of shearing, the sand exhibited hardening, initially associated with contractancy. Later, the shear stress reached the yield point at approximately  $u/L=0.035$ , and then exhibited softening associated with sliding of sand at the contact surface. Figure A.8b shows that the volumetric strains were also affected by the surface geometry. The dilatancy increased as the corrugation coefficient increased. For the surfaces with  $d/l$  in the range between 0.053 and 0.427, the sample initially exhibited contraction which was later followed by dilation. On the other hand, in the case of a flat surface ( $d/l=0.000$ ), only contraction was observed. The characteristic values recorded during the experiments are listed in the Table A.2.

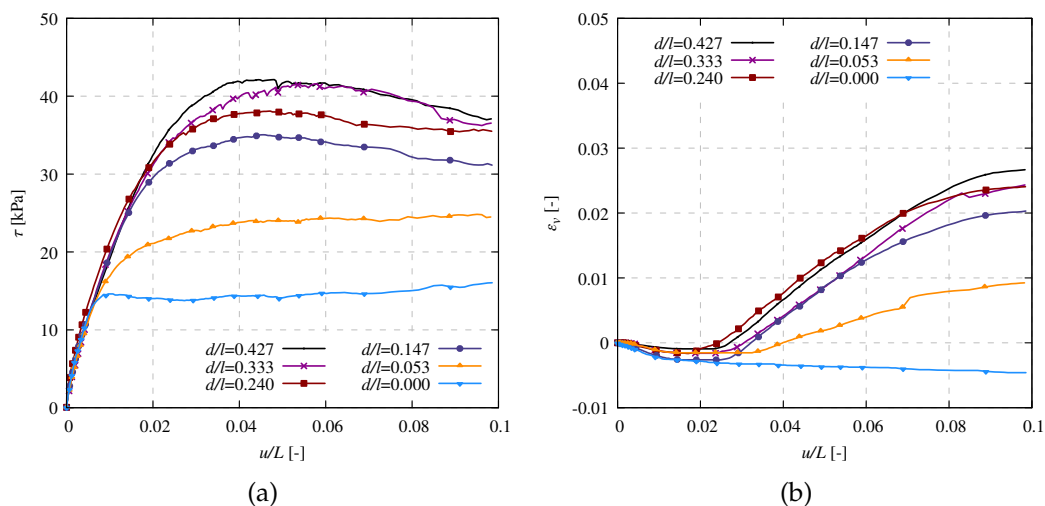


Figure A.8: Evolution of: a) mobilized shear stress  $\tau$  and b) volumetric strain  $\varepsilon_v$  versus normalized horizontal displacement  $u/L$  for different corrugation coefficient  $d/l$  obtained in laboratory tests ( $e_0=0.63$  and  $\sigma_n=48$  kPa) (Grabowski et al. (2023), CC BY 4.0).

Two types of surfaces are distinguished based on the macroscopic response of the sand sample. The first type is associated with surfaces that are considered smooth (corrugation coefficient  $d/l \leq 0.053$ ) and exhibit a bilinear elastic-plastic response. The second type is associated with surfaces with a corrugation coefficient  $d/l >$

Table A.2: Calculated values of peak effective wall friction coefficient  $\mu_{eff,max}$ , effective wall friction coefficient  $\mu_{eff,res}$  and residual volumetric strain  $\varepsilon_v$  for different corrugation coefficient  $d/l$ .

| $d/l$ [-] | $\mu_{eff,max}$ [-] | $\mu_{eff,res}$ [-] | $\varepsilon_v$ [-] |
|-----------|---------------------|---------------------|---------------------|
| 0.000     | 0.335               | 0.330               | -0.0051             |
| 0.053     | 0.520               | 0.472               | 0.0092              |
| 0.147     | 0.733               | 0.658               | 0.0203              |
| 0.240     | 0.798               | 0.728               | 0.0241              |
| 0.333     | 0.872               | 0.757               | 0.0243              |
| 0.427     | 0.883               | 0.781               | 0.0267              |

0.053, classified as deep. In these cases, the response of sand sample during shearing was characterized by an initial hardening until the shear resistance was yielded, followed by a softening of the sample after the peak. Unfortunately, based on the studied surfaces, it is difficult to clearly determine the precise boundary for distinguishing these two types of surfaces. The presented analysis showed that the critical corrugation coefficient was in the range between  $d/l = 0.053$  and  $d/l = 0.147$ . In addition, the analysis showed that there is a limit to the shear resistance of the interface. Increasing the corrugation coefficient above 0.333 resulted in a negligible increase in shear resistance.

### A.3.2 Friction of sand on corrugated sinusoidal surface

Based on the laboratory results, the friction between the sand and the corrugated sinusoidal surface was determined. The effective wall friction coefficient was calculated using the equation 4.5 presented in the Chapter 4.4. To calculate  $\mu_{eff}$  the peak and the residual values of the shear resistance were used. Figure A.9A presents the value of calculated effective wall friction coefficient (peak value of the internal friction angle of sand was  $\phi_{i,max} = 46^\circ$ ). The magnitude of the  $\mu_{eff}$  was significantly influenced by the profile geometry, and increased with the increase of the corrugation coefficient. Similarly as in the DEM analysis, the wall contact factor  $a_w$  was determined using the Equation 4.7 presented in Chapter 4.4. Figure A.9B presents the calculated value of the wall contact factor  $a_w$  based on the peak effective surface friction coefficient obtained in each test. The  $a_w=0.2$  recommended by EN 1991-4 (2006) is represented by a red line. The analysis reveals that as  $d/l$  increased, the wall contact factor decreased. These findings are consistent with those of other researchers (Zhang et al., 1994). The parameter reached an asymptotic limit of approximately 0.3 for surfaces with  $d/l \geq 0.333$ . For the smooth surfaces, the coefficient of friction was much closer to that of grain-on-surface friction than to the internal friction angle of sand, and reached  $a_w=1.0$  for a flat surface. It is evident that the value of this factor is not constant for the tested surfaces. Moreover, for any of the surfaces,  $a_w$  does not equal 0.2 as recommended in the EN 1991-4 (2006).

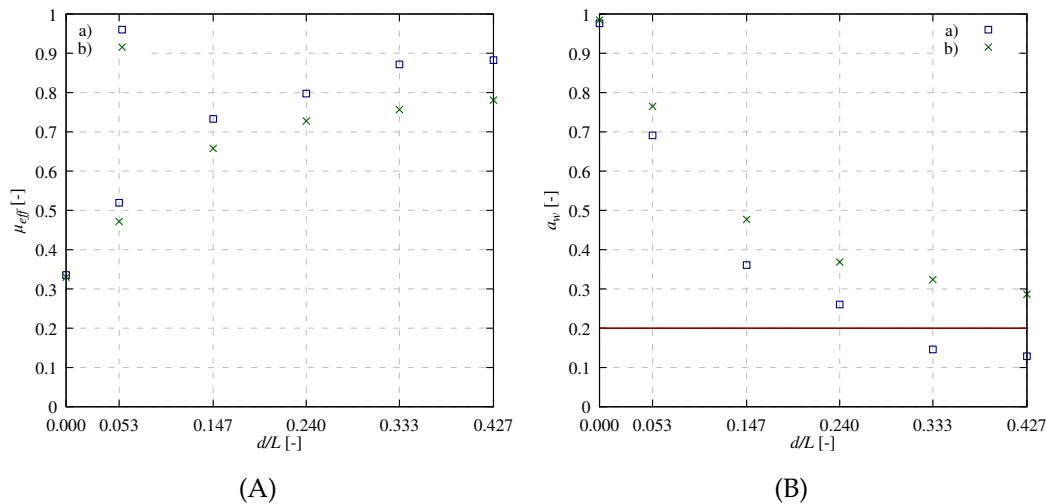


Figure A.9: Calculated: A) effective friction coefficient  $\mu_{eff}$  and B) wall contact factor  $a_w$  versus normalized horizontal displacement  $u/L$  for different corrugation coefficient  $d/l$  obtained in laboratory tests. The red line represents the value of  $a_w=0.2$  recommended by the the EN 1991-4 (2006).

### A.3.3 DIC analysis

The research, described in previous section, has so far focused on the macroscopic behavior of the interface between cohesionless sand and sinusoidal corrugated surfaces of various geometries. In this section, the effect of the surface profile on the mesoscopic behavior of the bulk solid-corrugated surface regime has been investigated. Experimental results on the evolution and formation of the shear zone in the contact zone, calculated using the DIC technique, are presented.

#### Effect of surface geometry

At the beginning, the influence of the corrugation coefficient  $d/l$  on the contact zone behavior was investigated. In the following paragraphs, the studied variables presented in the images were calculated for the final state of the test ( $u/L=0.1$ ) in reference to the initial state of the specimen ( $u/L=0.0$ ). Therefore, the displacements were accumulated from the beginning to the end of the test.

First, the effect of the corrugation coefficient  $d/l$  on the distribution of both horizontal and vertical displacements within the sand was studied (Figures A.10 and A.11). The movement of the corrugated surface was induced in the right-hand position, therefore the red color in Figure A.10 represents the movement of the sand in this direction. On the other hand, the blue color in this figure represents no motion of sand grains at all. In case of vertical displacements (Figure A.11) red color represents the displacements of sand grains towards the corrugated surface, while blue color represents the displacements towards the loading platen. These figures shows that the final deformation of the sand specimen was significantly influenced by the surface geometry.

The results correspond well with the evolution of the mobilized shear stress curves. For surfaces with  $d/l \leq 0.053$  the entire sand behaved like a quasi-rigid body during the test. In these cases, sand slipped directly at the surface, therefore

negligible or small horizontal and vertical displacements were observed (Figures A.10a,b and A.11a,b). In these cases it was assumed that the shear resistance was mostly or completely affected by the grain-on-surface friction. It was noticed that the grains initially located in the valleys moved towards the sand mass during the test. On the other hand, the sand mass located at the peaks was moved towards the surface throughout the study. This vertical movement was related to the horizontal motion of the surface. This movement was related to the horizontal motion of the surface, where the moving valleys confined the sand and the moving hills loosened it. For the surface with  $d/l=0.147$  (Figures A.10c and A.11c), the granular material in the valleys partially followed the movement of the bottom surface. The final horizontal displacements of the sand grains in those areas were smaller than the final displacement of the surface. In the remaining cases ( $d/l \geq 0.240$ ) bulk material was divided by the shear zone located slightly below the peaks of the corrugation. Part of the sand was locked directly in the valleys and followed the movement of the surface. The final displacement of these grains was equal to the total horizontal displacement of the surface (Figure A.10c-e). Above the shear zone, the sand sample behaved as a quasi-rigid body. As a result of the dilatancy occurring within the localized zone, the granular material locked in the valleys was pushed toward the surface (Figure A.11d-e). No significant vertical movement was observed at the peaks of the corrugation. In these regions, the sand grains were sliding directly on the surface. In addition, based on the distribution of vertical displacements, it can be seen that the shearing caused a counterclockwise rotation of the top platen. As a result, the sand on the left side of the specimen was compacted and the sand on the right side of the specimen was loosened (Figure A.11d-e). The total rotation of the top platen increased with the increase of corrugation coefficient  $d/l$ .

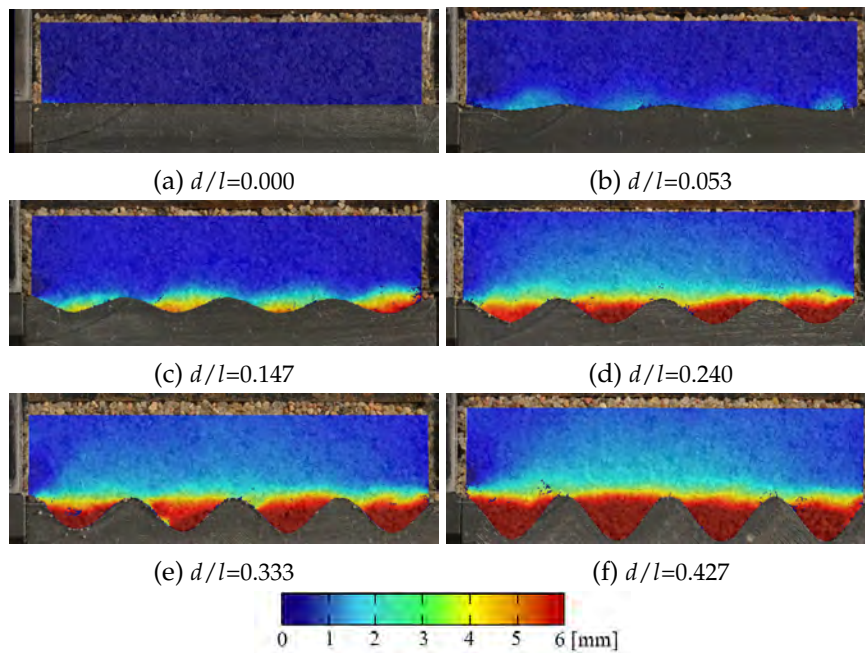


Figure A.10: Horizontal displacement  $v_x$  distribution at the final state ( $u/L=0.1$ ) obtained with DIC analysis for different corrugation coefficient  $d/l$  (Grabowski et al. (2023), CC BY 4.0).

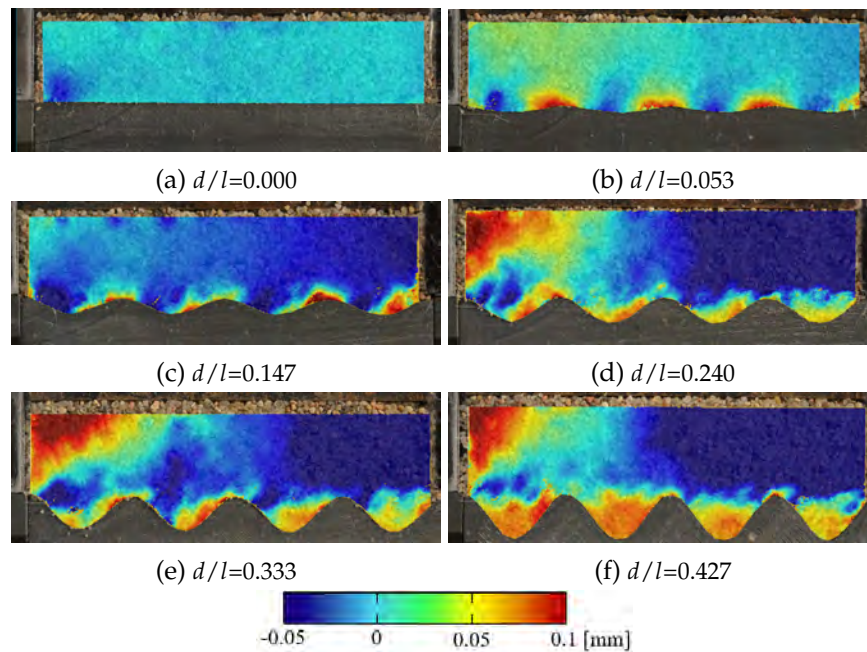


Figure A.11: Vertical displacement  $v_y$  distribution at the final state ( $u/L=0.1$ ) obtained with DIC analysis for different corrugation coefficient  $d/l$  (Grabowski et al. (2023), CC BY 4.0).

Based on the distribution of horizontal  $v_x$  and vertical displacements  $v_y$ , the strain fields within the sand sample were calculated using DIC method (Figures A.12-A.14). Figure A.12 shows the distribution of horizontal strains  $\varepsilon_{xx}$  in the specimen for each type of studied surface. Similarly to the previous paragraphs, for the flat surface no deformation occurred. The entire specimen behaved like a rigid body and slipped on the surface (Figure A.12a). For the surface with  $d/l=0.053$ , some small horizontal deformation was observed directly on the surface. Similar conclusions can be drawn for these surfaces based on the distribution of vertical  $\varepsilon_{yy}$  (Figure A.13a,b) and shear strains  $\varepsilon_{xy}$  (Figure A.14a,b). In the remaining cases ( $d/l \geq 0.147$ ), a more pronounced shear zone was observed with a consequent increase in the corrugation coefficient. For these tests, an interesting mechanism was captured using the horizontal strains  $\varepsilon_{xx}$  distribution. The localized zone was composed of alternating regions of dilating and contracting sand, despite the fact that the sand sheared globally in the direction related to the motion of the corrugated surface. This mechanism within the shear zone was previously observed in studies by Rechenmacher (2006) and Chupin et al. (2011), where it was associated with the successive formation and breakage of particle columns. Further analysis showed that this column collapse leads to the generation of almost periodic large voids (Oda and Kazama, 1998; Nitka et al., 2015). The distribution of vertical  $\varepsilon_{yy}$  (Figure A.13) and shear  $\varepsilon_{xy}$  (Figure A.14) strains agreed well for all types of corrugation profiles. For surfaces with  $d/l \geq 0.247$ , the localized zone between the peaks of the corrugations was most evident. Shearing occurred mainly within the granular material, with no significant deformation at the peaks. At the peaks, the interaction was mainly based on the sliding of the sand on the solid surface, creating a distinct horizontal shear zone that divided the sand into two quasi-rigid bodies.

Next, the shear strain fields  $\varepsilon_{xy}$  in the final state of the test for surfaces with

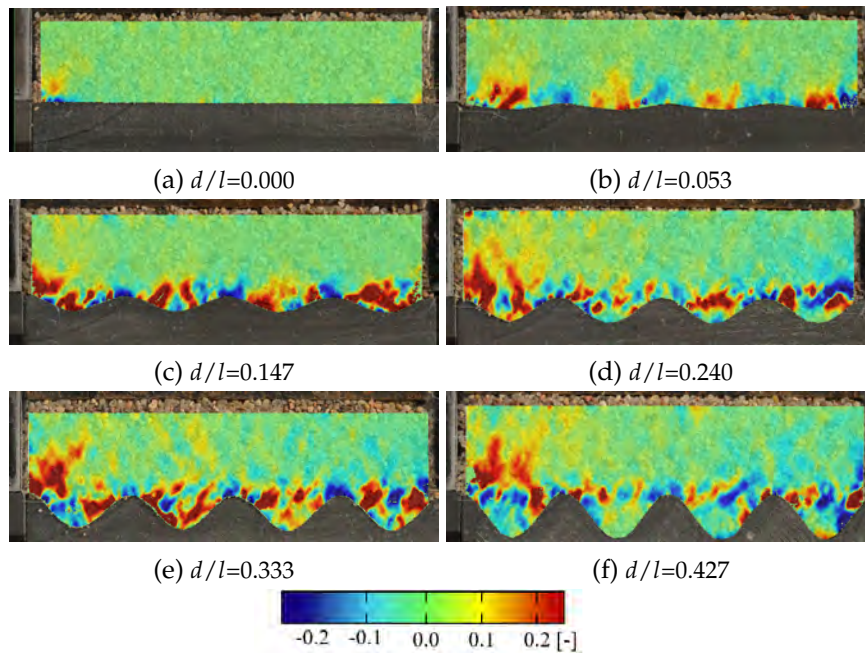


Figure A.12: Horizontal strain  $\varepsilon_{xx}$  distribution at the final state ( $u/L=0.1$ ) obtained with DIC analysis for different corrugation coefficient  $d/l$  (Grabowski et al. (2023), CC BY 4.0).

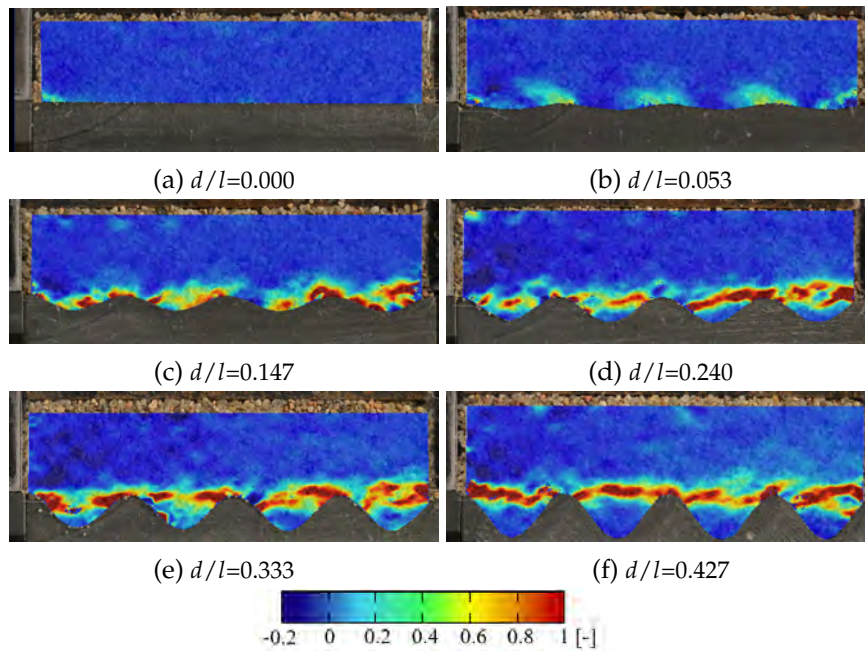


Figure A.13: Vertical strain  $\varepsilon_{yy}$  distribution at the final state ( $u/L=0.1$ ) obtained with DIC analysis for different corrugation coefficient  $d/l$  (Grabowski et al. (2023), CC BY 4.0).

$d/l \geq 0.147$  were selected to study the shear zones. The other two surfaces ( $d/l \leq 0.053$ ) were not examined because it was assumed that in the case of smooth surfaces, the granular material slipped on the surface and no shear zone occurred. The area of the analyzed digitized images was reduced to the internal waves to minimize the boundary effect of the shear frames. Initially, the approximate location of the shear zone was determined based on the fields shown in Figure A.15. In all studied cases, the shear zone was clearly visible. It was observed that as the corrugation

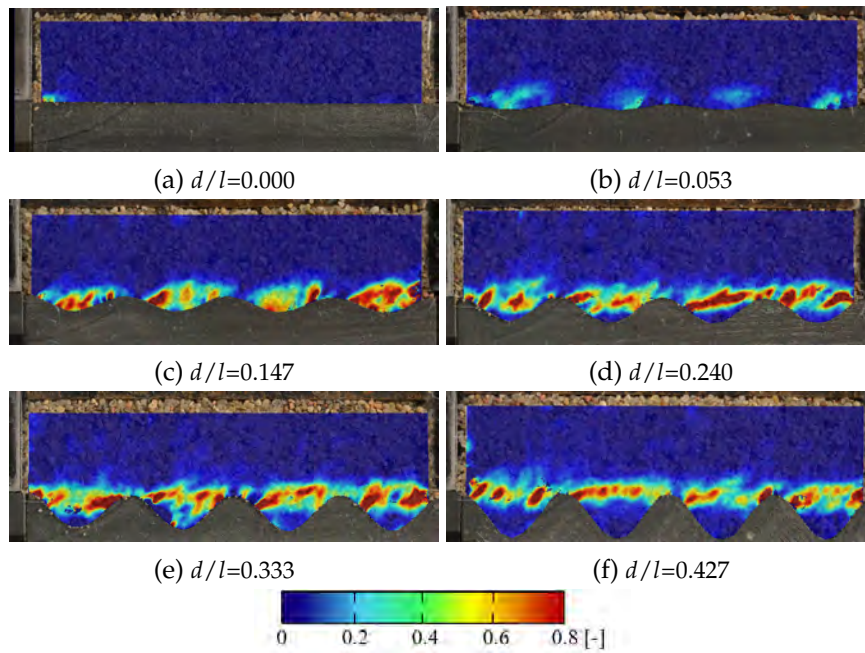


Figure A.14: Shear strain  $\varepsilon_{xy}$  distribution at the final state ( $u/L=0.1$ ) obtained with DIC analysis for different corrugation coefficient  $d/l$  (Grabowski et al. (2023), CC BY 4.0).

coefficient increased, the plane of the shear zone moved away from the valleys of the surface toward the sand mass. Based on the figures, an approximate relationship was established between the grain-on-grain ( $b_i$  in EN 1991-4 (2006) standard) and grain-on-surface ( $b_w$  in EN 1991-4 (2006) standard) components of friction. The wall contact factor was equal to  $a_w=0.333$  for  $d/l=0.147$ ,  $a_w=0.238$  for  $d/l=0.240$ ,  $a_w=0.227$  for  $d/l=0.333$ , and  $a_w=0.133$  for  $d/l=0.427$ . Finally, the thickness of the shear zone ( $t_s$ ) was analyzed. In all cases, it ranged between approximately 3.0 mm ( $4 \times d_{50}$ ) and 3.4 mm (about  $5 \times d_{50}$ ), which agrees well with other studies (Uesugi et al., 1988; Hu and Pu, 2004).

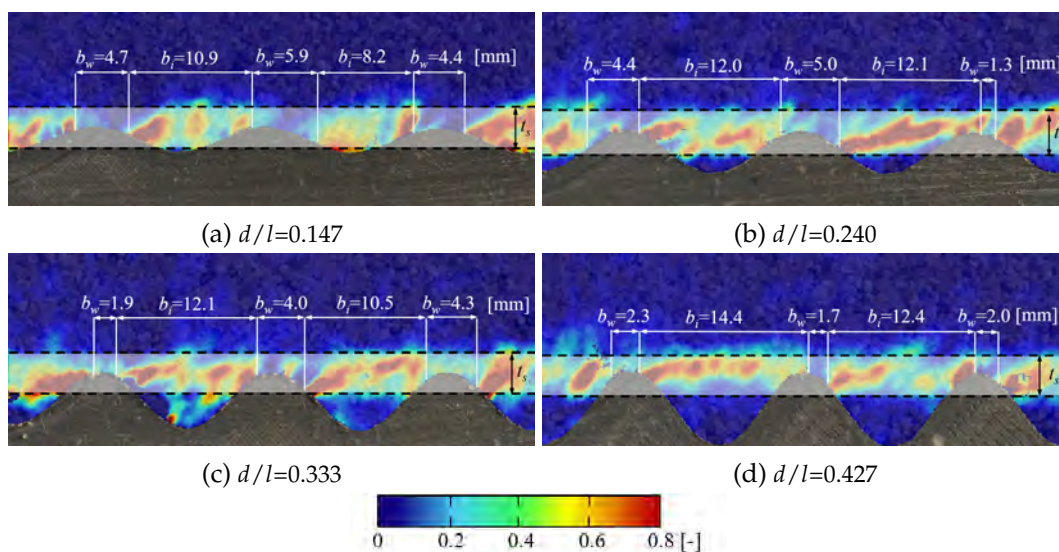


Figure A.15: Highlight of the shear zone based on shear strain  $\varepsilon_{xy}$  distribution at the final state ( $u/L=0.1$ ) obtained with DIC analysis for different corrugation coefficient  $d/l$  (Grabowski et al. (2023), CC BY 4.0).

### Shear zone evolution

The research, described in previous section, has so far focused on studying the effect of corrugation coefficient  $d/l$  on the shear zone characteristics at the final state of the shearing. In this section, the evolution of these characteristics during the sample deformation was analyzed. DIC analysis was performed on images taken at different horizontal motion steps of the test, starting from the initial state ( $u/L=0$ ) up to the final state of the test ( $u/L=0.1$ ) with an increment of  $du/L=0.02$ . All strain fields in successive steps were calculated with respect to the initial state of the sample ( $u/L=0$ ).

To study the shear zone evolution, two tests with different profiles were selected. The first surface had a corrugation coefficient  $d/l=0.053$  and the second had  $d/l=0.333$ . These surfaces were chosen specifically because of their distinct shearing mechanisms observed in the previous section. As demonstrated earlier, the first surface behaved like a smooth interface, while the second surface exhibited characteristics typical for a deep interface.

At the beginning, the evolution of the shear zone in the interface between sand and smooth surface was analyzed. Figures A.16-A.18 present the evolution of horizontal  $\varepsilon_{xx}$ , vertical  $\varepsilon_{yy}$  and shear strains  $\varepsilon_{xy}$  at the consecutive stages of the test. Initially, the sand deformation in the area adjacent to the surface was barely visible in both the horizontal and vertical directions (Figure A.16a-c and Figure A.17a-c). Small deformations of the granular mass can be observed after the surface has moved more than  $u/L=0.04$  (Figure A.16a-c and Figure A.17a-c). During the test, almost entire sand sample remained stationary, while the smooth surface was moving in the direction of the shearing. Only slight deformation was observed directly in the valleys and at the peaks of the waves. In the valleys, the granular material moved away from the surface. This caused local compaction of the sand. In contrast, at the peaks, the granular material moved toward the surface, causing local loosening of the sand (Figure A.17d-f).

Next, the analysis of the evolution of the shear zone was performed for the surface with corrugation coefficient  $d/l=0.333$  (Figures A.19-A.21). The strain fields in the subsequent time steps show that in this case the shear zone was observed just before the peak of the shear stress. The initiation points of the shear zones were localized near the top of the surface hills (Figure A.20c). As the shearing progressed, they propagated towards the granular mass (Figure A.20d-f). This behavior can be attributed to the difference between the internal friction angle and friction angle against the surface. The latter angle is lower, and therefore the deformation can be detected at an earlier stage. The analysis of the horizontal and vertical deformation fields (Figures A.19 and A.20) revealed that the mechanism in the contact area between the granular material and the corrugated surface is complex and non-uniform. It can be noted that the entire shear zone was composed of local alternating arc-shaped zones rather than a set of horizontal shear planes. These arc-shaped shear zones exhibited slightly non-horizontal levels of support, beginning simultaneously at the peak of the receding wave and extending well below the peak of the advancing wave (Figures A.20d-f and A.21d-f). Consequently, the shear zone occurring at the corrugation peak is not distributed evenly between the two sides of the wave. In particular, the sliding associated with the grain-on-surface friction angle is



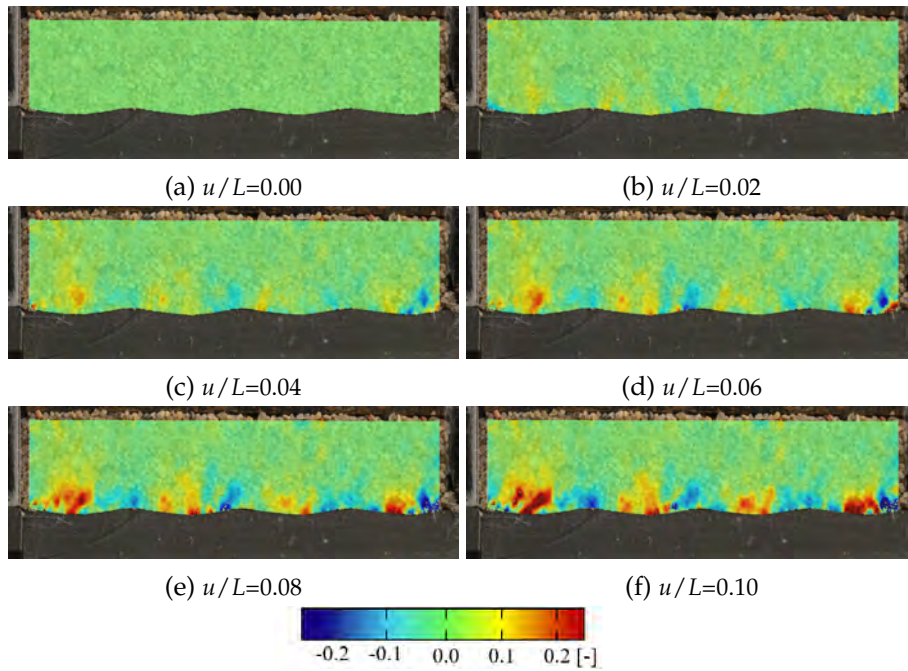


Figure A.16: Evolution of the horizontal strain  $\varepsilon_{xx}$  in the entire specimen obtained with DIC analysis at different phases of the test  $u/L$  for corrugation coefficient  $d/l=0.053$  (Grabowski et al. (2023), CC BY 4.0).

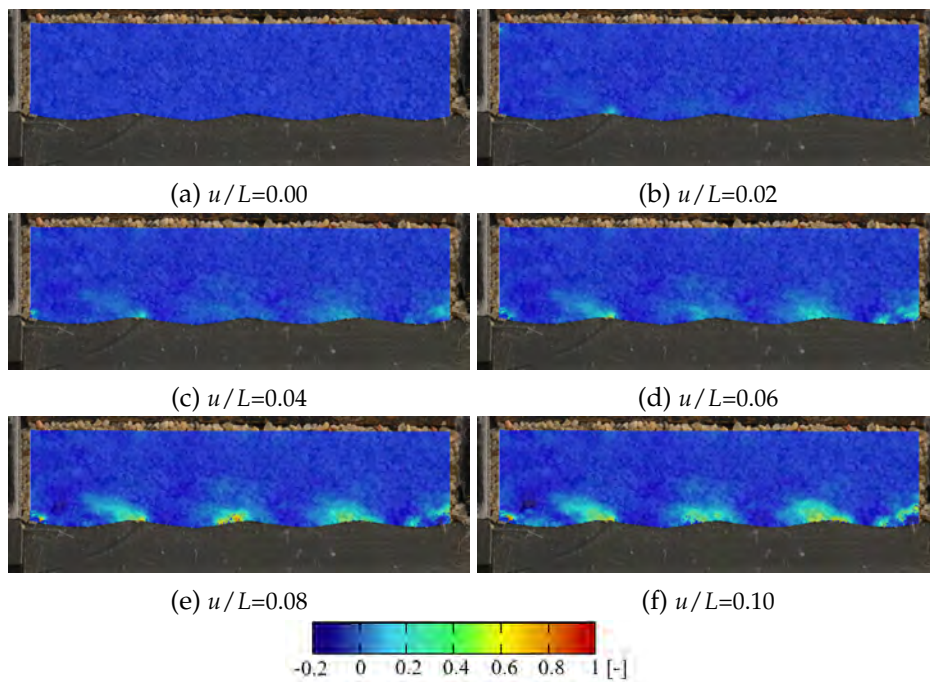


Figure A.17: Evolution of the horizontal strain  $\varepsilon_{yy}$  in the entire specimen obtained with DIC analysis at different phases of the test  $u/L$  for corrugation coefficient  $d/l=0.053$  (Grabowski et al. (2023), CC BY 4.0).

greater on the advancing side of the wave than on the opposite side. In other words, the surface shear is asymmetric and concentrated in one direction, as in case of e.g. confined granular flow in silo with corrugated steel walls.

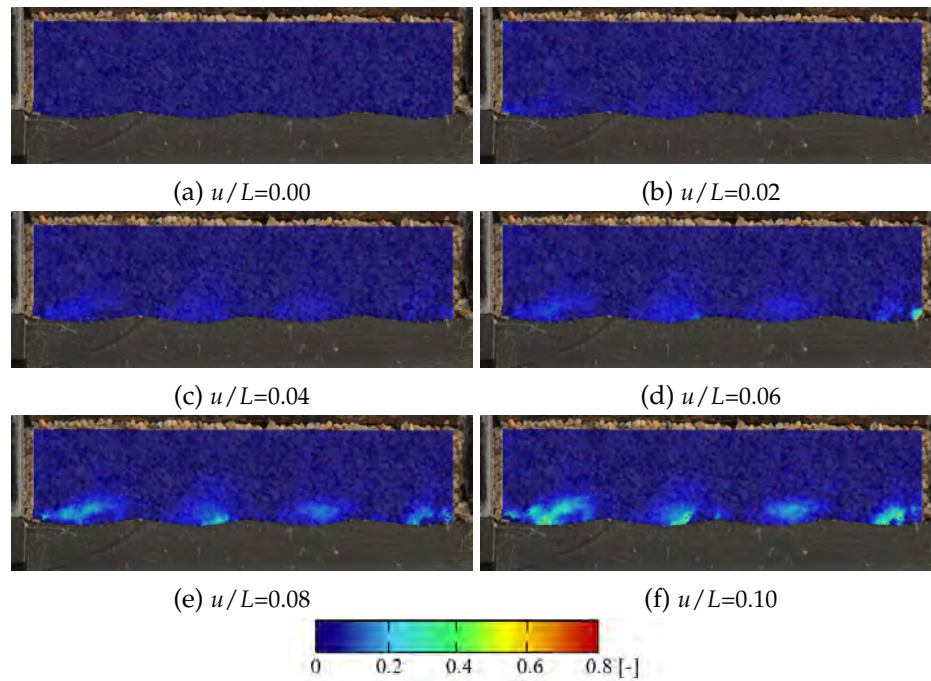


Figure A.18: Evolution of the horizontal strain  $\varepsilon_{xy}$  in the entire specimen obtained with DIC analysis at different phases of the test  $u/L$  for corrugation coefficient  $d/l=0.053$  (Grabowski et al. (2023), CC BY 4.0).

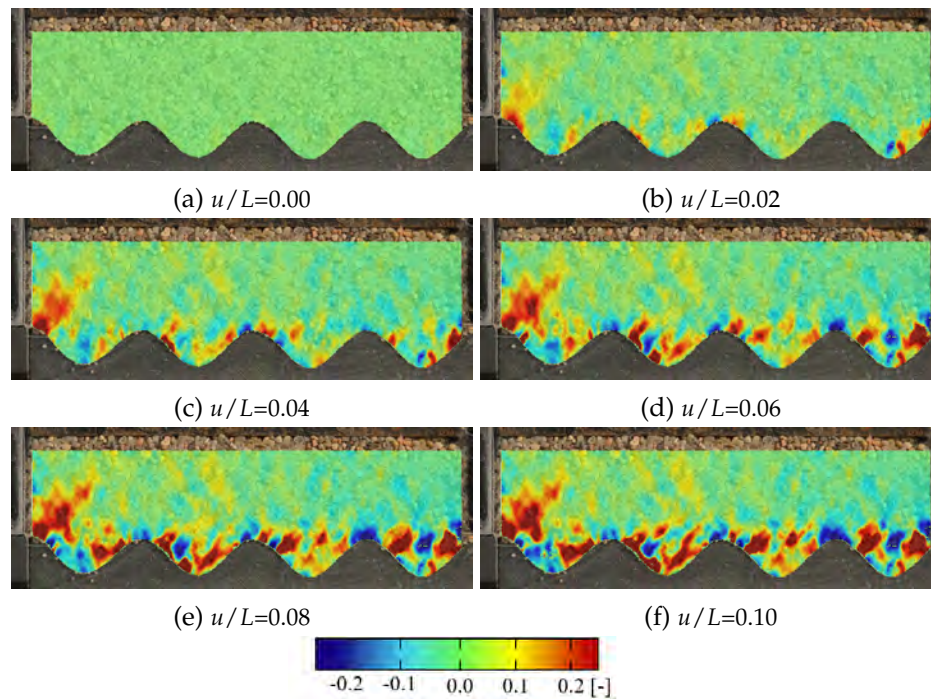


Figure A.19: Evolution of the horizontal strain  $\varepsilon_{xx}$  in the entire specimen obtained with DIC analysis at different phases of the test  $u/L$  for corrugation coefficient  $d/l=0.333$  (Grabowski et al. (2023), CC BY 4.0).

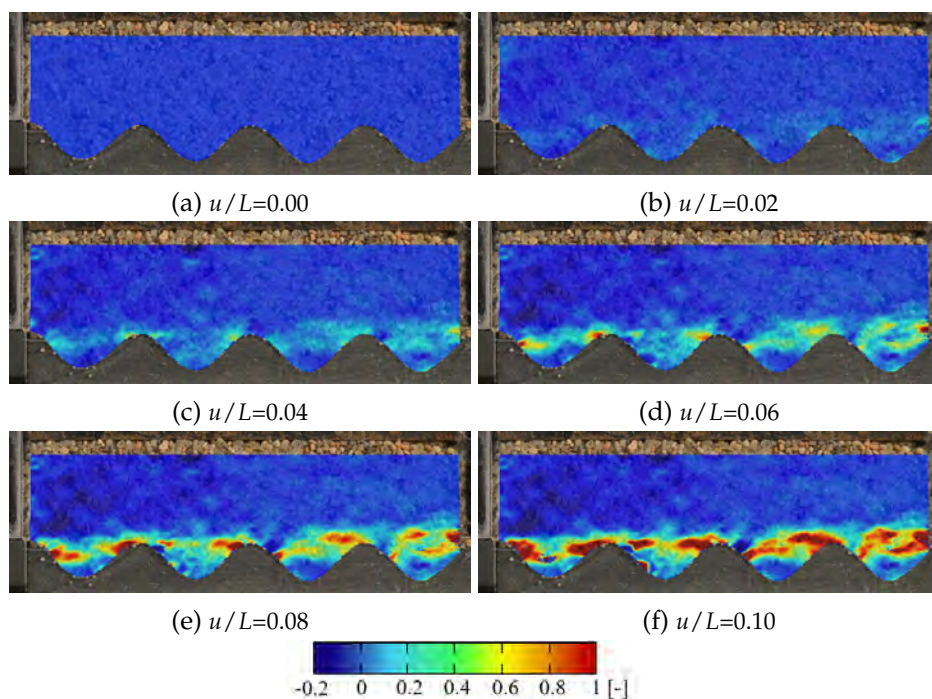


Figure A.20: Evolution of the horizontal strain  $\varepsilon_{yy}$  in the entire specimen obtained with DIC analysis at different phases of the test  $u/L$  for corrugation coefficient  $d/l=0.333$  (Grabowski et al. (2023), CC BY 4.0).

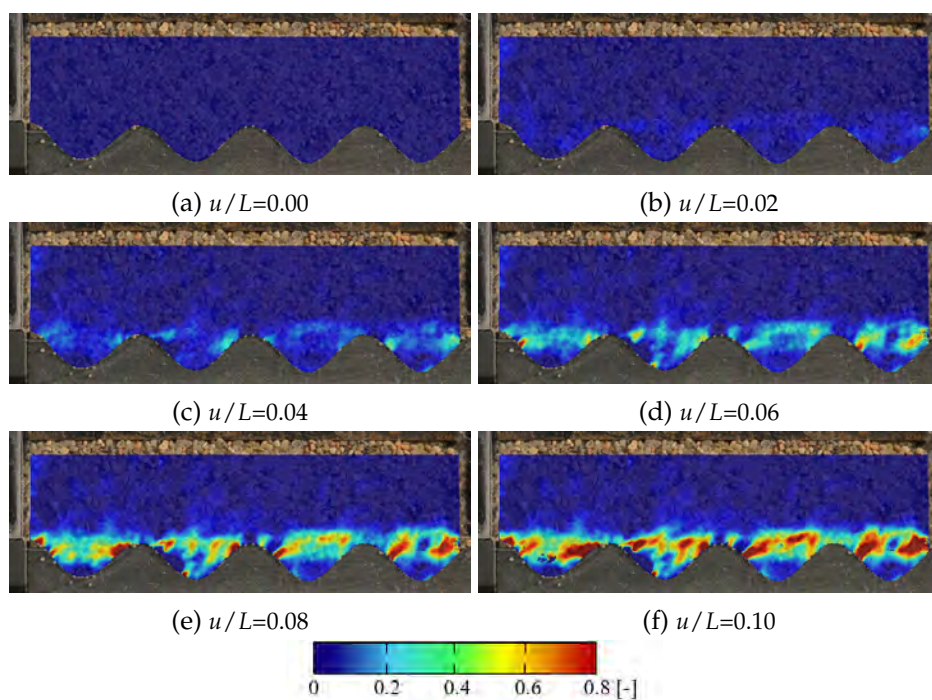


Figure A.21: Evolution of the horizontal strain  $\varepsilon_{xy}$  in the entire specimen obtained with DIC analysis at different phases of the test  $u/L$  for corrugation coefficient  $d/l=0.333$  (Grabowski et al. (2023), CC BY 4.0).

## A.4 Summary

In this section, a comprehensive laboratory analysis of the interface between sand and corrugated sinusoidal surfaces in modified direct shear apparatus were presented. The influence of the corrugation coefficient  $d/l$  on the shear resistance, specimen deformation and the localization phenomena was analyzed. Following major conclusions were drawn from the experimental study:

- The shear resistance and shear deformation of the specimen significantly depend on the geometry of the surface. As the corrugation coefficient  $d/l$  increased, the horizontal force acting on the surface and volumetric changes also increased. Based on macroscopic results, two types of surfaces were distinguished: shallow and deep surfaces. In the first case, behavior was mainly influenced by the friction angle against the surface, while in the second case, with increasing  $d/l$ , the internal friction angle of the sand had a greater impact. The critical corrugation coefficient that distinguishes these two types of surfaces could not be precisely determined. This distinction is important, as the type of interface (shallow or deep) is one of the parameters that influence the type of granular silo flow
- The wall contact factor  $a_w$  calculated according to the formula provided in EN 1991-4 (2006) was significantly influenced by the surface geometry. This parameter increased as the corrugation coefficient  $d/l$  decreased. For the peak value of effective friction coefficient  $a_w$  was in the range between  $a_w=0.976$  ( $d/l=0.000$ ) and  $a_w=0.129$  ( $d/l=0.427$ ). For the residual value of effective friction coefficient  $a_w$  was in the range between  $a_w=0.985$  ( $d/l=0.000$ ) and  $a_w=0.287$  ( $d/l=0.427$ ). The calculated values  $a_w$  shows that the recommendation of EN 1991-4 (2006) to set  $a_w=0.2$  tends to overestimate the pressures exerted on the sinusoidal corrugated surfaces in the typical range of wall profiles.
- The DIC method was used to calculate the displacement and strain fields within the sand sample based on the photographic data acquired during the interface shear test. This allowed for the study of the wall contact factor  $a_w$  for deep surfaces, which was estimated from the shear strain distribution  $e_{xy}$ . Contrary to the value recommended by EN 1991-4 (2006),  $a_w$  was not constant. For the residual value of the effective friction coefficient  $a_w$  was in the range between  $a_w=0.333$  ( $d/l=0.147$ ) and  $a_w=0.133$  ( $d/l=0.427$ ). These values were significantly lower than those calculated according to the EN 1991-4 (2006). Therefore, the visual method of determining  $a_w$  provides qualitative rather than quantitative results.
- The 3D printed experimental setup constructed for this study proved to be efficient and accurate, and allowed for DIC analysis of sand deformation within the contact zone. The differences in shear resistance and volumetric changes within the sample between the direct shear test performed with brass shear frames and PLA printed frames were negligible. The DIC method provided useful observations on the sand behavior. The effect of the  $d/l$  coefficient was significant: slipping occurred directly at the surface for shallow surfaces,



whereas for deep surfaces, arc-shaped shear zones were observed between the peaks of the corrugations instead of a single uniform shear plane. The thickness of these shear zones varied between  $4 \times d_{50}$  and  $5 \times d_{50}$ .

Further research is necessary to investigate the behavior of the interface between granular material and sinusoidal corrugated surfaces. Future experimental analyses will involve various grain types, such as wheat grains, under different pressures and moisture contents. Additionally, analysis of the contact zone will be conducted in a model-scale silo with corrugated sinusoidal walls. Experimental outcomes can be enhanced with numerical analysis using the discrete element method, which can provide insights into the grain-level behavior of granular materials. The laboratory study presented in this appendix provides a solid basis for the calibration and validation of numerical models.

# Bibliography

- Abedi, Sara, Amy L. Rechenmacher, and Andrés D. Orlando (Sept. 2012). "Vortex formation and dissolution in sheared sands". In: *Granular Matter* 14.6, pp. 695–705. ISSN: 1434-7636. DOI: 10.1007/s10035-012-0369-5.
- Aboul Hosn, Rodaina, Luc Sibille, Nadia Benahmed, and Bruno Chareyre (Nov. 2016). "Discrete numerical modeling of loose soil with spherical particles and interparticle rolling friction". In: *Granular Matter* 19.1. ISSN: 1434-7636. DOI: 10.1007/s10035-016-0687-0.
- Alhakim, G., C. Núñez-Temes, J. Ortiz-Sanz, M. Arza-García, Lina Jaber, and M.L. Gil-Docampo (Apr. 2023). "Experimental application and accuracy assessment of 2D-DIC in meso-direct-shear test of sandy soil". In: *Measurement* 211, p. 112645. ISSN: 0263-2241. DOI: 10.1016/j.measurement.2023.112645.
- Balevičius, R., I. Sielamowicz, Z. Mróz, and R. Kačianauskas (2011). "Investigation of wall stress and outflow rate in a flat-bottomed bin: A comparison of the DEM model results with the experimental measurements". In: *Powder Technology* 214.3, pp. 322–336. DOI: <https://doi.org/10.1016/j.powtec.2011.08.042>.
- Balevičius, R., I. Sielamowicz, Z. Mróz, and R. Kačianauskas (Dec. 2012). "Effect of rolling friction on wall pressure, discharge velocity and outflow of granular material from a flat-bottomed bin". In: *Particuology* 10.6, pp. 672–682. ISSN: 1674-2001. DOI: <http://dx.doi.org/10.1016/j.partic.2012.07.002>.
- Bareither, Christopher A., Tuncer B. Edil, Craig H. Benson, and David M. Mickelson (Oct. 2008). "Geological and Physical Factors Affecting the Friction Angle of Compacted Sands". In: *Journal of Geotechnical and Geoenvironmental Engineering* 134.10, pp. 1476–1489. ISSN: 1943-5606. DOI: 10.1061/(ASCE)1090-0241(2008)134:10(1476).
- Bauer, Erich (Mar. 1996). "Calibration of a Comprehensive Hypoplastic Model for Granular Materials". In: *Soils and Foundations* 36.1, pp. 13–26. ISSN: 0038-0806. DOI: <https://doi.org/10.3208/sandf.36.13>.
- Belheine, N., J.-P. Plassiard, F.-V. Donzé, F. Darve, and A. Seridi (2009). "Numerical simulation of drained triaxial test using 3D discrete element modeling". In: *Computers and Geotechnics* 36.1-2, pp. 320–331. DOI: 10.1016/j.compgeo.2008.02.003.
- Blaber, J., B. Adair, and A. Antoniou (Mar. 2015). "Ncorr: Open-Source 2D Digital Image Correlation Matlab Software". In: *Experimental Mechanics* 55.6, pp. 1105–1122. ISSN: 1741-2765. DOI: <https://doi.org/10.1007/s11340-015-0009-1>.
- Bourrier, Franck, François Kneib, Bruno Chareyre, and Thierry Fourcaud (Dec. 2013). "Discrete modeling of granular soils reinforcement by plant roots". In: *Ecological Engineering* 61, pp. 646–657. ISSN: 0925-8574. DOI: <https://doi.org/10.1016/j.ecoleng.2013.05.002>.



- Buist, K.A., L.J.H. Seelen, N.G. Deen, J.T. Padding, and J.A.M. Kuipers (2016). "On an efficient hybrid soft and hard sphere collision integration scheme for DEM". In: *Chemical Engineering Science* 153, pp. 363–373. DOI: <https://doi.org/10.1016/j.ces.2016.07.030>.
- Böhrnsen, J.U., H. Antes, M. Ostendorf, and J. Schwedes (Jan. 2004). "Silo Discharge: Measurement and Simulation of Dynamic Behavior in Bulk Solids". In: *Chemical Engineering Technology* 27.1, pp. 71–76. ISSN: 1521-4125. DOI: <https://doi.org/10.1002/ceat.200401913>.
- Caulk, Robert, Luc Scholtès, Marek Krzaczek, and Bruno Chareyre (2020a). "A pore-scale thermo-hydro-mechanical model for particulate systems". In: *Computer Methods in Applied Mechanics and Engineering* 372, p. 113292. DOI: <https://doi.org/10.1016/j.cma.2020.113292>.
- Caulk, Robert A., Emanuele Catalano, and Bruno Chareyre (Mar. 2020b). "Accelerating Yade's poromechanical coupling with matrix factorization reuse, parallel task management, and GPU computing". In: *Computer Physics Communications* 248, p. 106991. ISSN: 0010-4655. DOI: <https://doi.org/10.1016/j.cpc.2019.106991>.
- Chandler, R. J. and P. S Hamilton (Oct. 1999). "On the measurement of the undrained strength of discontinuities in the direct shear box". In: *Géotechnique* 49.5, pp. 615–620. ISSN: 1751-7656. DOI: [10.1680/geot.1999.49.5.615](https://doi.org/10.1680/geot.1999.49.5.615).
- Chen, J.F., J.M. Rotter, J.Y. Ooi, and Z. Zhong (June 2005). "Flow pattern measurement in a full scale silo containing iron ore". In: *Chemical Engineering Science* 60.11, pp. 3029–3041. ISSN: 0009-2509. DOI: <https://doi.org/10.1016/j.ces.2004.12.045>.
- Chen, Wei-Bin, Wan-Huan Zhou, and Jaime Alberto dos Santos (2020). "Analysis of consistent soil-structure interface response in multi-directional shear tests by discrete element modeling". In: *Transportation Geotechnics* 24, p. 100379. DOI: <https://doi.org/10.1016/j.trgeo.2020.100379>.
- Chupin, O., A. L. Rechenmacher, and S. Abedi (2011). "Finite strain analysis of nonuniform deformation inside shear bands in sands". In: *International Journal for Numerical and Analytical Methods in Geomechanics* 36.14, pp. 1651–1666. DOI: <https://doi.org/10.1002/nag.1071>.
- Cui, Deshan, Wei Wu, Wei Xiang, Thiep Doanh, Qiong Chen, Shun Wang, Qingbing Liu, and Jinge Wang (Nov. 2016). "Stick-slip behaviours of dry glass beads in triaxial compression". In: *Granular Matter* 19.1. ISSN: 1434-7636. DOI: [10.1007/s10035-016-0682-5](https://doi.org/10.1007/s10035-016-0682-5).
- Cundall, P. A. and O. D. L. Strack (1979). "A discrete numerical model for granular assemblies". In: *Géotechnique* 29.1, pp. 47–65. DOI: <https://doi.org/10.1680/geot.1979.29.1.47>.
- Cutress, J.O. and R.F. Pulfer (1967). "X-Ray investigations of flowing powders". In: *Powder Technology* 1.4, pp. 213–220. DOI: [https://doi.org/10.1016/0032-5910\(67\)80039-1](https://doi.org/10.1016/0032-5910(67)80039-1).
- DeJong, Jason T., Mark F. Randolph, and David J. White (2003). "Interface Load Transfer Degradation During Cyclic Loading: A Microscale Investigation". In: *Soils and Foundations* 43.4, pp. 81–93. DOI: [10.3208/sandf.43.4\\_81](https://doi.org/10.3208/sandf.43.4_81).

- DeJong, Jason T. and Zachary J. Westgate (2009). "Role of Initial State, Material Properties, and Confinement Condition on Local and Global Soil-Structure Interface Behavior". In: *Journal of Geotechnical and Geoenvironmental Engineering* 135.11, pp. 1646–1660. DOI: [https://doi.org/10.1061/\(ASCE\)1090-0241\(2009\)135:11\(1646\)](https://doi.org/10.1061/(ASCE)1090-0241(2009)135:11(1646)).
- DeJong, Jason T., David J. White, and Mark F. Randolph (2006). "Microscale Observation and Modeling of Soil-Structure Interface Behavior Using Particle Image Velocimetry". In: *Soils and Foundations* 46.1, pp. 15–28. DOI: <https://doi.org/10.3208/sandf.46.15>.
- Desrues, J. and R. Chambon (1989). "Shear band analysis for granular materials: The question of incremental non-linearity". In: *Ingenieur-Archiv* 59.3, pp. 187–196. ISSN: 1432-0681. DOI: [10.1007/BF00532249](https://doi.org/10.1007/BF00532249).
- Desrues, J., R. Chambon, M. Mokni, and F. Mazerolle (Sept. 1996). "Void ratio evolution inside shear bands in triaxial sand specimens studied by computed tomography". In: *Géotechnique* 46.3, pp. 529–546. ISSN: 1751-7656. DOI: <https://doi.org/10.1680/geot.1996.46.3.529>.
- Desrues, J., J. Lanier, and P. Stutz (Jan. 1985). "Localization of the deformation in tests on sand sample". In: *Engineering Fracture Mechanics* 21.4, pp. 909–921. ISSN: 0013-7944. DOI: [https://doi.org/10.1016/0013-7944\(85\)90097-9](https://doi.org/10.1016/0013-7944(85)90097-9).
- Desrues, Jacques and Gioacchino Viggiani (Mar. 2004). "Strain localization in sand: an overview of the experimental results obtained in Grenoble using stereophotogrammetry". In: *International Journal for Numerical and Analytical Methods in Geomechanics* 28.4, pp. 279–321. ISSN: 1096-9853. DOI: <https://doi.org/10.1002/nag.338>.
- Dosta, M et al. (2023). "Comparing open-source DEM frameworks for simulations of common bulk processes". en. In: DOI: <https://doi.org/10.5281/zenodo.8252892>.
- Drescher, A. (1991). *Analytical Methods in Bin-load Analysis*. Developments in civil engineering. Elsevier. ISBN: 9780444417152. URL: <https://books.google.pl/books?id=Q7YAQgAACAAJ>.
- Drescher, A. (1992). "On the criteria for mass flow in hoppers". In: *Powder Technology* 73.3, pp. 251–260. DOI: [https://doi.org/10.1016/0032-5910\(92\)85031-P](https://doi.org/10.1016/0032-5910(92)85031-P).
- Drescher, A., T. W. Cousens, and P. L. Bransby (1978). "Kinematics of the mass flow of granular material through a plane hopper". In: *Géotechnique* 28.1, pp. 27–42. DOI: [10.1680/GEOT.1978.28.1.27](https://doi.org/10.1680/GEOT.1978.28.1.27).
- Drescher, Andrew (Nov. 1998). "Some aspects of flow in granular materials in hoppers". In: *Philosophical Transactions of the Royal Society of London. Series A: Mathematical, Physical and Engineering Sciences* 356.1747. Ed. by D. Muir Wood, G. S. Boulton, and J. M. Rotter, pp. 2649–2666. ISSN: 1471-2962. DOI: <https://doi.org/10.1098/rsta.1998.0291>.
- Ebrahimian, Babak and Erich Bauer (Aug. 2011). "Numerical simulation of the effect of interface friction of a bounding structure on shear deformation in a granular soil". In: *International Journal for Numerical and Analytical Methods in Geomechanics* 36.12, pp. 1486–1506. ISSN: 1096-9853. DOI: [10.1002/nag.1059](https://doi.org/10.1002/nag.1059).
- EN 1991-4, Eurocode 1: Actions on structures. Part 4: Silos and tanks (2006).

- Feng, Shi-Jin, Xin Liu, Hong-Xin Chen, and T. Zhao (2018). "Micro-mechanical analysis of geomembrane-sand interactions using DEM". In: *Computers and Geotechnics* 94, pp. 58–71. DOI: <http://dx.doi.org/10.1016/j.compgeo.2017.08.019>.
- Fenistein, Denis and Martin van Hecke (Sept. 2003). "Wide shear zones in granular bulk flow". In: *Nature* 425.6955, pp. 256–256. ISSN: 1476-4687. DOI: <https://doi.org/10.1038/425256a>.
- Gallego, Eutiquio, José María Fuentes, Joanna Wiącek, José Ramón Villar, and Francisco Ayuga (Oct. 2019). "DEM analysis of the flow and friction of spherical particles in steel silos with corrugated walls". In: *Powder Technology* 355, pp. 425–437. ISSN: 0032-5910. DOI: <https://doi.org/10.1016/j.powtec.2019.07.072>.
- Gallego, Eutiquio, Angel Ruiz, and Pedro J. Aguado (Oct. 2015). "Simulation of silo filling and discharge using ANSYS and comparison with experimental data". In: *Computers and Electronics in Agriculture* 118, pp. 281–289. ISSN: 0168-1699. DOI: <https://doi.org/10.1016/j.compag.2015.09.014>.
- Gandia, Rômulo Marçal, Francisco Carlos Gomes, Wisner Coimbra De Paula, and Pedro José Aguado Rodriguez (Dec. 2021). "Evaluation of pressures in slender silos varying hopper angle and silo slenderness". In: *Powder Technology* 394, pp. 478–495. ISSN: 0032-5910. DOI: <https://doi.org/10.1016/j.powtec.2021.08.087>.
- González-Montellano, C., Á. Ramírez, E. Gallego, and F. Ayuga (2011). "Validation and experimental calibration of 3D discrete element models for the simulation of the discharge flow in silos". In: *Chemical Engineering Science* 66.21, pp. 5116–5126. DOI: <https://doi.org/10.1016/j.ces.2011.07.009>.
- Grabowski, A., J. Konkol, M. Wójcik, and M. Nitka (Nov. 2023). "Experimental analysis of interface behavior between sand and corrugated surfaces with DIC technique". In: DOI: <https://doi.org/10.21203/rs.3.rs-3525250/v1>.
- Grabowski, A. and M. Nitka (2020). "3D DEM simulations of basic geotechnical tests with early detection of shear localization". In: *Studia Geotechnica et Mechanica* 43.1, pp. 48–64. DOI: <https://doi.org/10.2478/sgem-2020-0010>.
- Grabowski, A., M. Nitka, and J. Tejchman (2020). "3D DEM simulations of monotonic interface behaviour between cohesionless sand and rigid wall of different roughness". In: *Acta Geotechnica* 16.4, pp. 1001–1026. DOI: <https://doi.org/10.1007/s11440-020-01085-6>.
- Grabowski, A., M. Nitka, and J. Tejchman (2021a). "Comparative 3D DEM simulations of sand–structure interfaces with similarly shaped clumps versus spheres with contact moments". In: *Acta Geotechnica* 16.11, pp. 3533–3554. DOI: <https://doi.org/10.1007/s11440-021-01255-0>.
- Grabowski, A., M. Nitka, and J. Tejchman (2021b). "Micro-modelling of shear localization during quasi-static confined granular flow in silos using DEM". In: *Computers and Geotechnics* 134, p. 104108. DOI: <https://doi.org/10.1016/j.compgeo.2021.104108>.
- Grabowski, Aleksander, Michał Nitka, and Jacek Tejchman (Dec. 2022). "DEM Analyses of Interface Behaviour Between Cohesionless Sand and Rigid Wall of Different Roughness". In: pp. 230–239. ISSN: 1866-8763. DOI: 10.1007/978-3-031-22213-9\_24.
- Grudzien, Krzysztof, Zbigniew Chaniecki, Andrzej Romanowski, Maciej Niedostatkiwicz, and Dominik Sankowski (2012). "ECT Image Analysis Methods for Shear Zone

- Measurements during Silo Discharging Process". In: *Chinese Journal of Chemical Engineering* 20.2, pp. 337–345.
- Gu, Xiaoqiang, Yuanwen Chen, and Maosong Huang (2017). "Critical state shear behavior of the soil-structure interface determined by discrete element modeling". In: *Particuology* 35, pp. 68–77. DOI: <https://doi.org/10.1016/j.partic.2017.02.002>.
- Guaita, M, A Couto, and F Ayuga (May 2003). "Numerical Simulation of Wall Pressure during Discharge of Granular Material from Cylindrical Silos with Eccentric Hoppers". In: *Biosystems Engineering* 85.1, pp. 101–109. ISSN: 1537-5110. DOI: [10.1016/S1537-5110\(03\)00037-0](https://doi.org/10.1016/S1537-5110(03)00037-0).
- Gutfraind, R. and O. Pouliquen (Dec. 1996). "Study of the origin of shear zones in quasi-static vertical chute flows by using discrete particle simulations". In: *Mechanics of Materials* 24.4, pp. 273–285. ISSN: 0167-6636. DOI: [https://doi.org/10.1016/S0167-6636\(96\)00040-3](https://doi.org/10.1016/S0167-6636(96)00040-3).
- Gutierrez, Marte, J. Wang, and M. Yoshimine (July 2009). "Modeling of the simple shear deformation of sand: effects of principal stress rotation". In: *Acta Geotechnica* 4.3, pp. 193–201. ISSN: 1861-1133. DOI: [10.1007/s11440-009-0094-3](https://doi.org/10.1007/s11440-009-0094-3).
- Hall, S.A., M. Bornert, J. Desrues, Y. Pannier, N. Lenoir, G. Viggiani, and P. Bésuelle (2010). "Discrete and continuum analysis of localised deformation in sand using X-ray microCT and volumetric digital image correlation". In: *Géotechnique* 60.5, pp. 315–322. DOI: [10.1680/geot.2010.60.5.315](https://doi.org/10.1680/geot.2010.60.5.315).
- Han, Chunhua and Andrew Drescher (Mar. 1993). "Shear Bands in Biaxial Tests on Dry Coarse Sand". In: *Soils and Foundations* 33.1, pp. 118–132. ISSN: 0038-0806. DOI: <https://doi.org/10.3208/sandf1972.33.118>.
- Han, Yanlong, Fuguo Jia, Gengrun Li, Hanru Liu, Jiming Li, and Peiyu Chen (Sept. 2019). "Numerical analysis of flow pattern transition in a conical silo with ellipsoid particles". In: *Advanced Powder Technology* 30.9, pp. 1870–1881. ISSN: 0921-8831. DOI: <https://doi.org/10.1016/j.apt.2019.06.004>.
- Hogue, Caroline and David Newland (1994). "Efficient computer simulation of moving granular particles". In: *Powder Technology* 78.1, pp. 51–66. DOI: [10.1016/0032-5910\(93\)02748-y](https://doi.org/10.1016/0032-5910(93)02748-y).
- Hoomans, B.P.B., J.A.M. Kuipers, W.J. Briels, and W.P.M. van Swaaij (1996). "Discrete particle simulation of bubble and slug formation in a two-dimensional gas-fluidised bed: A hard-sphere approach". In: *Chemical Engineering Science* 51.1, pp. 99–118. DOI: [https://doi.org/10.1016/0009-2509\(95\)00271-5](https://doi.org/10.1016/0009-2509(95)00271-5).
- Horabik, Józef and Marek Molenda (July 2016). "Parameters and contact models for DEM simulations of agricultural granular materials: A review". In: *Biosystems Engineering* 147, pp. 206–225. ISSN: 1537-5110. DOI: <https://doi.org/10.1016/j.biosystemseng.2016.02.017>.
- Hu, Liming and Jialiu Pu (2004). "Testing and Modeling of Soil-Structure Interface". In: *Journal of Geotechnical and Geoenvironmental Engineering* 130.8, pp. 851–860. DOI: [https://doi.org/10.1061/\(ASCE\)1090-0241\(2004\)130:8\(851\)](https://doi.org/10.1061/(ASCE)1090-0241(2004)130:8(851)).
- Huang, W., E. Bauer, and S. W. Sloan (2003). "Behaviour of interfacial layer along granular soil-structure interfaces". In: *Structural Engineering and Mechanics* 15.3, pp. 315–329.

- Härtl, Johannes and Jin Y. Ooi (Mar. 2008). "Experiments and simulations of direct shear tests: porosity, contact friction and bulk friction". In: *Granular Matter* 10.4, pp. 263–271. ISSN: 1434-7636. DOI: 10.1007/s10035-008-0085-3.
- Itasca Consulting Group, Inc. (2019). "PFC — Particle Flow Code, Ver. 6.0. manual". In: *Minneapolis: Itasca*.
- Iwashita, Kazuyoshi and Masanobu Oda (1998). "Rolling Resistance at Contacts in Simulation of Shear Band Development by DEM". In: *Journal of Engineering Mechanics* 124.3, pp. 285–292. DOI: [https://doi.org/10.1061/\(ASCE\)0733-9399\(1998\)124:3\(285\)](https://doi.org/10.1061/(ASCE)0733-9399(1998)124:3(285)).
- Janssen, H.A. (1895). "Versuche über Getreidedruck in Silozellen. Zeitschrift des Vereins deutscher Ingenieure". In: *Band 39, No. 35*.
- Jenike, A. W. (1961). *Gravity Flow of Bulk Solids*.
- Jenike, A. W. (1964). *Storage and Flow of Solids*.
- Jing, Xue-Ying, Wan-Huan Zhou, Hua-Xiang Zhu, Zhen-Yu Yin, and Yangmin Li (2017). "Analysis of soil-structural interface behavior using three-dimensional DEM simulations". In: *International Journal for Numerical and Analytical Methods in Geomechanics* 42.2, pp. 339–357. DOI: <https://doi.org/10.1002/nag.2745>.
- Kawaguchi, T., T. Tanaka, and Y. Tsuji (1998). "Numerical simulation of two-dimensional fluidized beds using the discrete element method (comparison between the two- and three-dimensional models)". In: *Powder Technology* 96.2, pp. 129–138. DOI: [https://doi.org/10.1016/S0032-5910\(97\)03366-4](https://doi.org/10.1016/S0032-5910(97)03366-4).
- Ketterhagen, William R., Jennifer S. Curtis, Carl R. Wassgren, and Bruno C. Hancock (Oct. 2009). "Predicting the flow mode from hoppers using the discrete element method". In: *Powder Technology* 195.1, pp. 1–10. ISSN: 0032-5910. DOI: <https://doi.org/10.1016/j.powtec.2009.05.002>.
- Kobyłka, R. and M. Molenda (Jan. 2013). "DEM modelling of silo load asymmetry due to eccentric filling and discharge". In: *Powder Technology* 233, pp. 65–71. ISSN: 0032-5910. DOI: <https://doi.org/10.1016/j.powtec.2012.08.039>.
- Kolymbas, D. and W. Wu (1990). "Recent results of triaxial tests with granular materials". In: *Powder Technology* 60.2, pp. 99–119. DOI: [https://doi.org/10.1016/0032-5910\(90\)80136-M](https://doi.org/10.1016/0032-5910(90)80136-M).
- Kozicki, J. and F.V. Donzé (2008). "A new open-source software developed for numerical simulations using discrete modeling methods". In: *Computer Methods in Applied Mechanics and Engineering* 197.49-50, pp. 4429–4443. DOI: <https://doi.org/10.1016/j.cma.2008.05.023>.
- Kozicki, J., M. Niedostatkiwicz, J. Tejchman, and H.-B. Mühlhaus (2013). "Discrete modelling results of a direct shear test for granular materials versus FE results". In: *Granular Matter* 15.5, pp. 607–627. DOI: 10.1007/s10035-013-0423-y.
- Kozicki, J. and J. Tejchman (2017). "Investigations of quasi-static vortex structures in 2D sand specimen under passive earth pressure conditions based on DEM and Helmholtz–Hodge vector field decomposition". In: *Granular Matter* 19.2. DOI: 10.1007/s10035-017-0714-9.
- Kozicki, J., J. Tejchman, and Z. Mróz (2012). "Effect of grain roughness on strength, volume changes, elastic and dissipated energies during quasi-static homogeneous triaxial compression using DEM". In: *Granular Matter* 14.4, pp. 457–468. DOI: 10.1007/s10035-012-0352-1.

- Kozicki, Jan, Jacek Tejchman, and Hans-Bernd Mühlhaus (2014). "Discrete simulations of a triaxial compression test for sand by DEM". In: *International Journal for Numerical and Analytical Methods in Geomechanics* 38.18, pp. 1923–1952. DOI: 10.1002/nag.2285.
- Krzaczek, M., M. Nitka, and J. Tejchman (Nov. 2020). "Effect of gas content in macropores on hydraulic fracturing in rocks using a fully coupled DEM/CFD approach". In: *International Journal for Numerical and Analytical Methods in Geomechanics* 45.2, pp. 234–264. ISSN: 1096-9853. DOI: <https://doi.org/10.1002/nag.3160>.
- Krzyżanowski, J., J. Tejchman, W. Sołowski, and M. Wójcik (2021). "Modelling of shear zones during quasi-static granular silo flow using material point method (MPM)". In: *Powder Technology* 378, pp. 538–560. DOI: 10.1016/j.powtec.2020.10.001.
- Krzyżanowski, J., J. Tejchman, and M. Wójcik (Nov. 2021). "Modelling of full-scale silo experiments with flow correcting inserts using material point method (MPM) based on hypoplasticity". In: *Powder Technology* 392, pp. 375–392. ISSN: 0032-5910. DOI: <https://doi.org/10.1016/j.powtec.2021.06.059>.
- Kuczyńska, N., M. Wójcik, and J. Tejchman (Dec. 2015). "Effect of bulk solid on strength of cylindrical corrugated silos during filling". In: *Journal of Constructional Steel Research* 115, pp. 1–17. ISSN: 0143-974X. DOI: <https://doi.org/10.1016/j.jcsr.2015.08.002>.
- Lade, Poul V. (1977). "Elasto-plastic stress-strain theory for cohesionless soil with curved yield surfaces". In: *International Journal of Solids and Structures* 13.11, pp. 1019–1035. ISSN: 0020-7683. DOI: [https://doi.org/10.1016/0020-7683\(77\)90073-7](https://doi.org/10.1016/0020-7683(77)90073-7).
- Langston, P.A., U. Tüzün, and D.M. Heyes (Mar. 1995). "Discrete element simulation of granular flow in 2D and 3D hoppers: Dependence of discharge rate and wall stress on particle interactions". In: *Chemical Engineering Science* 50.6, pp. 967–987. ISSN: 0009-2509. DOI: [https://doi.org/10.1016/0009-2509\(94\)00467-6](https://doi.org/10.1016/0009-2509(94)00467-6).
- Lee, Jysoo (Jan. 1994). "Density waves in the flows of granular media". In: *Physical Review E* 49.1, pp. 281–298. ISSN: 1095-3787. DOI: <https://doi.org/10.1103/PhysRevE.49.281>.
- Leśniewska, D., M. Nitka, J. Tejchman, and M. Pietrzak (2020). "Contact force network evolution in active earth pressure state of granular materials: photo-elastic tests and DEM". In: *Granular Matter* 22.3. DOI: 10.1007/s10035-020-01033-x.
- Leśniewska, Danuta, Antoinette Tordesillas, Magdalena Pietrzak, Shuo Zhou, and Michał Nitka (May 2023). "Structured deformation of granular material in the state of active earth pressure". In: *Computers and Geotechnics* 157, p. 105316. ISSN: 0266-352X. DOI: <https://doi.org/10.1016/j.compgeo.2023.105316>.
- Liu, Junwei, Nuo Duan, Liang Cui, and Na Zhu (June 2019). "DEM investigation of installation responses of jacked open-ended piles". In: *Acta Geotechnica* 14.6, pp. 1805–1819. ISSN: 1861-1133. DOI: <https://doi.org/10.1007/s11440-019-00817-7>.
- Luding, Stefan (2004). "Micro-macro transition for anisotropic, frictional granular packings". In: *International Journal of Solids and Structures* 41.21, pp. 5821–5836. DOI: 10.1016/j.ijsolstr.2004.05.048.

- Luding, Stefan, N. Rivas, and Thomas Weinhart (2017). "From soft and hard particle simulations to continuum theory for granular flows". In: *ALERT geomaterials Doctoral School*.
- Matsushima, Takashi, Kentaro Uesugi, Tsukasa Nakano, and Akira Tsuchiyama (Jan. 2006). "Visualization of Grain Motion inside a Triaxial Specimen by Micro X-ray CT at SPring-8". In: *Advances in X-ray Tomography for Geomaterials*, pp. 255–261. DOI: <https://doi.org/10.1002/9780470612187.ch24>.
- Michalowski, R. L. (Sept. 1990). "Strain localization and periodic fluctuations in granular flow processes from hoppers". In: *Géotechnique* 40.3, pp. 389–403. ISSN: 1751-7656. DOI: <https://doi.org/10.1680/geot.1990.40.3.389>.
- Michalowski, Radoslaw L. (1987). "Flow of granular media through a plane parallel/converging bunker". In: *Chemical Engineering Science* 42.11, pp. 2587–2596. DOI: [https://doi.org/10.1016/0009-2509\(87\)87010-0](https://doi.org/10.1016/0009-2509(87)87010-0).
- Michalowski, R.L. (Aug. 1984). "Flow of granular material through a plane hopper". In: *Powder Technology* 39.1, pp. 29–40. ISSN: 0032-5910. DOI: [https://doi.org/10.1016/0032-5910\(84\)85017-2](https://doi.org/10.1016/0032-5910(84)85017-2).
- Mindlin, R. D. and H. Deresiewicz (Sept. 1953). "Elastic Spheres in Contact Under Varying Oblique Forces". In: *Journal of Applied Mechanics* 20.3, pp. 327–344. ISSN: 1528-9036. DOI: <https://doi.org/10.1115/1.4010702>.
- Mishra, B.K (Sept. 2003). "A review of computer simulation of tumbling mills by the discrete element method: Part I—contact mechanics". In: *International Journal of Mineral Processing* 71.1–4, pp. 73–93. ISSN: 0301-7516. DOI: [10.1016/S0301-7516\(03\)00032-2](https://doi.org/10.1016/S0301-7516(03)00032-2).
- Modenese, C., S. Utili, and G.T. Houlsby (Aug. 2012). "A Numerical Investigation of Quasi-static Conditions for Granular Media". In: pp. 187–195. DOI: <https://doi.org/10.1039/9781849735032-00187>.
- Mohamed, Abdalsalam and Marte Gutierrez (2010). "Comprehensive study of the effects of rolling resistance on the stress–strain and strain localization behavior of granular materials". In: *Granular Matter* 12.5, pp. 527–541.
- Molenda, M., J. Horabik, I. J. Ross, and M. D. Montross (2002). "Friction of Wheat: Grain-on-Grain and on Corrugated Steel". In: *Transactions of the ASAE* 45.2. ISSN: 2151-0059. DOI: <https://doi.org/10.13031/2013.8522>.
- Moore, Dwight W., G. M. White, and I. J. Ross (1984). "Friction of Wheat on Currogated Metal Surfaces". In: *Transactions of the ASAE* 27.6, pp. 1842–1847. ISSN: 2151-0059. DOI: [10.13031/2013.33055](https://doi.org/10.13031/2013.33055).
- Munjiza, A., D.R.J. Owen, and N. Bicanic (1995). "A combined finite-discrete element method in transient dynamics of fracturing solids". In: *Engineering Computations* 12.2, pp. 145–174. DOI: <https://doi.org/10.1108/02644409510799532>.
- Munjiza, Ante (2004). "The Combined Finite-Discrete Element Method". In: DOI: [10.1002/0470020180](https://doi.org/10.1002/0470020180).
- Mühlhaus, H. B. and I. Vardoulakis (Sept. 1987). "The thickness of shear bands in granular materials". In: *Géotechnique* 37.3, pp. 271–283. ISSN: 1751-7656. DOI: <https://doi.org/10.1680/geot.1987.37.3.271>.

- Mühlhaus, Hans-Bernd (Nov. 1990). "Stress and couple stress in a layered half plane with surface loading". In: *International Journal for Numerical and Analytical Methods in Geomechanics* 14.8, pp. 545–563. ISSN: 1096-9853. DOI: <https://doi.org/10.1002/nag.1610140803>.
- Nedderman, R.M. and C. Laohakul (Jan. 1980). "The thickness of the shear zone of flowing granular materials". In: *Powder Technology* 25.1, pp. 91–100. ISSN: 0032-5910. DOI: [https://doi.org/10.1016/0032-5910\(80\)87014-8](https://doi.org/10.1016/0032-5910(80)87014-8).
- Nguyen, Trung-Kien, Jacques Desrues, Thanh-Trung Vo, and Gaël Combe (Jan. 2022). "FEM×DEM multi-scale model for cemented granular materials: Inter- and intra-granular cracking induced strain localisation". In: *International Journal for Numerical and Analytical Methods in Geomechanics* 46.5, pp. 1001–1025. ISSN: 1096-9853. DOI: [10.1002/nag.3332](https://doi.org/10.1002/nag.3332).
- Niedostatkiewicz, M., D. Lesniewska, and J. Tejchman (Dec. 2011). "Experimental Analysis of Shear Zone Patterns in Cohesionless for Earth Pressure Problems Using Particle Image Velocimetry". In: *Strain* 47.s2, pp. 218–231. ISSN: 1475-1305. DOI: <https://doi.org/10.1111/j.1475-1305.2010.00761.x>.
- Nisar, F., J. Rojek, S. Nosewicz, K. Kaszyca, and M. Chmielewski (Mar. 2024). "Evaluation of effective thermal conductivity of sintered porous materials using an improved discrete element model". In: *Powder Technology* 437, p. 119546. ISSN: 0032-5910. DOI: <https://doi.org/10.1016/j.powtec.2024.119546>.
- Nitka, M. and A. Grabowski (Oct. 2021). "Shear band evolution phenomena in direct shear test modelled with DEM". In: *Powder Technology* 391, pp. 369–384. ISSN: 0032-5910. DOI: <https://doi.org/10.1016/j.powtec.2021.06.025>.
- Nitka, M., J. Tejchman, J. Kozicki, and D. Leśniewska (2015). "DEM analysis of microstructural events within granular shear zones under passive earth pressure conditions". In: *Granular Matter* 17.3, pp. 325–343. DOI: [10.1007/s10035-015-0558-0](https://doi.org/10.1007/s10035-015-0558-0).
- Nitka, Michał, Gaël Combe, Cristian Dascalu, and Jacques Desrues (Mar. 2011). "Two-scale modeling of granular materials: a DEM-FEM approach". In: *Granular Matter* 13.3, pp. 277–281. ISSN: 1434-7636. DOI: [10.1007/s10035-011-0255-6](https://doi.org/10.1007/s10035-011-0255-6).
- Nosewicz, S., J. Rojek, K. Pietrzak, and M. Chmielewski (2013). "Viscoelastic discrete element model of powder sintering". In: *Powder Technology* 246, pp. 157–168. DOI: <https://doi.org/10.1016/j.powtec.2013.05.020>.
- Oda, M. and H. Kazama (Aug. 1998). "Microstructure of shear bands and its relation to the mechanisms of dilatancy and failure of dense granular soils". In: *Géotechnique* 48.4, pp. 465–481. ISSN: 1751-7656. DOI: [10.1680/geot.1998.48.4.465](https://doi.org/10.1680/geot.1998.48.4.465).
- Oda, M., T. Takemura, and M. Takahashi (Oct. 2004). "Microstructure in shear band observed by microfocus X-ray computed tomography". In: *Géotechnique* 54.8, pp. 539–542. ISSN: 1751-7656. DOI: [10.1680/geot.2004.54.8.539](https://doi.org/10.1680/geot.2004.54.8.539).
- Oda, Masanobu (Dec. 1972). "Deformation Mechanism of Sand in Triaxial Compression Tests". In: *Soils and Foundations* 12.4, pp. 45–63. ISSN: 0038-0806. DOI: [https://doi.org/10.3208/sandf1972.12.4\\_45](https://doi.org/10.3208/sandf1972.12.4_45).
- Oda, Masanobu and Kazuyoshi Iwashita (Oct. 2000). "Study on couple stress and shear band development in granular media based on numerical simulation analyses". In: *International Journal of Engineering Science* 38.15, pp. 1713–1740. ISSN: 0020-7225. DOI: [https://doi.org/10.1016/S0020-7225\(99\)00132-9](https://doi.org/10.1016/S0020-7225(99)00132-9).

- Oñate, E. and J. Rojek (2004). "Combination of discrete element and finite element methods for dynamic analysis of geomechanics problems". In: *Computer Methods in Applied Mechanics and Engineering* 193.27-29, pp. 3087–3128. DOI: <https://doi.org/10.1016/j.cma.2003.12.056>.
- Parafiniuk, Piotr, Marek Molenda, and Józef Horabik (2013). "Discharge of rapeseeds from a model silo: Physical testing and discrete element method simulations". In: *Computers and Electronics in Agriculture* 97, pp. 40–46. DOI: <https://doi.org/10.1016/j.compag.2013.06.008>.
- Parhami, F. and R.M. McMeeking (1998). "A network model for initial stage sintering". In: *Mechanics of Materials* 27.2, pp. 111–124. DOI: [https://doi.org/10.1016/S0167-6636\(97\)00034-3](https://doi.org/10.1016/S0167-6636(97)00034-3).
- Pariseau, William G. (1969). "Discontinuous velocity fields in gravity flows of granular materials through slots". In: *Powder Technology* 3.1, pp. 218–226. DOI: [https://doi.org/10.1016/0032-5910\(69\)80081-1](https://doi.org/10.1016/0032-5910(69)80081-1).
- Peters, W. H. and W. F. Ranson (June 1982). "Digital Imaging Techniques In Experimental Stress Analysis". In: *Optical Engineering* 21.3. ISSN: 0091-3286. DOI: <https://doi.org/10.1117/12.7972925>.
- Pincus, HJ, SG Paikowsky, CM Player, and PJ Connors (1995). "A Dual Interface Apparatus for Testing Unrestricted Friction of Soil Along Solid Surfaces". In: *Geotechnical Testing Journal* 18.2, p. 168. DOI: 10.1520/GTJ10320J.
- Podlozhnyuk, Alexander, Stefan Pirker, and Christoph Kloss (2016). "Efficient implementation of superquadric particles in Discrete Element Method within an open-source framework". In: *Computational Particle Mechanics* 4.1, pp. 101–118. DOI: 10.1007/s40571-016-0131-6.
- Porcino, D, L David Suits, TC Sheahan, V Fioravante, VN Ghionna, and S Pedroni (2003). "Interface Behavior of Sands from Constant Normal Stiffness Direct Shear Tests". In: *Geotechnical Testing Journal* 26.3, p. 19513. ISSN: 0149-6115. DOI: 10.1520/GTJ11308J.
- Potyondy, J. G. (Dec. 1961). "Skin Friction between Various Soils and Construction Materials". In: *Géotechnique* 11.4, pp. 339–353. ISSN: 1751-7656. DOI: <https://doi.org/10.1680/geot.1961.11.4.339>.
- Pöschel, Thorsten and Thomas Schwager (2005). "Computational Granular Dynamics". In: DOI: <https://doi.org/10.1007/3-540-27720-X>.
- Rechenmacher, Amy L. (2006). "Grain-scale processes governing shear band initiation and evolution in sands". In: *Journal of the Mechanics and Physics of Solids* 54.1, pp. 22–45. DOI: <https://doi.org/10.1016/j.jmps.2005.08.009>.
- Richefeu, V., G. Combe, and G. Viggiani (Sept. 2012). "An experimental assessment of displacement fluctuations in a 2D granular material subjected to shear". In: *Géotechnique Letters* 2.3, pp. 113–118. ISSN: 2045-2543. DOI: <https://doi.org/10.1680/geolett.12.00029>.
- Rojek, Jerzy, Szymon Nosewicz, Marcin Maździarz, Piotr Kowalczyk, Krzysztof Wawrzyk, and Dmytro Lumelskyj (2017). "Modeling of a Sintering Process at Various Scales". In: *Procedia Engineering* 177, pp. 263–270. ISSN: 1877-7058. DOI: <https://doi.org/10.1016/j.proeng.2017.02.210>.
- Rojek, Jerzy, Aleksander Zubelewicz, Nikhil Madan, and Szymon Nosewicz (Feb. 2018). "The discrete element method with deformable particles". In: *International*

- Journal for Numerical Methods in Engineering* 114.8, pp. 828–860. ISSN: 1097-0207. DOI: <https://doi.org/10.1002/nme.5767>.
- Roscoe, K. H. (June 1970). "The Influence of Strains in Soil Mechanics". In: *Géotechnique* 20.2, pp. 129–170. ISSN: 1751-7656. DOI: [10.1680/geot.1970.20.2.129](https://doi.org/10.1680/geot.1970.20.2.129).
- Rotter, J. (2001). *Guide for the Economic Design of Circular Metal Silos*. CRC Press.
- Rotter, J. M., J. M.F. G. Holst, J. Y. Ooi, and A. M. Sanad (1998). "Silo pressure predictions using discrete–element and finite–element analyses". In: *Philosophical Transactions of the Royal Society of London. Series A: Mathematical, Physical and Engineering Sciences* 356.1747. Ed. by D. Muir Wood, G. S. Boulton, and J. M. Rotter, pp. 2685–2712. DOI: <https://doi.org/10.1098/rsta.1998.0293>.
- Roux, Jean-Noël and François Chevoir (Jan. 2005). "Discrete numerical simulation and this mechanical behavior of granular materials". In: *Bulletin des Laboratoires des Ponts et Chaussées*, pp. 109–138.
- Réthoré, Julien, François Hild, and Stéphane Roux (Nov. 2007). "Shear-band capturing using a multiscale extended digital image correlation technique". In: *Computer Methods in Applied Mechanics and Engineering* 196.49–52, pp. 5016–5030. ISSN: 0045-7825. DOI: <https://doi.org/10.1016/j.cma.2007.06.019>.
- Salazar, Antonio, Esteban Sáez, and Gislaine Pardo (2015). "Modeling the direct shear test of a coarse sand using the 3D Discrete Element Method with a rolling friction model". In: *Computers and Geotechnics* 67, pp. 83–93. DOI: [10.1016/j.compgeo.2015.02.017](https://doi.org/10.1016/j.compgeo.2015.02.017).
- Saleh, Khashayar, Shahab Golshan, and Reza Zarghami (Dec. 2018). "A review on gravity flow of free-flowing granular solids in silos – Basics and practical aspects". In: *Chemical Engineering Science* 192, pp. 1011–1035. ISSN: 0009-2509. DOI: <https://doi.org/10.1016/j.ces.2018.08.028>.
- Salot, Christophe, Philippe Gotteland, and Pascal Villard (Apr. 2009). "Influence of relative density on granular materials behavior: DEM simulations of triaxial tests". In: *Granular Matter* 11.4, pp. 221–236. ISSN: 1434-7636. DOI: [10.1007/s10035-009-0138-2](https://doi.org/10.1007/s10035-009-0138-2).
- Shibuya, S., T. Mitachi, and S. Tamate (Sept. 1997). "Interpretation of direct shear box testing of sands as quasi-simple shear". In: *Géotechnique* 47.4, pp. 769–790. ISSN: 1751-7656. DOI: <https://doi.org/10.1680/geot.1997.47.4.769>.
- Slominski, Cezary, Maciej Niedostatkiewicz, and Jacek Tejchman (2007). "Application of particle image velocimetry (PIV) for deformation measurement during granular silo flow". In: *Powder Technology* 173.1, pp. 1–18. DOI: [10.1016/j.powtec.2006.11.018](https://doi.org/10.1016/j.powtec.2006.11.018).
- Smilauer, Vaclav et al. (2023). "Yade Documentation". In: DOI: [10.48550/arXiv.2301.00611](https://doi.org/10.48550/arXiv.2301.00611).
- Stanier, Sam, Jelke Dijkstra, Danuta Leśniewska, James Hambleton, David White, and David Muir Wood (Feb. 2016). "Vermiculate artefacts in image analysis of granular materials". In: *Computers and Geotechnics* 72, pp. 100–113. ISSN: 0266-352X. DOI: <https://doi.org/10.1016/j.compgeo.2015.11.013>.
- Stazhevskii, S. B. (Sept. 1982). "Stresses in the neighborhoods of defects in bunker walls". In: *Soviet mining science* 18.5, pp. 379–387. ISSN: 1573-8736. DOI: <https://doi.org/10.1007/BF02528442>.

- Su, Li-Jun, Wan-Huan Zhou, Wei-Bin Chen, and Xixi Jie (2018). "Effects of relative roughness and mean particle size on the shear strength of sand-steel interface". In: *Measurement* 122, pp. 339–346. DOI: 10.1016/j.measurement.2018.03.003.
- Takahashi, Hiroshi and Hiroshi Yanai (Apr. 1973). "Flow profile and void fraction of granular solids in a moving bed". In: *Powder Technology* 7.4, pp. 205–214. ISSN: 0032-5910. DOI: [https://doi.org/10.1016/0032-5910\(73\)80026-9](https://doi.org/10.1016/0032-5910(73)80026-9).
- Tejchman, J. (1989). "Scherzonenbildung und Verspannungseffekte in Granulaten unter Berücksichtigung von Korndrehungen." In: *Institute for Soil- and Rock-Mechanics, University of Karlsruhe*.
- Tejchman, J. and E. Bauer (Jan. 2005). "Fe-simulations of a direct and a true simple shear test within a polar hypoplasticity". In: *Computers and Geotechnics* 32.1, pp. 1–16. ISSN: 0266-352X. DOI: 10.1016/j.compgeo.2004.11.004.
- Tejchman, J. and J. Górski (2009). "Finite element study of patterns of shear zones in granular bodies during plane strain compression". In: *Acta Geotechnica* 5.2, pp. 95–112. DOI: 10.1007/s11440-009-0103-6.
- Tejchman, J. and M. M. Wójcik (2011). *Experimental and Theoretical Investigations of Some Characteristic Silo Phenomena*.
- Tejchman, J. and W. Wu (1995). "Experimental and numerical study of sand-steel interfaces". In: *International Journal for Numerical and Analytical Methods in Geomechanics* 19.8, pp. 513–536. DOI: <https://doi.org/10.1002/nag.1610190803>.
- Tejchman, J. and W. Wu (Jan. 2009). "FE-investigation of shear localization in granular bodies under high shear rate". In: *Granular Matter* 11.2, pp. 115–128. ISSN: 1434-7636. DOI: 10.1007/s10035-009-0128-4.
- Tejchman, J. and W. Wu (2010). "FE-investigations of micro-polar boundary conditions along interface between soil and structure". In: *Granular Matter* 12.4, pp. 399–410. DOI: 10.1007/s10035-010-0191-x.
- Tejchman, Jacek (Dec. 2004). "Influence of a characteristic length on shear zone formation in hypoplasticity with different enhancements". In: *Computers and Geotechnics* 31.8, pp. 595–611. ISSN: 0266-352X. DOI: 10.1016/j.compgeo.2004.10.001.
- Tejchman, Jacek (2013). "Confined Granular Flow in Silos: Experimental and Numerical Investigations". In: *Springer Series in Geomechanics and Geoengineering*. ISSN: 1866-8763. DOI: <https://doi.org/10.1007/978-3-319-00318-4>.
- Thornton, C. and L. Zhang (2003). "Numerical Simulations of the Direct Shear Test". In: *Chemical Engineering and Technology* 26.2, pp. 153–156. DOI: <https://doi.org/10.1002/ceat.200390022>.
- Tsuji, Y., T. Kawaguchi, and T. Tanaka (1993). "Discrete particle simulation of two-dimensional fluidized bed". In: *Powder Technology* 77.1, pp. 79–87. DOI: [https://doi.org/10.1016/0032-5910\(93\)85010-7](https://doi.org/10.1016/0032-5910(93)85010-7).
- Uesugi, Morimichi and Hideaki Kishida (1986a). "Frictional Resistance at Yield between Dry Sand and Mild Steel". In: *Soils and Foundations* 26.4, pp. 139–149. DOI: <https://doi.org/10.3208/sandf1972.26.4\139>.
- Uesugi, Morimichi and Hideaki Kishida (1986b). "Influential Factors of Friction Between Steel and Dry Sands". In: *Soils and Foundations* 26.2, pp. 33–46. DOI: [https://doi.org/10.3208/sandf1972.26.2\\_33](https://doi.org/10.3208/sandf1972.26.2_33).

- Uesugi, Morimichi, Hideaki Kishida, and Yasunori Tsubakihara (1988). "Behavior of Sand Particles in Sand-Steel Friction". In: *Soils and Foundations* 28.1, pp. 107–118. DOI: <https://doi.org/10.3208/sandf1972.28.107>.
- Vardoulakis, I. (Apr. 1980). "Shear band inclination and shear modulus of sand in biaxial tests". In: *International Journal for Numerical and Analytical Methods in Geomechanics* 4.2, pp. 103–119. ISSN: 1096-9853. DOI: 10.1002/NAG.1610040202.
- Vardoulakis, I. and B. Graf (Sept. 1985). "Calibration of constitutive models for granular materials using data from biaxial experiments". In: *Géotechnique* 35.3, pp. 299–317. ISSN: 1751-7656. DOI: 10.1680/GEOT.1985.35.3.299.
- Vardoulakis, I., K.R. Shah, and P. Papanastasiou (Nov. 1992). "Modelling of tool-rock shear interfaces using gradient-dependent flow theory of plasticity". In: *International Journal of Rock Mechanics and Mining Sciences & Geomechanics Abstracts* 29.6, pp. 573–582. ISSN: 0148-9062. DOI: 10.1016/0148-9062(92)91615-C.
- Walker, D.M. (Nov. 1966). "An approximate theory for pressures and arching in hoppers". In: *Chemical Engineering Science* 21.11, pp. 975–997. ISSN: 0009-2509. DOI: [https://doi.org/10.1016/0009-2509\(66\)85095-9](https://doi.org/10.1016/0009-2509(66)85095-9).
- Walters, J.K. (Jan. 1973). "A theoretical analysis of stresses in silos with vertical walls". In: *Chemical Engineering Science* 28.1, pp. 13–21. ISSN: 0009-2509. DOI: 10.1016/0009-2509(73)85081-X.
- Wan, Jiangfeng, Fugang Wang, Guanghui Yang, Sheng Zhang, Mengke Wang, Ping Lin, and Lei Yang (July 2018). "The influence of orifice shape on the flow rate: A DEM and experimental research in 3D hopper granular flows". In: *Powder Technology* 335, pp. 147–155. ISSN: 0032-5910. DOI: 10.1016/j.powtec.2018.03.041.
- Wang, J., J. E. Dove, and M. S. Gutierrez (Aug. 2007a). "Discrete-continuum analysis of shear banding in the direct shear test". In: *Géotechnique* 57.6, pp. 513–526. ISSN: 1751-7656. DOI: <https://doi.org/10.1680/geot.2007.57.6.513>.
- Wang, Jianfeng, Marte S. Gutierrez, and Joseph E. Dove (Feb. 2007b). "Numerical studies of shear banding in interface shear tests using a new strain calculation method". In: *International Journal for Numerical and Analytical Methods in Geomechanics* 31.12, pp. 1349–1366. ISSN: 1096-9853. DOI: <https://doi.org/10.1002/nag.589>.
- Wang, Yin, Yong Lu, and Jin Y. Ooi (Sept. 2015). "A numerical study of wall pressure and granular flow in a flat-bottomed silo". In: *Powder Technology* 282, pp. 43–54. ISSN: 0032-5910. DOI: <https://doi.org/10.1016/j.powtec.2015.01.078>.
- White, D. J., W. A. Take, and M. D. Bolton (Sept. 2003). "Soil deformation measurement using particle image velocimetry (PIV) and photogrammetry". In: *Géotechnique* 53.7, pp. 619–631. ISSN: 1751-7656. DOI: 10.1680/geot.2003.53.7.619.
- Widulinski, L., J. Kozicki, J. Tejchman, M. Nakagawa, and S. Luding (2009). "Modeling of the Behavior of Granular Bodies using DEM with Contact Moments". In: DOI: <https://doi.org/10.1063/1.3179912>.
- Widuliński, Ł., J. Tejchman, J. Kozicki, and D. Leśniewska (2011). "Discrete simulations of shear zone patterning in sand in earth pressure problems of a retaining wall". In: *International Journal of Solids and Structures* 48.7-8, pp. 1191–1209. DOI: 10.1016/j.ijsolstr.2011.01.005.



- Więckowski, Z., S. Youn, and J. Yeon (1999). "A particle-in-cell solution to the silo discharging problem". In: *International Journal for Numerical Methods in Engineering* 45.9, pp. 1203–1225.
- Wiącek, J., J. Horabik, M. Molenda, and R. Kobyłka (May 2024). "Discharge rate influenced by friction and shape of dimers: Numerical study". In: *Tribology International* 193, p. 109421. ISSN: 0301-679X. DOI: <https://doi.org/10.1016/j.triboint.2024.109421>.
- Wiącek, Joanna, Eutiquio Gallego, Piotr Parafiniuk, Rafał Kobyłka, Maciej Bańda, Józef Horabik, and Marek Molenda (Sept. 2021). "Experimental analysis of wheat-wall friction and grain flow in a steel silo with corrugated walls". In: *Biosystems Engineering* 209, pp. 216–231. ISSN: 1537-5110. DOI: <https://doi.org/10.1016/j.biosystemseng.2021.07.003>.
- Wiącek, Joanna, Piotr Parafiniuk, Marek Molenda, Józef Horabik, and Eutiquio Gallego (May 2023). "DEM study of microstructural effects in friction of wheat on corrugated steel surface". In: *Tribology International* 183, p. 108435. ISSN: 0301-679X. DOI: <https://doi.org/10.1016/j.triboint.2023.108435>.
- Więckowski, Z. (Oct. 2004). "The material point method in large strain engineering problems". In: *Computer Methods in Applied Mechanics and Engineering* 193.39–41, pp. 4417–4438. ISSN: 0045-7825. DOI: 10.1016/j.cma.2004.01.035.
- Wójcik, M. (2008). "Experimental and Theoretical Investigations of Flow Pattern and Wall Pressures in Silos With and Without Inserts [Doctoral Thesis, Gdańsk University of Technology]". In.
- Wójcik, M. and J. Tejchman (2009). "Modeling of shear localization during confined granular flow in silos within non-local hypoplasticity". In: *Powder Technology* 192.3, pp. 298–310. DOI: 10.1016/j.powtec.2009.01.021.
- Wu, W. (1992). "Hypoplastizität als mathematisches Modell zum mechanischen Verhalten granularer Stoffe." In: *Heft 129. Institute for Soil- and Rock-Mechanics, University of Karlsruhe*.
- Wójcik, M., P. Iwicki, and J. Tejchman (Aug. 2011). "3D buckling analysis of a cylindrical metal bin composed of corrugated sheets strengthened by vertical stiffeners". In: *Thin-Walled Structures* 49.8, pp. 947–963. ISSN: 0263-8231. DOI: <https://doi.org/10.1016/j.tws.2011.03.010>.
- Wójcik, M., M. Sondej, K. Rejowski, and J. Tejchman (Apr. 2017). "Full-scale experiments on wheat flow in steel silo composed of corrugated walls and columns". In: *Powder Technology* 311, pp. 537–555. ISSN: 0032-5910. DOI: <https://doi.org/10.1016/j.powtec.2017.01.066>.
- Xu, B.H. and A.B. Yu (1997). "Numerical simulation of the gas-solid flow in a fluidized bed by combining discrete particle method with computational fluid dynamics". In: *Chemical Engineering Science* 52.16, pp. 2785–2809. DOI: [https://doi.org/10.1016/S0009-2509\(97\)00081-X](https://doi.org/10.1016/S0009-2509(97)00081-X).
- Zeghal, M. and U. El Shamy (2004). "A continuum-discrete hydromechanical analysis of granular deposit liquefaction". In: *International Journal for Numerical and Analytical Methods in Geomechanics* 28.14, pp. 1361–1383. DOI: 10.1002/nag.390.
- Zeng, Yong, Fuguo Jia, Yaxiong Zhang, Xiangyi Meng, Yanlong Han, and Hui Wang (May 2017). "DEM study to determine the relationship between particle velocity

- fluctuations and contact force disappearance". In: *Powder Technology* 313, pp. 112–121. ISSN: 0032-5910. DOI: 10.1016/j.powtec.2017.03.022.
- Zhang, L. and C. Thornton (May 2007). "A numerical examination of the direct shear test". In: *Géotechnique* 57.4, pp. 343–354. ISSN: 1751-7656. DOI: 10.1680/geot.2007.57.4.343.
- Zhang, Nan and T. Matthew Evans (2018). "Three dimensional discrete element method simulations of interface shear". In: *Soils and Foundations* 58.4, pp. 941–956. DOI: <https://doi.org/10.1016/j.sandf.2018.05.010>.
- Zhang, Q., M. G. Britton, and R. J. Kieper (1994). "Interactions Between Wheat and a Corrugated Steel Surface". In: *Transactions of the ASAE* 37.3, pp. 951–956. ISSN: 2151-0059. DOI: 10.13031/2013.28164.
- Zhao, Dawei, Erfan G. Nezami, Youssef M.A. Hashash, and Jamshid Ghaboussi (2006). "Three-dimensional discrete element simulation for granular materials". In: *Engineering Computations* 23.7, pp. 749–770. DOI: 10.1108/02644400610689884.
- Zhao, Shiwei, T. Matthew Evans, and Xiaowen Zhou (2018). "Shear-induced anisotropy of granular materials with rolling resistance and particle shape effects". In: *International Journal of Solids and Structures* 150, pp. 268–281. DOI: <https://doi.org/10.1016/j.ijsolstr.2018.06.024>.
- Zhao, Shiwei and Jidong Zhao (2019). "A poly-superellipsoid-based approach on particle morphology for DEM modeling of granular media". In: *International Journal for Numerical and Analytical Methods in Geomechanics* 43.13, pp. 2147–2169. DOI: 10.1002/nag.2951.
- Zhou, Qiang, Hayley H Shen, Brian T Helenbrook, and HongWu Zhang (Sept. 2009). "Scale dependence of direct shear tests". In: *Science Bulletin* 54.23, pp. 4337–4348. ISSN: 2095-9281. DOI: 10.1007/s11434-009-0516-5.
- Zhou, Wan-Huan, Xue-Ying Jing, Zhen-Yu Yin, and Xueyu Geng (2019). "Effects of particle sphericity and initial fabric on the shearing behavior of soil-rough structural interface". In: *Acta Geotechnica* 14.6, pp. 1699–1716. DOI: 10.1007/s11440-019-00781-2.
- Zhu, H.P., Z.Y. Zhou, R.Y. Yang, and A.B. Yu (2008). "Discrete particle simulation of particulate systems: A review of major applications and findings". In: *Chemical Engineering Science* 63.23, pp. 5728–5770. DOI: <https://doi.org/10.1016/j.ces.2008.08.006>.
- Zuriguel, Iker, Angel Garcimartín, Diego Maza, Luis A. Pugnaloni, and J. M. Pastor (May 2005). "Jamming during the discharge of granular matter from a silo". In: *Physical Review E* 71.5, p. 051303. ISSN: 1550-2376. DOI: 10.1103/PhysRevE.71.051303.

# List of publications

List of own publications published during doctoral dissertation from the Journal Citation Reports (JCR) list:

1. **Grabowski, A.**, Nitka, M. and Tejchman, J. (2020). "3D DEM simulations of monotonic interface behaviour between cohesionless sand and rigid wall of different roughness". In: *Acta Geotechnica* 16.4, pp. 1001–1026. DOI: <https://doi.org/10.1007/s11440-020-01085-6>.
2. Nitka, M. and **Grabowski, A.** (2021). "Shear band evolution phenomena in direct shear test modelled with DEM". In: *Powder Technology* 391, pp. 369–384. DOI: <https://doi.org/10.1016/j.powtec.2021.06.025>.
3. **Grabowski, A.**, Nitka, M. and Tejchman, J. (2021a). "Comparative 3D DEM simulations of sand–structure interfaces with similarly shaped clumps versus spheres with contact moments". In: *Acta Geotechnica* 16.11, pp. 3533–3554. DOI: <https://doi.org/10.1007/s11440-021-01255-0>.
4. **Grabowski, A.**, Nitka, M. and Tejchman, J. (2021b). "Micro-modelling of shear localization during quasi-static confined granular flow in silos using DEM". In: *Computers and Geotechnics* 134, p. 104108. DOI: <https://doi.org/10.1016/j.compgeo.2021.104108>.

List of other publications published during doctoral dissertation:

1. **Grabowski, A.** and Nitka, M. (2020). "3D DEM simulations of basic geotechnical tests with early detection of shear localization". In: *Studia Geotechnica et Mechanica* 43.1, pp. 48–64. DOI: <https://doi.org/10.2478/sgem-2020-0010>.

List of conference publications:

1. **Grabowski, A.**, Nitka, M., Tejchman, J. (2023). "DEM Analyses of Interface Behaviour Between Cohesionless Sand and Rigid Wall of Different Roughness". In: Pasternak, E., Dyskin, A. (eds) *Multiscale Processes of Instability, Deformation and Fracturing in Geomaterials*. IWBDG 2022. Springer Series in Geomechanics and Geoengineering. Springer, Cham. DOI: [https://doi.org/10.1007/978-3-031-22213-9\\_24](https://doi.org/10.1007/978-3-031-22213-9_24)

List of works currently under review:

1. **Grabowski, A.**, Konkol, J., Wójcik, M., and Nitka, M. (2023). "Experimental analysis of interface behavior between sand and corrugated surfaces with DIC technique". In: *Acta Geotechnica*. <https://doi.org/10.21203/rs.3.rs-3525250/v1>.



# List of conferences

List of international scientific conferences with personal oral presentations:

1. **Grabowski, A.**, Nitka, M. and Tejchman, J. "Effect of wall roughness on friction behaviour of granular materials in DEM calculations", *PCM-CMM 2019, Kraków, Poland*, 8-12.09.2019.
2. **Grabowski, A.**, Nitka, M. and Tejchman, J. "DEM analyses of interface behaviour between cohesionless sand and rigid wall of different roughness", *IWBDG 2020, Perth, Australia*, 28.11-01.12.2022 (online participation).
3. **Grabowski, A.** and Nitka, M. "3D DEM analysis of interface behavior between sand and corrugated surfaces", *Particles 2023, Milan, Italy*, 09-11.10.2023.



# List of Symbols

## Roman symbols:

|          |  |    |
|----------|--|----|
| $a_w$    | the wall contact factor                                  | -  |
| $b_i$    | bulk solid friction component of the wall contact factor | -  |
| $b_s$    | silo width   | m  |
| $b_w$    | wall friction component of the wall contact factor       | -  |
| $d_{50}$ | mean grain/particle diameter                             | m  |
| $d_s$    | silo depth   | m  |
| $e$      | void ratio of the sample                                 | -  |
| $e_0$    | initial void ratio of the sample                         | -  |
| $E$      | global modulus of elasticity of discrete material        | Pa |
| $E_c$    | local modulus of elasticity of discrete material         | Pa |
| $h_g$    | height of the surface grooves                            | m  |
| $h_s$    | silo height  | m  |
| $K$      | lateral pressure coefficient of bulk solid               | -  |
| $N$      | resultant normal force acting on silo wall               | -  |
| $P$      | resultant normal force acting on silo bottom             | -  |
| $s_g$    | spacing of the surface grooves                           | m  |
| $T$      | resultant friction force acting on silo wall             | -  |

## Greek symbols:

|                  |   |                   |
|------------------|---|-------------------|
| $\alpha_g$       | inclination of the surface grooves                                | °                 |
| $\beta$          | rolling stiffness coefficient (rotational resistance contact law) | -                 |
| $\gamma$         | volumetric weight of bulk solid                                   | kN/m <sup>3</sup> |
| $\varepsilon_1$  | strain component the x-axis                                       | -                 |
| $\varepsilon_2$  | strain component the y-axis                                       | -                 |
| $\varepsilon_3$  | strain component the z-axis                                       | -                 |
| $\varepsilon_v$  | volumetric strain   | -                 |
| $\eta$           | limit rolling coefficient (rotational resistance contact law)     | -                 |
| $\lambda_d$      | damping coefficient   | -                 |
| $\mu_c$          | interparticle friction angle                                      | °                 |
| $\mu_{eff}$      | wall friction coefficient   | -                 |
| $\mu_s$          | surface friction angle  | °                 |
| $\mu_w$          | wall friction angle   | °                 |
| $\sigma_1$       | normal stress component along the x-axis                          | Pa                |
| $\sigma_{1,max}$ | maximum normal stress component along the x-axis                  | Pa                |
| $\sigma_{1,res}$ | residual normal stress component along the x-axis                 | Pa                |
| $\sigma_2$       | normal stress component along the y-axis                          | Pa                |
| $\sigma_3$       | normal stress component along the z-axis                          | Pa                |
| $\sigma_c$       | confining pressure applied to the specimen                        | Pa                |



|                  |   |     |
|------------------|---|-----|
| $\sigma_n$       | normal pressure applied to the specimen | Pa  |
| $\sigma_{11}$    | horizontal normal stress                | Pa  |
| $\sigma_{12}$    | horizontal shear stress                 | Pa  |
| $\sigma_{21}$    | vertical shear stress                   | Pa  |
| $\sigma_{22}$    | vertical normal stress                  | Pa  |
| $\bar{\sigma}_z$ | mean vertical normal stress in silo     | Pa  |
| $\tau$           | shear stress                            | Pa  |
| $\nu_c$          | shear/normal local stiffness ratio      | -   |
| $\phi_i$         | internal friction angle                 | °   |
| $\phi_{i,max}$   | maximum internal friction angle         | °   |
| $\phi_{i,res}$   | residual internal friction angle        | °   |
| $\phi_s$         | surface friction angle                  | °   |
| $\phi_{s,max}$   | maximum surface friction angle          | °   |
| $\phi_{s,res}$   | residual surface friction angle         | °   |
| $\phi_w$         | wall friction angle                     | °   |
| $\phi_{w,max}$   | maximum wall friction angle             | °   |
| $\phi_{w,res}$   | residual wall friction angle            | °   |
| $\psi$           | contractancy/dilatancy angle            | °   |
| $\omega$         | particle rotation                       | rad |
| $\omega_c$       | micropolar Cosserat rotation            | rad |

# List of Figures

- 2.1 Magnitude of the grain rotations plotted for vertical slices through the middle of the specimen during triaxial compression test obtained with V-DIC (Hall et al., 2010). . . . . 8
- 2.2 History of rotations for a selected grains positioned inside and outside the shear zone during the triaxial compression test (left: plot of total rotations for each selected grain as a function of nominal axial strain of the specimen, and right: the selected grains indicated on the located through a slice of a sample) (Hall et al., 2010). . . . . 9
- 2.3 Global and local evolution of the void ratio in loose and dense sand specimens submitted to axisymmetric triaxial test (Desrues et al., 1996) 9
- 2.4 A photograph of a shear zone obtain during plain strain compression test in: a) a cylindrical sample of 24 mm diameter and 38 mm height, b) a magnified image of the mesostructure within the localized zone and c) a sketch of the shear zone to emphasize the column-like structures noted (Oda et al., 2004). . . . . 10
- 2.5 Raw photo-elastic image of the force network in granular media composed of: a) glass beads with b) approximate localization of the shear strain in the active earth pressure state (the brightest areas represent the strongest grain contacts, while the darkest areas represent the weaker ones) (Leśniewska et al., 2020). . . . . 10
- 2.6 Illustrations of: A) x-radiographs and B) schemes of shear localizations during mass flow of sand in a plane parallel/converging silo (Michalowski, 1987) . . . . . 11
- 2.7 Illustrations of: A) x-radiographs and B) schemes of shear localizations during funnel flow of sand in a plane parallel/converging silo (Michalowski, 1987) . . . . . 12
- 2.8 X-radiographs of shear localizations during: a) mass and b) funnel flow of dry powder in a hoppers with different wall inclination (Cutress and Pulfer, 1967) . . . . . 12
- 2.9 Measured displacements in model silo with convergent walls using colored layers during quasi-static flow for different initial conditions: a) smooth walls and initially loose sand, b) rough walls and initially loose sand, c) rough walls and initially dense sand and d) very rough walls and initially dense sand (wall inclination  $\alpha=5.6^\circ$ ) (Tejchman, 1989) 13
- 2.10 Shear zones during mass flow visualized by displacements profiles in sand (left) and distribution of deviatoric strain obtained with PIV technique (right) for: a) initially dense sand and smooth walls and b) initially dense sand and very rough walls (Slominski et al., 2007). . . . 14



|      |   |    |
|------|---|----|
| 2.11 | Deformation of initially medium dense sand during direct shear test with the distribution of: A) Cosserat rotation and B) void ratio at the different stages of the test (Kozicki et al., 2013). . . . .  | 15 |
| 2.12 | Evolution of void ratio during quasi-static plane strain granular flow in silo for: a) initially dense sand in a bin with very rough vertical walls and b) a hopper with smooth walls (Wójcik and Tejchman, 2009).  | 16 |
| 2.13 | Evolution of void ratio in initially dense sand in quasi-static plane strain granular flow after bottom displacement $u$ for silo with: a) asymmetric outlet and very rough walls, and b) with smooth walls (Krzyżanowski et al., 2021). . . . .  | 17 |
| 2.14 | Illustrations of: a) specimen deformation, b) development of column-like structures, and c) porosity changes in biaxial compression test using granular material composed of spherical discs (Iwashita and Oda, 1998). . . . .  | 19 |
| 2.15 | Evolution of: a) specimen deformation, b) grain rotations, c) internal forces in the entire specimen, and d) void ratio distribution within the shear zone during direct shear test of initially medium dense sand for horizontal displacement of $u=20$ mm obtained with DEM (Kozicki et al., 2013). . . . .   | 19 |
| 2.16 | Shear zone location near the walls captured with velocity profiles for: a) the bin 15 particle diameters wide and b) for the bin 20 particle diameters wide (Gutfraind and Pouliquen, 1996). . . . .  | 20 |
| 2.17 | Normal force chain network in granular material during: A) quasi-static flow in a bin and B) a close-up on the normal force chains at four different time steps of (A) (Gutfraind and Pouliquen, 1996). . . . .   | 20 |
| 3.1  | Simulation loop in discrete software YADE that includes: body-centered calculations (red color) followed by interaction calculations (blue color), force estimation (green color), and other engines, such as user-defined components (black color) (Smilauer et al., 2023). . . . .  | 24 |
| 3.2  | Mechanical response of linear contact model with rotational resistance: a) normal contact model, b) tangential contact model, c) loading and unloading path for tangential force and d) rolling contact model, e) loading and unloading path for rolling contact model (Kozicki et al., 2013). . . . .  | 27 |
| 3.3  | Interaction between two spheres in DEM at time $t$ (Belheine et al., 2009).   | 27 |
| 3.4  | Overview of typical particle shapes used in DEM simulations: A) spheres and clumps composed of spheres (Kozicki et al., 2012), B) poly-superellipsoid particles (Zhao and Zhao, 2019), C) superquadric particles (Podlozhnyuk et al., 2016) and D) polyhedral particles (Zhao et al., 2006). . . . .  | 30 |
| 4.1  | Numerical setup for triaxial compression test. . . . .  | 36 |
| 4.2  | Triaxial compression test on initially dense sand ( $e_0=0.55$ and $\sigma_c=200$ kPa): a) vertical normal stress $\sigma_1$ and b) volumetric strain $\varepsilon_v$ versus vertical normal strain $\varepsilon_1$ from DEM for different mean grain diameter $d_{50}$ ( $\mu_c=18^\circ$ , $E_c=300$ kPa, $\nu_c=0.3$ , $\eta=0.4$ and $\beta=0.7$ ). . . . . | 36 |

- 4.3 Triaxial compression test on initially dense sand ( $e_0=0.55$  and  $\sigma_c=200$  kPa): a) vertical normal stress  $\sigma_1$  and b) volumetric strain  $\varepsilon_v$  versus vertical normal strain  $\varepsilon_1$  from DEM for different interparticle friction angle  $\mu_c$  ( $E_c=200$  MPa,  $\nu_c=0.3$ ,  $\eta=1.0$  and  $\beta=1.0$ ). . . . . 37
- 4.4 Triaxial compression test on initially dense sand ( $e_0=0.55$  and  $\sigma_c=200$  kPa): a) vertical normal stress  $\sigma_1$  and b) volumetric strain  $\varepsilon_v$  versus vertical normal strain  $\varepsilon_1$  from DEM for different local modulus of the elasticity  $E_c$  ( $\mu_c=15^\circ$ ,  $\nu_c=0.3$ ,  $\eta=1.0$  and  $\beta=1.0$ ). . . . . 38
- 4.5 Triaxial compression test on initially dense sand ( $e_0=0.55$  and  $\sigma_c=200$  kPa): a) vertical normal stress  $\sigma_1$  and b) volumetric strain  $\varepsilon_v$  versus vertical normal strain  $\varepsilon_1$  from DEM for different shear/normal local stiffness ratio  $\nu_c$  ( $\mu_c=15^\circ$ ,  $E_c=200$  MPa,  $\eta=1.0$  and  $\beta=1.0$ ). . . . . 38
- 4.6 Triaxial compression test on initially dense sand ( $e_0=0.55$  and  $\sigma_c=200$  kPa): a) vertical normal stress  $\sigma_1$  and b) volumetric strain  $\varepsilon_v$  versus vertical normal strain  $\varepsilon_1$  from DEM for different limit rolling coefficient  $\eta$  ( $\mu_c=15^\circ$ ,  $E_c=200$  MPa,  $\nu_c=0.3$  and  $\beta=1.0$ ). . . . . 39
- 4.7 Triaxial compression test on initially dense sand ( $e_0=0.55$  and  $\sigma_c=200$  kPa): a) vertical normal stress  $\sigma_1$  and b) volumetric strain  $\varepsilon_v$  versus vertical normal strain  $\varepsilon_1$  from DEM for different rolling stiffness coefficient  $\beta$  ( $\mu_c=15^\circ$ ,  $E_c=200$  MPa,  $\nu_c=0.3$  and  $\eta=1.0$ ). . . . . 40
- 4.8 Triaxial compression test on initially dense sand ( $e_0 = 0.53$ ): a) calculated vertical normal stress  $\sigma_1$  and b) volumetric strain  $\varepsilon_v$  versus vertical normal strain  $\varepsilon_1$  from: DEM calculations (black empty dots) compared to laboratory experiments (red full dots) (Kolymbas and Wu, 1990) for different initial confining pressure  $\sigma_c$  ( $\mu_c = 18^\circ$ ,  $E_c = 300$  MPa,  $\nu_c = 0.3$ ,  $\eta = 0.4$  and  $\beta = 0.7$ ). . . . . 41
- 4.9 Direct shear test in DEM: a) numerical setup, b) sample at the initial state and c) deformed sample at the final state (Grabowski and Nitka, 2020; Nitka and Grabowski, 2021). . . . . 44
- 4.10 Direct shear test on initially medium-dense sand ( $e_0 = 0.63$  and  $\sigma_n = 50$  kPa): a) calculated shear stress ratio  $\tau/\sigma_n$  and b) volumetric strain  $\varepsilon_v$  versus total horizontal displacement  $u$  for different depth of the sand specimen  $d$ . . . . . 45
- 4.11 Example of: a) void ratio distribution, b) normal contact forces distribution, and c) contact orientation at the initial state of the test, prior to applying pressure ( $e_0 = 0.63$  and  $\sigma_n = 200$  kPa). . . . . 46
- 4.12 Direct shear test on initially medium-dense sand: a) calculated shear stress ratio  $\tau/\sigma_n$  and b) volumetric strain  $\varepsilon_v$  versus total horizontal displacement  $u$  from discrete simulation (Nitka and Grabowski, 2021) and laboratory test (Salazar et al., 2015) ( $e_0 = 0.63$  and  $\sigma_n = 80$  kPa). . . 47
- 4.13 Calculated: A) shear stress ratio  $\tau/\sigma_n$  and B) volumetric strain  $\varepsilon_v$  versus total horizontal displacement  $u$  from discrete simulations of direct shear test for different normal stresses: a)  $\sigma_n = 50$  kPa, b)  $\sigma_n = 200$  kPa, and c)  $\sigma_n = 500$  kPa ( $e_0 = 0.60$ ) (Grabowski and Nitka, 2020; Nitka and Grabowski, 2021). . . . . 48



|      |  |    |
|------|--|----|
| 4.15 | Front view of the specimen at the final state of the test for different vertical load: a) $\sigma_n=50$ kPa, b) $\sigma_n=200$ kPa and c) $\sigma_n=500$ kPa ( $e_0=0.60$ ) (Grabowski and Nitka, 2020). . . . .   | 49 |
| 4.16 | Distribution of sphere rotations $\omega$ in granular specimen at the final state of the test for different vertical load: a) $\sigma_n=50$ kPa, b) $\sigma_n=200$ kPa and c) $\sigma_n=500$ kPa ( $e_0=0.60$ ) (red color-clockwise rotations, blue color-counterclockwise rotations) (Grabowski and Nitka, 2020). . . . .  | 49 |
| 4.17 | Distribution of void ratio $e$ in granular specimen at the final state of the test for different vertical load: a) $\sigma_n=50$ kPa, b) $\sigma_n=200$ kPa and c) $\sigma_n=500$ kPa ( $e_0=0.60$ ). . . . .  | 50 |
| 4.18 | Distribution of normal force chains in granular specimen at the final state of the test for different vertical load: a) $\sigma_n=50$ kPa, b) $\sigma_n=200$ kPa and c) $\sigma_n=500$ kPa ( $e_0=0.60$ ) (Grabowski and Nitka, 2020). . . . .   | 50 |
| 4.19 | Polar mean contact force distribution in granular specimen at the initial state (black line) and final state of the test (red line) for different vertical load: a) $\sigma_n=50$ kPa, b) $\sigma_n=200$ kPa and c) $\sigma_n=500$ kPa ( $e_0=0.60$ ) (the graphs scale has been adjusted to ensure good readability, considering the varying magnitudes of the vertical load). . . . .  | 51 |
| 4.20 | Front view of the specimen at the final state of the test for different initial void ratio $e_0$ : a) $e_0=0.53$ , b) $e_0=0.60$ and c) $e_0=0.75$ ( $\sigma_n=200$ kPa) (Grabowski and Nitka, 2020). . . . .  | 52 |
| 4.21 | Distribution of sphere rotations $\omega$ in granular specimen at the final state of the test for different initial void ratio $e_0$ : a) $e_0=0.53$ , b) $e_0=0.60$ and c) $e_0=0.75$ ( $\sigma_n=200$ kPa) (red color-clockwise rotations, blue color-counterclockwise rotations) (Grabowski and Nitka, 2020). . . . .   | 52 |
| 4.22 | Distribution of void ratio in granular specimen at the final state of the test for different initial void ratio $e_0$ : a) $e_0=0.53$ , b) $e_0=0.60$ and c) $e_0=0.75$ ( $\sigma_n=200$ kPa). . . . .   | 53 |
| 4.23 | Distribution of normal force chains in granular specimen at the final state of the test for different initial void ratio $e_0$ : a) $e_0=0.53$ , b) $e_0=0.60$ and c) $e_0=0.75$ ( $\sigma_n=200$ kPa) (Grabowski and Nitka, 2020; Nitka and Grabowski, 2021). . . . .   | 53 |
| 4.24 | Polar mean contact force distribution in granular specimen at the initial state (black line) and final state of the test (red line) for different initial void ratio $e_0$ : a) $e_0=0.53$ , b) $e_0=0.60$ and c) $e_0=0.75$ ( $\sigma_n=200$ kPa). . . . .  | 53 |
| 4.25 | Evolution of displacements fluctuations $\vec{u}_i - \vec{u}_{avg}$ in the entire specimen for: a) $u_x=0.10$ mm, b) $u_x=0.50$ mm, c) $u_x=0.75$ mm, d) $u_x=1.00$ mm, e) $u_x=1.25$ mm, f) $u_x=1.50$ mm, g) $u_x=1.75$ mm, h) $u_x=2.00$ mm and i) $u_x=6.00$ mm ( $e_0=0.60$ and $\sigma_n=200$ kPa) (black vectors, multiplied by $1e03$ , shows only every 50 elements for readability) (Grabowski and Nitka, 2020). . . . . | 54 |
| 4.26 | Evolution of horizontal displacements $u_x$ in the entire specimen for: a) $u_x=0.10$ mm, b) $u_x=0.50$ mm, c) $u_x=1.00$ mm, d) $u_x=1.50$ mm, e) $u_x=2.00$ mm and f) $u_x=6.00$ mm ( $e_0=0.60$ and $\sigma_n=200$ kPa) (Nitka and Grabowski, 2021). . . . .  | 55 |

- 4.27 Evolution of vertical displacements  $u_y$  in the entire specimen for: a)  $u_x=0.10$  mm, b)  $u_x=0.50$  mm, c)  $u_x=1.00$  mm, d)  $u_x=1.50$  mm, e)  $u_x=2.00$  mm and f)  $u_x=6.00$  mm ( $e_0=0.60$  and  $\sigma_n=200$  kPa) (Nitka and Grabowski, 2021). . . . . 56
- 4.28 Evolution of the gradient of horizontal displacements  $u_x^*$  in the entire specimen for: a)  $u_x=0.10$  mm, b)  $u_x=0.50$  mm, c)  $u_x=1.00$  mm, d)  $u_x=1.50$  mm, e)  $u_x=2.00$  mm and f)  $u_x=6.00$  mm ( $e_0=0.60$  and  $\sigma_n=200$  kPa) (Nitka and Grabowski, 2021). . . . . 57
- 4.29 Evolution of the gradient of vertical displacements  $u_y^*$  in the entire specimen for: a)  $u_x=0.10$  mm, b)  $u_x=0.50$  mm, c)  $u_x=1.00$  mm, d)  $u_x=1.50$  mm, e)  $u_x=2.00$  mm and f)  $u_x=6.00$  mm ( $e_0=0.60$  and  $\sigma_n=200$  kPa) (Nitka and Grabowski, 2021). . . . . 57
- 4.30 Evolution of the gradient of particle rotations  $\omega^*$  in the entire specimen for: a)  $u_x=0.10$  mm, b)  $u_x=0.50$  mm, c)  $u_x=1.00$  mm, d)  $u_x=1.50$  mm, e)  $u_x=2.00$  mm and f)  $u_x=6.00$  mm ( $e_0=0.60$  and  $\sigma_n=200$  kPa) (Nitka and Grabowski, 2021). . . . . 58
- 4.31 Evolution of gradient of horizontal stresses  $\sigma_{11}$  in the entire specimen for: a)  $u_x=0.10$  mm, b)  $u_x=0.50$  mm, c)  $u_x=1.00$  mm, d)  $u_x=1.50$  mm, e)  $u_x=2.00$  mm and f)  $u_x=6.00$  mm ( $e_0=0.60$  and  $\sigma_n=200$  kPa) (Nitka and Grabowski, 2021). . . . . 59
- 4.32 Evolution of gradient of vertical stresses  $\sigma_{22}$  in the entire specimen for: a)  $u_x=0.10$  mm, b)  $u_x=0.50$  mm, c)  $u_x=1.00$  mm, d)  $u_x=1.50$  mm, e)  $u_x=2.00$  mm and f)  $u_x=6.00$  mm ( $e_0=0.60$  and  $\sigma_n=200$  kPa) (Nitka and Grabowski, 2021). . . . . 59
- 4.33 Evolution of gradient of shear stresses  $\sigma_{12}$  in the entire specimen for: a)  $u_x=0.10$  mm, b)  $u_x=0.50$  mm, c)  $u_x=1.00$  mm, d)  $u_x=1.50$  mm, e)  $u_x=2.00$  mm and f)  $u_x=6.00$  mm ( $e_0=0.60$  and  $\sigma_n=200$  kPa) (Nitka and Grabowski, 2021). . . . . 60
- 4.34 Asymmetric convex clump of 0.5 mm diameter in XYZ coordinate space, composed of 4 spheres used in discrete simulations (0.1 mm grid size) (Grabowski et al. (2021a), licensed under CC BY 4.0). . . . . 63
- 4.35 Interface shear test in DEM: a) numerical setup, b) sample at the initial state and c) deformed sample at the final state (Grabowski et al. (2020), licensed under CC BY 4.0). . . . . 64
- 4.36 Rigid bottom surface sections with different normalized surface roughness  $R_n$ : a)  $R_n=2.0$ , b)  $R_n=1.0$ , c)  $R_n=0.75$ , d)  $R_n=0.5$ , e)  $R_n=0.25$ , f)  $R_n=0.1$  and g)  $R_n=0.01$  (Grabowski et al. (2020), licensed under CC BY 4.0). . . . . 65
- 4.37 Mobilized surface friction angle  $\phi_s$  versus horizontal displacement  $u$  obtained for: A) spheres (Grabowski et al., 2020) and B) clumps (Grabowski et al., 2021a) for different normalized surface roughness  $R_n$ : a)  $R_n=2.0$ , b)  $R_n=1.0$ , c)  $R_n=0.75$ , d)  $R_n=0.50$ , e)  $R_n=0.25$ , f)  $R_n=0.10$  and g)  $R_n=0.01$  ( $e_0=0.55$  and  $\sigma_n=100$  kPa) (Adapted graphics licensed under CC BY 4.0; changes include font, line style and size adjustments). 66

- 4.38 Volumetric strain  $\varepsilon_v$  versus horizontal displacement  $u$  obtained for: A) spheres (Grabowski et al., 2020) and B) clumps (Grabowski et al., 2021a) for different normalized surface roughness  $R_n$ : a)  $R_n=2.0$ , b)  $R_n=1.0$ , c)  $R_n=0.75$ , d)  $R_n=0.50$ , e)  $R_n=0.25$ , f)  $R_n=0.10$  and g)  $R_n=0.01$  ( $e_0=0.55$  and  $\sigma_n=100$  kPa) (Adapted graphics licensed under CC BY 4.0; changes include font, line style and size adjustments). . . . . 67
- 4.39 Relationship between maximum surface friction angle  $\phi_{s,max}$  and residual surface friction angle  $\phi_{s,res}$  for different normalized surface roughness  $R_n$  for: a) spheres and b) clumps (black color represents  $\phi_{s,max}$  and red color represents  $\phi_{s,res}$ ) (adapted from Grabowski et al. (2021a), licensed under CC BY 4.0. Graphic changes include color and size adjustments). . . . . 68
- 4.40 DEM results obtained for spheres of: a) mobilized surface friction angle  $\phi_s$  and b) volumetric strain  $\varepsilon_v$  versus horizontal displacement  $u$  compared to experimental results by Tejchman and Wu (1995) for different normalized surface roughness  $R_n$ :  $R_n=1.0$ ,  $R_n=0.25$  and  $R_n=0.01$  ( $e_0=0.55$  and  $\sigma_n=100$  kPa) (adapted from Grabowski et al. (2020), licensed under CC BY 4.0. Graphic changes include color and size adjustments). . . . . 69
- 4.41 DEM results obtained for clumps of: a) mobilized surface friction angle  $\phi_s$  and b) volumetric strain  $\varepsilon_v$  versus horizontal displacement  $u$  compared to experimental results by Tejchman and Wu (1995) for different normalized wall roughness  $R_n$ :  $R_n=1.0$ ,  $R_n=0.25$  and  $R_n=0.01$  ( $e_0=0.55$  and  $\sigma_n=100$  kPa) (adapted from Grabowski et al. (2021a), licensed under CC BY 4.0. Graphic changes include color and size adjustments). . . . . 69
- 4.42 DEM results obtained for spheres of: a) mobilized surface friction angle  $\phi_s$  and b) volumetric strain  $\varepsilon_v$  versus horizontal displacement  $u$  compared to experimental results by Tejchman and Wu (1995) with two different initial void ratios of sand:  $e_0=0.55$  and  $e_0=0.80$  ( $\sigma_n=100$  kPa and  $R_n=1.0$ ) (adapted from Grabowski et al. (2020), licensed under CC BY 4.0. Graphic changes include color and size adjustments). . . . . 70
- 4.43 DEM results obtained for clumps of: a) mobilized surface friction angle  $\phi_s$  and b) volumetric strain  $\varepsilon_v$  versus horizontal displacement  $u$  compared to experimental results by Tejchman and Wu (1995) with two different initial void ratios of sand:  $e_0=0.55$  and  $e_0=0.80$  ( $\sigma_n=100$  kPa and  $R_n=1.0$ ). . . . . 71
- 4.44 Front view of the sand specimen composed of spheres at the final state of the test ( $u_{tot}=7.0$  mm) for different normalized surface roughness parameter  $R_n$ : a)  $R_n=2.0$ , b)  $R_n=1.0$ , c)  $R_n=0.75$ , d)  $R_n=0.5$ , e)  $R_n=0.25$ , f)  $R_n=0.1$  and g)  $R_n=0.01$  ( $e_0=0.55$  and  $\sigma_n=100$  kPa). . . . . 72
- 4.45 Front view of the sand specimen composed of clumps the final state of the test ( $u_{tot}=7.0$  mm) for different normalized surface roughness parameter  $R_n$ : a)  $R_n=2.0$ , b)  $R_n=1.0$ , c)  $R_n=0.75$ , d)  $R_n=0.5$ , e)  $R_n=0.25$ , f)  $R_n=0.1$  and g)  $R_n=0.01$  ( $e_0=0.55$  and  $\sigma_n=100$  kPa). . . . . 72

- 4.46 Distribution of horizontal grain displacement  $u$  across normalized specimen height  $h/d_{50}$  at the specimen mid-point at residual state for  $u_{tot}=7.0$  mm for: A) spheres (Grabowski et al., 2020) and B) clumps (Grabowski et al., 2021a) for different normalized surface roughness  $R_n$ : a)  $R_n=2.0$ , b)  $R_n=1.0$ , c)  $R_n=0.75$ , d)  $R_n=0.50$ , e)  $R_n=0.25$ , f)  $R_n=0.10$  and g)  $R_n=0.01$  ( $e_0=0.55$  and  $\sigma_n=100$  kPa) (Adapted graphics licensed under CC BY 4.0; changes include font, line style and size adjustments). . . . . 73
- 4.47 A zoom on the distribution of particle rotations  $\omega$  in sand specimen composed of spheres at the final state of the test ( $u_{tot}=7.0$  mm) for different normalized surface roughness  $R_n$ : a)  $R_n=1.0$ , b)  $R_n=0.5$  and c)  $R_n=0.1$  ( $e_0=0.55$  and  $\sigma_n=100$  kPa) (adapted from Grabowski et al. (2020), licensed under CC BY 4.0. Graphic changes include color and size adjustments). . . . . 74
- 4.48 A zoom on the distribution of particle rotations  $\omega$  in sand specimen composed of clumps at the final state of the test ( $u_{tot}=7.0$  mm) for different normalized surface roughness  $R_n$ : a)  $R_n=1.0$ , b)  $R_n=0.5$  and c)  $R_n=0.1$  ( $e_0=0.55$  and  $\sigma_n=100$  kPa) (adapted from Grabowski et al. (2021a), licensed under CC BY 4.0. Graphic changes include color and size adjustments). . . . . 74
- 4.49 Distribution of particle rotations  $\omega$  in sand specimen composed of spheres at the final state of the test ( $u_{tot}=7.0$  mm) for different normalized surface roughness  $R_n$ : a)  $R_n=2.0$ , b)  $R_n=1.0$ , c)  $R_n=0.75$ , d)  $R_n=0.5$ , e)  $R_n=0.25$ , f)  $R_n=0.1$  and g)  $R_n=0.01$  ( $e_0=0.55$  and  $\sigma_n=100$  kPa). 75
- 4.50 Distribution of particle rotations  $\omega$  in sand specimen composed of clumps at the final state of the test ( $u_{tot}=7.0$  mm) for different normalized surface roughness  $R_n$ : a)  $R_n=2.0$ , b)  $R_n=1.0$ , c)  $R_n=0.75$ , d)  $R_n=0.5$ , e)  $R_n=0.25$ , f)  $R_n=0.1$  and g)  $R_n=0.01$  ( $e_0=0.55$  and  $\sigma_n=100$  kPa). 75
- 4.51 Distribution of grain rotation  $\omega$  across normalized specimen height  $h/d_{50}$  at the specimen mid-point at residual state for  $u_{tot}=7.0$  mm for: A) spheres (Grabowski et al., 2020) and B) clumps (Grabowski et al., 2021a) for different normalized roughness  $R_n$ : a)  $R_n=2.0$ , b)  $R_n=1.0$ , c)  $R_n=0.75$ , d)  $R_n=0.50$ , e)  $R_n=0.25$ , f)  $R_n=0.10$  and g)  $R_n=0.01$  ( $e_0=0.55$ , and  $\sigma_n=100$  kPa) (Adapted graphics licensed under CC BY 4.0; changes include font, line style and size adjustments). . . . . 76
- 4.52 Distribution of void ratio  $e$  in sand specimen composed of spheres at the final state of the test ( $u_{tot}=7.0$  mm) for different normalized surface roughness  $R_n$ : a)  $R_n=2.0$ , b)  $R_n=1.0$ , c)  $R_n=0.75$ , d)  $R_n=0.5$ , e)  $R_n=0.25$ , f)  $R_n=0.1$  and g)  $R_n=0.01$  ( $e_0=0.55$  and  $\sigma_n=100$  kPa). . . . . 77
- 4.53 Distribution of void ratio  $e$  in sand specimen composed of clumps at the final state of the test ( $u_{tot}=7.0$  mm) for different normalized surface roughness  $R_n$ : a)  $R_n=2.0$ , b)  $R_n=1.0$ , c)  $R_n=0.75$ , d)  $R_n=0.5$ , e)  $R_n=0.25$ , f)  $R_n=0.1$  and g)  $R_n=0.01$  ( $e_0=0.55$  and  $\sigma_n=100$  kPa). . . . . 77

- 4.54 Distribution of void ratio  $e$  across normalized specimen height  $h/d_{50}$  at the specimen mid-point at residual state for  $u_{tot}=7.0$  mm for: A) spheres (Grabowski et al., 2020) and B) clumps (Grabowski et al., 2021a) for different normalized roughness  $R_n$ : a)  $R_n=2.0$ , b)  $R_n=1.0$ , c)  $R_n=0.75$ , d)  $R_n=0.50$ , e)  $R_n=0.25$ , f)  $R_n=0.10$  and g)  $R_n=0.01$  ( $e_0=0.55$  and  $\sigma_n=100$  kPa) (Adapted graphics licensed under CC BY 4.0; changes include font, line style and size adjustments). . . . . 78
- 4.55 Distribution of normal force chains in sand specimen composed of spheres at the final state of the test ( $u_{tot}=7.0$  mm) for different normalized surface roughness  $R_n$ : a)  $R_n=2.0$ , b)  $R_n=1.0$ , c)  $R_n=0.75$ , d)  $R_n=0.5$ , e)  $R_n=0.25$ , f)  $R_n=0.1$  and g)  $R_n=0.01$  ( $e_0=0.55$  and  $\sigma_n=100$  kPa) (red color corresponds to normal contact forces higher than mean value, maximum value of forces is 0.05 N) (Grabowski et al. (2020), licensed under CC BY 4.0). . . . . 79
- 4.56 Distribution of normal force chains in sand specimen composed of clumps at the final state of the test ( $u_{tot}=7.0$  mm) for different normalized surface roughness  $R_n$ : a)  $R_n=2.0$ , b)  $R_n=1.0$ , c)  $R_n=0.75$ , d)  $R_n=0.5$ , e)  $R_n=0.25$ , f)  $R_n=0.1$  and g)  $R_n=0.01$  ( $e_0=0.55$  and  $\sigma_n=100$  kPa) (red color corresponds to normal contact forces higher than mean value, maximum value of forces is 0.05 N) (Grabowski et al. (2021a), licensed under CC BY 4.0). . . . . 79
- 4.57 Polar mean contact force distribution in granular sand composed of spheres at the initial state (black line) and final state of the test ( $u_{tot}=7.0$  mm) (red line) for different normalized surface roughness  $R_n$ : a)  $R_n=2.0$ , b)  $R_n=1.0$ , c)  $R_n=0.75$ , d)  $R_n=0.5$ , e)  $R_n=0.25$ , f)  $R_n=0.1$  and g)  $R_n=0.01$  ( $e_0=0.55$  and  $\sigma_n=100$  kPa) (Grabowski et al. (2020), licensed under CC BY 4.0). . . . . 81
- 4.58 Polar mean contact force distribution in sand specimen composed of clumps at the initial state (black line) and final state of the test ( $u_{tot}=7.0$  mm) (red line) for different normalized surface roughness  $R_n$ : a)  $R_n=2.0$ , b)  $R_n=1.0$ , c)  $R_n=0.75$ , d)  $R_n=0.5$ , e)  $R_n=0.25$ , f)  $R_n=0.1$  and g)  $R_n=0.01$  ( $e_0=0.55$  and  $\sigma_n=100$  kPa) (Grabowski et al. (2021a), licensed under CC BY 4.0). . . . . 82
- 4.59 Distribution of: A) horizontal  $\sigma_{12}$  and B) vertical shear stress  $\sigma_{21}$  across normalized height  $h/d_{50}$  for spheres at residual state ( $u_{tot}=7.0$  mm) at specimen mid-point with different normalized surface roughness  $R_n$ : a)  $R_n=2.0$ , b)  $R_n=1.0$ , c)  $R_n=0.75$ , d)  $R_n=0.5$ , e)  $R_n=0.25$ , f)  $R_n=0.10$  and g)  $R_n=0.01$  ( $e_0=0.55$  and  $\sigma_n=100$  kPa) (adapted from Grabowski et al. (2020), licensed under CC BY 4.0. Graphic changes include color and size adjustments). . . . . 83

- 4.60 Distribution of: A) horizontal  $\sigma_{12}$  and B) vertical shear stress  $\sigma_{21}$  across normalized height  $h/d_{50}$  for clumps at residual state ( $u_{tot}=7.0$  mm) at specimen mid-point with different normalized surface roughness  $R_n$ : a)  $R_n=2.0$ , b)  $R_n=1.0$ , c)  $R_n=0.75$ , d)  $R_n=0.5$ , e)  $R_n=0.25$ , f)  $R_n=0.10$  and g)  $R_n=0.01$  ( $e_0=0.55$  and  $\sigma_n=100$  kPa) (adapted from Grabowski et al. (2021a), licensed under CC BY 4.0. Graphic changes include color and size adjustments). . . . . 83
- 4.61 Distribution of stress components for spheres: a) horizontal normal stress  $\sigma_{11}$ , b) vertical normal stress  $\sigma_{22}$ , c) horizontal shear stress  $\sigma_{12}$  and d) vertical shear stress  $\sigma_{21}$  across normalized specimen height  $h/d_{50}$  at residual state ( $u_{tot}=7.0$  mm) at specimen mid-point with different normalized interface roughness  $R_n$ : A)  $R_n=1.0$ , B)  $R_n=0.50$  and C)  $R_n=0.01$  ( $e_0=0.55$  and  $\sigma_n=100$  kPa) (adapted from Grabowski et al. (2020), licensed under CC BY 4.0. Graphic changes include color and size adjustments). . . . . 84
- 4.62 Distribution of stress components for clumps: a) horizontal normal stress  $\sigma_{11}$ , b) vertical normal stress  $\sigma_{22}$ , c) horizontal shear stress  $\sigma_{12}$  and d) vertical shear stress  $\sigma_{21}$  across normalized specimen height  $h/d_{50}$  at residual state ( $u_{tot}=7.0$  mm) at specimen mid-point with different normalized interface roughness  $R_n$ : A)  $R_n=1.0$ , B)  $R_n=0.50$  and C)  $R_n=0.01$  ( $e_0=0.55$  and  $\sigma_n=100$  kPa) (adapted from Grabowski et al. (2021a), licensed under CC BY 4.0. Graphic changes include color and size adjustments). . . . . 84
- 4.63 Discrete results obtained at the final state of the test ( $u_{tot}=7.0$  mm) for initially loose sand ( $e_0=0.80$ ) composed of spheres: a) front view of the specimen, b) particle rotations distribution (red color represents the clockwise rotations, blue color the counterclockwise rotations), c) void ratio distribution, and d) normal force chains distribution in the specimen (red color corresponds to normal contact forces higher than mean value, maximum value of forces is 0.05 N) ( $R_n=1.0$  and  $\sigma_n=100$  kPa) (Grabowski et al. (2020), licensed under CC BY 4.0). . . . . 86
- 4.64 Discrete results obtained at the final state of the test ( $u_{tot}=7.0$  mm) for initially loose sand ( $e_0=0.80$ ) composed of clumps: a) front view of the specimen, b) particle rotations distribution (red color represents the clockwise rotations, blue color the counterclockwise rotations), c) void ratio distribution, and d) normal force chains distribution in the specimen (red color corresponds to normal contact forces higher than mean value, maximum value of forces is 0.05 N) ( $R_n=1.0$  and  $\sigma_n=100$  kPa) (Grabowski et al. (2021a), licensed under CC BY 4.0). . . . . 86
- 4.65 Polar mean contact force distribution in granular specimen at the initial state (black line) and final state of the test (red line) for initially loose sand ( $e_0=0.80$ ) composed of spheres ( $R_n=1.0$ ,  $\sigma_n=100$  kPa and  $d_{50}=0.5$  mm). . . . . 86

- 4.66 Polar mean contact force distribution in granular specimen at the initial state (black line) and final state of the test (red line) for initially loose sand ( $e_0=0.80$ ) composed of clumps ( $R_n=1.0$ ,  $\sigma_n=100$  kPa and  $d_{50}=0.5$  mm). . . . . 86
- 4.67 Evolution of ratio  $A = \omega d_{50}/u$  across the normalized specimen height  $h/d_{50}$  at the specimen center at the end of the test ( $u_x=7.0$ ) obtained for clumps for different normalized surface roughness  $R_n$ : a)  $R_n=2.0$ , b)  $R_n=1.0$ , c)  $R_n=0.75$ , d)  $R_n=0.50$ , e)  $R_n=0.25$ , f)  $R_n=0.10$  and g)  $R_n=0.01$  ( $e_0=0.55$  and  $\sigma_n=100$  kPa) (adapted from Grabowski et al. (2021a), licensed under CC BY 4.0. Graphic changes include color and size adjustments). . . . . 88
- 4.68 Normal and tangential interface forces  $n$  and  $t$  acting on surface grooves ('O' is the center of the clump, 'C' is the wall contact point, and  $r_n$  and  $r_t$  are the lever arms of the contact forces against point 'O') (Grabowski et al. (2021a), licensed under CC BY 4.0). . . . . 89
- 4.69 Relationship between: a) normal interface force  $n'$  in vertical direction (squares) and tangential interface force  $t'$  (crosses) in horizontal direction and tangential interface forces  $n$  and  $t$  acting on inclined surface grooves) (Grabowski et al. (2021a), licensed under CC BY 4.0). . . . . 89
- 4.70 Dimension of profile for sinusoidal corrugated surfaces with the approximate location of shear plane (dashed line) according to EN 1991-4 (2006). . . . . 93
- 4.71 Interface shear test in DEM: a) numerical setup, b) sample at the initial state and c) deformed sample at the final state. . . . . 95
- 4.72 Rigid bottom corrugated sinusoidal surfaces with different corrugation coefficient  $d/l$ : a)  $d/l=0.000$ , b)  $d/l=0.053$ , c)  $d/l=0.147$ , d)  $d/l=0.240$ , e)  $d/l=0.333$  and f)  $d/l=0.428$  ( $d$  - corrugation depth and  $l$  - corrugation length). . . . . 96
- 4.73 Mobilized shear stress  $\tau$  versus normalized horizontal displacement  $u/L$  for different corrugation coefficient  $d/l$  obtained with: a) DEM simulations and b) experimental analysis ( $e_0=0.63$  and  $\sigma_n=48$  kPa). . . . . 97
- 4.74 Volumetric strain  $\varepsilon_v$  versus normalized horizontal displacement  $u/L$  for different corrugation coefficient  $d/l$  obtained with: a) DEM simulations and b) experimental analysis ( $e_0=0.63$  and  $\sigma_n=48$  kPa). . . . . 98
- 4.75 Calculated: A) effective friction coefficient  $\mu_{eff}$  and B) wall contact factor  $a_w$  versus normalized horizontal displacement  $u/L$  at the: a) peak and b) residual state for different corrugation coefficient  $d/l$  obtained with DEM (red line represents the  $a_w=0.2$  recommended by EN 1991-4 (2006)). . . . . 100
- 4.76 Front view of the sand specimen composed at the final state of the test ( $u/L=0.1$ ) for different corrugation coefficient  $d/l$ : a)  $d/l=0.000$ , b)  $d/l=0.053$ , c)  $d/l=0.147$ , d)  $d/l=0.240$ , e)  $d/l=0.333$  and f)  $d/l=0.427$  ( $e_0=0.63$  and  $\sigma_n=48$  kPa). . . . . 101

- 4.77 Distribution of particle rotations  $\omega$  in sand specimen at the final state of the test ( $u/L=0.1$ ) for different corrugation coefficient  $d/l$ : a)  $d/l=0.000$ , b)  $d/l=0.053$ , c)  $d/l=0.147$ , d)  $d/l=0.240$ , e)  $d/l=0.333$  and f)  $d/l=0.427$  ( $e_0=0.63$  and  $\sigma_n=48$  kPa). . . . . 101
- 4.78 Distribution of void ratio  $e$  in sand specimen at the final state of the test ( $u/L=0.1$ ) for different corrugation coefficient  $d/l$ : a)  $d/l=0.000$ , b)  $d/l=0.053$ , c)  $d/l=0.147$ , d)  $d/l=0.240$ , e)  $d/l=0.333$  and f)  $d/l=0.427$  ( $e_0=0.63$  and  $\sigma_n=48$  kPa). . . . . 102
- 4.79 Distribution of normal force chains in sand specimen at the final state of the test ( $u/L=0.1$ ) for different corrugation coefficient  $d/l$ : a)  $d/l=0.000$ , b)  $d/l=0.053$ , c)  $d/l=0.147$ , d)  $d/l=0.240$ , e)  $d/l=0.333$  and f)  $d/l=0.428$  ( $e_0=0.63$  and  $\sigma_n=48$  kPa) (red color corresponds to the force chain above the mean value). . . . . 103
- 4.80 Distribution of the horizontal strain  $\varepsilon_{xx}$  in sand specimen at the final state of the test ( $u/L=0.1$ ) obtained with DIC analysis for different corrugation coefficient  $d/l$ : a)  $d/l=0.000$ , b)  $d/l=0.053$ , c)  $d/l=0.147$ , d)  $d/l=0.240$ , e)  $d/l=0.333$  and f)  $d/l=0.427$  ( $e_0=0.63$  and  $\sigma_n=48$  kPa). . . 104
- 4.81 Distribution of the vertical strain  $\varepsilon_{yy}$  in sand specimen at the final state of the test ( $u/L=0.1$ ) obtained with DIC analysis for different corrugation coefficient  $d/l$ : a)  $d/l=0.000$ , b)  $d/l=0.053$ , c)  $d/l=0.147$ , d)  $d/l=0.240$ , e)  $d/l=0.333$  and f)  $d/l=0.427$  ( $e_0=0.63$  and  $\sigma_n=48$  kPa). . . 105
- 4.82 Distribution of the shear strain  $\varepsilon_{xy}$  in sand specimen at the final state of the test ( $u/L=0.1$ ) obtained with DIC analysis for different corrugation coefficient  $d/l$ : a)  $d/l=0.000$ , b)  $d/l=0.053$ , c)  $d/l=0.147$ , d)  $d/l=0.240$ , e)  $d/l=0.333$  and f)  $d/l=0.427$  ( $e_0=0.63$  and  $\sigma_n=48$  kPa). . . . 105
- 4.83 Distribution of the: A) horizontal strain  $\varepsilon_{xx}$ , B) vertical strain  $\varepsilon_{yy}$  and C) shear strain  $\varepsilon_{xy}$  in sand specimen at the final state of the test ( $u/L=0.1$ ) obtained with DIC method in: a) discrete analysis and b) experiments (Appendix A, Grabowski et al. (2023)) for the surface with corrugation coefficient  $d/l=0.053$  ( $e_0=0.63$  and  $\sigma_n=48$  kPa). . . . . 106
- 4.84 Distribution of the: A) horizontal strain  $\varepsilon_{xx}$ , B) vertical strain  $\varepsilon_{yy}$  and C) shear strain  $\varepsilon_{xy}$  in sand specimen at the final state of the test ( $u/L=0.1$ ) obtained with DIC method in: a) discrete analysis and b) in experiments (Appendix A, Grabowski et al. (2023)) for the surface with corrugation coefficient  $d/l=0.333$  ( $e_0=0.63$  and  $\sigma_n=48$  kPa). . . . . 107
- 4.85 Highlight of the shear zone based on shear strain  $\varepsilon_{xy}$  distribution at the final state ( $u/L=0.1$ ) obtained with discrete analysis for different corrugation coefficient  $d/l$ . . . . . 108
- 4.86 Distribution of the horizontal strain  $\varepsilon_{xx}$  for: a)  $u/L=0$ , b)  $u/L=0.02$ , c)  $u/L=0.04$ , d)  $u/L=0.06$ , e)  $u/L=0.08$ , and f)  $u/L=0.1$  obtained with DIC analysis for corrugation coefficient  $d/l=0.053$  ( $e_0=0.63$  and  $\sigma_n=48$  kPa). . . . . 109
- 4.87 Distribution of the vertical strain  $\varepsilon_{yy}$  for: a)  $u/L=0$ , b)  $u/L=0.02$ , c)  $u/L=0.04$ , d)  $u/L=0.06$ , e)  $u/L=0.08$ , and f)  $u/L=0.1$  obtained with DIC analysis for corrugation coefficient  $d/l=0.053$  ( $e_0=0.63$  and  $\sigma_n=48$  kPa). . . . . 109

|      |  |     |
|------|--|-----|
| 4.88 | Distribution of the shear strain $\varepsilon_{xy}$ for: a) $u/L=0$ , b) $u/L=0.02$ , c) $u/L=0.04$ , d) $u/L=0.06$ , e) $u/L=0.08$ , and f) $u/L=0.1$ obtained with DIC analysis for corrugation coefficient $d/l=0.053$ ( $e_0=0.63$ and $\sigma_n=48$ kPa). . . . .   | 110 |
| 4.89 | Distribution of the horizontal strain $\varepsilon_{xx}$ for: a) $u/L=0$ , b) $u/L=0.02$ , c) $u/L=0.04$ , d) $u/L=0.06$ , e) $u/L=0.08$ , and f) $u/L=0.1$ obtained with DIC analysis for corrugation coefficient $d/l=0.333$ ( $e_0=0.63$ and $\sigma_n=48$ kPa). . . . .  | 110 |
| 4.90 | Distribution of the vertical strain $\varepsilon_{yy}$ for: a) $u/L=0$ , b) $u/L=0.02$ , c) $u/L=0.04$ , d) $u/L=0.06$ , e) $u/L=0.08$ , and f) $u/L=0.1$ obtained with DIC analysis for corrugation coefficient $d/l=0.333$ ( $e_0=0.63$ and $\sigma_n=48$ kPa). . . . .  | 111 |
| 4.91 | Distribution of the shear strain $\varepsilon_{xy}$ for: a) $u/L=0$ , b) $u/L=0.02$ , c) $u/L=0.04$ , d) $u/L=0.06$ , e) $u/L=0.08$ , and f) $u/L=0.1$ obtained with DIC analysis for corrugation coefficient $d/l=0.333$ ( $e_0=0.63$ and $\sigma_n=48$ kPa). . . . .   | 111 |
| 5.1  | Triaxial compression test results of a: A) mobilized internal friction angle $\phi_i$ and B) volumetric strain $\varepsilon_v$ versus vertical normal strain $\varepsilon_1$ for sand specimens composed of spheres with rotational resistance for two different initial void ratios of sand: a) $e_0=0.60$ and b) $e_0=0.80$ ( $\sigma_0=5$ kPa and $d_{50}=5.0$ mm) (Grabowski et al., 2021b). . . . . | 116 |
| 5.2  | DEM model setup of silo with parallel walls (height $h_s=0.5$ m and width $b_s=0.2$ m) with: a) constant outlet velocity applied along entire bottom and b) bottom outlet of various width and location ( $h_g$ - groove height, $\alpha_g$ - groove inclination and $s_g$ - groove spacing) (Grabowski et al., 2021b). . . . .  | 117 |
| 5.3  | Rigid silo walls with different normalized surface roughness parameter $R_n=h_g/d_{50}$ : a) $R_n=1.0$ , b) $R_n=0.25$ and c) $R_n=0.01$ (Grabowski et al., 2021b). . . . .  | 118 |
| 5.4  | The size and the location of silo outlets used in discrete calculations: a) type '1' - symmetric outlet with a width of $b=30$ mm, b) type '2' - asymmetric outlet with a width of $b=30$ mm, c) type '3' - asymmetric outlet with a width of $b=60$ mm. . . . .   | 118 |
| 5.5  | Experimental (Tejchman, 2013) (empty dots) and numerical (full dots) evolution of: a) normalized resultant bottom force $P/G$ , b) normalized resultant wall friction force $T/G$ and c) normalized resultant wall normal force $N/G$ after bottom displacement $u$ for initially dense sand ( $e_0=0.60$ ) with different normalized roughness $R_n$ ( $G$ -sand weight). . . . .                       | 121 |
| 5.6  | Experimental (Tejchman, 2013) (empty dots) and numerical (full dots) evolution of: a) normalized resultant bottom force $P/G$ , b) normalized resultant wall friction force $T/G$ and c) normalized resultant wall normal force $N/G$ after bottom displacement $u$ with very rough wall for different initial void ratio $e_0$ of the sample ( $G$ -sand weight). . . . .                               | 121 |

|      |   |     |
|------|---|-----|
| 5.7  | Experimental (Tejchman, 2013) (empty dots) and numerical (full dots) evolution of resultant mobilized wall friction angle $\phi_w$ after bottom displacement $u$ for: a) initially dense sand ( $e_0=0.60$ ) with different normalized roughness $R_n$ , and b) very rough wall ( $R_n=1.0$ ) for different initial void ratio $e_0$ of the sample. . . . . | 122 |
| 5.8  | Distribution of: a) wall horizontal stress $\sigma_{11}$ and b) wall shear stress $\sigma_{21}$ in silo with very rough walls ( $R_n=1.0$ ) for initially dense sand ( $e_0 = 0.60$ ) at initial state, maximum state and residual state of quasi-static flow (Grabowski et al., 2021a). . . . .  | 125 |
| 5.9  | Distribution of: a) wall horizontal stress $\sigma_{11}$ and b) wall shear stress $\sigma_{21}$ in silo with rough walls ( $R_n=0.25$ ) for initially dense sand ( $e_0 = 0.60$ ) at initial state, maximum state and residual state of quasi-static flow (Grabowski et al., 2021a). . . . .  | 125 |
| 5.10 | Distribution of: a) wall horizontal stress $\sigma_{11}$ and b) wall shear stress $\sigma_{21}$ in silo with smooth walls ( $R_n=0.01$ ) for initially dense sand ( $e_0 = 0.60$ ) at initial state, maximum state and residual state of quasi-static flow (Grabowski et al., 2021a). . . . .   | 125 |
| 5.11 | Distribution of: a) wall horizontal stress $\sigma_{11}$ and b) wall shear stress $\sigma_{21}$ in silo with very rough walls ( $R_n=1.0$ ) for initially loose sand ( $e_0 = 0.76$ ) at initial state, maximum state and residual state of quasi-static flow (Grabowski et al., 2021a). . . . .  | 125 |
| 5.12 | Displacements in sand after bottom displacement $u$ in initially dense sand ( $e_0 = 0.60$ ) with normalized wall roughness $R_n = 1.0$ : a) $u = 10$ mm, b) $u = 20$ mm, c) $u = 30$ mm and d) zoomed view of (c) showing detailed displacements at the right wall (Grabowski et al., 2021b). . . . .  | 126 |
| 5.13 | Displacements in sand after bottom displacement $u$ in initially dense sand ( $e_0 = 0.60$ ) with normalized wall roughness $R_n = 0.25$ : a) $u = 10$ mm, b) $u = 20$ mm, c) $u = 30$ mm and d) zoomed view of (c) showing detailed displacements at the right wall (Grabowski et al., 2021b). . . . .   | 127 |
| 5.14 | Displacements in sand after bottom displacement $u$ in initially dense sand ( $e_0 = 0.60$ ) with normalized wall roughness $R_n = 0.01$ : a) $u = 10$ mm, b) $u = 20$ mm, c) $u = 30$ mm and d) zoomed view of (c) showing detailed displacements at the right wall (Grabowski et al., 2021b). . . . .   | 127 |
| 5.15 | Distribution of particle displacements $u$ across silo width at cross-section located: a) 10 cm, b) 25 cm and c) 40 cm above silo bottom after bottom displacement $u = 30$ mm from DEM for initially dense sand ( $e_0 = 0.60$ ) with different normalized wall roughness $R_n$ (Grabowski et al., 2021b). . . . .   | 128 |
| 5.16 | Distribution of particle rotations $\omega$ across silo width at cross-section located: a) 10 cm, b) 25 cm and c) 40 cm above silo bottom after bottom displacement $u = 30$ mm from DEM for initially dense sand ( $e_0 = 0.60$ ) with different normalized wall roughness $R_n$ (Grabowski et al., 2021b). . . . .  | 129 |

|      |   |     |
|------|---|-----|
| 5.17 | Distribution of void ratio $e$ across silo width at cross-section located:<br>a) 10 cm, b) 25 cm and c) 40 cm above silo bottom after bottom displacement $u = 30$ mm from DEM for initially dense sand ( $e_0 = 0.60$ ) with different normalized wall roughness $R_n$ (Grabowski et al., 2021b).              | 129 |
| 5.18 | Distribution of particle rotations after bottom displacement $u$ in initially dense sand ( $e_0 = 0.60$ ) with normalized wall roughness $R_n = 1.00$ : a) $u = 2.5$ mm, b) $u = 5.0$ mm, c) $u = 7.5$ mm, d) $u = 10.0$ mm, e) $u = 20.0$ mm and f) $u = 30.0$ mm (Grabowski et al., 2021b).                   | 130 |
| 5.19 | Distribution of particle rotations after bottom displacement $u$ in initially dense sand ( $e_0 = 0.60$ ) with normalized wall roughness $R_n = 0.25$ : a) $u = 2.5$ mm, b) $u = 5.0$ mm, c) $u = 7.5$ mm, d) $u = 10.0$ mm, e) $u = 20.0$ mm and f) $u = 30.0$ mm (Grabowski et al., 2021b).                   | 130 |
| 5.20 | Distribution of particle rotations after bottom displacement $u$ in initially dense sand ( $e_0 = 0.60$ ) with normalized wall roughness $R_n = 0.01$ : a) $u = 2.5$ mm, b) $u = 5.0$ mm, c) $u = 7.5$ mm, d) $u = 10.0$ mm, e) $u = 20.0$ mm and f) $u = 30.0$ mm (Grabowski et al., 2021b).                   | 130 |
| 5.21 | Distribution of void ratio after bottom displacement $u$ in initially dense sand ( $e_0 = 0.60$ ) with normalized wall roughness $R_n = 1.00$ : a) $u = 0.0$ mm, b) $u = 2.5$ mm, c) $u = 5.0$ mm, d) $u = 7.5$ mm, e) $u = 10.0$ mm, f) $u = 20.0$ mm and g) $u = 30.0$ mm (Grabowski et al., 2021b).          | 131 |
| 5.22 | Distribution of void ratio after bottom displacement $u$ in initially dense sand ( $e_0 = 0.60$ ) with normalized wall roughness $R_n = 0.25$ : a) $u = 0.0$ mm, b) $u = 2.5$ mm, c) $u = 5.0$ mm, d) $u = 7.5$ mm, e) $u = 10.0$ mm, f) $u = 20.0$ mm and g) $u = 30.0$ mm (Grabowski et al., 2021b).          | 131 |
| 5.23 | Distribution of void ratio after bottom displacement $u$ in initially dense sand ( $e_0 = 0.60$ ) with normalized wall roughness $R_n = 0.01$ : a) $u = 0.0$ mm, b) $u = 2.5$ mm, c) $u = 5.0$ mm, d) $u = 7.5$ mm, e) $u = 10.0$ mm, f) $u = 20.0$ mm and g) $u = 30.0$ mm (Grabowski et al., 2021b).          | 131 |
| 5.24 | Distribution of normal force chains after bottom displacement $u$ in initially dense sand ( $e_0 = 0.60$ ) with normalized wall roughness $R_n = 1.00$ : a) $u = 0.0$ mm, b) $u = 2.5$ mm, c) $u = 5.0$ mm, d) $u = 7.5$ mm, e) $u = 10.0$ mm, f) $u = 20.0$ mm and g) $u = 30.0$ mm (Grabowski et al., 2021b). | 132 |
| 5.25 | Distribution of normal force chains after bottom displacement $u$ in initially dense sand ( $e_0 = 0.60$ ) with normalized wall roughness $R_n = 0.25$ : a) $u = 0.0$ mm, b) $u = 2.5$ mm, c) $u = 5.0$ mm, d) $u = 7.5$ mm, e) $u = 10.0$ mm, f) $u = 20.0$ mm and g) $u = 30.0$ mm (Grabowski et al., 2021b). | 132 |
| 5.26 | Distribution of normal force chains after bottom displacement $u$ in initially dense sand ( $e_0 = 0.60$ ) with normalized wall roughness $R_n = 0.01$ : a) $u = 0.0$ mm, b) $u = 2.5$ mm, c) $u = 5.0$ mm, d) $u = 7.5$ mm, e) $u = 10.0$ mm, f) $u = 20.0$ mm and g) $u = 30.0$ mm (Grabowski et al., 2021b). | 132 |

- 5.27 Polar mean contact force distribution in sand specimen at the end of filling (black line) and after bottom displacement of  $u = 30$  mm (red line) with different normalized roughness  $R_n$ : a)  $R_n=1.0$ , b)  $R_n=0.25$  and c)  $R_n=0.01$  ( $e_0 = 0.60$ ) (Grabowski et al., 2021b). . . . . 133
- 5.28 Displacements in sand after bottom displacement  $u$  in initially loose sand ( $e_0 = 0.76$ ) with normalized wall roughness  $R_n = 1.0$ : a)  $u = 10$  mm, b)  $u = 20$  mm and c)  $u = 30$  mm (Grabowski et al., 2021b). . . . 134
- 5.29 Distribution of particle rotations after bottom displacement  $u$  in initially loose sand ( $e_0 = 0.76$ ) with normalized wall roughness  $R_n = 1.00$ : a)  $u = 2.5$  mm, b)  $u = 5.0$  mm, c)  $u = 7.5$  mm, d)  $u = 10.0$  mm, e)  $u = 20.0$  mm and f)  $u = 30.0$  mm (Grabowski et al., 2021b). . . . . 135
- 5.30 Distribution of void ratio after bottom displacement  $u$  in initially loose sand ( $e_0 = 0.76$ ) with normalized wall roughness  $R_n = 1.00$ : a)  $u = 0.0$  mm, b)  $u = 2.5$  mm, c)  $u = 5.0$  mm, d)  $u = 7.5$  mm, e)  $u = 10.0$  mm, f)  $u = 20.0$  mm and g)  $u = 30.0$  mm (Grabowski et al., 2021b). . . . . 135
- 5.31 Distribution of normal force chains after bottom displacement  $u$  in initially loose sand ( $e_0 = 0.76$ ) with normalized wall roughness  $R_n = 1.00$ : a)  $u = 0.0$  mm, b)  $u = 2.5$  mm, c)  $u = 5.0$  mm, d)  $u = 7.5$  mm, e)  $u = 10.0$  mm, f)  $u = 20.0$  mm and g)  $u = 30.0$  mm (Grabowski et al., 2021b). . . . . 135
- 5.32 Polar mean contact force distribution in sand specimen at the end of filling (black line) and after bottom displacement of  $u = 30$  mm (red line) for initially loose specimen ( $e_0 = 0.76$ ) with normalized roughness  $R_n=1.0$  (Grabowski et al., 2021b). . . . . 136
- 5.33 Evolution of: a) normalized resultant bottom force  $P/G$ , b) normalized resultant wall friction force  $T/G$  and c) normalized resultant wall normal force  $N/G$  during the discharge of a silo with the outlet of type '1' and a different normalized wall roughness  $R_n$  ( $e_0=0.60$ ) ( $G$ -sand weight). . . . . 138
- 5.34 Evolution of: a) normalized resultant bottom force  $P/G$ , b) normalized resultant wall friction force  $T/G$  and c) normalized resultant wall normal force  $N/G$  during the discharge of a silo with the outlet of type '2' and a different normalized wall roughness  $R_n$  ( $e_0=0.60$ ) ( $G$ -sand weight). . . . . 138
- 5.35 Evolution of: a) normalized resultant bottom force  $P/G$ , b) normalized resultant wall friction force  $T/G$  and c) normalized resultant wall normal force  $N/G$  during the discharge of a silo with the outlet of type '3' and a different normalized wall roughness  $R_n$  ( $e_0=0.60$ ) ( $G$ -sand weight). . . . . 138
- 5.36 Evolution of: a) normalized resultant bottom force  $P/G$ , b) normalized resultant wall friction force  $T/G$  and c) normalized resultant wall normal force  $N/G$  during the discharge of a silo with the outlet of type '1' and a different initial void ratio of sand ( $R_n=1.00$ ) ( $G$ -sand weight). . . . . 139

|      |  |     |
|------|--|-----|
| 5.37 | Evolution of: a) normalized resultant bottom force $P/G$ , b) normalized resultant wall friction force $T/G$ and c) normalized resultant wall normal force $N/G$ during the discharge of a silo with the outlet of type '2' and a different initial void ratio of sand ( $R_n=1.00$ ) (G-sand weight). . . . .   | 139 |
| 5.38 | Evolution of: a) normalized resultant bottom force $P/G$ , b) normalized resultant wall friction force $T/G$ and c) normalized resultant wall normal force $N/G$ during the discharge of a silo with the outlet of type '3' and a different initial void ratio of sand ( $R_n=1.00$ ) (G-sand weight). . . . .   | 139 |
| 5.39 | Sand deformation at different stages of discharge for silo filled with initially medium-dense sand ( $e_0 = 0.60$ ) with symmetric outlet of type '1' for different normalized roughness $R_n$ of the walls: A) $R_n = 1.00$ and B) $R_n = 0.01$ (the percentages indicate the amount of sand that has flowed out of the silo). . . . .                    | 141 |
| 5.40 | Sand deformation at different stages of discharge for silo filled with initially medium-dense sand ( $e_0 = 0.60$ ) with asymmetric outlet of type '2' for different normalized roughness $R_n$ of the walls: A) $R_n = 1.00$ and B) $R_n = 0.01$ (the percentages indicate the amount of sand that has flowed out of the silo). . . . .                   | 142 |
| 5.41 | Sand deformation at different stages of discharge for silo filled with initially medium-dense sand ( $e_0 = 0.60$ ) with asymmetric outlet of type '3' for different normalized roughness $R_n$ of the walls: A) $R_n = 1.00$ and B) $R_n = 0.01$ (the percentages indicate the amount of sand that has flowed out of the silo). . . . .                   | 142 |
| 5.42 | Distribution of particle rotations at different stages of discharge for silo filled with initially medium-dense sand ( $e_0 = 0.60$ ) with symmetric outlet of type '1' for different normalized roughness $R_n$ of the walls: A) $R_n = 1.00$ and B) $R_n = 0.01$ (the percentages indicate the amount of sand that has flowed out of the silo). . . . .  | 143 |
| 5.43 | Distribution of particle rotations at different stages of discharge for silo filled with initially medium-dense sand ( $e_0 = 0.60$ ) with asymmetric outlet of type '2' for different normalized roughness $R_n$ of the walls: A) $R_n = 1.00$ and B) $R_n = 0.01$ (the percentages indicate the amount of sand that has flowed out of the silo). . . . . | 144 |
| 5.44 | Distribution of particle rotations at different stages of discharge for silo filled with initially medium-dense sand ( $e_0 = 0.60$ ) with asymmetric outlet of type '3' for different normalized roughness $R_n$ of the walls: A) $R_n = 1.00$ and B) $R_n = 0.01$ (the percentages indicate the amount of sand that has flowed out of the silo). . . . . | 145 |
| 5.45 | Distribution of void ratio at different stages of discharge for silo filled with initially medium-dense sand ( $e_0 = 0.60$ ) with symmetric outlet of type '1' for different normalized roughness $R_n$ of the walls: A) $R_n = 1.00$ and B) $R_n = 0.01$ (the percentages indicate the amount of sand that has flowed out of the silo). . . . .          | 146 |

- 5.46 Distribution of void ratio at different stages of discharge for silo filled with initially medium-dense sand ( $e_0 = 0.60$ ) with asymmetric outlet of type '2' for different normalized roughness  $R_n$  of the walls: A)  $R_n = 1.00$  and B)  $R_n = 0.01$  (the percentages indicate the amount of sand that has flowed out of the silo). . . . . 147
- 5.47 Distribution of void ratio at different stages of discharge for silo filled with initially medium-dense sand ( $e_0 = 0.60$ ) with asymmetric outlet of type '3' for different normalized roughness  $R_n$  of the walls: A)  $R_n = 1.00$  and B)  $R_n = 0.01$  (the percentages indicate the amount of sand that has flowed out of the silo). . . . . 147
- 5.48 Distribution of normal force chains at different stages of discharge for silo filled with initially medium-dense sand ( $e_0 = 0.60$ ) with symmetric outlet of type '1' for different normalized roughness  $R_n$  of the walls: A)  $R_n = 1.00$  and B)  $R_n = 0.01$  (the percentages indicate the amount of sand that has flowed out of the silo). . . . . 149
- 5.49 Distribution of normal force chains at different stages of discharge for silo filled with initially medium-dense sand ( $e_0 = 0.60$ ) with asymmetric outlet of type '2' for different normalized roughness  $R_n$  of the walls: A)  $R_n = 1.00$  and B)  $R_n = 0.01$  (the percentages indicate the amount of sand that has flowed out of the silo). . . . . 149
- 5.50 Distribution of normal force chains at different stages of discharge for silo filled with initially medium-dense sand ( $e_0 = 0.60$ ) with asymmetric outlet of type '3' for different normalized roughness  $R_n$  of the walls: A)  $R_n = 1.00$  and B)  $R_n = 0.01$  (the percentages indicate the amount of sand that has flowed out of the silo). . . . . 150
- 5.51 Sand deformation for initially loose sand ( $e_0 = 0.76$ ) during flow in silo with rough walls ( $R_n = 1.00$ ) with: A) symmetric outlet of type '1', B) asymmetric outlet of type '2' and C) asymmetric outlet of type '3' (percentages indicate the amount of sand that flow out of the silo). . 152
- 5.52 Distribution of particle rotations for initially loose sand ( $e_0 = 0.76$ ) during flow in silo with rough walls ( $R_n = 1.00$ ) with: A) symmetric outlet of type '1', B) asymmetric outlet of type '2' and C) asymmetric outlet of type '3' (percentages indicate the amount of sand that flow out of the silo). . . . . 153
- 5.53 Distribution of void ratio for initially loose sand ( $e_0 = 0.76$ ) during flow in silo with rough walls ( $R_n = 1.00$ ) with: A) symmetric outlet of type '1', B) asymmetric outlet of type '2' and C) asymmetric outlet of type '3' (percentages indicate the amount of sand that flow out of the silo). . . . . 154
- 5.54 Distribution of normal force chains for initially loose sand ( $e_0 = 0.76$ ) during flow in silo with rough walls ( $R_n = 1.00$ ) with: A) symmetric outlet of type '1', B) asymmetric outlet of type '2' and C) asymmetric outlet of type '3' (percentages indicate the amount of sand that flow out of the silo). . . . . 155

|      |  |     |
|------|--|-----|
| 5.55 | Calculated distribution of: A) wall horizontal stresses $\sigma_{11}$ and B) wall shear stresses $\sigma_{21}$ during the flow in silo at the: a) initial state, b) maximum state and c) in the residual phase (type '1', $e_0=0.60$ , $R_n=1.00$ ). . .   | 157 |
| 5.56 | Calculated distribution of: A) wall horizontal stresses $\sigma_{11}$ and B) wall shear stresses $\sigma_{21}$ during the flow in silo at the: a) initial state, b) maximum state and c) in the residual phase (type '1', $e_0=0.60$ , $R_n=0.01$ ). . .   | 157 |
| 5.57 | Calculated distribution of: A) wall horizontal stresses $\sigma_{11}$ and B) wall shear stresses $\sigma_{21}$ during the flow in silo at the: a) initial state, b) maximum state and c) in the residual phase (type '2', $e_0=0.60$ , $R_n=1.00$ ). . .   | 158 |
| 5.58 | Calculated distribution of: A) wall horizontal stresses $\sigma_{11}$ and B) wall shear stresses $\sigma_{21}$ during the flow in silo at the: a) initial state, b) maximum state and c) in the residual phase (type '2', $e_0=0.60$ , $R_n=0.01$ ). . .   | 158 |
| 5.59 | Calculated distribution of: A) wall horizontal stresses $\sigma_{11}$ and B) wall shear stresses $\sigma_{21}$ during the flow in silo at the: a) initial state, b) maximum state and c) in the residual phase (type '3', $e_0 = 0.60$ , $R_n = 1.0$ ) .   | 158 |
| 5.60 | Calculated distribution of: A) wall horizontal stresses $\sigma_{11}$ and B) wall shear stresses $\sigma_{21}$ during the flow in silo at the: a) initial state, b) maximum state and c) in the residual phase (type '3', $e_0 = 0.60$ , $R_n = 0.01$ )  | 158 |
| 5.61 | Calculated distribution of: A) wall horizontal stresses $\sigma_{11}$ and B) wall shear stresses $\sigma_{21}$ during the flow in silo at the: a) initial state, b) maximum state and c) in the residual phase (type '1', $e_0 = 0.76$ , $R_n = 1.0$ ) .   | 159 |
| 5.62 | Calculated distribution of: A) wall horizontal stresses $\sigma_{11}$ and B) wall shear stresses $\sigma_{21}$ during the flow in silo at the: a) initial state, b) maximum state and c) in the residual phase (type '2', $e_0 = 0.76$ , $R_n = 1.0$ ) .   | 159 |
| 5.63 | Calculated distribution of: A) wall horizontal stresses $\sigma_{11}$ and B) wall shear stresses $\sigma_{21}$ during the flow in silo at the: a) initial state, b) maximum state and c) in the residual phase (type '3', $e_0 = 0.76$ , $R_n = 1.0$ ) .   | 159 |
| A.1  | Experimental setup: a) photograph of the experimental setup with a sand sample prepared for the shear test and b) computer visualization of individual parts of the modified box of the direct shear apparatus (Grabowski et al. (2023), CC BY 4.0). . . . .   | 166 |
| A.2  | Photograph of: a) a PLA-printed shear box, and b) an exemplary PLA-printed sinusoidal corrugated surface used during the investigation. .  | 167 |
| A.3  | Evolution of: A) mobilized shear stress $\tau$ and B) volumetric strain $\varepsilon_v$ versus normalized horizontal displacement $u/L$ for sample composed of cohesionless sand obtained in direct shear test for: a) brass shear box and b) PLA printed shear box ( $e_0=0.63$ and $\sigma_n=48$ kPa). . . . | 167 |
| A.4  | Cross-sections (3D STL models) of sinusoidal corrugated surfaces used in experiments with different corrugation coefficients $d/l$ (Grabowski et al. (2023), CC BY 4.0). . . . .   | 168 |
| A.6  | Front view of the sand sample: a) prepared for the interface shear test and b) at the final state of the test for exemplary surface with corrugation coefficient $d/l=0.147$ . . . . .   | 170 |



|      |  |     |
|------|--|-----|
| A.7  | DIC analysis: a) view of the sample with defined region of interest and b) close up view of the speckle pattern in a subset window (from the Ncorr software) (Grabowski et al. (2023), CC BY 4.0). . . . .   | 171 |
| A.8  | Evolution of: a) mobilized shear stress $\tau$ and b) volumetric strain $\varepsilon_v$ versus normalized horizontal displacement $u/L$ for different corrugation coefficient $d/l$ obtained in laboratory tests ( $e_0=0.63$ and $\sigma_n=48$ kPa) (Grabowski et al. (2023), CC BY 4.0). . . . .                   | 172 |
| A.9  | Calculated: A) effective friction coefficient $\mu_{eff}$ and B) wall contact factor $a_w$ versus normalized horizontal displacement $u/L$ for different corrugation coefficient $d/l$ obtained in laboratory tests. The red line represents the value of $a_w=0.2$ recommended by the the EN 1991-4 (2006). . . . . | 174 |
| A.10 | Horizontal displacement $v_x$ distribution at the final state ( $u/L=0.1$ ) obtained with DIC analysis for different corrugation coefficient $d/l$ (Grabowski et al. (2023), CC BY 4.0). . . . .   | 175 |
| A.11 | Vertical displacement $v_y$ distribution at the final state ( $u/L=0.1$ ) obtained with DIC analysis for different corrugation coefficient $d/l$ (Grabowski et al. (2023), CC BY 4.0). . . . .   | 176 |
| A.12 | Horizontal strain $\varepsilon_{xx}$ distribution at the final state ( $u/L=0.1$ ) obtained with DIC analysis for different corrugation coefficient $d/l$ (Grabowski et al. (2023), CC BY 4.0). . . . .  | 177 |
| A.13 | Vertical strain $\varepsilon_{yy}$ distribution at the final state ( $u/L=0.1$ ) obtained with DIC analysis for different corrugation coefficient $d/l$ (Grabowski et al. (2023), CC BY 4.0). . . . .  | 177 |
| A.14 | Shear strain $\varepsilon_{xy}$ distribution at the final state ( $u/L=0.1$ ) obtained with DIC analysis for different corrugation coefficient $d/l$ (Grabowski et al. (2023), CC BY 4.0). . . . .   | 178 |
| A.15 | Highlight of the shear zone based on shear strain $\varepsilon_{xy}$ distribution at the final state ( $u/L=0.1$ ) obtained with DIC analysis for different corrugation coefficient $d/l$ (Grabowski et al. (2023), CC BY 4.0). . . . .  | 178 |
| A.16 | Evolution of the horizontal strain $\varepsilon_{xx}$ in the entire specimen obtained with DIC analysis at different phases of the test $u/L$ for corrugation coefficient $d/l=0.053$ (Grabowski et al. (2023), CC BY 4.0). . . . .  | 180 |
| A.17 | Evolution of the horizontal strain $\varepsilon_{yy}$ in the entire specimen obtained with DIC analysis at different phases of the test $u/L$ for corrugation coefficient $d/l=0.053$ (Grabowski et al. (2023), CC BY 4.0). . . . .  | 180 |
| A.18 | Evolution of the horizontal strain $\varepsilon_{xy}$ in the entire specimen obtained with DIC analysis at different phases of the test $u/L$ for corrugation coefficient $d/l=0.053$ (Grabowski et al. (2023), CC BY 4.0). . . . .  | 181 |
| A.19 | Evolution of the horizontal strain $\varepsilon_{xx}$ in the entire specimen obtained with DIC analysis at different phases of the test $u/L$ for corrugation coefficient $d/l=0.333$ (Grabowski et al. (2023), CC BY 4.0). . . . .  | 181 |
| A.20 | Evolution of the horizontal strain $\varepsilon_{yy}$ in the entire specimen obtained with DIC analysis at different phases of the test $u/L$ for corrugation coefficient $d/l=0.333$ (Grabowski et al. (2023), CC BY 4.0). . . . .  | 182 |

A.21 Evolution of the horizontal strain  $\varepsilon_{xy}$  in the entire specimen obtained with DIC analysis at different phases of the test  $u/L$  for corrugation coefficient  $d/l=0.333$  (Grabowski et al. (2023), CC BY 4.0). . . . . 182

# List of Tables

|     |  |     |
|-----|--|-----|
| 4.1 | Discrete material local variables used in parametric study. . . . .  | 35  |
| 4.2 | Properties of the 'Karlsruhe' sand (Kolymbas and Wu, 1990). . . . .  | 35  |
| 4.3 | Determined discrete material local variables. . . . .  | 41  |
| 4.4 | Discrete material parameters for interface shear test. . . . .   | 63  |
| 4.5 | Calculated values of maximum surface friction angle $\phi_{s,max}$ , residual surface friction angle $\phi_{s,res}$ and residual volumetric strain $\varepsilon_v$ for different normalized surface roughness $R_n$ using spheres and clumps (Grabowski et al. (2021a), licensed under CC BY 4.0). . . . .         | 67  |
| 4.6 | Horizontal slip along the rigid bottom surface. . . . .  | 73  |
| 4.7 | Discrete material parameters for interface shear test. . . . .   | 94  |
| 4.8 | Calculated values of peak effective wall friction coefficient $\mu_{eff,max}$ , effective wall friction coefficient $\mu_{eff,res}$ and residual volumetric strain $\varepsilon_v$ for different corrugation coefficient $d/l$ . . . . .   | 98  |
| 4.9 | Comparison between experimental and numerical values of the wall contact factor $a_w$ in the residual state calculated with the Equation 1.7 and with the DIC technique. . . . .   | 107 |
| 5.1 | Discrete material parameters for the quasi-static silo flow. . . . .   | 115 |
| 5.2 | Experimental (Tejchman, 2013) and numerical values of the normalized resultant vertical bottom force $P_{min}$ , the resultant vertical wall friction force $T$ , the resultant horizontal wall force $N$ , and the resultant mobilized wall friction angle $\phi_w$ for initially dense sand during flow. . . . . | 120 |
| 5.3 | Experimental and numerical values of the resultant vertical bottom force $P$ in the residual state for initially dense sand during flow as compared to the theoretical silo formula by Drescher (1991) and standard formula by EN 1991-4 (2006). . . . .   | 123 |
| 5.4 | Thickness of the wall shear zones $t_s$ at the mid-height of the silo obtained in DEM simulations ( $d_{50}=1.5$ mm) compared to the experiments ( $d_{50}=0.5$ mm) and ( $d_{50}=1.0$ mm) (Grabowski et al., 2021b). . . . .  | 129 |
| A.1 | Properties of dry cohesionless sand used in the experiments (Grabowski et al. (2023), CC BY 4.0). . . . .  | 169 |
| A.2 | Calculated values of peak effective wall friction coefficient $\mu_{eff,max}$ , effective wall friction coefficient $\mu_{eff,res}$ and residual volumetric strain $\varepsilon_v$ for different corrugation coefficient $d/l$ . . . . .   | 173 |

